THÈSE

Pour obtenir le grade de

DOCTEUR DE L'UNIVERSITÉ GRENOBLE ALPES

École doctorale : STEP - Sciences de la Terre de l'Environnement et des Planètes
Spécialité : Sciences de la Terre et de l'Environnement
Unité de recherche : Institut des Sciences de la Terre

Réhabilitation des sites aurifères en Guyane Française : Stabilisation et devenir du mercure et métalloïdes

Restoration of gold mines in French Guiana : stabilisation and fate of mercury and metal(oid)s

Présentée par :

Naomi NITSCHKE

Direction de thèse :

Stephane GUEDRON Université Grenoble Alpes	Directeur de thèse
David AMOUROUX Directeur de Recherche, CNRS	Co-directeur de thèse
Jennifer HELLAL Ingénieure-chercheuse au BRGM d'Orléans	Co-directrice de thèse
Arnauld HEURET Enseignant-chercheur, Université de Guyane	Co-encadrant de thèse

Rapporteurs :

Cécile QUANTIN
PROFESSEURE DES UNIVERSITES, Université Paris-Saclay
Adrien MESTROT
FULL PROFESSOR, Universität Bern

Thèse soutenue publiquement le **11 juin 2025**, devant le jury composé de :

Stéphane GUEDRON, DIRECTEUR DE RECHERCHE, IRD délégation Sud-Est	Directeur de thèse
David AMOUROUX, DIRECTEUR DE RECHERCHE, CNRS délégation Aquitaine	Co-directeur de thèse
Cécile QUANTIN, PROFESSEURE DES UNIVERSITES, Université Paris-Saclay	Rapporteure
Adrien MESTROT, FULL PROFESSOR, Universität Bern	Rapporteur
Agnès RICHAUME, PROFESSEURE DES UNIVERSITES, Université Lyon 1 - Claude Bernard	Examinatrice
Laurie BOITHIAS, PHYSICIENNE ADJOINTE, Observatoire Midi-Pyrénées	Examinatrice
Cécile GAUTHERON, PROFESSEURE DES UNIVERSITES, Université Grenoble Alpes	Présidente

Invités :

Arnauld Heuret
MAITRE DE CONFERENCES, Université de Guyane
Jennifer Harris
SCIENTIST, BRGM Orléans

THÈSE

UNIVERSITÉ GRENOBLE ALPES

École doctorale des sciences de la Terre, de l'environnement et des planètes

Présentée par

Naomi NITSCHKE

Pour l'obtention du grade de docteur de l'Université Grenoble Alpes

Sujet de la thèse :

Réhabilitation de mines d'or en Guyane : stabilisation et devenir du mercure et métalloïdes

MEMBRES DU JURY

RAPPORTEURS

• Cécile QUANTIN	Université Paris Saclay, France
• Adrien MESTROT	Universität Bern, Switzerland

EXAMINATEURS

• Agnès RICHAUME	Université Claude Bernard, France.
• Laurie BOITHIAS	Université Toulouse III – Paul Sabatier
• Cécile GAUTHERON	Université Grenoble Alpes, France

DIRECTEURS

• Stéphane GUÉDRON	Université Grenoble Alpes, France
• David AMOUROUX	Université de Pau et des Pays de l'Adour, France

ENCADRANTS

• Jennifer HARRIS	Bureau de Recherches Géologiques et Minières, France
• Arnauld HEURET	Université de Guyane, France
• Stéphane TARAVELLA	SAS GAIA, France

Abstract

Gold mining is responsible for a combination of environmental impacts, including soil erosion and metal(loid) export to surrounding hydrosystems. In Amazonian ecosystems, this impact is exacerbated due to strong and frequent rainfall, and to elevated background concentrations of metals like mercury (Hg) in the soils which are remobilised during the extraction process. Additionally, anthropogenic Hg is used by illegal miners in artisanal and small-scale gold mining (ASGM) for gold amalgamation and can be released to the environment. Although there are guidelines for gold mine restoration, the impact of this restoration on the reduction of particle and metal(loid) export is not well assessed.

This work aims to investigate gold mines and their restoration in an Amazonian ecosystem (French Guiana), focusing on their impact on metal(loid) export and fate, more specifically Hg, lead (Pb) and arsenic (As). To do so, particle and metal(loid) export, as well as Hg distribution, were investigated at several scales from the square-meter scale to the whole territory of French Guiana.

At the square-meter scale, a strong reduction in particle export was observed 4 years after restoration, coupled to a 200-fold decrease in metal(loid) export resulting from the rapid spontaneous colonisation by herbaceous plants. However, the soil microbiological activity did not increase significantly in this timespan, possibly due to the depletion of nutrients by the herbaceous plant growth.

At the scale of the gold mined watershed, the mining flat was shown to still contribute to an input of 100-300 $kg.km^{-2}$ of particles to the river, 8 months after restoration. This led to a 2-fold increase in metal(loid) export downstream of the mining flat compared to upstream. The origin of suspended particles in the river was investigated by coupling the hydrological decomposition of two flood events using geochemical tracers in the filtered fraction, to multielemental and infra-red data of the suspended particles. The results point towards riverbank erosion and riverbed sediment remobilisation as the main source of particles to the river. However, the input of particulate total Hg (THg) appears to also originate from overland flow inducing topsoil erosion.

Hg distribution was then assessed in different compartments on two mining sites. Hg isotopic composition showed a significant contribution (3 – 82 %) of anthropogenic Hg in illegal mining pond sediments, but not in legally mined soils. Additionnally, high dissolved gaseous mercury (DGM) concentrations were measured in these same ponds, making them a potential source of elemental Hg to the atmosphere through volatilisation. When comparing two mining sites, higher THg and methylmercury (MeHg) concentrations were observed in mining ponds where the illegal activity was more recent and more extensive.

Finally, at the scale of French Guiana, Hg isotopic composition was measured in archive sediments distributed across the territory's main rivers. A binary mixing model was constructed using literature data to distinguish between anthropogenic Hg used by miners and pristine geogenic Hg. The contribution of anthropogenic Hg in river sediments varied widely and reflected the geographical extent of ASGM activities in French Guiana.

This work provides both mining companies and regulating agencies with i) insights on the fate of restored gold mines concerning particle and metal(loid) export, ii) recommendations on the critical points which need attention in the restoration process, and iii) tools to assess the impact and distribution of legal and/or illegal gold mining.

Résumé

L'exploitation aurifère est responsable de nombreux impacts environnementaux, notamment l'érosion des sols et l'export de métaux vers les hydrosystèmes environnants. Dans les écosystèmes amazoniens, cet impact est accentué en raison de fortes pluies ainsi que par les fonds géochimiques élevés de métaux comme le mercure (Hg) dans les sols qui sont remobilisés lors du procédé d'extraction. En outre, du Hg d'origine anthropique est utilisé par les orpailleurs illégaux pour l'amalgamation de l'or, et peut être relâché dans l'environnement. Bien qu'il existe des directives pour la réhabilitation des sites miniers, l'effet de cette réhabilitation sur la réduction de l'export des particules et des contaminants reste peu évalué.

Ce travail vise à étudier les sites aurifères et leur réhabilitation dans un écosystème amazonien (Guyane française), en évaluant leur impact sur l'export et le devenir des métaux et métalloïdes, plus spécifiquement le Hg, le plomb (Pb) et l'arsenic (As). Pour ce faire, l'export des particules et des contaminants, ainsi que la distribution du Hg ont été étudiés à plusieurs échelles, de l'échelle du mètre carré à celle du territoire guyanais.

À l'échelle du mètre carré, une forte réduction de l'export des particules a été observée quatre ans après la réhabilitation, accompagnée d'une diminution d'un facteur 200 de l'export des contaminants, liée à une colonisation spontanée par des plantes herbacées. Toutefois, l'activité microbiologique des sols n'a pas significativement augmenté durant cette période, possiblement en raison de l'épuisement des nutriments par la croissance des herbacées.

À l'échelle du bassin versant, il a été démontré que la zone exploitée contribuait encore à hauteur de 100 à 300 $kg.km^{-2}$ d'apport de particules dans la rivière huit mois après la réhabilitation. Cela a entraîné un doublement de l'exportation des contaminants en aval par rapport à l'amont. L'origine des particules en suspension dans la rivière a été étudiée en couplant une décomposition hydrologique de deux crues à l'aide de traceurs géochimiques dans la fraction filtrée, avec des données multi-élémentaires et infrarouges sur les particules en suspension. Les résultats indiquent que l'érosion des berges et la remobilisation des sédiments du lit de la rivière seraient les principales sources de particules.

La distribution du Hg dans différents compartiments a ensuite été évaluée sur deux sites miniers. La composition isotopique du Hg a révélé une contribution significative (de 3 à 82 %) de Hg anthropique dans les sédiments des bassins d'orpaillage illégaux, mais pas dans les sols exploités légalement. De plus, des concentrations élevées de Hg gazeux dissous ont été mesurées dans ces mêmes bassins, qui deviennent une source potentielle de Hg élémentaire pour l'atmosphère.

Enfin, à l'échelle de la Guyane, la composition isotopique du Hg a été mesurée dans des sédiments d'archives répartis dans les principales rivières du territoire. Un modèle de mélange binaire a été construit pour distinguer le Hg anthropique utilisé par les orpailleurs du Hg géogénique naturel. La contribution du Hg anthropique dans les sédiments fluviaux reflète l'étendue géographique des activités d'orpaillage illégal en Guyane.

Ce travail a permis de fournir, à la fois aux entreprises minières et aux organismes de régulation : i) des éléments de compréhension sur le devenir des sites réhabilités en matière d'export de particules et de contaminants, ii) des recommandations sur les points critiques nécessitant une attention particulière lors du processus de réhabilitation, et iii) des outils pour évaluer l'impact et la répartition de l'orpaillage légal et/ou illégal.

Acknowledgements

First of all, I would like to thank my advisors, Stéphane, David, Jenny and Arnauld. Although there were many of you, I think we managed to create a nice working environment where each of you helped me grow scientifically in different ways.

I would like to thank Cécile Quantin and Adrien Mestrot, as well as Agnès Richaume, Laurie Boithias and Cécile Gautheron for agreeing to review this work.

During the past three years, I have spent time in different places and labs, and everywhere I found people I could rely on. In Grenoble I thank Djami, my "co-bureau" who always brightened the day with her happiness. Courage, you're getting there too! I thank all the engineers (Sylvain, Sabine, Delphine, …) who introduced me to their instruments and helped with the analyses. In Pau, I thank Manu, for his help and guidance in the lab, and on the field. Also, thank you for the help in digging those holes in the placettes, I know you always enjoyed it. I also want to thank Océane who helped in a lot of mercury analyses and became a friend. Thank you Alina for so many things, amongst which the discussions about science and patriarchy. In French Guiana, I want to thank the mining company SAS GAIA who provided funding and logistical support. Thank you Stéphane Taravella for your interest in this work and for your help in understanding all the regulations in place in French Guiana. I also want to thank Akram, who was involved in all the sampling campaigns and helped with practical aspects, but also ended up sampling and filtering the water samples with us. I want to thank Benoit Burban who was in charge of installing and replacing the passive mercury samplers in the Guyaflux.

I also want to thank Cédric Legout and Antonio Martinez Cortizas. In their respective field, both got much more implicated than I would have expected and helped me navigate the worlds of hydrology and infrared spectroscopy that were previously unknown to me. Many thanks to Jean-Christophe Roggy, Laurent Oxarango, Valérie Laperche and Muriel Raveton for the fruitful discussions and advice every year concerning the advancement of the project.

Thank you to my "little hands", Oumou and Camille, the interns that I got to supervise. Through them, I got to experience the joy of transmission.

Finally, I want to thank my friends and family for their emotional support during the past three years.

Merci Margaux d'avoir relu certaines parties de mon manuscrit, mais surtout, merci pour les escapades du midi, qui m'aéraient l'esprit et me permettaient d'y retourner régénérée.

Merci à mon papa, pour le soutien, les conseils, et pour venir faire la nounou quand j'avais besoin de m'enfermer pour écrire. Pour tout, merci.

Y finalmente quiero agradecer a mis peruanos favoritos. Alex y Fabi, gracias por aguantar mis ausencias, y por recordarme que hay cosas más importantes que el trabajo. Los amo más que la pizza!

Table of contents

Abstract i

Résumé ii

Acknowledgements iii

Table of contents iv

List of Figures vii

List of Tables x

List of Abbreviations xi

General Introduction 1

1. Motivation 1

2. Thesis objectives 2

3. Document structure 3

1. Chapter 1. Current state of knowledge 5

1.1. Generalites on the Guyana Shield and French Guiana 6

1.2. Gold mining in French Guiana 8

1.3. Mercury in the Amazon 15

1.4. Additional metal(loid)s of concern in French Guiana and the Amazon 22

2. Chapter 2. Study area and sampling strategy 27

2.1. Description of the mining sites 28

2.2. Particle and metal(loid) export: experimental design 31

2.3. Sampling strategies 33

3. Chapter 3. 39

Introduction 40

3.1. Article I – Post-exploitation fate of alluvial goldmines in the Amazon: soil erosion, metal(loid) remobilisation, and ecological functions evolution during restoration 41

3.1.1. Abstract 42

3.1.2. Introduction 43

3.1.3. Materials and Methods 45

3.1.4. Results 50

3.1.5. Discussion 57

3.1.6. Conclusion 63

3.1.7. Supplementary Information 64

4. Chapter 4. 81

Introduction 82

4.1. Article II – Restored gold mine in an Amazonian catchment (French Guiana): source tracking and hydro-sedimentary mass balance of carbon and particulate emissions 83
4.1.1. Abstract 84
4.1.2. Introduction 85
4.1.3. Materials and Methods 87
4.1.4. Results and discussion 92
4.1.5. Conclusion 105
4.1.6. Supplementary Information 106
4.2. Article III – Distribution and exports of mercury and metal(loid)s in a restored gold-mined Amazonian watershed (French Guiana) 112
4.2.1. Abstract 113
4.2.2. Introduction 114
4.2.3. Materials and Methods 116
4.2.4. Results and Discussion 119
4.2.5. Conclusion 126
4.2.6. Supplementary Information 127
5. Chapter 5. 133
Introduction 134
5.1. Article IV – Legal and illegal gold mining in the Amazon: distribution of mercury species and isotopes in a "mine ecosystem" 135
5.1.1. Abstract 136
5.1.2. Introduction 137
5.1.3. Materials and Methods 139
5.1.4. Results and Discussion 145
5.1.5. Conclusion 155
5.1.6. Supplementary Information 157
6. Chapter 6. 159
Introduction 160
6.1. Article V – Evaluation of the Hg contamination from goldmining in French Guiana at the watershed scale using Hg isotopic composition in river sediments 161
6.1.1. Abstract 162
6.1.2. Introduction 163
6.1.3. Materials and Methods 165
6.1.4. Results and Discussion 168
6.1.5. Conclusion 175
6.1.6. Supplementary Information 176
7. Chapter 7. Conclusions and Outlook 185

7.1. Initial objectives 186
7.2. Synthesis of the main results and perspectives. 187
7.3. Propositions for an efficient gold mine restoration 190
8. Annexe : Synthèse en Français 193
8.1. Introduction 194
8.2. Sites d'étude 197
8.3. Résultats 201
8.4. Conclusions et propositions et conseils pour la réhabilitation minière 214

List of Figures

Figure 1.1 Simplified geological map of French Guiana, adapted from Kroonenberg et al. (2016). 7
Figure 1.2. Illegal gold miners using a high-pressure water hose (left), and modern alluvial gold exploitation showing an excavator, gravel pump, screen with bars and gold mat. Reproduced from (Jébrak et al. 2021) with permission from P. Rostan. 9
Figure 1.3. Exploitation and restoration steps of an alluvial gold mine. 13
Figure 1.4. Synthesis of the Hg dynamics in the Amazon reproduced from Crespo-Lopez et al. (2021). 20
Figure 2.1. Awa gold mining site with legal (brown) and illegal (red) exploitation areas. The location of the upstream and downstream hydrological stations are displayed as orange dots. 28
Figure 2.2. Selected pictures from the Awa gold mining site with A) the landscaped gold mining flat, tree plantations B) in the nursery and C) on site, and D) reconstructed river path. 29
Figure 2.3. Sophie gold mining site (named Guerilha with the limits of the PER in the black square) with surrounding streams in blue and the evidence of illegal gold mining in red (qualitative assessment based on observations). 30
Figure 2.4. Pictures on the Sophie prospection site, with A) shafts constructed by illegal gold miners to access the gold bearing vein, B) washing site where the ore is crushed and then mixed with water and Hg is added to recover the gold, C) 10 m depth core sampling for Au analysis in prospection stage.. 31
Figure 2.5. Erosion plots on the landscaped (A) and the tree-covered (B) sites, and erodibility measurements on mining flat topsoil (C) and river bed sediment (D)..... 32
Figure 2.6. Hydrological station with A) staff gauge, B) turbidity and water height sensors and C) automatic water sampler. 33
Figure 2.7. Localisation of the illegal mining ponds sampled on the Awa site (red dots). 34
Figure 2.8. Examples of sample collection and treatment for different compartments: A) soil profile, B) interstitial soil water, C) wet deposition, D) throughfall, E) active gaseous mercury sampling, F) passive gaseous mercury sampling (MerPAS), G) herbaceous plant (Cyperaceae), G) water filtering station on-site. 36
Figure 3.1. Study site, timeline with rainfall data (Grand-Santi meteorological station (meteo.data.gouv.fr [last accessed on 3rd February 2025])) and sampling points for the erosion (round) and soil function (diamond) experiments. 46
Figure 3.2. Evolution of exports of A) particle, B) Hg, C) Pb, D) As normalised by rainfall (mm) and E) root density over time after rehabilitation. 53
Figure 3.3. Evolution of soil functions linked to the carbon (A) and nitrogen (B) cycles at different time points after restoration. The top panels are radar plots, normalized by the value at T0 (dark brown). 54
Figure 3.4. NMDS ordination of bacterial diversity profiles from the mining site soils during time after restoration. Significant environmental variables ($p<0.05$) are represented by vectors fitted to the NMDS ordination that indicate the direction and magnitude of the change of the variable. (WHC: water holding capacity, URE: urease enzyme activity, 18S: fungi 18S gene qPCR). 56
Figure 3.5. Synthesis of parameters impacting the restoration of a gold mined soil. Natural parameters are depicted in yellow circles, and human intervention is in red circles. Red arrows represent negative impact and green arrows positive impact. 58
Figure 4.1. Study site with the two monitoring and sampling stations on the Awa gold-mined river. 88
Figure 4.2. Chronicles of discharge (Q), suspended solid concentrations (SSC) and rainfall at two monitoring stations located downstream and upstream of a mining flat. The positions of the two flood events studied subsequently (Evt-1 and -2) are depicted as vertical bands. 92

Figure 4.3. A) Discharge (Q, blue) and cumulated volume (black), B) SSC (brown) and cumulated particles (black) on two rain events upstream (full line) and downstream (dotted line) of the mining site. 94
Figure 4.4. Selected tracers in the different endmembers from the filtered fraction (Si and U, blue) and from the particulate fraction (POC and δ13C, brown) on a restored gold-mined river, as well as kaolinite order evolution along a forest soil profile. 96
Figure 4.5. A) Concentrations of U (brown) and Si (green), B) Contribution of overland flow and C) reconstruction of the groundwater (green) and overland flow (brown) to the total (blue) discharge during two flood events, upstream (full line) and downstream (dotted line) of the mining flat. The total flow coefficient (C_{TF}) and overland flow coefficient (C_{OF}) are inserted in the bottom panels. 97
Figure 4.6. A) FTIR averaged spectra with standard deviation. The main peaks with their corresponding wavenumber and bond type are highlighted in blue for peaks attributed to kaolinite, and in brown for peaks attributed to organic matter (OM), extracted scores for B) tPC1 and C) tPC3 as well as the relationships of their respective loadings vs Al and C respectively and D) example of an XRD diffractogram of river particulate matter 99
Figure 4.7. Evolution of A) SSC, B) OM (red) and kaolinite (purple), and C) reconstruction of the hydrograph with groundwater (green) and runoff (brown) to the total (blue) discharge during a rain event (event-1). 101
Figure 4.8. Concentration in the filtered and particulate (per volume and per SPM mass) fractions of A) THg, B) MeHg, C) Pb and D) As in river water downstream (yellow) and upstream (green) of the mining flat pooled from sampling campaigns G2-G3. 120
Figure 4.9. Dissolved Gaseous Mercury (DGM, circles) and discharge (Q, lines) during flood events upstream (green) and downstream (yellow) of the mining flat. 122
Figure 4.10. Superposition of the decomposed hydrograph (overland flow, brown; groundwater, green; total, blue from article 4.1) with concentrations of filtered THg and MeHg, as well as particulate THg and MeHg. The arrival of groundwater and overland flow are depicted as green and brown bands respectively. 123
Figure 4.11. Estimation of seasonal filtered (blue lines and areas) and particulate (brown lines and areas) metal(loid)s exports downstream of the mining flat. Dashed areas represent a period during which discharge data was lacking. 124
Figure 5.1. Maps with location and sample type on the two studied mining sites Awa and Sophie. 140
Figure 5.2. A) Total Hg in three soil profiles around the mining site and B) THg and MeHg in surface soils and sediments. 145
Figure 5.3. Δ^{199}Hg vs δ^{202}Hg in soil and sediment samples on the mining site. The isotopic signatures for anthropogenic and pristine (geogenic) Hg are estimated from literature data (Laffont et al. 2011, Guédron et al. 2018, Schudel et al. 2018, Goix et al. 2019). 147
Figure 5.4. A) THg and B) MIF (Δ^{199}Hg) in plants compartments on the legal mine (brown) or close to illegal mining ponds (red). Isotopic data for gaseous elemental mercury (GEM) is from the Peruvian Amazon (Szponar et al. 2025). 148
Figure 5.5. A) Hg in the filtered (or dissolved) fraction. Total Hg (THg) as boxplots and the proportion of MeHg as gray bar charts, as well as dissolved gaseous mercury (DGM). B) Hg in the particulate fraction. THg as boxplots (expressed as ng per L and ng per g of particulate matter) and the proportion of MeHg as gray barcharts. 149
Figure 5.6. Total gaseous mercury (TGM) concentrations by site (A), and seasonal evolution (B) measured using active (up) or passive (down) sampling. 151
Figure 5.7. Synthesis of mercury pools and speciation on an alluvial mining site in French Guiana. The compartments displayed are the vegetation (green), water (blue), sediments and soils (brown), and gaseous Hg (white). THg and MeHg are average concentration values expressed in $ng.kg^{-1}$, Hg^0 in TGM

and DGM are in ng.m^{-3}, in the water compartment, values correspond to the sum of the particulate and filtered fractions except for wet deposition, throughfall and runoff where only the filtered fraction is displayed. The red dashed square represents an illegally mined section of the mining site, and red stars represent compartments where the presence of anthropogenic Hg was witnessed using Hg stable isotopes. 152
Figure 5.8. Mercury concentration and speciation in mining pond A) water and B) sediments. 154
Figure 6.1. Map of South America (Top left) with location of published mercury isotopic data in tropical sites (Adler Miserendino et al. 2018, Guédron et al. 2018, Schudel et al. 2018, Goix et al. 2019). Map of French Guiana (right) with the location of sediment sampling points (2003-2005). Symbol colours indicate the range of total Hg concentration in sediment and symbol shapes indicate the watershed it was sampled on. 165
Figure 6.2. Mass-independent fractionation (Δ^{199}Hg) (A) and mass-dependent fractionation (δ^{202}Hg) (B) vs the inverse of the total mercury concentration. The symbol colour represents the total Hg concentration of the sample and the symbol shape represents the watershed it was sampled on. Empty symbols represent data from this study with coloured for the Maroni river, and grey for data from other watersheds. Datapoints with fill and black border represent data from the literature on the Oyapock watershed, F. Guiana (Goix et al. 2019). Regression line (dashed line) only considers samples from the Maroni River with R^2 of 0.78 and 0.67 for Δ^{199}Hg and δ^{202}Hg, respectively, and the 95 % confidence interval is represented by dotted lines. 170
Figure 6.3. Mass-independent fractionation (Δ^{199}Hg) vs mass-dependent fractionation (δ^{202}Hg) in sediment samples from this study (empty symbols) and comparison with literature data (filled symbols) in Amazonian regions of South America (Laffont et al. 2011, Adler Miserendino et al. 2018, Guédron et al. 2018, Schudel et al. 2018, Goix et al. 2019). The equation of the regression (dashed line, this study) is $\Delta^{199}Hg = 0.33 * \delta^{202}Hg + 0.23$, with the 95 % confidence interval in dotted lines. The symbol colour represents the total Hg concentration of the sample and the symbol shape represents the watershed it was sampled on. The pristine endmember (green circle) was determined using literature data of deep-soils in French Guiana (Guédron et al. 2018, Goix et al. 2019) and the anthropogenic (red circle) was determined using literature data of liquid Hg used in ASGM (Laffont et al. 2011, Goix et al. 2019) and highly contaminated soils in F. Guiana (Guédron et al. 2018) and Ecuador (Schudel et al. 2018). 171
Figure 6.4. Map of French Guiana coloured by watershed and surface of ASGM in light red (A) and theoretical contribution of anthropogenic mercury in sediment samples using a binary mixing model, with the MIF Δ^{199}Hg data from this study and from the literature (Goix et al. 2019) (anthropogenic Hg (%)) versus the ASGM spatial density as derived from the map (B). The regression Hg_{anth} = 3.49 + 2.60*ASGM-density, R^2 = 0.91, p = 0.0031, with the 95 % confidence interval in dashed lines. 174
Figure 8.1. Site d'extraction d'or d'Awa avec les zones d'exploitation légales (marron) et illégales (rouge). La localisation des stations hydrologiques en amont et en aval est représentée par des points orange. 197
Figure 8.2. Images prises sur le site minier Awa. A) le flat minier terrassé, B) les plantations d'arbres en pépinière, C) pousse de revégétalisation plantée sur le site, C) cours de rivière reconstruit. 198
Figure 8.3. Site minier de Sophie (limites du PER dans le carré noir). Les criques autour du site minier sont indiquées en bleu avec les criques impactées par de l'activité illégale en rouge (évaluation qualitative basée sur des observations visuelles). 199
Figure 8.4. Images du site de Sophie. A) tunnels construits par les orpailleurs clandestins pour accéder aux filons aurifères, B) site de lavage, C) échantillonnage de 10m de profondeur pour analyse des teneurs en or lors de l'étape de prospection. 200
Figure 8.5. Évolution des exports de A) particules, B) Hg, C) Pb, D) As normalisées par les précipitations (mm) et E) densité des racines au fil du temps après la réhabilitation. 203

Figure 8.6. Synthèse des paramètres influençant la réhabilitation d'un sol orpaillé. Les paramètres naturels sont représentés par des cercles jaunes et l'intervention humaine par des cercles rouges. Les flèches rouges représentent l'impact négatif et les flèches vertes l'impact positif..... 204
Figure 8.7. Traceurs sélectionné dans les différentes sources de la fraction filtrée (Si et U, bleu) et de la fraction particulaire (POC et δ13C, brun) sur une rivière orpaillée réhabilitée. 207
Figure 8.8. Estimation des exports saisonniers de métaux et métalloïdes filtrés (lignes et zones bleues) et particulaires (lignes et zones brunes) en aval du flat minier. Les zones en pointillés représentent une période pendant laquelle les données de débit étaient manquantes. 208
Figure 8.9. *Synthèse des pools de mercure et spéciation sur un site minier alluvial en Guyane française. Les compartiments représentés sont la végétation (vert), l'eau (bleu), les sédiments et sols (brun), et le Hg gazeux (blanc). Le THg et le MeHg sont des valeurs de concentrations moyennes exprimées en* $ng.kg^{-1}$*, le* Hg^0 *dans TGM et DGM est en* $ng.m^{-3}$*, dans le compartiment eau, les valeurs correspondent à la somme des fractions particulaires et filtrées sauf pour les dépôts humides, l'eau de ruissellement de la végétation, et le ruissellement de surface où seule la fraction filtrée est affichée. Le carré rouge en pointillé représente une section illégalement exploitée du site minier, et les étoiles rouges représentent les compartiments dans lesquels la présence de Hg anthropique a été mise en évidence à l'aide d'isotopes stables du Hg.* 210
Figure 8.10. (A) Carte de la Guyane colorée par bassin versant et surface de l'ASGM en rouge clair et (B) contribution théorique du mercure anthropique dans les échantillons de sédiments (Hg anthropique) en fonction de la densité spatiale de l'orpaillage (B). La régression Hg_{anth} = 3.49 + 2.60 × densité orpaillage, R^2 = 0.91, p = 0.0031, avec l'intervalle de confiance à 95 % en pointillés. 213

List of Tables

Table 4.1. Main hydrological parameters integrated at the seasonal scale. miR = minor rainy season, MaR = major rainy season, DS = dry season, SSC = suspended solid concentrations.....93
Table 4.2. Hydrosedimentary budget upstream and downstream of the gold-mined flats for two events recorded during different seasons (event-1 in the minor rainy season, miR, and event-2 in the major rainy season, MaR).....94
Table 4.3. Mass budget of THg, MeHg, Pb and As upstream and downstream of the gold-mined flats for two events recorded during different seasons (event-1 in the minor rainy season, miR, and event-2 in the major rainy season, MaR).....123
Table 4.4. Specific seasonal fluxes of THg, MeHg, Pb and As, and estimation of the cumulated downstream export for each season, as well as the percentage of total export between brackets. miR: minor rainy season, MaR: major rainy season, DS: dry season, SSC: suspended solid concentrations.125
Table 5.1. Comparison of reported values in French Guiana of gaseous Hg in the water (DGM), in the atmosphere (TGM) and the volatilisation fluxes when available. Values are expressed as mean±SD (median).....156
Table 8.1. Bilan hydro-sédimentaire en amont et en aval du flat minier pour deux événements enregistrés au cours de saisons différentes (événement-1 en petite saison des pluies, miR, et événement-2 en grande saison des pluies, MaR).....206

List of Abbreviations

ASGM – artisanal and small-scale gold mining

Hg – mercury

Hg^0 – elemental mercury

Hg_F – filtered mercury

Hg_P – particulate mercury

THg – total mercury

MeHg – methylmercury

TGM – total gaseous mercury

GEM – gaseous elemental mercury

DGM – dissolved gaseous mercury

Pb – lead

As – arsenic

MDF – mass dependent fractionation

MIF – mass independent fractionation

SSC – suspended solid concentration

SPM – suspended particulate matter

DOC – dissolved organic carbon

POC – particulate organic carbon

TOC – total organic carbon

MaR – major rainy (season)

miR – minor rainy (season)

PCA – principal component analysis

NMDS – non-metric dimensional scaling

General Introduction

1. Motivation

Gold (Au) has been extracted for millenia. One of the oldest discovered gold mines dates back to the 4th or 3rd millenium BC (Hauptmann and Klein 2009). In 1511, the king Ferdinand of Spain famously said "Get gold, humanely if possible, but at all hazards, get gold" (Bernstein 2012). This statement still appears to hold true, as nowadays gold mining is on-going and even expanding due to increasing gold-prices. It is responsible for considerable impacts on the environment, as well as on population health. Globally, artisanal and small-scale gold mining (ASGM) is responsible for the production of up to 20 % of the world's gold, and employs an estimated 10-15 million miners (AMAP/UNEP 2019). In the Amazon region, the population directly involved in ASGM activites has more than doubled in the last 15 years, reaching 1.5 million workers, and up to 80 % of the gold is produced informally or illegally (Harlow et al. 2019). The majority of gold mining exploitation in the region is alluvial mining, where secondary gold deposits located below or in the vicinity of river beds are extracted. This type of mining activity (be it legal or illegal) is associated to deforestation and topsoil remobilisation in order to access the gold-bearing gravel layer. As a result, gold mined soils are highly susceptible to erosion. On one hand this causes the loss of organic matter, seeds and micro-organisms, which hampers natural revegetation of the site at the end of the mining operations (Gomes and Luizão 2011, Veldkamp et al. 2020). On the other hand, the eroded material is transported to rivers where it has a detrimental impact on ecosystems (Mol and Ouboter 2004, Tudesque et al. 2012, Wantzen and Mol 2013).

In addition to soil erosion, gold mining also generates environmental contamination with mercury (Hg), which is used in the extraction process to amalgamate the gold. Indeed, in French Guiana, the use of Hg has been prohibited in 2006 but is still widely used by illegal gold miners. In addition to this anthropogenic Hg, the increase in soil erosion also leads to the remobilisation of Hg and other metal(loid)s (lead – Pb, arsenic – As, …), which are naturally associated to those soils. In Amazonian ecosystems, high Hg concentrations in soils are due to the uptake of atmospheric Hg in leaves and incorporation in the soils through litterfall over millions of years, as well as to the presence of Hg carrier phases like iron oxides and organic matter (Roulet and Grimaldi 2001, Fostier et al. 2015, Feinberg et al. 2022). Once released to the rivers, Hg (anthropogenic or natural) can be methylated by methanogenic bacteria [usually sulfate- or iron-reducing bacteria (Achá et al. 2011)], and this methylmercury (MeHg) is easily bioaccumulated in individuals and bioamplified along the food chain (Azevedo-Silva et al. 2016). As a result, high concentrations of Hg are observed in predatory fish (Maury-Brachet et al. 2006), whose consumption is the main pathway of contamination for local populations (Pignoux et al. 2019).

In French Guiana, the juxtaposition of legal, illegal and historical gold mining sites makes it sometimes hard to disentangle the specific environmental impact of each mining practice. This is especially true as legal companies often choose to work on areas that have undergone historical or illegal gold mining in the past, potentially remobilising anthropogenic Hg stored in these soils. Additionally, after gold mining operations, legal gold mines are legally obliged to restore their site, including landscaping and tree plantation. The impact of this restoration on the potential reduction of particle export has yet to be quantified. Finally, due to the informal nature of ASGM, the exact extent of Hg emissions to the atmosphere, and to soil and water is not well qualified.

2. Thesis objectives

This work was supported by the gold mining company SAS GAIA, which provided salary during the span of the PhD and logistical support during the sampling campaigns. It was designed to fulfill the scientific expectations of different actors, with the broad objective of understanding the fate of mercury and other metal(loid)s in different gold mining contexts, including a focus on the restoration phase:

I- The first aspect is operational. The aim of the mining company (SAS GAIA) was to assess the successfulness of the restoration practice and understand the effects of restoration in terms of particle and metal(loid) export and revegetation. Elaborating on these results, the expectations were to provide advice on where the restoration efforts should be focused and what can be improved in the current practices. Additionally, state agencies which are involved in accompanying and regulating mining operations in French Guiana (e.g. DGTM, Office de l'eau) require tools and guidelines on how to evaluate the progress or success of a mining site restoration (thereby meeting the first objective of the mining company), and methods that are easy to implement, to assess the impact of legal and/or illegal gold mining at the watershed scale.

As a synthesis, the initial ambition was to ammend the existing list of good practices for gold mine restoration.

II- This work also aimed at solving more fundamental scientific questions concerning the biogeochemical cycle of Hg and other metal(loid)s. The first objective was to provide data to establish background values, which are still scarce in the area for certain metal(loid)s (e.g. Pb and As), or in certain compartments (e.g. atmospheric Hg). Building up on this, the intention was to provide an understanding on where Hg is stored on the mining site and in what form, as well as the transfers ocurring between different compartments, and understanding how Hg cycling is affected by gold mining (both legal and illegal). The second objective was to provide a deeper understanding on the recovery of soil functions after restoration, and the potential parameters impacting this recovery. Finally, this work aimed at assessing the hydrological

functioning of the gold mined watershed, by tracing both water and suspended particle sources in the river.

3. Document structure

The results presented in this work follow a structure that is built by working at different scales, starting at the elemental scale to gradually zoom out to the whole territory of French Guiana. The majority of the studies presented here focused on one legal mining site (Awa), but the two last chapters (5 and 6) expanded the study to other mining sites and to the whole territory of French Guiana.

- **Chapter 1** proposes a synthesis of knowledge on gold mining in the Amazon and French Guiana. The biogeochemical cycle of Hg is discussed, as well as the impact of ASGM on this cycle. The environmental issues concerning Pb and As in the Amazon region are also discussed.
- **Chapter 2** describes in the study sites and the sampling strategies
- **Chapter 3** assesses the temporal evolution over 5 years of the restored gold mining flat and its impact on particle and metal(loid) (Hg, Pb, As) fluxes, as well as on the recovery of biological soil functions, studied at the scale of 2 by 2 m erosion plots.
- **Chapter 4** is divided into two sub-chapters and considers the watershed scale. It examines the impact of the restored gold mining flat on a) the hydrological functioning of the gold-mined river as well as particle and carbon export, and b) the speciation and export of metal(loid)s (Hg, Pb, As).
- **Chapter 5** focuses on Hg and assesses its repartition and transfers in different compartments on and around the gold mining flat, considers the impact of illegal gold mining on Hg partitioning and aims at comparing two gold mining sites (Awa and Sophie) with different gold mining practices and history.
- **Chapter 6** examines the use of Hg isotopes in the estimation of anthropogenic Hg contribution in sediments across the main watersheds of French Guiana.
- **Chapter 7** synthesises and discusses the main results and outlooks of this work.
- Finally**,** a synthesis of the main results from this work translated to French language can be found in annex.

Chapter 1.

Current state of knowledge

1.1. Generalites on the Guyana Shield and French Guiana

French Guiana is a French overseas territory in South America spread over a surface of 84 000 km², with a population of 290 000 inhabitants [sensus 2022, INSEE (last accessed 10 April 2025)], mainly located on the Atlantic coast. Although not belonging to the Amazon river basin, French Guiana is considered to be part of the Amazon region in the broader sense, (Eva and Huber 2005). It is located on the Guiana Shield ("Plateau des Guyanes"), with the Atlantic Ocean as the northern border, and the Amazon basin to the South, which includes French Guiana, Guyana, Surinam, as well as a part of north-eastern Brazil (Amapá), eastern Venezuela and a some of north-eastern Colombia.

1.1.1. Climate

French Guiana is located in tropical latitudes (5°N), and more specifically within the inter-tropical convergence zone (ITCZ) where northeast and southeast trade winds converge. This ITCZ undergoes seasonal North-South oscillations, which lead to seasonal variations in rainfall and temperatures resulting in four seasons: the major rainy season, (MaR, April – July), the major dry season (August – November), the minor rainy season (miR, November – February), and the minor dry season, also called the "March short summer", in February/March. The majority of rainfall occurs during the two (major and minor) rainy seasons, and the total annual precipitation amounts to 2000 – 4000 mm/year with stable monthly temperatures between 25 °C and 30 °C.

1.1.2. Geology

The Guiana Shield consists of an ancient (1.3-2.5 Ga) igneous-metamorphic Archean-Proterozoic basement. Within this shield, the French Guiana bedrock is mostly composed of an association of greenstones and tonalite–trondhjemite–granodiorite intrusions (TTG), where gold (Au) deposits are located mainly on greenstones (Figure 1.1). These geological settings were formed during the Trans-Amazonian Orogeny, between 2.26 and 1.98 Ga, due to the collision of the Guiana Shield and the West-African craton (Kroonenberg et al. 2019). In French Guiana, these greenstones belong to two belts, one located at the North of the territory close to the coast, and the other one located further South.

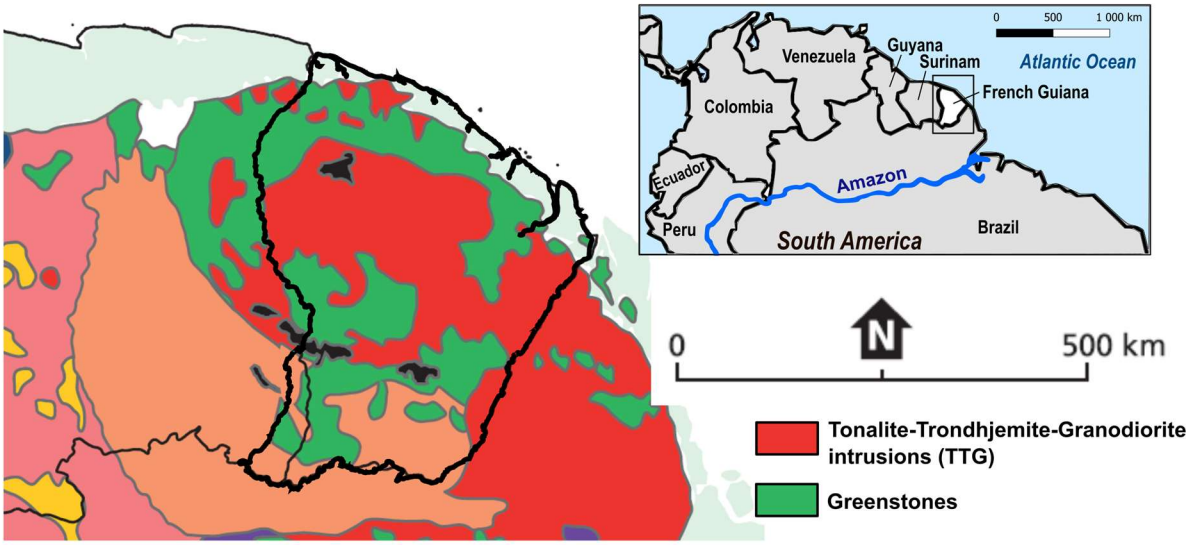

Figure 1.1 *Simplified geological map of French Guiana, adapted from Kroonenberg et al. (2016).*

1.1.3. Pedology

The long-time exposure of bed rocks of the Guiana Shield (more than 100 Ma) (Barron et al. 1981) to high temperatures and heavy rainfalls, typical for tropical latitudes, resulted in strong weathering and the formation of important laterite horizons of up to 100 m.

These ferralitic soils, enriched in iron and aluminium, granting them their characteristic red colour, are widespread in French Guiana. Along slopes, soil catenas develop due to erosion and hydromorphy processes (Boulet et al. 1993). This results in the succession from up to downslope of i) oxisols or ferralsols (i.e., US/French classification), which are clayey permeable soils rich in iron oxides, to ii) acrisols in midslopes, and iii) hydromorphic soil or gleysols in the lowlands, where soils are water-saturated leading to reducing conditions and the leaching of iron oxides, and the prevalence of clay minerals mostly as kaolinite (Grimaldi et al. 2002).

1.1.4. Hydrology of French Guiana

The etymology of the word “Guyana” is said to mean “Land of many waters” in an Amerindian language (Ramraj 2002), and is due to the dense network of rivers present on the Guyana Shield. The natural borders of French Guiana consist of two rivers, the Maroni on the western border with Suriname, and the Oyapock on the eastern border with Brazil. The main rivers of French Guiana are, in order of watershed area, the Maroni (66 800 km²), Oyapock (32 900 km²), Mana (12 200 km²), Approuague (10 900 km²), Sinnamary (6 500 km²), and Comté (3 700 km²). A large variability (up to 3 fold) in river discharge is observed between the dry and rainy season, with highest discharges observed in May/June, and lowest in October/November (Monfort and Ruf 2005).

1.2. Gold mining in French Guiana

1.2.1. Types of deposits and exploitations

In French Guiana, two main kinds of gold deposits have been typically exploited, both by legal and illegal gold mining. The most prevalently mined in the region because easily accessible with little infrastructure and machinery is alluvial gold mining. It originates from secondary deposits, formed by the alteration of primary deposits, transported by water, and accumulated in a gravel layer below the river beds. In this type of deposit, the gold grains are usually small in size and form gold flakes. The secondary alterated deposits can also result in eluvial or colluvial accumulations (Thomassin et al. 2017). For alluvial gold-mining, to access the gold-bearing layer, the topsoil needs to be removed, usually using high-pressure water hoses (Figure 1.2).

The second type of gold deposits are the primary gold deposits, i.e. the “source” of the secondary deposits described above. These primary deposits can be found in early massive sulfide deposits, in disseminated gold deposits or in quartz veins (Thomassin et al. 2017, Jébrak et al. 2021). They can go down to 3 km depth and are starting to draw more attention, both from legal companies (in open-pits exploitations), and illegal gold miners (in rudimentary vertical pits). In the case of primary gold, a first step consists in excavating the ore (from open-pits or tunnels), followed by crushing and grinding in order to liberate the gold particles.

In both types of mining (primary and alluvial), the gold-bearing soil or crushed ore is then mixed with water to form a slurry that is transferred to Z-shaped carpeted tables (Figure 1.2) where a first gravimetric separation is performed, with fine particles being washed off the table while heavier gold particles are retained on the carpet. In the case of illegal gold mining, some mercury might already be added at this step, spread on copper plates where the slurry is washed, to help with gold retention. These carpets are then washed and the resulting concentrate undergoes a second separation step, i) gravimetric or using cyanide extraction techniques in legal gold mines, the use of mercury having been prohibited in 2006; or ii) using mercury amalgamation and subsequent amalgam burning to recover the pure gold, in illegal mines. Cyanidation is not prevalent in French Guiana, with only mining company performing it (Auplata Mining Group on the Dieu-Merci site).

Recently, a method was proposed to trace the provenance of gold and to distinguish gold that was extracted using mercury amalgamation versus the one extracted legally by a combination of geochemical methods including Hg and Ag content measurements in gold grains (Pochon et al. 2021).

Legally, these deposits can be exploited by means of different authorisation steps. Companies are first given permits by state agencies to survey a site in order to estimate whether its exploitation would be profitable. They can then ask for an “authorisation of exploitation” (AEX), a “permit of exploitation” (PEX) or a concession. While PEX and concessions are not limited in size and shape, AEX were bound

to have a rectangular shape and maximum area of 1 km² before 2022, and are now not limited in shape but the maximal allowed area is 0.25 km² (JORF 2022). Companies are limited to a maximum of three simultaneous AEX, and the authorisation is given for a duration of 4 years (Marquis 2015). Legal exploitations of alluvial gold mining is usually performed at a small-scale (1km²) under the form of AEX.



Figure 1.2. *Illegal gold miners using a high-pressure water hose (left), and modern alluvial gold exploitation showing an excavator, gravel pump, screen with bars and gold mat. Reproduced from (Jébrak et al. 2021) with permission from P. Rostan.*

1.2.2. History

Gold mining in the Guyana Shield started in the 1850's, relatively late compared to other parts of the Amazon basin, where gold rushes have been documented earlier, like for instance back in 1690 in Brazil. Four major periods were observed in French Guiana with respect to gold mining, namely: 1) a first gold rush (1858-1880), where the extraction techniques were not mechanised and placers were centered on highly concentrated sites, followed by 2) a period of high gold production (1880 – 1914), 3) a decline in activities (1915 – 1970), and 4) a second gold rush starting in 1980 (Hammond et al. 2007, Jébrak et al. 2021). Historical gold mining villages and modern exploitations are located on and in the vicinity of the two greenstone belts presented in Figure 1.1 (Jébrak et al. 2021). Today, gold mining (both legal and illegal) is still on-going in the region. While illegal gold mining is expanding, especially on the western border with Surinam, on the Maroni river (Gallay et al. 2018), legal gold mining activities are stable or decreasing (Camino [last accessed 10 April 2025]). Illegal gold mining uses mercury (Hg) amalgamation for gold extraction, unlike legal gold mining companies as its use has been prohibited in French Guiana in 2006. During the last 85 years, the extent of gold mining in the Guyana Shield has generally been following gold prices (Hammond et al. 2007), with higher gold prices correlated to higher gold production.

1.2.3. Gold miner communities in French Guiana

French Guiana displays a complex mixture of populations with Amerindians, Metropolitans (individuals from mainland France), Creoles, Bushinenge, as well as migrants from Laos, Suriname and Brazil. Historical gold mining was essentially performed by Guianese as well as Metropolitans and Caribbeans

attracted by the first gold rush. Bushinenge populations, if not directly involved in the gold extraction process, supported activities by providing transport of people and supplies. This first gold boom led to an important intermixing of populations creating the Guianese creole culture and driving the creation of mining villages in the southern hinterlands (Strobel 1998).

Since the 1980s, gold mining in French Guiana has been driven and performed predominantly by Brazilian immigrants called “garimpeiros”. The latter were initially farmers who have been pushed into gold mining activities by empoverishment due to the mechanisation of agriculture. This population, highly mobile and versatile, is involved both in legal and illegal exploitations, sometimes alternating between both (Le Tourneau 2020).

Legal gold mining companies can be separated between large (>40 employees) international companies, and smaller (2-20 employees) local companies. International companies have mainly focused on the prospection of previously unmined primary deposits with the aim to perform open pit operations. However, strong popular opposition to the opening of megamines like the highly mediatised “Montagne d’or” (Baumes Malfant 2020) has led to the abandonment of projects of large open-pit mining and the withdrawal of the majority of international companies from French Guiana. Smaller companies tend to focus primarily on alluvial deposits and with a small number also working on weathered primary deposits (Jébrak et al. 2021).

In April 2025, these AEX make up the majority (83 %) of authorisations or permits allocated by the government, but represent only 12 % of the total area of active mining permits, which are dominated by 13 concessions belonging to 5 large local companies. In total, between 2021 and 2024, legal gold mines account for the production of around 1.02 tons of gold annually, and employ 400 workers (Camino [last accessed 10 April 2025]).

In comparison, illegal gold production, although difficult to assess, is estimated at 5-10 tons annually and involves around 10 000 garimpeiros (Escat 2015, Le Tourneau 2020, Le Tourneau 2021). Military repression activities have been conducted to limit illegal gold mining proliferation in the territory, first as operation “Anaconda” from 2002 to 2008, and now “Harpie” since 2008. The objective of these operations is to destroy or seize the means of production (generators, motor pumps) so that illegal gold production becomes unprofitable. These operations have somewhat hampered the illegal activities, but they are still prevalent due to the resilience of garimpeiros and the high price of gold, which results in profitable operations in spite of material losses (Escat 2015, Le Tourneau 2020).

1.2.4. Consequences of gold mining

1.2.4.1. Deforestation

The Amazon region comprises 50 % of rainforests worldwide (Xiao et al. 2009) while they cover 95 % of French Guiana territory (Rahm et al. 2020). Although deforestation is mainly driven by agricultural

expansion in the whole Amazon, regional differences exist, with artisanal and small-scale gold mining (ASGM) believed to be the main driver for deforestation in parts of the Guiana Shield (i.e., Surinam and Guyana) and having an intermediate impact in French Guiana (Stach et al. 2009, Hänggli et al. 2023). Additionally, mining can be an indirect cause of deforestation, due to road building fueling urban and agricultural expansion, where these indirect impacts exceed the impact within the mining areas by a factor 10 (Sonter et al. 2017).

The extent of deforestation due to gold mining can be followed through satellite remote sensing and shows that over the last 20 years 13,500 ha have been deforested in French Guiana due to illegal gold mining (Linarès et al. 2024). However, a notable decrease in the magnitude of deforestation has been observed since the beginning of the military repression program "Harpie", as the average annual deforestation was reduced by 39 % compared to pre-Harpie deforestation (Linarès et al. 2024). This is not necessarily due to a lower amount of gold miners, but more probably to a change towards more discreet practices in order to evade detection and repression.

On a longer timescale, large-scale deforestation might affect the fundamental hydrological functioning of the region, with lower rainfall due to lower evapotranspiration, as well as increased overland flow (Lima et al. 2013).

1.2.4.2. Soil erosion and turbidity

The soils laid bare by deforestation are more prone to soil erosion, especially in tropical regions where rainfall is intense and frequent (Lal 1990, Labrière et al. 2015), inducing soil loss and increased particle export to the surrounding rivers. In the case of ASGM, this erosion is exacerbated by the fact that the mining process in itself does not only include the forest cover removal, but also topsoil destructuration to access the gold-bearing layer. This increase in soil erosion leads to increased particle loads (i.e. siltation) in the surrounding river ecosystems. As a result, these ecosystems are negatively impacted in several ways. First, siltation induces a reduced light penetration (Lobo et al. 2017), which can affect phytoplankton productivity and community structure (Tudesque et al. 2012) impacting the whole food chain up to piscivorous fish. Additionally, the increased river bed and bank sedimentation suppresses hiding and spawning habitats for fish, and additionally affects fish which would normally graze on periphyton (Mol and Ouboter 2004). Finally, the increased concentration of suspended particles can directly harm the fish through clogging or abrasion of their gills (Wantzen and Mol 2013).

The increased particle remobilisation additionally leads to the remobilisation of metal(loid)s associated to these particles as will be developed in more detail in section 1.3.

1.2.4.3. Soil biological activity

Amazonian soils are highly weathered and usually already nutrient-depleted in their undisturbed state, in comparison to temperate soils (Quesada et al. 2010, Lange et al. 2024) due to leaching during

precipitation events, and to occlusion of the remaining nutrients within soil minerals limiting their availability (Tiessen et al. 1984). As a result, nutrient cycling to sustain the rainforests above these soils depends strongly on efficient organic matter (OM) recycling and occurs mostly in the organic and litter layer, through the participation of soil microbial activity (Richardson and Simpson 2011) and important superficial root growth (Martins et al. 2021).

Land cover and land use change (LCLUC) involving deforestation is associated with changes in soil microbial community structures (Danielson and Mazza Rodrigues 2022), soil enzymes activity (Silva-Olaya et al. 2021), and nutrient cycling (Figueiredo et al. 2019). These changes lead to long term impacts on ecosystems, for example the nitrogen cycle was found to be affected in some secondary forests even 20 years after having been abandoned (Gomes and Luizão 2011, Veldkamp et al. 2020).

As discussed in section 1.2.4.2, alluvial gold mining practices do not only involve clear-cutting of the vegetation but are also associated with soil reworking over several meters depth. The exposure of reworked bare soils to rain and wind makes them even more vulnerable to leaching, especially of essential nutrients like phosphorous and nitrogen. In addition, soil compaction by heavy machinery renders plant regrowth more arduous (So et al. 2022).

As a result, topsoil on gold mining sites typically display reduced nutrient levels including carbon and nitrogen (Schimann et al. 2012) and microbial biomass (Dos Santos et al. 2013) compared to undisturbed forest soils. In the case of illegal ASGM, where Hg is added in the gold mining process, Hg contamination of the soils can lead to a change in soil microbial communities, with an increase in bacteria bearing the *merA* gene responsible for Hg reduction as a detoxification pathway (Cardona et al. 2024).

1.2.4.4. Societal consequences

Asides from its ecological impact, gold mining, and in particular illegal gold mining also carries a significant amount of societal repercussions, among the miners communities and beyond. Gold miner communities are exposed to a variety of zoonoses due to extended contact with animals in the rainforest (mosquitoes, ticks and bats amongst others). As a result of this increased exposure, the percentage of malaria infections was shown to be correlated to gold production in Colombia (Castellanos et al. 2016), and is often more prevalent in gold miners than in the general population. The exposure to mosquitoes, coupled to the high mobility of the illegal miners within and between countries make them highly vulnerable to malaria and a reservoir for malaria propagation to the general population (Douine et al. 2020). Their distance from health care centers, scarce access to drinkable water, and sometimes limited access to food sources makes the population of illegal gold miners vulnerable to digestive health issues (Douine et al. 2023) and dietary deficiencies (Mosnier et al. 2017). Finally, although not as widespread and extensive as commonly assumed (Egmann et al.

2018), violence and conflicts are present in ASGM (Salman and de Theije 2017) and armed groups can sometimes append themselves on mining operations, extorting the miners of their gold (Le Tourneau 2020). The garimpeiros gold miners however, do not envision themselves as criminals, but as informal workers : “garimpeiro não é bandido, é trabalhador” (Le Tourneau 2020).

1.2.5. Existing guidelines for gold mining in French Guiana

French Guiana being part of France, all mining laws applicable on the mainland are also applicable in oversea territories. The sequence of mining operations are under the supervision of several state agencies, including the forest agency (“office national des forêts”, ONF), the biodiversity agency (“office français de la biodiversité”, OFB) and the “Direction Générale des Territoires et de la Mer” (DGTM) (Marquis 2015), which perform controls and validate the progress of operations (pre-, syn- and post-exploitation).

In the case of alluvial gold mining, before exploitation operations, the guidelines include the removal of the tree-cover from the mining site, and the tree trunks are stored on the sides of the mining site, along with the topsoil organic layer. For rivers of widths under 7.5 m, the riverbed is then diverted to one flank of the site, in order to limit the impact of mining operations. For rivers above 7.5 m width, operations cannot be conducted directly on the river bed, and must be at a distance of 20 m or further from the river banks (Marquis 2015).

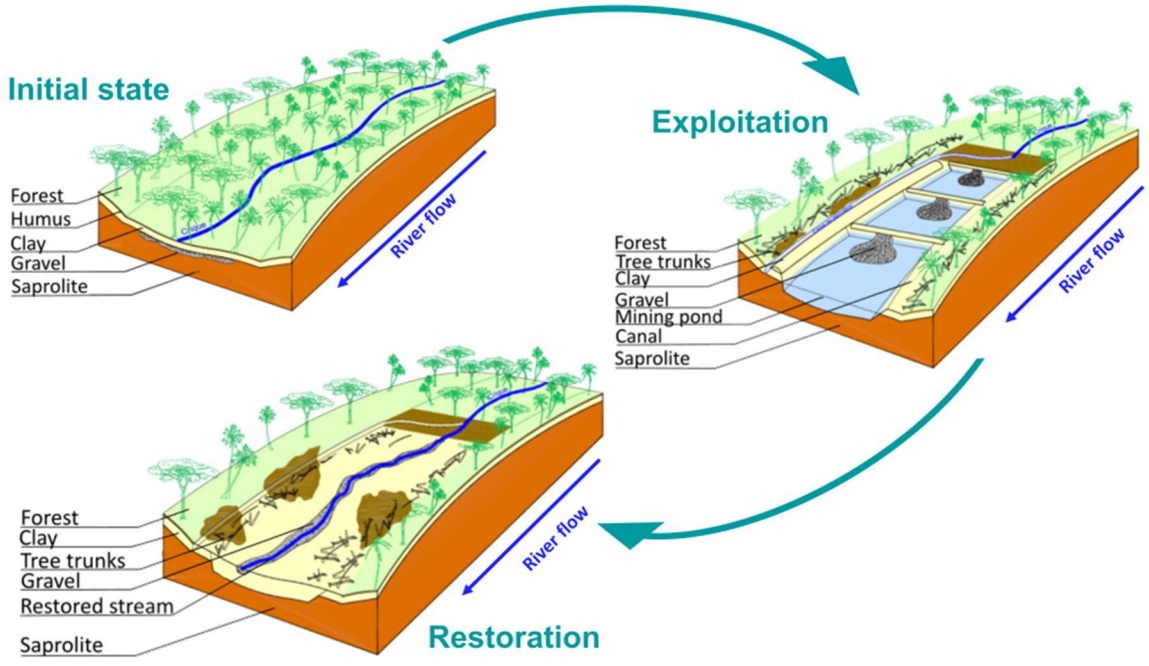

Figure 1.3. *Exploitation and restoration steps of an alluvial gold mine.*

During mining operations, the extraction process is performed from downstream to upstream, in closed-circuit, with the water from the downstream mining pond used to remobilise the upstream gold-bearing layer and so on. The particles from the remobilised soil are then left to settle and the

mining ponds are emptied into the adjacent river once the suspended sediment concentration is below 35 $mg.L^{-1}$. Unlike in illegal gold mining, mercury is not used to extract the gold, since its use has been banned in France in 2006. Therefore, the extraction is performed by gravimetry, first on carpets, followed by shaking tables and/or by gold panning.

Once the exploitation of one section is finished and the mining ponds are emptied, the mining site is landscaped by filling the mining ponds with the extracted material, mimicking as much as possible the initial stratification. This landscaping should be performed during the dry season in order to avoid soil compaction by the excavators. The organic layer, or what is left of it after months and sometimes years of storage and being exposed to rain and wind erosion, as well as the tree trunks are positioned on the mining site to help promote spontaneous revegetation of the site by input of organic matter, microorganisms and seeds (Figure 1.3). Additionally, trees grown in nurseries on-site are then replanted at a distance of 3 m, and the final extent of revegetation is expected to be superior to 30 % of the mined area. The trees species include sun-resistant species and many species from the *Fabaceae* family, which are able to form symbioses with nitrogen-fixing bacteria, in order to retrieve atmospheric nitrogen and help restart the nitrogen cycle in the soils. However, tree replanting is not trivial, as past restoration works have included replanting using the tree species *acacia mangium* which originates from Australia and South East Asia and has proven to be invasive (Delnatte and Meyer 2011). Tree-species used for replanting are now exclusively local species, ideally from seeds found in the forest in the vicinity of the mining site. In order to limit the loss of organic matter, microorganisms and seeds from the organic layer, it is stated that restoration works should be performed within 6 months after exploitation, but this timespan is not always respected.

1.2.6. Temporal evolution of restored or abandoned mining sites: state of the art in French Guiana and the Amazon region

Recent meta-analyses at the global scale have proposed that natural regeneration is more efficient than or similar to active restoration (Crouzeilles et al. 2017, Meli et al. 2017) in forest recovery, thereby questioning the needs for restoration. However, Reid et al. (2018) propose that this finding might be explained by a positive site selection bias as natural regeneration is usually performed on less degraded sites, where the restoration success is more likely. They advocate for paired experimentation comparing restoration methods in the same conditions. On highly degraded sites, like gold mining sites, which include topsoil removal and reworking over several meters, active restoration is probably necessary. In the Brazilian Amazon, higher tree abundance, species richness and diversity was achieved with seedling planting compared to natural regeneration (Conrado da Cruz et al. 2020).

Because restoration takes time, most studies in the Amazon region involve chrono-sequences of mining sites over decades, looking amongst others at the growth of tree species (Chambi-Legoas et al.

2021), soil enzyme activity (Couic et al. 2018), nutrients (Couic et al. 2022), and microbial respiration (Schimann et al. 2012, Couic et al. 2022). Soil carbon and nitrogen as well as soil microbial respiration increased after 15 years when trees from the *Fabaceae* family are used in the plantations, compared to natural recovery (Couic et al. 2022). Shorter term studies (< 5 years) observe only limited recovery of plant biomass under natural regeneration in Guyana (Kalamandeen et al. 2020), again promoting the need for active restoration on these types of degraded sites.

To stimulate the efficiency of restoration and plant growth, the tree seedlings' soils can be directly inoculated with N-fixing bacteria. This practice increases the cost of restoration, and is therefore not universally used, but it is thought to significantly increase the restoration efficiency (Salomon et al. 2016). Finally, the use of satellite data to follow the revegetation status of a mine in the Amazon may prove useful especially in remote sites (as is often the case for mining sites) where access is limited (Gastauer et al. 2022).

While (understandably) most studies on post-mining focus on the speed of tree-cover recovery and soil functions (nutrients, microorganisms, …), little information is available on the temporal reduction of particulate export, despite it being known to be considerable during the exploitation phase (section 1.2.4.2).

1.3. Mercury in the Amazon

Mercury (Hg) is a toxic element, widely used in ASGM for gold extraction through amalgamation. Its toxicity was raised to public awareness in the 1960s, when it came to light that a factory had been releasing wastewater with elevated concentrations of methylated Hg (MeHg) into the Minamata bay (Japan) during decades. This led to its biomagnification in the food web and contamination of the surrounding population through fish consumption, resulting in deaths and body deformations (Harada 1995). The Minamata Convention on Mercury was created in response, with the goal to reduce the use and adverse impact of Hg on human health and the environment.

Worldwide, ASGM makes up 40 % of all anthropogenic Hg emissions to the atmosphere. In South America ASGM is estimated to be the main anthropogenic source of Hg to both the atmosphere (83 %), and to land and water (94 %) (AMAP/UNEP 2019), which is one of the reasons it has attracted a lot of scientific attention in the Amazon basin. However, due to the illegal or informal nature of ASGM, the exact extent of emissions to the environment resulting from it are not well constrained and additional data and evaluation methods are thus needed to estimate the large-scale impact of ASGM pollution.

1.3.1. Mercury species and background levels in environmental compartments

1.3.1.1. Description of the main Hg species

Hg is present in the environment as different species depending on its oxidation state, organic ligands, and the phase it is in. As such, the inorganic forms comprise "elemental Hg" (Hg^0 or Hg(0)), and "inorganic Hg" (Hg^{2+} or Hg(II)) and the organic form is methylated mercury (MeHg), which comprises monomethyl Hg (CH_3Hg^+ or MMHg) and dimethyl Hg ($(CH_3)_2Hg$ or DMHg). Hg^0 and DMHg are mainly found as gaseous species in the environment, although Hg^0 is also present in its liquid form when used by illegal gold miners in the amalgamation process. DMHg is studied mostly in marine environments (Baya et al. 2015, Jonsson et al. 2016), whereas in freshwater ecosystems it has been observed only in contaminated sites up until now (Wallschläger et al. 1995, Wang et al. 2019).

Dissolved gaseous mercury (DGM) is operationally defined and corresponds to the Hg^0 (and DMHg if any) dissolved in water. Total gaseous mercury (TGM) is defined as the fraction of atmospheric Hg passing through a filter (0.45 µm to 2.5 µm pore size), with the remaining fraction being termed particulate bound mercury (PBM). PBM represents less than 10 % of atmospheric Hg but has a significant role in the distribution and transport of Hg (Zhang et al. 2019). TGM consists of the sum of Hg^0 and Hg^{2+} in the atmosphere. In the atmospheric compartment, these two species are called gaseous elemental mercury (GEM) and gaseous oxidised mercury (GOM) respectively (McLagan et al. 2016). GEM has a much longer residence time in the atmosphere (0.5-1 year) than GOM (days to weeks) which is more reactive and readily removed from the atmosphere through wet or dry deposition (Selin 2009). Therefore, GEM has been shown to generally make up more than 95 % of TGM (Pandey et al. 2011), and the terms TGM and GEM are sometimes used indiscriminately.

In water, particulate-bound Hg is operationally defined as the fraction superior to 0.45 or 0.2 µm depending on the study (Lamborg et al. 2016, Diringer et al. 2020). Finally, total Hg (THg) is commonly referred to as the sum of all Hg species in a given compartment. In Amazonian environments, Hg concentrations have been widely studied in soil and water compartments as will be described in the following sections.

1.3.1.2. Hg in soils.

Amazonian soils display on average much higher THg concentrations than soils in temperate regions where THg is usually below 50 $ng.g^{-1}$ (Marchant et al. 2017). Amazonian topsoils however, typically exhibit THg concentrations in the 100 to 500 $ng.g^{-1}$ range (Roulet et al. 2001, Guédron et al. 2006, Figueiredo et al. 2018, Fostier et al. 2023). In Amazonian soils, the main known carrier phases for Hg are iron oxides and organic matter (Grimaldi et al. 2001, Roulet and Grimaldi 2001). However, the rapid turnover of OM in tropical soils and uptake by the vegetation prevents the development of a thick organic layer, and thereby limits the role of OM in the accumulation of Hg in tropical soils. The highest

concentration of Hg in soil profiles are thus generally encountered in subsurface mineral horizons (~0.5 m depth), where clay and iron contents are highest (Grimaldi et al. 2008). In addition, the decrease of THg concentration in topsoils along a topographic gradient on hills from upslope to downslope as observed in French Guiana, can be related to the presence or absence of these carrier phases. There, upslope oxisols, enriched in iron oxides exhibit high (> 400 $ng.g^{-1}$) THg in opposition to downslope hydromorphic soils under more reducing conditions, where iron oxides are dissolved and lost, resulting in the absence of carrier phases for Hg, and thus lower topsoil concentrations in the lowlands (~100 $ng.g^{-1}$) (Guédron et al. 2009).

Although less frequently studied, MeHg in undisturbed soils is around 1-3 $ng.g^{-1}$ and accounts for less than 1 % of THg (Roulet and Lucotte 1995, Roulet et al. 2001, Fostier et al. 2023). MeHg in soils was found to be correlated to organic carbon concentrations, highlighting the role of OM as a significant carrier phase for MeHg (Roulet et al. 2001).

1.3.1.3. Hg in rivers

In the Amazon basin, water is stored mainly in the many rivers, and in floodplain lakes, which are old river branches connected to the main river stream during high water periods. In undisturbed rivers, more than 90 % of THg is particulate-bound Hg. Particulate Hg concentrations are typically ranging from 100 to 300 $ng.g^{-1}$ while filtered THg concentrations are lower, with around 1-5 $ng.L^{-1}$ (Guédron et al. 2011, Lacerda et al. 2012, Hellal et al. 2020). However, lower THg (filtered and particulate) have been measured in undisturbed rivers in Peru at 1 ± 0.5 $ng.L^{-1}$, likely due to particles being depleted in THg [10-20 $ng.g^{-1}$ (Gerson et al. 2020)]. Previous studies conducted in rivers in French Guiana reported MeHg concentrations of 0.01-0.1 $ng.L^{-1}$ in the dissolved and 1-2 $ng.g^{-1}$ in the particulate phase, comprising a small fraction of the dissolved and particle bound THg with 1-5 % and less than 1 %, respectively (Guédron et al. 2011, Hellal et al. 2020). While little data is available for DGM in undisturbed rivers, concentrations in lakes in Brazil and French Guiana range between 5 – 100 $pg.L^{-1}$ (Amouroux et al. 1999, Muresan et al. 2007, Jardim et al. 2009).

Finally, riverbed sediments exhibit both THg and MeHg concentrations in the same range as on suspended particles presented above (Lino et al. 2019, Hellal et al. 2020). A large-scale survey on river sediments in the main watersheds of French Guiana established the background THg concentration to be 100 ± 50 $ng.g^{-1}$ (Laperche et al. 2014), but MeHg was not included in this study.

1.3.1.4. Atmospheric Hg

Atmospheric Hg concentrations can be measured either through active or passive sampling. Active sampling involves pumping a defined air volume through a Hg trap (usually gold coated quartz) at a controlled flow rate in the minutes to hours timescale. Passive samplers are deployed for weeks to months and Hg concentrations are calculated based on the diffusion rate of Hg^0 through a diffusive

barrier and onto the sorbent, and corrected with windspeed and temperature meteorological data (McLagan et al. 2016). Some passive samplers have been shown to filter out GOM and thus measure exclusively GEM (Stupple et al. 2018), but this is not the case for all passive samplers. In any case, both for active and passive sampling, because GOM is usually low compared to GEM, the difference in concentration between TGM and GEM is low.

As for DGM, atmospheric Hg concentrations are scarce in the Amazon region, but active sampling has resulted in 1 – 5 $ng.m^{-3}$ in remote areas in Brazil and French Guiana (Amouroux et al. 1999, Magarelli and Fostier 2005, Muresan et al. 2007, Almeida et al. 2009). Passive sampling yielded similar results, but in the lower range, with concentrations around or below 1 $ng.m^{-3}$ near the city of Manaus, Brazil and in remote forests (Sprovieri et al. 2016, Szponar et al. 2025).

1.3.2. Hg biogeochemical cycle

The largest sink of Hg in the Amazonian environment is soil. As discussed in section 1.3.1.2, natural Hg concentrations in Amazonian soils are much higher than in temperate regions, and the origin of this Hg is mainly exogenic (de Oliveira et al. 2001, Guédron et al. 2006). Indeed, bedrock Hg concentrations were found to be extremely low in French Guiana [2.1 ± 0.7 $ng.g^{-1}$ (Goix et al. 2019)]. In natural systems, the main pathway for exogenic Hg input to the soils is atmospheric Hg^0 and/or Hg^{2+} adsorbed on or taken up in tree leaves, which are then incorporated into the soil through litterfall (Jiskra et al. 2015). The large leaf area index and long leaf lifespan in tropical evergreen forests coupled to important litterfall rates makes tropical forests an efficient sink for atmospheric Hg input to the soils through litterfall (Fostier et al. 2015, Wang et al. 2016, Feinberg et al. 2022). As a result, the accumulation of atmospheric Hg through litterfall over millions of years, coupled to the presence of Hg carrier phases like iron oxides leads to the important Hg soil concentrations observed in Amazonian soils.

In rivers and lakes, Hg originates from inputs through soil erosion and/or wet deposition. There, the methylation of inorganic Hg to MeHg is mainly mediated by sulfur- or iron-reducing bacteria (Achá et al. 2011) which possess the hgcAB genes coding for the complex that is responsible for Hg methylation (Gilmour et al. 2013). These bacteria are predominantly anaerobic and methylation can lead to MeHg formation in sediments, bottom waters, or water-saturated hydromorphic soils (Guimarães et al. 1998, Huguet et al. 2010, Guédron et al. 2011).

Like in other environments, Hg bio-concentrates, -accumulates, and magnifies in riverine food webs (Azevedo-Silva et al. 2016, Lemaire et al. 2024). Both inorganic- ($7 \cdot 10^4$ fold) and MeHg ($4 \cdot 10^5$ fold) are concentrated in biofilm with respect to water concentrations (Maury-Brachet et al. 2008). The proportion of MeHg withing the THg increases along the food chain, and therefore, MeHg is the predominant species (> 90 %) in piscivorous fish, reaching THg concentrations in the range of 1-10 $\mu g.g^{-1}$ (Maury-Brachet et al. 2006, Maury-Brachet et al. 2019, Basta et al. 2023).

1.3.3. Impact of ASGM on the Hg cycle

Hg amalgamation is the most common gold extraction technique used by small-scale gold miners and on average, it is estimated that around 1.3 kg of Hg are used for every kg of gold produced (Keane et al. 2023). In French Guiana, Hg amalgamation was performed in historical gold mining between the 1850s and 2006 when its use was banned, and is also carried out by illegal gold miners nowadays. This Hg is elemental mercury in its liquid form, and a part of this Hg^0 is lost during the amalgamation process directly to the soils and aquatic systems, where it can be oxidised to Hg^{2+} and potentially methylated to MeHg. The rest is lost to the atmosphere as Hg^0, during the amalgamation process, and more importantly during the roasting of this amalgam in order to recover the pure gold (Figure 1.4). This roasting is performed directly on the mining site, and in gold-shops when the gold is sold. As a result, elevated TGM concentrations have been measured inside (300 – 10 000 $ng.m^{-3}$) and outside (3 – 500 $ng.m^{-3}$) gold shops in Brazil and Peru (Hachiya et al. 1998, Szponar et al. 2025). The emitted Hg^0 can be oxidised to Hg^{2+} in the atmosphere and be both redeposited in the immediate vicinity (as GEM or GOM), or transported over larger distances due to the long atmospheric lifetime of Hg^0 of 0.5 to 1 year (Selin 2009). Interestingly however, gold mining sites are not always linked to an increase of Hg concentrations in soils. The mined soils are destructured, contain low amounts of OM and are very sandy because the majority of fine particles have been exported during the exploitation process. As a consequence, they display a lower Hg retention capacity compared to natural soils, and an important amount of Hg (natural and anthropogenic) might be lost to the rivers or through volatilisation (Velasquez Ramirez et al. 2021). The fate of anthropogenic Hg in tropical rivers is thus not straightforward and depends on biogeochemical, grain-size and hydrological factors (Moreno-Brush et al. 2020).

Additionally, the deforestation that is associated with ASGM, along with deep soil destructuration leads to increased erosion as discussed in section 1.2.4.2. In Amazonian environments, due to the high natural Hg concentrations in soils, this erosion is coupled to the remobilisation of natural background Hg, and also potentially of historical anthropogenic Hg. As a result, ASGM leads to increased particulate Hg concentrations in rivers downstream of mining sites, which is often coupled to an increase in suspended solid concentrations (Martinez et al. 2018). This emphasizes the role of erosion in Hg export from ASGM sites (Telmer et al. 2006, Diringer et al. 2020).

Additionally, the presence of stagnant water and reducing conditions in mining ponds on gold mining sites (both legal and illegal) has the potential to increase MeHg production in these ponds, which can then become a source of MeHg contamination to the adjacent river (Guédron et al. 2011). Similarly in an artificial hydroelectric dam in French Guiana, anoxic conditions were more important than ASGM Hg input in controlling the MeHg concentrations in water and fish upstream and downstream of the dam (Boudou et al. 2005). The use of a piscivorous fish as a bioindicator for mapping Hg contamination

in the main rivers of French Guiana has pointed towards anoxia and gold mining activities as two important drivers for high Hg concentrations in fish muscle (Maury-Brachet et al. 2019).

With the exception of gold miners burning the Hg-Au amalgam, the main Hg exposure route to the population in the region and globally is through fish consumption.

Elevated Hg concentrations in blood and hair observed in local riverine populations have been liked to high Hg concentrations in piscivorous fish, which is the main protein source for local populations (Pignoux et al. 2019, Hacon et al. 2020). Previous studies established a link between high Hg contamination and (mild) motor and neurological deficiencies (Dolbec et al. 2000, Cordier et al. 2002).

In the case of gold miners who are directly in contact with liquid elemental mercury, Hg exposure appears to occur through a mixing of sources including fish consumption and Hg^0 vapor during the roasting of the amalgam (Laffont et al. 2011, Gibb and O'Leary 2014).

It has to be kept in mind that gold mining is not the only anthropogenic activity affecting the Hg cycle in the Amazon. Biomass burning coupled to deforestation for agriculture also increases soil erosion and Hg export to rivers (Crespo-Lopez et al. 2021). Additionally forest fires increase Hg emissions to the atmosphere and reduce the capacity of the rainforest to act as a sink for atmospheric Hg (Michelazzo et al. 2010, Fisher et al. 2023). In South America, agriculture is the main cause of deforestation with an estimated additional 3 million hectares used for agriculture annually between 2000 and 2014 (Franco-Solís and Montanía 2021, Hänggli et al. 2023).

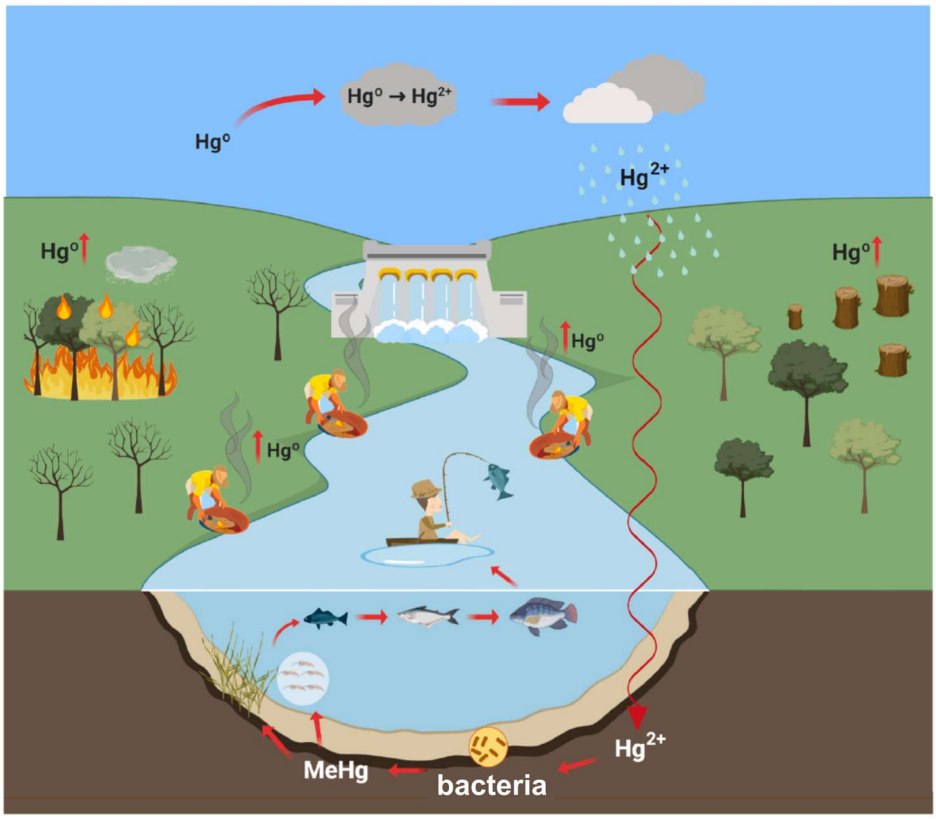

Figure 1.4. *Synthesis of the Hg dynamics in the Amazon reproduced from Crespo-Lopez et al. (2021).*

1.3.4. Hg stable isotopes and their application to Amazonian environments

Hg has 7 stable isotopes, with the following natural relative abundances as measured in the NIST 3133 reference material: ^{196}Hg = 0.16 %, ^{198}Hg = 10.04 %, ^{199}Hg = 16.94 %, ^{200}Hg = 23.14 %, ^{201}Hg = 13.17 %, ^{202}Hg = 29.73 %, and ^{204}Hg = 6.83 %.

Hg isotopic ratio nomenclature was standardised according to recommendations by Blum and Bergquist (2007), using ^{198}Hg as a denominator as it is the isotope with smallest mass which is still abundant enough to provide reliable measurements. Hg stable isotopic composition is measured relative to the standard reference material NIST 3133 and reported as:

$$\delta^{XXX}\mathrm{Hg}\ (‰) = \left[\frac{(^{XXX}\mathrm{Hg}/^{198}\mathrm{Hg})_{\mathrm{unknown}}}{(^{XXX}\mathrm{Hg}/^{198}\mathrm{Hg})_{\mathrm{NIST\ 3133}}} - 1\right] \times 1000$$

where XXX is the studied Hg isotope between ^{199}Hg and ^{204}Hg and where δ^{XXX} Hg is used to express mass dependent fractionation (MDF). MDF occurs during physical, chemical or biological processes (Bergquist and Blum 2009) and is only preserved in incomplete processes (Wiederhold 2015). Additionally, Hg has been shown to undergo mass-independent fractionation (MIF) of odd-mass numbers (^{199}Hg, ^{201}Hg, "odd-MIF") and also of even-mass numbers (^{200}Hg, ^{204}Hg, "even-MIF"). MIF is expressed as the difference between the measured δ^{XXX} value, and the theoretical value that would be observed if only MDF would be taking place, based on its δ^{202}Hg. The MIF is reported as:

$$\Delta^{xxx}\mathrm{Hg}\ (‰) = \delta^{xxx}\mathrm{Hg} - (\delta^{202}\mathrm{Hg} \times \beta_{xxx})$$

Where the β_{xxx} corresponds to 0.2520, 0.5024, 0.7520 and 1.4930 for ^{199}Hg, ^{200}Hg, ^{201}Hg and ^{204}Hg isotopes respectively.

The largest MIF is observed for odd isotopes because they have nuclear magnetic moments and nuclear spin, causing fractionation due to the magnetic isotope effect (MIE), ocurring during photochemical reactions (Blum et al. 2014). A smaller MIF (<0.5 ‰) fractionation in both odd and even isotopes, ocurrs due to the nuclear volume effect (NVE), because the nuclear radii do not scale linearly with mass (Wiederhold et al. 2010). Even-MIF is thought to be exclusively generated by photochemical reactions in the upper troposphere and/or stratosphere, making it a conservative tracer (Cai and Chen 2016).

The large number of isotopes and the diverse fractionation mechanisms they can undergo makes Hg stable isotopes a useful tool to trace both processes (Sherman et al. 2010) and sources (Yin et al. 2010) in various environments (Wiederhold 2015, Obrist et al. 2018).

1.3.4.1. Hg stable isotopic composition for tracing Hg sources in the Amazon.

Because the isotopic composition of natural Hg measured in soils is significantly different from the one of anthropogenic Hg used by gold miners for amalgamation, the majority of studies involving Hg

isotopes in the Amazon region have aimed at distinguishing these two Hg sources in different compartments. While a study in French Guiana estimated that anthropogenic Hg makes up a significant part of the Hg in river sediments downstream of ASGM sites (Goix et al. 2019), other studies in Brazil and Ecuador concluded that the increase in THg in river sediments is mainly due to land use change and increased soil erosion (Adler Miserendino et al. 2018, Schudel et al. 2019). In soils, less negative odd-MIF values were observed in formerly goldmined topsoils compared to pristine topsoils (Guédron et al. 2018). Similarly, Hg isotopes were measured in fish in goldmined and pristine sectors but the complexity and interconnection of the processes involved (biotic such as methylation, and abiotic as photochemistry) did not allow for an apportionment of Hg sources in fish (Laffont et al. 2021). The analysis of Hg isotopes in hair of gold miners and indigenous communities in Bolivia showed differences in Hg exposure between the different populations. For indigenous people, the main exposure route was through fish consumption, while Hg contamination in gold miners occurred through a mixture of Hg^0 vapor inhalation and fish consumption (Laffont et al. 2011). Finally, a recent study on atmospheric Hg showed that ASGM-derived Hg contributed to 50 – 100 % of GEM in towns, near the highway, and also in forests near ASGM sites (Szponar et al. 2025).

In addition, Hg isotopes have also been used to follow processes in Amazonian environments. The decrease to more negative odd-MIF in deep pristine soil horizons was attributed to processes occuring during pedogenesis such as abiotic reduction and complexation to Fe/Al oxides, as well as potentially to a different pre-anthropogenic GEM signature compared to its modern signature (Guédron et al. 2018). In the Brazilian Amazon, MDF was observed between soil and ashes only in a large-scale forest fires, suggesting that fractionation during burning of the soil and litter is dependent on temperature (Richter et al. 2023).

1.4. Additional metal(loid)s of concern in French Guiana and the Amazon

Given its prevalence in the region and impacts on the environment and the population as detailed above, the majority of studies in mining areas have focused on Hg, which was measured in 40 % of sediment samples and 50 % of water samples in a recent meta-analysis on metal contamination in the Amazon region (Moulatlet et al. 2023). However, other metals and metalloids are starting to draw attention in French Guiana due to health concerns.

1.4.1. Lead

Lead (Pb) is a toxic element that readily crosses the blood-brain barrier, resulting in acute health problems including anemia, immunotoxicity, and irreversible neurological disorders (Rocha and Trujillo 2019). The first considerations about Pb poisoning in French Guiana arose in 2011, after a blood lead level (BLL) of 1700 $\mu g.L^{-1}$ was measured in a 3-year old girl (Rorive et al. 2015). As a comparison, the

world health organisation threshold for Pb poisoning in children was set at 50 $\mu g.L^{-1}$ (WHO 2021). However, there is no known BLL threshold for the absence of adverse effects on children, and impaired intellectual functions have even been observed in children with low BLL of < 100 $\mu g.L^{-1}$ (Lanphear et al. 2005). Further studies revealed that Pb poisoning was present in more than 20 % of Guyanese children (using a BLL threshold of 50 $\mu g.L^{-1}$) (Andrieu et al. 2020), and 45 % of illegal gold miners (BLL threshold at 100 $\mu g.L^{-1}$) (Douine et al. 2025). These results prompted the creation of a working group supported by the regional health agency, which aims to understand the potential contamination sources for heavy metals and metalloids in French Guiana, with an emphasis on Hg and Pb ("StraMeLo"). Further studies have proposed manioc consumption and possibly the exposure to Pb from bullets used in hunting activities as the main exposure routes to Guianese riverine populations (Rimbaud et al. 2017, Maurice et al. 2021). Up until now, little is known about background levels of Pb in soils and waters of French Guiana, with one study measuring Pb in soils observing elevated concentrations (10 – 30 $\mu g.g^{-1}$) (Maurice et al. 2021). As a result, and similarly to Hg, soil remobilisation due to gold mining might increase Pb export to the rivers through erosion.

1.4.2. Arsenic

Arsenic (As), is a highly toxic metalloid, although its toxicity is known to be highly dependent on its speciation, with As(III) displaying a much larger toxicity compared to As(V) (Moe et al. 2016). Chronic As exposure is linked to an increased risk of cancer (skin, lung, …), and to cardiovascular diseases, with the main pathway for this exposure being water consumption (Kapaj et al. 2006). Accordingly, in the Amazon, most studies on As have focused on groundwater as this is a major pathway for population contamination. Elevated As concentrations (up to 430 $\mu g.L^{-1}$) have been observed in aquifers along the main Amazon tributaries in Peru and Brazil, with 70 % of wells located near the river channel displaying concentrations above the WHO threshold of 10.$\mu g.L^{-1}$ (de Meyer et al. 2023). Geogenic As remobilisation by mining activities has been investigated, especially in the Iron Quadrangle region in Brazil known for its gold, diamonds and iron deposits. There, high As concentrations were observed in mine tailing materials, and also in urine of children in local communities (Matschullat et al. 2007, Ono et al. 2012, Bueno Guerra et al. 2023).

In the stream water of the main tributaries of the Amazon, higher filtered and particulate As concentrations were measured in streams draining the Andes than in the others. This highlights that the Andes mountain range is the main source of As transport to the ocean by the Amazon river, but the majority of samples staying below the WHO limit of 10.$\mu g.L^{-1}$ (Scarpelli 2005). In French Guiana, detailed information on As background concentrations in soils and streams is lacking. A mapping in the main stream of French Guiana showed that total As concentrations in stream water were low, at 0.12 ± 0.07 $\mu g.L^{-1}$ (Saplairoles et al. 2010). However, As concentrations in sediments were more

important (31 ± 7 $\mu g.g^{-1}$). The potential remobilisation of As by mining activites is not studied. As a result, information on background As concentrations in different compartments would be valuable in order to apprehend possible contamination sources (if any) to the population.

While the impact of gold mining on particle and metal(loid) (especially Hg) exports to the river has been extensively studied in different sites across the Amazon region, less is known concerning the effect of restoration on these exports. Additionally, Hg isotopes have been used to trace the use of anthropogenic Hg in gold mining versus non-impacted areas. In French Guiana, the juxtaposition of legal and illegal gold mining practices calls for the investigation of this tool to discriminate between the two practices. Finally, in the region, background concentrations in soils and water are less well constrained for other metal(loid)s like Pb and As.

Chapter 2.

Study area and sampling strategy

This doctoral work focused on two legal mining sites on which the mining company SAS GAIA had authorisation to operate, named “Awa” and “Sophie”. Five sampling campaigns were conducted over the span of the doctoral project (from 2022 to 2024): G0 (01/22), G1 (04/22), G2 (12/22), G3 (05/23), G4 (04/24). Sampling was performed on the Awa site during all 5 campaigns, and only during G0 and G2 on the Sophie site.

This chapter briefly describes the two study sites, as well as the fieldwork experimental design. Sampling on and around these mining sites targeted stream and mining pond water (filtered and particulate), rainfall, soils, sediments, vegetation and atmosphere as detailed more specifically in each chapter of this thesis.

2.1. Description of the mining sites

2.1.1. The Awa alluvial mining site

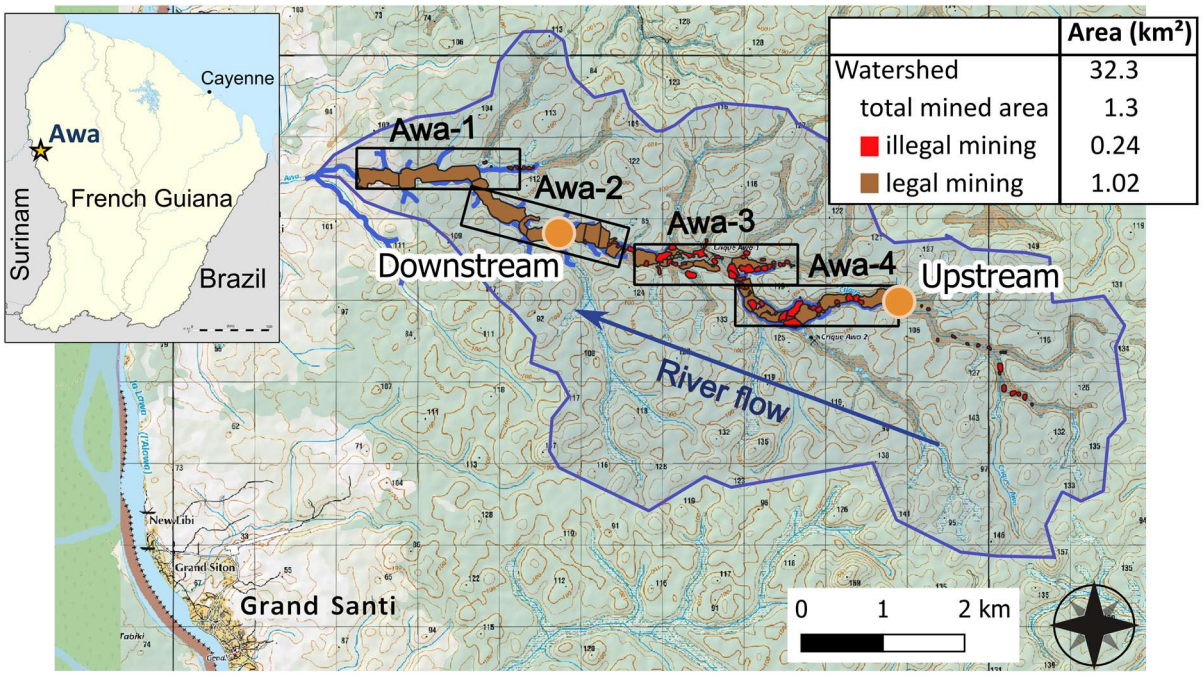

Figure 2.1. *Awa gold mining site with legal (brown) and illegal (red) exploitation areas. The location of the upstream and downstream hydrological stations are displayed as orange dots.*

The Awa gold mining site (54°20’34”W, 4°19’8”N) is located on the eponymous river, close to the town of Grand-Santi. It is located within the Maroni watershed, the river which forms the western border of French Guiana with Suriname. Rainfall was measured on a meteorological station in Grand Santi, 7 km away from the mining site (meteo.data.gouv.fr [last accessed on 3rd February 2025]). The average annual rainfall over the three years of the study amounts to 2500 mm. It is an alluvial gold mine, where the exploitation and restoration steps followed guidelines detailed in section 1.2.5. There are 4 AEX (1 km² exploitation areas), numbered 1 to 4 from downstream to upstream (Figure 2.1). Awa-1 and -2 were exploited between September 2017 and April 2020, followed by Awa-3 and -4 which were

exploited between May 2020 and April 2021. First restoration works were performed locally in May-July 2019, but the main restoration effort, starting from downstream (Awa-1) to upstream (Awa-4) was performed between May 2021 to August 2022. Restoration involved filling the mining ponds followed by landscaping and replanting 100 % of the (legal) mining site, at 3-meter intervalls. Six on-site tree nurseries were created for a total of 7000 planted saplings. The tree species used are *Euterpe oleracea* (açaí palm), *Inga sp*., *Senna multijuga*, and *Hymenaea courbaril*, the three latter being part of the *Fabaceae* family (Figure 2.2).

Illegal gold mining had taken place on the site, prior to the arrival of the gold mining company, as evidenced by the presence of mining ponds, mainly present in the sectors of Awa-3 and -4. These areas were left in their original state, with no exploitation nor restoration performed on them by the company. Concerning historical gold mining (before year 2000), little information is available on the Awa sector specifically, but first exploitation licences "on the right bank of the Maroni river" can be found starting in 1873, and one exploitation licence on the Awa river was recorded in 1901 (personal communication, Pierre Rostan, Mine et avenir).

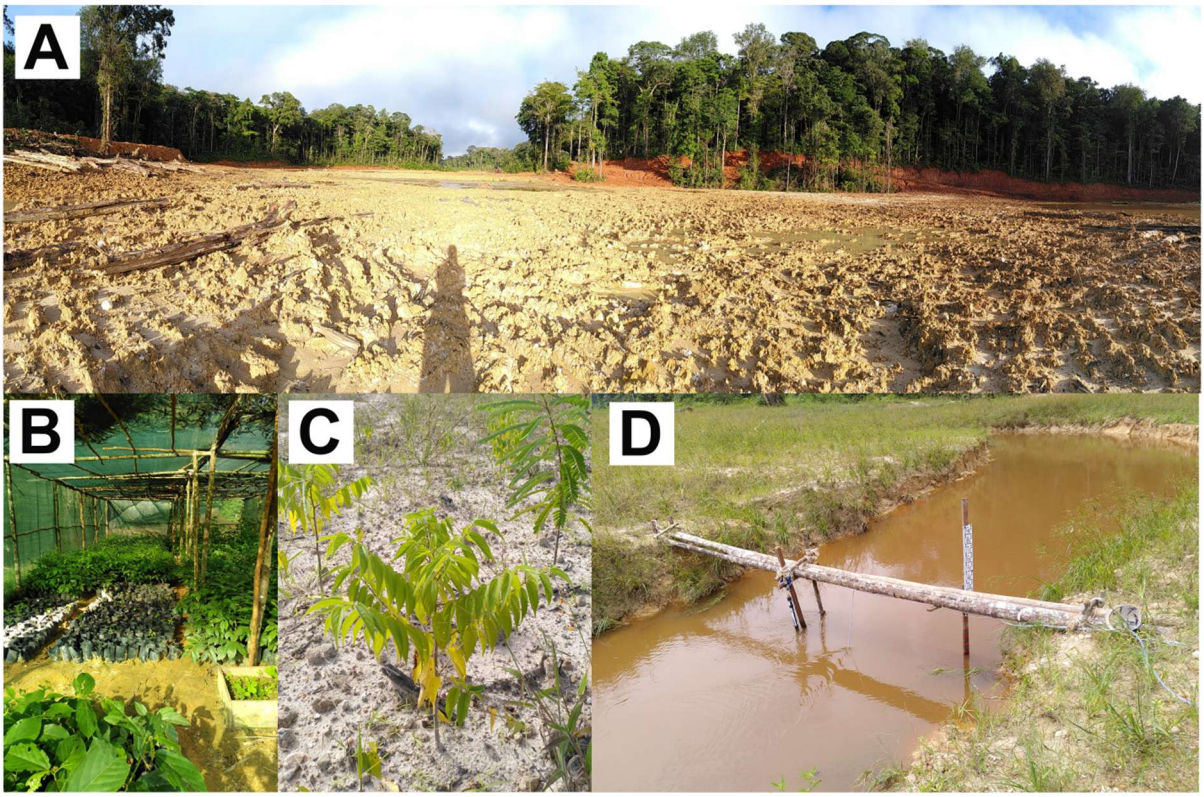

Figure 2.2. *Selected pictures from the Awa gold mining site with A) the landscaped gold mining flat, tree plantations B) in the nursery and C) on site, and D) reconstructed river path.*

2.1.2. The Sophie primary gold mining site

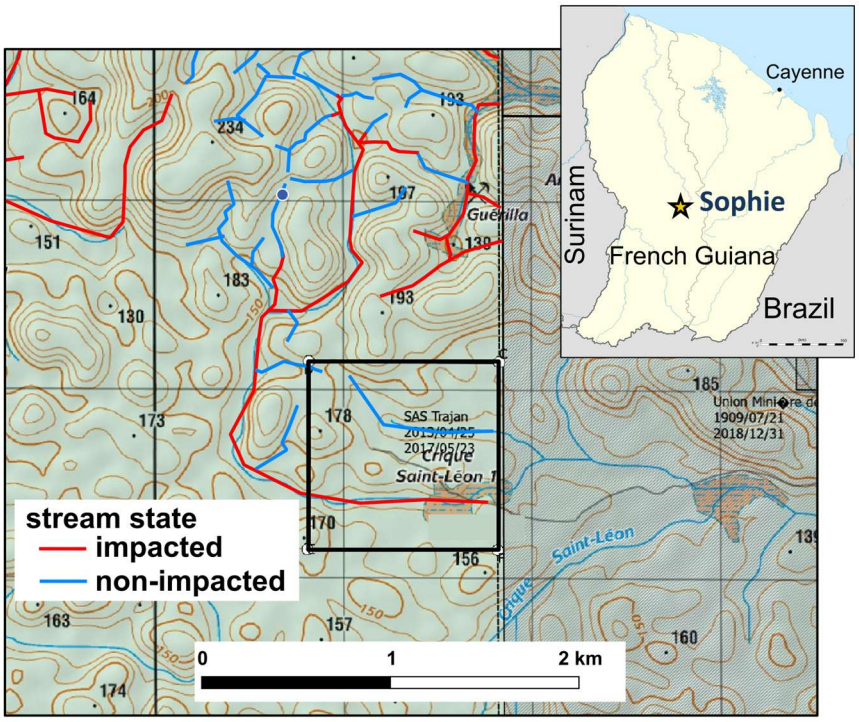

Figure 2.3. *Sophie gold mining site (named Guerilha with the limits of the PER in the black square) with surrounding streams in blue and the evidence of illegal gold mining in red (qualitative assessment based on observations).*

The "Sophie" mining site is located on the Mana watershed (Figure 2.3). It is a site of primary gold deposits although the presence of alluvial gold (deriving from the primary deposits) has been shown by prospection works. The absence of alluvial gold mining activities on this site can be explained by i) the proximity of gold-rich sites which might have diverted the miners from somewhat less profitable sites like this one, and ii) the large silt cover (>7 m) over the auriferous gravel, which makes it unaccessible for informal miners without heavy machinery, and not economically viable for small mining companies. The mining company SAS GAIA obtained an exploration permit (PER) in order to determine the gold content in soils and assess whether exploitation of the area would be cost-effective. 10 m depth core sampling was performed on a grid on the prospection site, and further 100 m depth sampling was then performed on targeted spots. No legal exploitation activity took place during the timespan of this doctoral work. Additionally no historical gold mining activity has been registered on the Sophie mining site. However, the presence of extensive illegal gold mining activities for the last 20 years is documented by the presence of mining shafts (Figure 2.4 A), and old camp sites scattered around the Sophie mining site. There, the ore was extracted through rudimentary tunnels, crushed and ground at the surface and then mixed with water and washed on Hg-coated copper plates to retain the gold (Le Tourneau 2020).

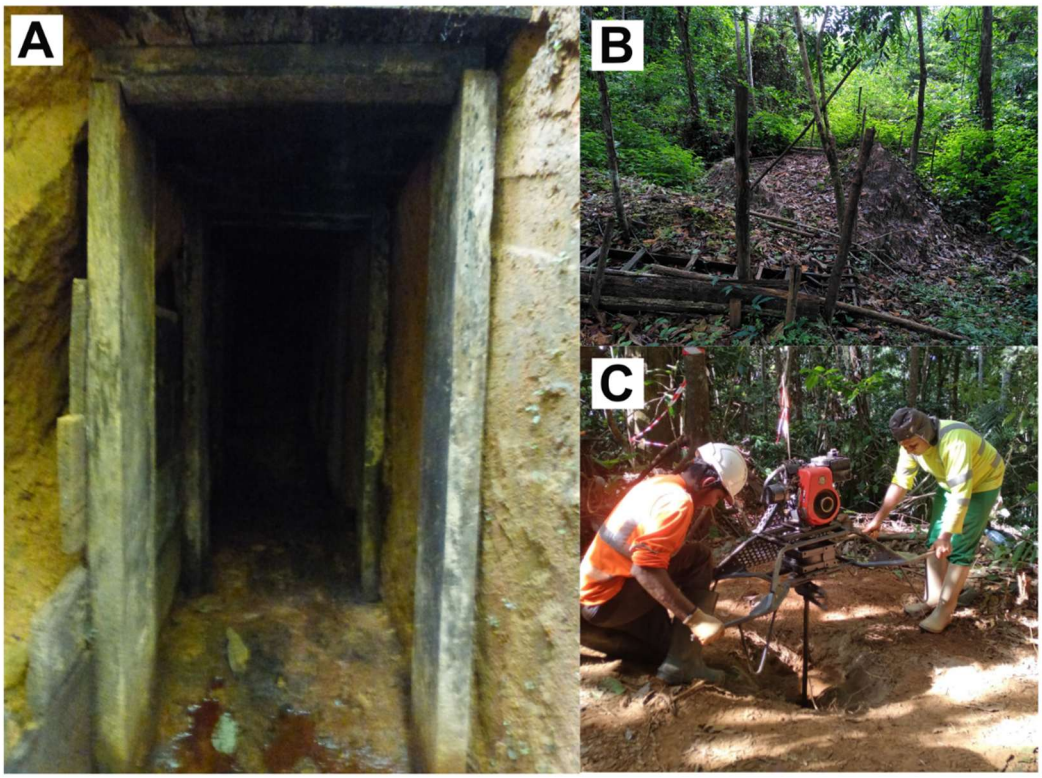

Figure 2.4. *Pictures on the Sophie prospection site, with A) shafts constructed by illegal gold miners to access the gold bearing vein, B) washing site where the ore is crushed and then mixed with water and Hg is added to recover the gold, C) 10 m depth core sampling for Au analysis in prospection stage.*

2.2. Particle and metal(loid) export: experimental design

On the Awa site, two experimental designs were constructed to follow particle and metal(loid) exports at the square-meter scale (2.2.1) and at the watershed scale (2.2.2). These designs are described in the following sections.

2.2.1. Square-meter scale: soil erosion experimental design

Erosion plots were installed in triplicate at two sampling sites. One restored and replanted in April 2022, just before the first sampling campaign, and one restored three years before. Hereafter the two sites are termed “landscaped” and “tree-covered”, respectively (Figure 2.5 A and B). The purpose of these plots was to recover the eroded material and overland flow water from a defined area during a rain event. Each plot consisted of wood panels (2 m × 2 m, 4 m²) inserted 10 cm into the soil and extending 15 cm above the soil. Each plot was connected to an 80L bucket installed at the lowest point of the slope and buried in the soil.

After a rain event, the total volume of water collected in the bucket was measured, a 250 mL aliquot of the suspension was sampled in an FEP bottle, to measure both suspended solid concentrations, Hg speciation, and major and trace elements in the filtered and particulate fractions, the rest was discarded and the coarse matter sedimented at the bottom was retrieved, freeze-dried and weighed.

Additionally, soil erodibility and critical erosion shear-stress were measured using an EROMES device as described in (Haddad 2022, Joensuu, et al. 2017, Lanuru, et al. 2007, Schünemann and Kühl 1991). These erodibility measures were performed on surface soil and riverbed sediments (Figure 2.5 C and D)

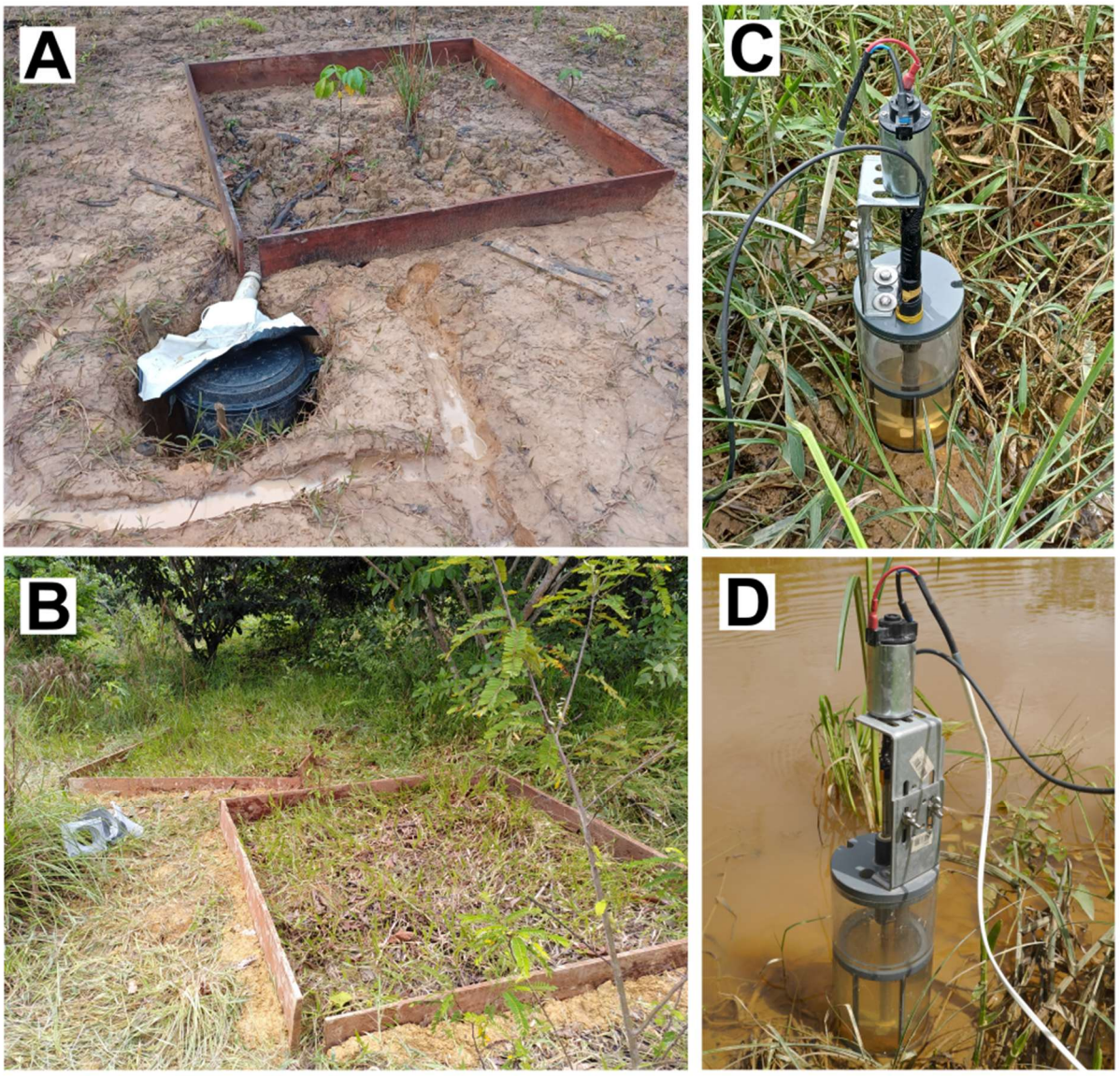

Figure 2.5. *Erosion plots on the landscaped (A) and the tree-covered (B) sites, and erodibility measurements on mining flat topsoil (C) and river bed sediment (D).*

2.2.2. Watershed scale: hydrological monitoring

Two sites on the Awa river were chosen for hydrological monitoring, one upstream and the other downstream of the mining site (Figure 2.1). On each of these sites a hydrological monitoring station was installed. This consisted of i) a staff gauge to record the river's water level by visual observation, ii) a pressure sensor measuring the water level (OTT-PLS), and iii) a turbidity sensor (Hydrolab HL4) (**Figure 2.6**). The water level and turbidity sensors were recording data continuously, even oustide of field campaigns, at a time step of 1 h.

During the field campaigns, the river discharge was measured at both stations using two devices (an impeller current meter, OTT and a hand-held surface velocity radar, Viatronics). The repetition of discharge measurements at different water levels enabled the construction of stage discharge rating curves. Using these curves, the hourly river discharge was calculated based on the water level measurements.

In addition, discrete sampling of river water was performed during flood events during the different campaigns using an automatic sampler (ISCO 3700 or 2900, Teledyne, Figure 2.6C).

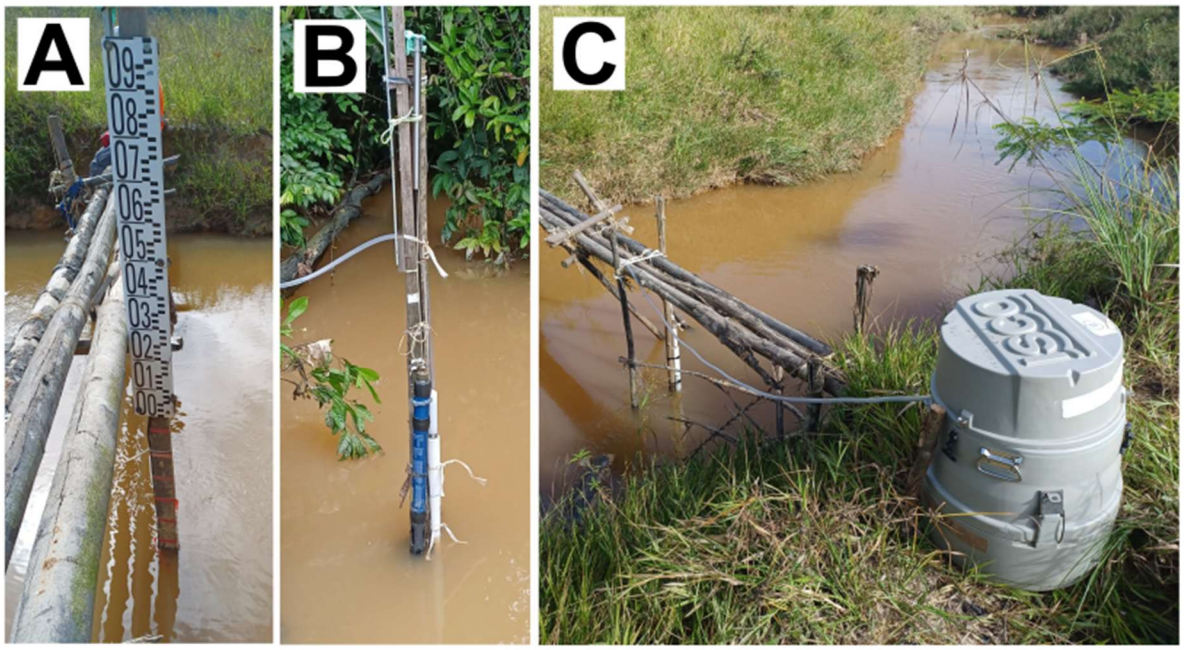

Figure 2.6. *Hydrological station with A) staff gauge, B) turbidity and water height sensors and C) automatic water sampler.*

2.3. Sampling strategies

On both mining sites, samples from different compartments were collected. This section describes briefly the different compartments and the sampling strategies associated to each.

2.3.1. Soils and sediments

Surface soils and soil profiles were collected using a manual auger as depicted in **Figure 2.8**A. Surface soils were sampled on the Awa site around the erosion plots (2.2.1) on the landscaped and tree-covered sites. Additional surface soil samples were taken at other locations on the Awa site, in areas exploited legally, and in sections of previous illegal exploitation, in the vicinity of the mining ponds. Soils profiles were sampled in the forest around the Awa mining site, and on a hilltop on the Sophie site.

Sediment samples were collected using a manual auger or directly in a plastic containter. On the Awa site, sediment samples were collected in the river, upstream and downstream of the mining area, and

on a small non-impacted stream. Mining pond sediments were sampled on both the Awa and the Sophie sites. The location of sampled mining ponds on the Awa site is presented in **Figure 2.7**.

Results and detailed methods for the analysis of soil functions can be found in chapter 3, geochemical data of surface soils and river sediments is presented in chapter 4, and Hg concentrations and isotopic composition in soils and sediments can be found in chapter 5.

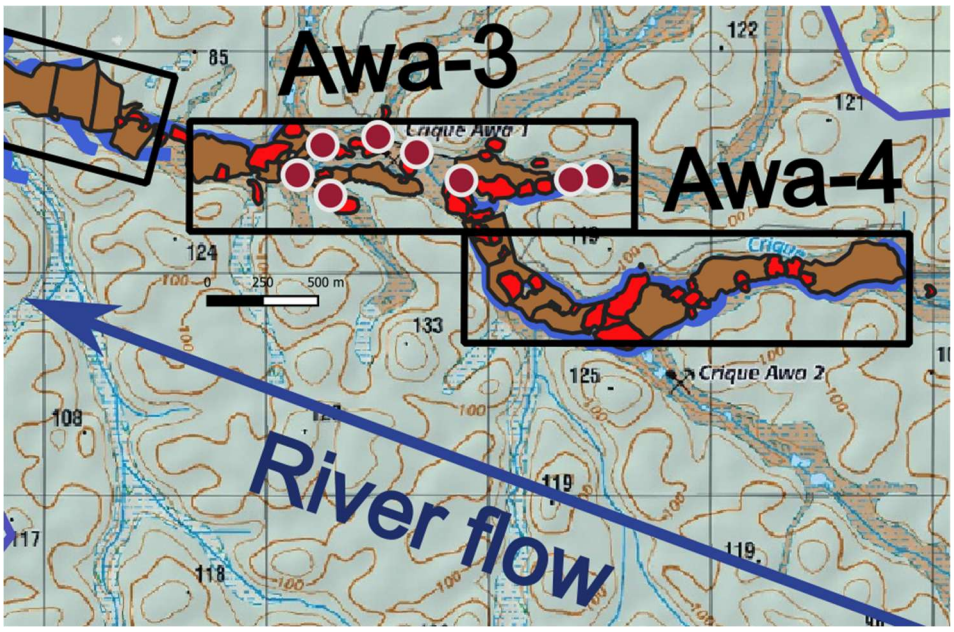

Figure 2.7. *Localisation of the illegal mining ponds sampled on the Awa site (red dots).*

2.3.2. Water

On the Awa site, overland flow water samples and river samples were collected as described in section 2.2. In addition, water samples were collected on the Awa site, in the same illegal mining ponds where sediment had been collected (Figure 2.7), and also on the Sophie site. Rainfall water was collected exclusively on the Awa site, in pre-washed teflon containers both on the open mining area without the presence of trees in the vicinity (wet deposition, Figure 2.8C), and under the adjacent forest cover (throughfall, Figure 2.8D). Interstitial soil water was collected using acid-washed syringes connected to microporous polymer tube samplers (Rhizon® SMS, Rhizosphere Research Products, Figure 2.8B). Water samples were then filtered on-site, on 0.45µm PVDF filters (Figure 2.8H).

Suspended particle concentration and metal(loid) (Hg, Pb, As) concentrations in overland flow water was used in chapter 3 and 4 to assess their export at the square-meter scale and the watershed scale, respectively. Geochemical data in overland flow water, interstitial soil water (ground water) and river water is also presented in chapter 4. Hg distribution and speciation in all water compartments is presented in chapter 5.

2.3.3. Atmosphere

Atmospheric mecury concentrations were collected during the sampling campaigns by pumping air on gold-coated quartz used as Hg-traps (Figure 2.8E). This sampling was performed under controlled air flow and during a specific amount of time (20-60 min). the traps were then sealed and stored until analysis. Atmospheric Hg by active sampling was performed on the Awa site on legal portions of the mining site, in the vicinity of illegal mining ponds, and under forest cover. On the Sophie site, atmospheric Hg sampling was performed exclusively in the vicinity of a mining pond.

Additionally, passive atmospheric mercury samplers (MerPAS, Figure 2.8F) were installed on the Awa site. Similarly to active sampling, these samplers were set up on legal portions of the mining site, in the vicinity of illegal mining ponds, and under forest cover. Atmospheric Hg sampling (both active and passive) is presented in chapter 5.

2.3.4. Vegetation

Finally, herbaceous plants were collected on the Awa mining site (Figure 2.8G). These plants were sampled at various locations on the mining site, in legal and illegal areas. The aerial part was separated from the roots, and each fraction was washed, dried and ground for Hg analysis. Additionally, around the landscaped and tree-cover sites, the roots and aerial portions were sampled on a defined soil volume to assess the root density and above-ground biomass.

Data on Hg concentration and isotopic composition in plants is found in chapter 5, and the root density and above-ground biomass are detailed in chapter 3.

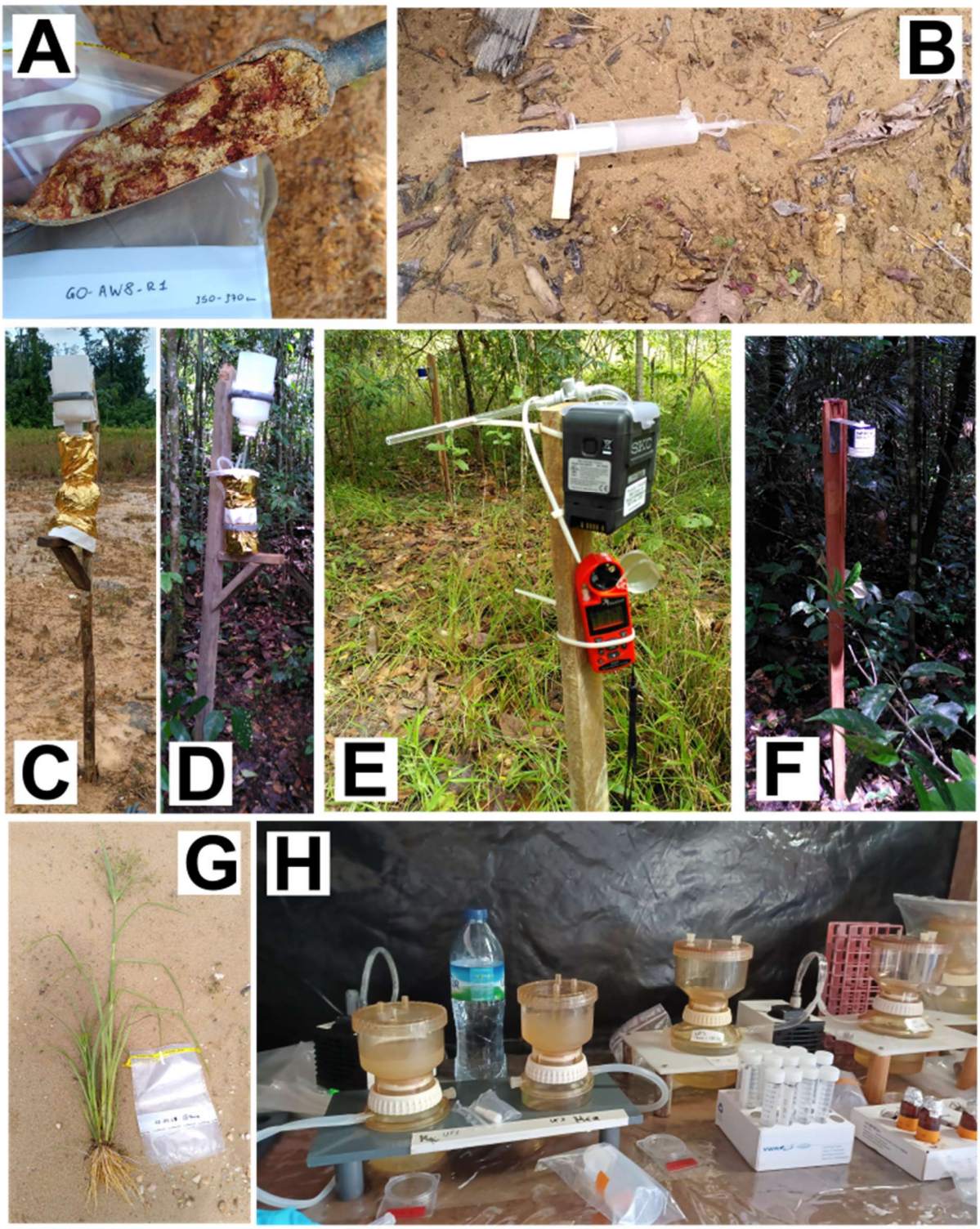

Figure 2.8. *Examples of sample collection and treatment for different compartments: A) soil profile, B) interstitial soil water, C) wet deposition, D) throughfall, E) active gaseous mercury sampling, F) passive gaseous mercury sampling (MerPAS), G) herbaceous plant (Cyperaceae), G) water filtering station on-site.*

Chapter 3.

Impact of gold mine restoration on the export of particles and metal(loid)s and the recovery of soil functions at the square-meter scale

Introduction

In the Amazon, the impact of gold mining on erosion inducing both particle and metal(loid) export has been widely studied (Telmer et al. 2006, Diringer et al. 2015). However, little is known about the fate of these mines after their restoration.

The following chapter describes the temporal evolution of a legal gold mine after restoration with a focus on the following aspects:

- Erosion (i.e. particle export and overland flow water)
- Contamination (i.e. metal(loid) partitioning and export)
- Revegetalisation (i.e. root density and above ground biomass of herbaceous plants)
- Biological soil functions (i.e. soil enzyme activity, DNA content, microbial diversity, …)

It aims at providing a quantification of i) the timespan necessary for the reduction of export and the recovery of vegetation and soil functions, and ii) the extent of this reduction or recovery. To do so, erosion plots have been installed

This chapter has been submitted for publication in *Science of the Total Environment* and is currently under review.

3.1. Article I –

Post-exploitation fate of alluvial goldmines in the Amazon: soil erosion, metal(loid) remobilisation, and ecological functions evolution during restoration

Naomi NITSCHKE[a,b,c,e*], Jennifer HARRIS[b], David AMOUROUX[c], Emmanuel TESSIER[c], Cédric LEGOUT[d], Sylvain CAMPILLO[a], Stéphane TARAVELLA[e], and Stéphane GUÉDRON[a]

[a] Univ. Grenoble Alpes, Univ. Savoie Mont Blanc, CNRS, IRD, IFSTTAR, ISTerre, 38000 Grenoble, France

[b] BRGM, F-45071 Orléans, France

[c] Université de Pau et des Pays de l'Adour, E2S UPPA, CNRS, IPREM, Institut des Sciences Analytiques et de Physico-chimie pour l'Environnement et les Matériaux, Pau, France

[d] Université Grenoble Alpes, CNRS, IRD, IGE, 38000 Grenoble, France

[e] SAS GAIA, Cayenne, France

* Corresponding authors: naomi.nitschke@univ-grenoble-alpes.fr

Acknowledgments

We thank Océane Asensio (UPPA-Tech, IPREM UPPA/CNRS), Cindy Arnoldi (LECA, UGA), Catherine Joulian (BRGM) and Hafida Tris (BRGM) for analytical support in the laboratory. Thanks to Mélanie Roy (IRD) for help in plant identification. Finally, we thank Akram Ali (SAS GAIA) for field assistance.

3.1.1. Abstract

Artisanal and small-scale gold mining is responsible for deforestation and habitat degradation in Amazonian ecosystems due to soil reworking and increased turbidity in surrounding rivers. In French Guiana, legal mines are required to perform rehabilitation after the gold extraction. To assess the successfulness of this rehabilitation, the temporal evolution of particles and metal(loid)s (mercury, lead, arsenic) export was measured, as well as several parameters linked to soil functions (soil carbon and nitrogen, microbial diversity, enzymatic activities). Results show a rapid decrease in particle export (i.e., 3-fold reduction within the first 8 months, and up to 2000-fold reduction after 4 years), linked to an increase in spontaneous colonisation by herbaceous plants. This decrease in particle export induced an efficient decrease in metal(loid)s (Hg, Pb, As) export predominantly associated to the particulate fraction. The parameters associated with ecological functions did not show any significant increase within 5 years after rehabilitation, possibly due to depletion of nitrogen stocks by the herbaceous growth inducing a competition for resources with the soil microbial communities. Microbial communities on the mining site displayed significant evolutions during the 5 years after restoration, with no visible convergence with forest-soil communities, but underlining the adaptability to climatic conditions and a changing environment. These results highlight that current rehabilitation practices are efficient in limiting particle and major metal(loid) export while more attention needs to be addressed to the recovery of soil functions and biological activities.

Keywords Gold mining; Amazon; mine restoration; soil functions; mercury; arsenic; lead

Highlights

- The restoration (landscaping and replanting) of a goldmine was studied.
- Spontaneous revegetation rapidly decreased particle and metal(loid) fluxes.
- No evidence of the recovery of ecological functions over 5 years after restoration.
- A limitation in nitrogen stocks limits the recovery of soil functions.
- Changes in microbial communities on the mining site reflected an adaptation capacity.

3.1.2. Introduction

The Amazon rainforest comprises 50 % of all rainforests worldwide (Xiao et al. 2009). Deforestation has caused forest loss of up to 20 % in the last 40 years, (Fearnside 2005, da Cruz et al. 2020, Hänggli et al. 2023) leading to losses in biodiversity (Brandão et al. 2022) as well as warming at the local and regional scale (Artaxo 2023, Butt et al. 2023).

Amazonian soils are typically highly weathered and nutrient-depleted compared to temperate soils (Quesada et al. 2010). The presence of a rainforest above these soils is made possible by rapid and efficient nutrient cycling thanks to fast organic matter (OM) degradation by soil (micro)organisms present in the thin organic top layer, followed by reuptake by trees (Wagg et al. 2014). However, this equilibrium is fragile, and once the thin organic top-layer is lost, the recovery of a forest ecosystem is not guaranteed. Hence, deforestation in the Amazon basin is often linked to a decrease in soil biodiversity (Franco et al. 2019). In addition, deforestation leads to enhanced soil erosion, particularly in tropical regions where rainfall is intense and frequent (Lal 1990, Labrière et al. 2015). Such a loss in nutrients and microorganism diversity has long-term consequences on soil properties, with impacts observed on soil functions even decades after reforestation (Veldkamp et al. 2020).

At the scale of the Amazon region, the main drivers for deforestation are agriculture and artisanal and small-scale gold mining (ASGM), although regional differences exist (Hänggli et al. 2023). In the Guiana Shield, due to extensive gold mining and less extensive agriculture, ASGM is the major cause of deforestation, mostly in Guyana and Suriname, but also to some extent in French Guiana (Hänggli et al. 2023). In the case of ASGM, erosion is exacerbated, as alluvial gold mining involves not only the removal of the vegetation cover but also topsoil stripping using water hoses in order to access the gold-bearing gravel layer. This leads to important exports of particles to rivers, which negatively affects downstream ecosystems (Mol and Ouboter 2004, Tudesque et al. 2012). Such an increase in river turbidity is accompanied by an increase in geogenic mercury (Hg) fluxes, which results from the accumulation in the soil of atmospheric Hg taken up by vegetation over millions of years (Guédron et al. 2006, Fostier et al. 2015). Once deposited on the river bed, Hg bound to fine particles can undergo methylation and biomagnification along the food webs, where methylmercury (MeHg) neurotoxicity can cause health problems in indigenous communities relying mainly on fishing (Maury-Brachet et al. 2006, Pignoux et al. 2019). Additionally, the discovery of lead (Pb) poisoning and high blood lead levels in children of French Guiana communities in 2011 (Rimbaud et al. 2017) prompted the creation of a working group supported by the regional health agency to unravel the contamination sources and mechanisms of different heavy metals and metalloids (including arsenic) in French Guiana (“Stratégie Métaux Lourds”, StraMeLo). High blood lead levels were proposed to be linked mainly to manioc

consumption, and possibly to exposure to lead bullets through hunting activities (Andrieu et al. 2020, Maurice et al. 2021).

Numerous studies have documented the direct impact of ASGM on Hg pollution and SPM release during operations (Pfeiffer et al. 1989, Telmer et al. 2006, Dethier et al. 2019, Diringer et al. 2020). Presently, there is a strong demand from stakeholders and authorities about the fate of ASGM sites after operations and/or rehabilitation with regard to these two aspects (Hellal et al. 2020). After clear-cutting, the ASGM area is usually first colonised by pioneer species (mainly herbaceous), which are less nutrient-demanding and resist strong insolation. This reduces soil erosion and provides organic matter and nutrients for other plants that appear later on in the succession towards the potential establishment of a secondary forest. Successful rehabilitation therefore attempts to restore soil stratification, stabilize them, and ultimately allow the accumulation of newly produced OM. Therefore, this promotes the stabilisation of geogenic Hg originally present in these soils thanks to its affinity for OM and iron oxy(hydr)oxides, thereby reducing its export to the surrounding watershed. The availability of nutrients and their carrier phases in the soil can be a limiting factor that prevents the creation of a secondary forest, especially carbon and nitrogen (Gomes and Luizão 2011), but also phosphorous (Cunha et al. 2022), and trace elements, which can be involved in essential functions like nitrogen-fixation (Barron et al. 2008).

In French Guiana, legal gold mines are required to restore the mining site after exploitation. Mines are therefore subject to controls during and after exploitation to limit their impact on the environment and assess their rehabilitation efforts (Marquis 2015). To promote rapid vegetation recovery in addition to natural regeneration, replanting is performed on at least 30 % of the mining site, usually with plants from the Fabaceae family, which are able to form a symbiosis with nitrogen-fixing bacteria through root nodules. However, no regulations exist for gold mine rehabilitation concerning microbial diversity or soil functions. Few studies in the area have investigated the evolution of soil functions on a mining site after restoration (Schimann et al. 2012, Couic et al. 2021), and the timespan for the recovery of these soil functions is yet poorly documented.

The overall objective of this study is to follow the short-term temporal evolution of a gold-mined flat after exploitation and its impact on both metal(loid) fluxes and on the recovery of soil functions. To this end, soil erosion and metal(loid) contaminant fluxes (Hg, Pb, As...) were monitored on experimental plots to document their evolution during rainfall events over several years after the mining site rehabilitation. In addition, soil biotic and abiotic indicators related to soil functions were analysed (i.e., total carbon and nitrogen contents, soil microbial diversity through DNA metabarcoding and enzymatic activities) to document the evolution of soil functions during the human-assisted mine restoration process.

3.1.3. Materials and Methods

Study area. French Guiana (87,500 km²) is part of the Guiana Shield located in the north-eastern region of South America between Brazil and Surinam (2-6°N and 51°30'-54°30'W). It experiences an equatorial humid climate with an average annual rainfall of around 4000 mm and 96 % of the territory is covered by a tropical rainforest. Samples were collected from the Awa site, an alluvial gold mine (54°20'34" W, 4°19'8" N) located on the eponymous river and under control of the mining company SAS GAIA (Figure 3.1). The Awa River is part of the bigger Maroni watershed, the largest river of French Guiana (66 814 km²), which is densely gold-mined (Gallay et al. 2018) and has a long history of gold mining dating back to the 1900s (Jébrak et al. 2021). The Awa watershed area is 32 km². Alluvial gold mining exploitation was performed below a riverbed, to extract gold from gravel deposits resulting from the weathering of auriferous quartz veins (Thomassin et al. 2017). These downslope valleys typically consist of sandy hydromorphic soils exhibiting reducing conditions due to the presence of water flowing very slowly (Guédron et al. 2009). The mineralogy of these soils is dominated by quartz and kaolinite, with some goethite. Exploitation and production was conducted on the site from downstream to upstream between September 2017 and April 2021, and the first restoration works were operated between May and July 2019. Full restoration was then performed between May 2021 and August 2022. Restoration of the mining site consists in filling the mining ponds with the gravel and clay removed during exploitation, performing landscaping respecting as much as possible initial soil stratification, and then replanting trees grown on nurseries on-site, at a three-meter interval. The tree species used are *Euterpe oleracea* (açaí palm), *Inga sp.*, *Senna multijuga,* and *Hymenaea courbaril*, the three latter being part of the Fabaceae family.

Four sampling campaigns were conducted over three years (from 2022 to 2024) to follow the evolution of restoration on the mining flat: G1 (04/22), G2 (12/22), G3 (05/23), G4 (04/24), on two different sites (Figure 3.1). One restored and replanted in April 2022, just before the first sampling campaign, and one restored three years before. Hereafter the two sites are termed "landscaped" and "tree-covered", respectively. The samples were labelled based on the time since restoration, with samples on the landscaped site labelled T=0 months (G1), T=8 months (G2), T=13 months (G3), and T= 24 months (G4) and the samples on the tree-covered site labelled T=36 months (G1), T=44 months (G2), T=49 months (G3), and T=60 months (G4) (Figure 3.1). For soil function analyses, a nearby reference site under forest cover was studied during the last sampling campaign (G4).

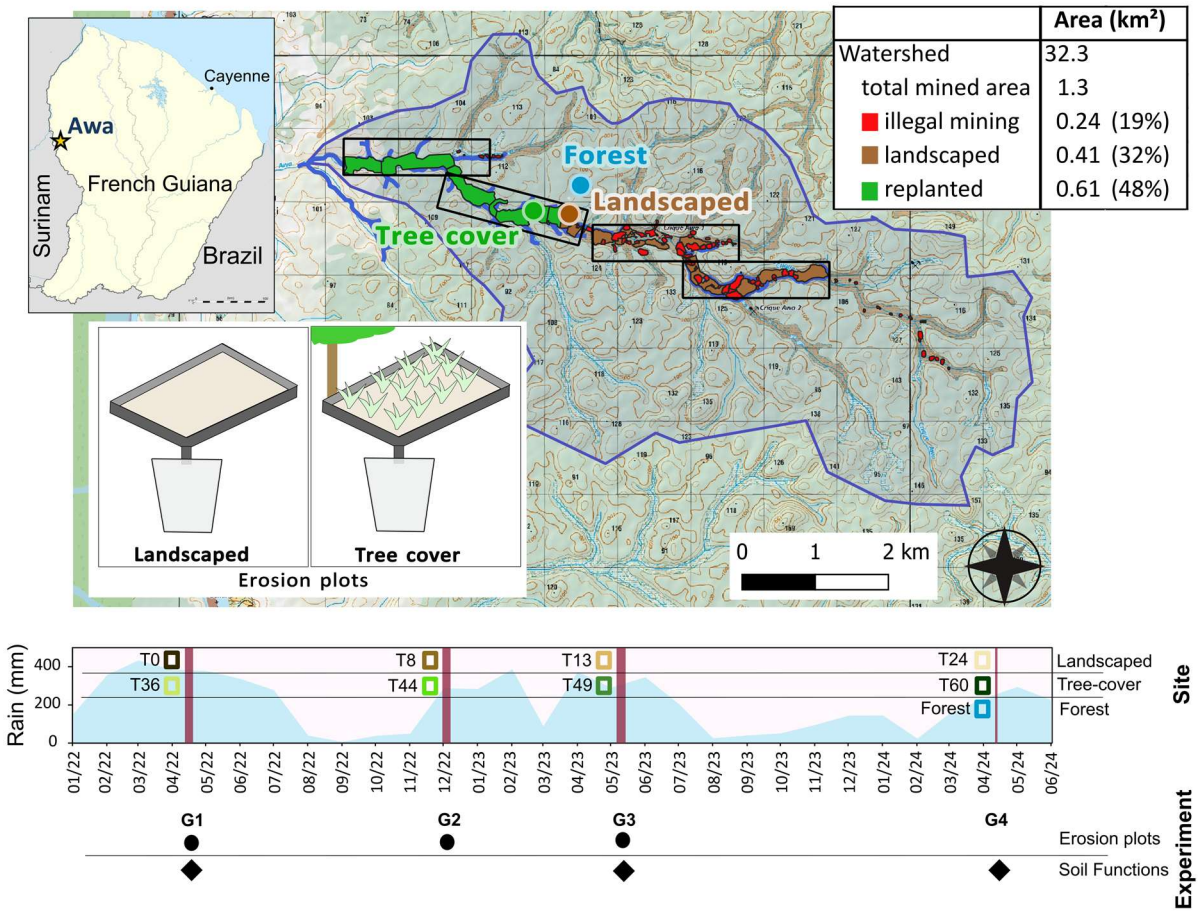

Figure 3.1. *Study site, timeline with rainfall data (Grand-Santi meteorological station (meteo.data.gouv.fr [last accessed on 3rd February 2025])) and sampling points for the erosion (round) and soil function (diamond) experiments.*

Experimental design for erosion monitoring.

Erosion plots were installed in triplicate at each sampling site to recover the eroded material from a defined area during a rain event. Each plot consisted of wood panels (2 m × 2 m, 4 m²) inserted 10 cm into the soil and extending 15 cm above the soil. Each plot was connected to an 80L bucket installed at the lowest point of the slope and buried in the soil.

Meteorological data. Hourly temperature and rainfall data for the determination of annual meteorological trends were retrieved from the Meteo France meteorological station at Grand-Santi (GS) (meteo.data.gouv.fr [last accessed on 3rd February 2025]), which is located 7 km away from the mining site. For specific events, a garden rain gauge was used and the duration of the rainfall event was recorded.

Sample collection. All samples were collected in pre-cleaned vials following ultra-clean technique protocols (Stoichev et al. 2006). Surface runoff water and particles were collected after each rain event during the sampling campaigns G1, G2, and G3. The total volume of water was measured, a 250 mL aliquot of the suspension was sampled in an FEP bottle, to measure both SPM, Hg speciation, and

major and trace elements in the filtered and particulate fractions. The rest was discarded and the coarse matter sedimented at the bottom was retrieved, freeze-dried and weighed. The 250 mL aliquot was filtered on a 0.45µm PVDF filter (Sharif et al. 2014, Stoichev et al. 2016). The filtrate was collected in FEP bottles acidified to HCl 0.02 % for Hg analyses, and in trace grade falcon tubes acidified to HNO_3 2 % for multi-elemental analyses. The PVDF filters were air-dried in a laminar flow hood for 48h and weighed to determine the amount of particles. This particle mass was divided by the total water volume that was filtered in order to determine the suspended particulate matter (SPM) concentration in $mg.L^{-1}$.

Experimental design for soil function monitoring.

Soils were sampled on the two sites monitored for erosion, i.e., the landscaped site and the tree-covered site during three out of the four campaigns (G1, G3, G4), always at one-year intervals, during the beginning of the rainy season. Additionally, samples were also collected from a forest site at G4 as a reference site for comparison.

Sample collection. From each sampling spot, three areas of ~20m² were defined and 9-10 soil cores from the 0-20cm depth were sampled using a manual auger. These cores were pooled and homogenised to form a composite sample for each replicate for further physico-chemical and biological analyses. Soil cubes of 10×10×10 cm were also collected from each site to measure soil density as described below. Plant above- and below-ground biomass was also collected and analysed as described below.

Chemical analysis.

All details for protocols and QA/QC are provided in S.I.1.2. Briefly, total Hg on solid coarse samples was analysed by atomic absorption spectroscopy after pyrolysis and gold amalgamation (AMA 254, Altec) as described elsewhere (Roos-Barraclough et al. 2002, Guédron et al. 2009). Hg speciation in filtered water and on suspended particulate matter (SPM) collected on filter samples was analysed following established methods using single-spike isotope dilution analysis by gas chromatography – inductively coupled plasma mass spectrometry [SS-ID GC-ICP-MS (Monperrus et al. 2005, Monperrus et al. 2008, Sharif et al. 2014, Cavalheiro et al. 2016)]. The concentration of major elements and trace metal(loid)s (i.e., As, Pb) was measured by inductively coupled plasma-atomic emission spectrometry (ICP-AES) (Agilent, Varian 720-ES) and by inductively coupled plasma mass spectrometry (ICP-MS) (Agilent 7900 coupled to an ESI PrepFast IC module) respectively. Organic carbon (C) and nitrogen (N) concentrations were obtained using a Flash Smart elemental analyser (ThermoFisher Scientific) (Piton et al. 2020).

Soil erosion measurements.

Soil erosion rates and critical erosion shear-stress were measured using an EROMES device as described elsewhere (Schünemann and Kühl 1991, Lanuru et al. 2007, Joensuu et al. 2017, Haddad 2022), and detailed in section 3.1.7.1.3.

Soil physico-chemical characterization.

Soil Water Holding Capacity (WHC), apparent density (DA), pH, and granulometry were measured as detailed in the supplementary material (S.I.1.4). Briefly, soil density was obtained by collecting soil volumes of 10×10×10 cm from each site. The total volume of soil removed was measured by filling the hole (covered with a plastic foil) with water. The total amount of soil was weighed, and an aliquot was taken to be dried and weighed again, to measure the soil apparent density (DA). pH was measured in the laboratory after resuspending 5 g of soil in mQ water volume of 25 mL. Soil granulometry was obtained using a laser granulometer (Malvern, Mastersizer 2000) following the protocol detailed in (Grangeon et al. 2012). Finally, plant biomass over the soil surface was obtained by cutting the aerial part of the plants, which were washed with H_2O mQ, and dried. The above-ground biomass (AGB) was then calculated by dividing the plant weight by the total soil surface. Roots were also separated manually, washed with H_2O mQ, dried, and weighed. The root density (RD) was calculated by dividing the weight of dried roots by the total soil volume.

Soil biological analyses.

Soil extracellular enzymatic activities of arylsulfatase (ARS), β-glucosidase (β-GLU), N-acetyl-glucosaminidase (NAG), and phosphatase (PHOS) were measured according to ISO 20130:2018. Soils for enzymatic analyses were frozen at -80°C prior to analysis.

Soil DNA was extracted from 0.6 to 0.7 g of soil (dry weight), previously frozen at -20°C, using the FastDNA® SPIN Kit for soil (MP Biomedicals, Illkirch, France) and the FastPrep R-24 classic Instrument used per the manufacturer's instructions. Soil DNA extract concentrations were measured with the Quantus fluorimeter and the QuantiFluor™ dsDNA System, according to the manufacturer's instructions (Promega, Madison, WI, USA). Real-time quantitative polymerase chain reaction (qPCR) was performed to assess gene abundances as a measure of bacterial abundance (16S rRNA) and abundance of genes linked to the nitrogen cycle (*narG*, *amoA*, *nosZ, nifH*, *nirS*). The primers used are listed in Table S 3.1.

Bacterial and archaeal diversity were determined by 16S rRNA gene metabarcoding. Sequences were processed on the Galaxy platform using FROGS (Escudie et al. 2018) based on the Galaxy analysis platform (Galaxy 2022). Bacterial double affiliation was performed by blasting amplicon sequence variants (ASVs) against the SILVA database 138.1 (Quast et al. 2013). ASVs with affiliation <100 % at the phylum level were removed from the dataset.

Statistical analyses.

All statistical analyses were performed using R. The Student's t-test was performed when the data was normally distributed and the variances between the two studied groups were equal. When this was not the case, the Wilcoxon test was performed. Regressions are shown only if the p-value is below 0.05. To visualize dissimilarities in bacterial community structures, two-dimensional nonmetric multidimensional scaling (NMDS) based on Bray-Curtis dissimilarities of log-transformed data was applied using the R software. The relationship between community profiles and hydrogeochemical variables was evaluated by fitting environmental vectors a posteriori onto the NMDS.

3.1.4. Results

3.1.4.1. Fate of surface soil after landscaping

3.1.4.1.1. Anthroposol characteristics

Reworked soils after mining operations consist mainly of sand and gravel mixed with the fine fractions that settled in the tailing banks. The physicochemical characteristics of the top-soils (0-20 cm) on the mining site are rather consistent over time and differ mostly between the two sites by granulometry, with the landscaped site being sandier (66 ± 2 % on the landscaped site and 50 ± 5 % on the tree-covered site), and the tree-covered site showing higher proportions of clay and silt (Figure S 3.4). This increase of the clay fraction over time has also been observed, on a much larger timescale, in the restoration of a sandy desertified land in China, and was attributed to the sequestration and immobilisation of fine particles by the vegetation cover (Zhang et al. 2016). The water holding capacity (WHC) of the soil was similar between the two sites. The total mercury (THg) concentration in these mine top-soils is 102 ± 36 $ng.g^{-1}$, somewhat lower than what was measured on pristine soils around the mine site (143 ± 45 $ng.g^{-1}$) which is typical for non-contaminated soils in French Guiana and the Amazon region (Beliveau et al. 2017, Guédron et al. 2018, Goix et al. 2019). The lower Hg concentrations on the mine soil compared to the pristine soils can be attributed to the reworking and mixing of the soil over several meters, where deep soil horizons are depleted in Hg as observed here (42 ± 10 $ng.g^{-1}$ below 2 m), and elsewhere in French Guiana (Guédron et al. 2006). This can also be due to Hg loss from soils to the river during the mine exploitation phase. Many studies report an increase in Hg concentrations in suspended matter and sediments downstream of gold-mining areas (Lino et al. 2019, Moreno-Brush et al. 2020), but few studies have focused specifically on the export of natural Hg from a mining site during the exploitation phase (Grimaldi et al. 2015). Concerning Pb, soil concentrations were similar in the mined soils and in the forested soils (3.2 ± 1 $\mu g.g^{-1}$), but As concentrations were significantly depleted in mine top-soils (0.27 ± 0.04 $\mu g.g^{-1}$) compared to pristine soils (1.2 ± 0.4 $\mu g.g^{-1}$).

3.1.4.1.2. Rapid attenuation of particles and contaminant export from soil

To document the evolution of reworked soils during the mine restoration, exported particles and metal(loid)s were studied in experimental plots from the initial landscaping (T0) to 49 (T49) months. Immediately after landscaping and revegetation (T0), the export of soil particles during a rain event was high (78 ± 48 $g.m^{-2}$), and in the range of values on bare agricultural land in Brazil (40 ± 20 $g.m^{-2}$) (Beliveau et al. 2017), indicating strong erosion of the mining flat right after restoration. In contrast, the amount of eroded soil particles on the tree-covered site (T = 49 months since rehabilitation) was significantly lower (p=0.001, Wilcoxon), and virtually reduced to zero, at 0.01 – 0.3 $g.m^{-2}$, which is comparable or even lower than what was observed on forested areas in Brazil and other tropical forest

soils (Hartanto et al. 2003, Beliveau et al. 2017). Because the amount of eroded particles depends on the rain event intensity, particle exports were normalised by the total amount of rainfall (in mm) in order to derive particle fluxes. The total particle flux exported during a rain event was significantly decreased (p=0.0034, Wilcoxon) 4 years after rehabilitation, leading to a 2000-fold reduction of particle export when taking into account all eroded particles (fine and coarse), and a still a 200-fold reduction when considering only the fine (suspended) particles (Figure 3.2A).

The concentration of total mercury (THg) and its speciation as methylmercury (MeHg) as well as other trace metal(loid)s (i.e., Pb, As) were measured on eroded particles and in the filtered fraction. Mercury concentration on the fine particles was 172 ± 73 $ng.g^{-1}$, and did not differ significantly between the two sites, suggesting that the nature of particles exported from the two sites is similar. In the filtered fraction, THg was 1.5 ± 0.8 $ng.L^{-1}$ (Figure S 3.1A), with no significant difference between the two sites (p=0.6), or evolution during the time after rehabilitation. However, this runoff water appears significantly depleted in THg (p=0.002) in comparison with the Hg concentration in rainfall samples on the same mining site (3.1 ± 1.2 $ng.L^{-1}$). This indicates that Hg from rainfall might adsorb to soil particles, thereby immobilising it on the mining site, consistently with other sites in French Guiana (Guédron et al. 2011). Methylmercury (MeHg) accounts for less than 5 % of total Hg, but this proportion significantly (p=0.001) increased over time, likely due to an increase in the particulate MeHg concentration over time (p=0.014). Particulate Hg dominated the partitioning between particles (Hg_P) and water (Hg_F), representing almost 100 % of total Hg (THg= Hg_P + Hg_F) at T0, and more than 75 % at T49 (Figure S 3.1A). As a result, the total Hg fluxes are mainly driven by the erosion of the mining flat soil, and the decrease in particle export observed after 49 months results in a steep decrease in total Hg fluxes (p=0.003, Figure 3.2). However, because the decrease in water export was less extensive (40-fold reduction) than the fine particle export (200-fold reduction) between T0 and T49, the proportion of mercury (Hg_P) associated with the particulate fraction significantly decreased over time (Figure S 3.1A).

Lead (Pb) concentrations in the particulate fraction were stable over time and were identical in the landscaped and tree-covered sites at 12 ± 6 $\mu g.g^{-1}$, in the same range that has been measured in French Guianese topsoils (Guédron et al. 2006, Maurice et al. 2021). In contrast, As concentrations were significantly lower (p= 0.00012) in the tree-covered site (1.4 ± 0.4 $\mu g.g^{-1}$) than in the landscaped site (2.8 ± 0.8 $\mu g.g^{-1}$), in the range of soils in the Brazilian Amazon region (da Silva Junior et al. 2019). In the filtered fraction, both Pb and As concentrations were constant over time after restoration with a mean of 0.08 ± 0.1 $\mu g.L^{-1}$ and 0.04 ± 0.02 $\mu g.L^{-1}$, respectively (Figure S 3.1B). The partitioning coefficient between the filtered and particulate fractions ($[Pb_F]/[Pb_P]$ or $[As_F]/[As_P]$ using concentrations in $\mu g.L^{-1}$) was generally lower (by a factor 10) for Pb than for As. As a result, the particle export reduction over time results in a more drastic decrease of the proportion of As in the particulate fraction (down to

52 ± 13 %) compared to Pb (83 ± 12 %), which exhibits a behaviour that is more similar to Hg. In any case, the reduction of both particle and water export over time leads to a significant reduction of both As (150-fold) and Pb (100-fold) fluxes over time (Figure 3.2).

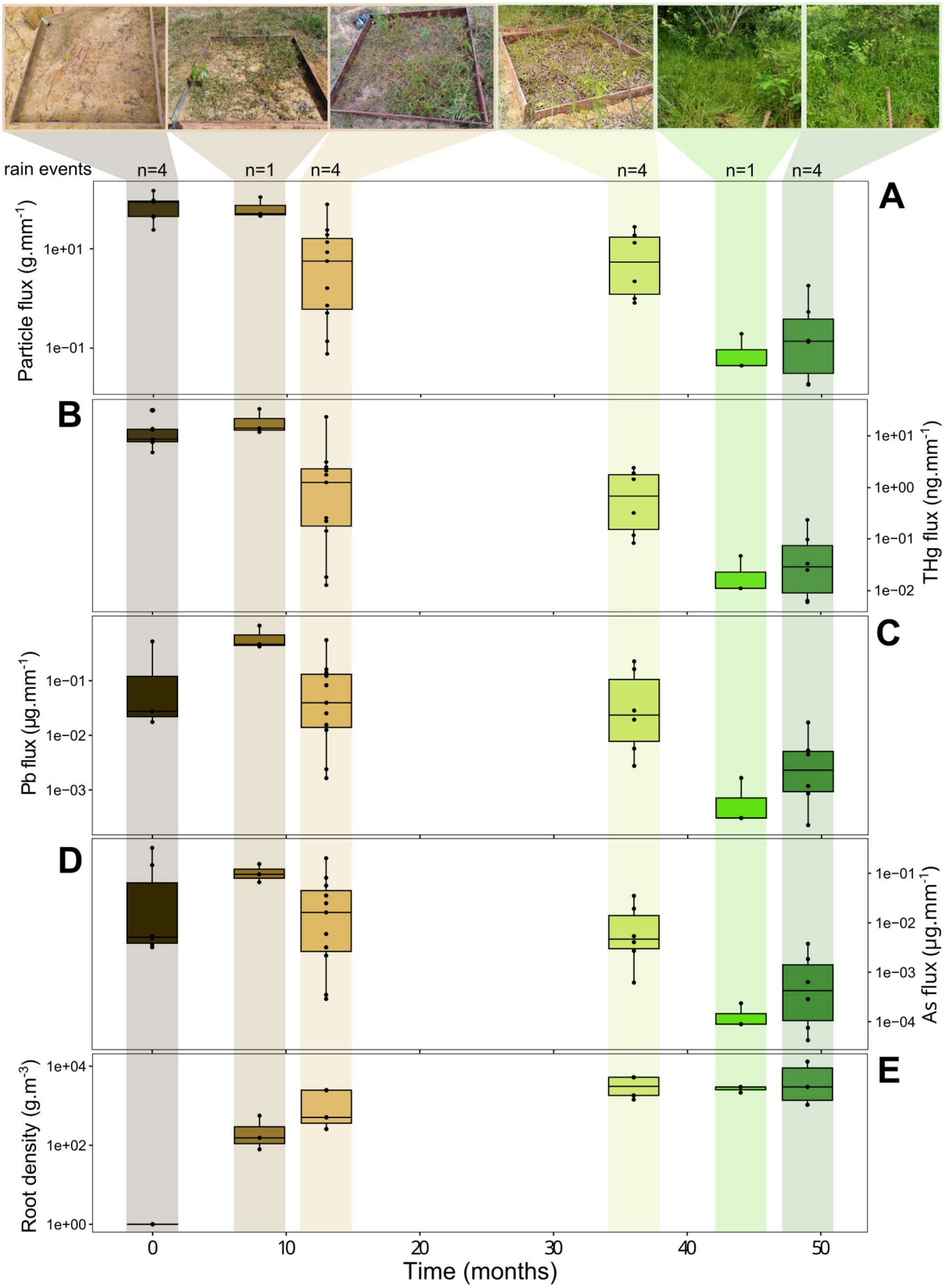

Figure 3.2. *Evolution of exports of A) particle, B) Hg, C) Pb, D) As normalised by rainfall (mm) and E) root density over time after rehabilitation.*

3.1.4.1.3. Pioneer plants (herbaceous) as a basis for soil surface stabilisation

Over the first year following landscaping, a sharp increase in root density due to spontaneous colonisation by herbaceous plants was observed (Figure 3.2E). In addition to an increase in root density, the above-ground biomass also increased with time, with high variability between plots and sites. Finally, the presence of biological soil crusts was observed on the soils (Figure S 3.3), resembling a biofilm- or moss-like matrix covering soil surfaces. No ecological characterisation has been performed on these crusts. The herbaceous plants, together with the colonisation of soil surfaces by biological soil crusts are the most likely hypothesis for the observed decrease in particle and metal(loid) export.

The large heterogeneity in particle and metal(loid) exports observed at T=13 months between the 3 plots is most probably due to their distance to the forest edge, whose nutrient inputs may have affected the ability of pioneer plants to colonize the site. The herbaceous plant cover was heterogeneous between the three plots (Figure S 3.2), increasing with their proximity to the forest edge. Thus, the variability in particles and metal(loid) export reflects the heterogeneity of plant colonisation within a site, which is then smoothed out over time as herbaceous colonisation becomes ubiquitous.

Such observations were confirmed by erodibility experiments performed on surface soils at the edge of each plot at T=13 months. An increased erosion constant coupled to a lower critical erosion threshold (Figure S 3.2A) were found on the soil with little herbaceous cover, whereas the plot with more pronounced vegetation showed an increased soil stability. This further characterises the role played by the spontaneous colonisation of herbaceous plants in the stabilisation of soil and metal(loid)s on the mining site. These erodibility measurements cannot be directly related to the particle flux observed during the rain events, as the experimental setup is designed to simulate shear stress due to surface runoff and disregards the effect of raindrops on soil aggregate breakdown (Legout et al. 2005), but it provides an indication of differences in erodibility between the sites.

Hence, the rapid decrease in particle and metal(loid) export after 1 year of rehabilitation of the mining flat is mostly attributed to the spontaneous colonisation of herbaceous plants that helps to stabilise the soil. However, in order to go beyond the vegetative state and obtain a closure of the mining site, with a secondary forest, several functional cycles in the soil need to be restored. Microbiological indicators were thus followed over time to assess the recovery of soil functions on the restored mining site.

3.1.4.2. Evolution of soil functions and microbial communities during revegetation

3.1.4.2.1. Carbon and nitrogen cycles

To study the recovery of soil functions, the six plots ("landscaped" and "tree-covered" triplicates) were studied for two years at time steps of 12 months, to document soil ecology in similar seasonal conditions as soil biological activity can be greatly impacted by seasonal changes (Cusack et al. 2019, Madegwa and Uchida 2021). Studied plots were then compared to a reference forest site located close to the mining site for comparison with a reference undisturbed forest.

Analysis of biological indicators linked to the carbon (C) and nitrogen (N) cycle, i.e., total C and N content in the soil, total DNA and 16S qPCR for the C-cycle, and functional genes linked to the N-cycle (*narG*, *nifH*, *nirS*, *nosZ*) did not show any significant increase over time after restoration (Figure 3.3).

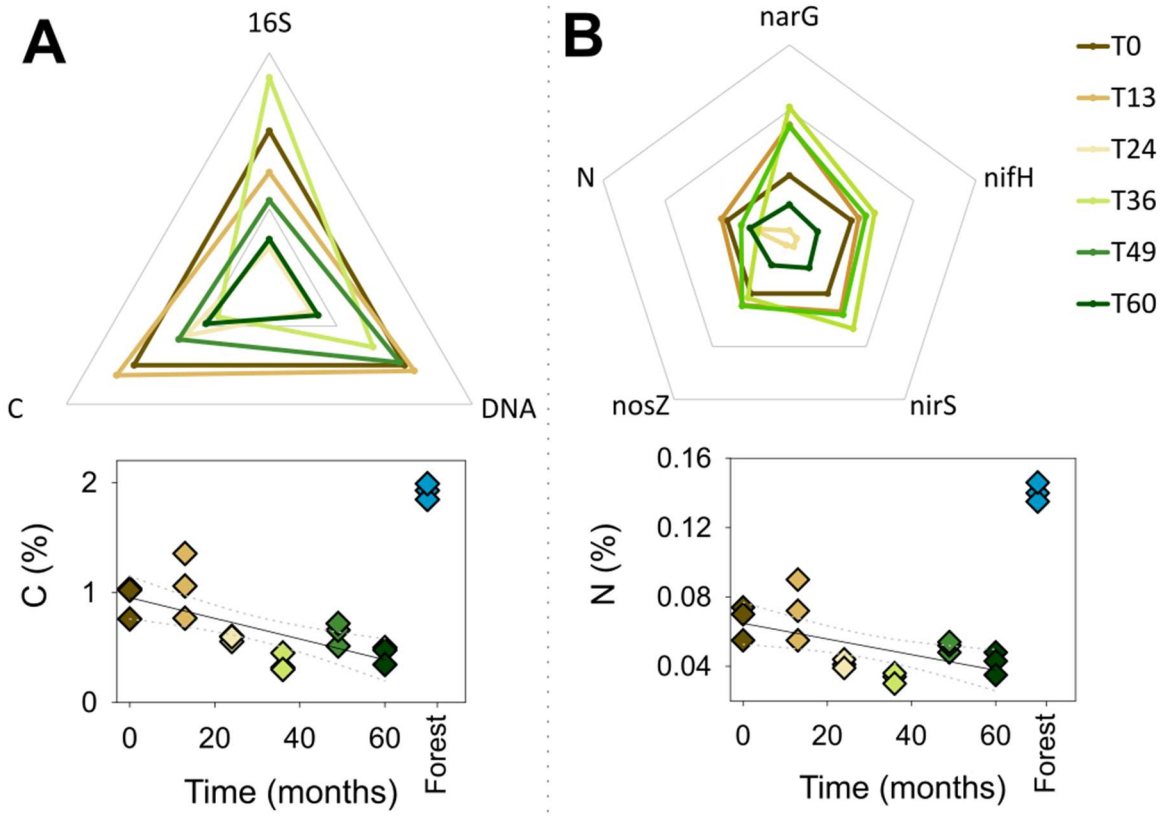

Figure 3.3. *Evolution of soil functions linked to the carbon (A) and nitrogen (B) cycles at different time points after restoration. The top panels are radar plots, normalized by the value at T0 (dark brown).*

Total C and N contents are much lower for the mining site than for the nearby forest ($p = 0.001$ and 0.008 respectively, Figure 3.3), and in the range of data reported for other mining sites in French Guiana (Schimann et al. 2012, Couic et al. 2021). This was expected as most of the organic layer is usually eroded and washed away during the exploitation and early restoration phases. On the foresteded site, in addition to the higher concentrations of C and N observed, higher amounts of total

DNA and functional genes linked to the N-cycle were detected. C and N trends on the mining site showed a decrease over time, with a sharp decrease after 13 months, followed by low C and N contents afterwards (Figure 3.3). The C/N ratio was significantly (p=0.0002) lower on the tree-covered site (11.1 ± 1.4) than on the landscaped site (14.3 ± 0.8), due to a steeper decrease in C than in N over time. Landscaped site C/N ratio is close to the one for the reference forest site at 13.7 ± 0.1, which is also similar to reported values in forests in French Guiana (Schimann et al. 2012).

Amongst indicators of soil microbial activity, only arylsulfatase, an enzyme involved in the sulfur cycle, which hydrolyses sulfuric esters to phenols and sulfates, displayed an increase in activity over time (ARS, p = 0.002, linear regression). This suggests that ARS might be a relevant early-stage indicator to detect precursors of soil microbial activity recovery.

3.1.4.2.2. Evolution of microbial communities on a restored gold mined flat

From a total of 1551 ASVs obtained from the 16S rRNA sequencing, the major bacterial phyla observed in soil samples (Figure S 3.8) were Acidobacteria (33 ± 6 %), Proteobacteria (27 ± 6 %), Chloroflexi (16 ± 5 %), Actinobacteria (8 ± 2 %) and Planctomycetia (5 ± 1 %), with relative abundances in the range of what was previously found in tropical forest soils in French Guiana (Zinger et al. 2019), and on gold mining sites in Colombia (Cardona et al. 2024). Alpha diversity indices (Shannon, Chao1, inverse Simpson) did not show any significant differences in diversity between mine soils and the forest soil. However, a difference in alpha diversity was observed only for the time point T49 compared to all the other points before and after. This indicated a reduced richness (Chao1), but an increased community diversity (inverse Simpson index) compared to other mine soils and the forest (p=0.00164, ANOVA). Consistently, the bacterial ASVs for time point T49, showed an increase in the presence of classes linked to anoxic environments, like *Desulfuromonadia* (Greene 2014) and *Anaerolinae* (Yamada and Sekiguchi 2018), which might be explained by wetter conditions, with the 30 days previous to sampling accumulating 357 mm, corresponding to a 20 % rainfall increase compared to the year before, and 150 % compared to the following year, resulting in soil saturation and potentially anoxia.

Non-metric multidimensional scaling (NMDS) performed on Bray-Curtis dissimilarities allowed to analyse the beta-diversity and potential changes in the communities' composition over time. Indeed the alpha diversity indices might not reflect changes in diversity in the cases where some species are replaced by others, leading to the same richness, but a difference in community structure. When superimposing the NMDS with environmental and soil functions data, microbial diversity appears mostly driven by soil water holding capacity (WHC), climate parameters (rainfall), enzymatic activities (urease), and fungi abundance (qPCR 18S). Possibly, fungi diversity would provide additional insight into the impact of restoration on soil microbial communities.

The bacterial community changed significantly in the first year, between T0 and T13, and remained comparable for the three following years (i.e., at time points T13, T24 and T36), with strong similarities between the landscaped and tree-covered sites for these time points (Figure 3.4). The change in beta-diversity from T0 to T13 can be mainly attributed to a loss in Firmicutes, Desulfobacterota and Crenoarchaeota, which showed higher relative abundances at T0. The shift in community composition at T49 observed in the NMDS could be driven by the change in environmental conditions that were more anoxic due to high rainfall as discussed above.

Finally, another shift in community composition was observed at T60, concomitant to a change in ecological vegetation succession. Indeed, at T60, an increase in litter was observed, as well as a reduction in herbaceous plants, with a two-fold decrease in above-ground biomass (AGB) between T49 and T60 (Table S 3.3).

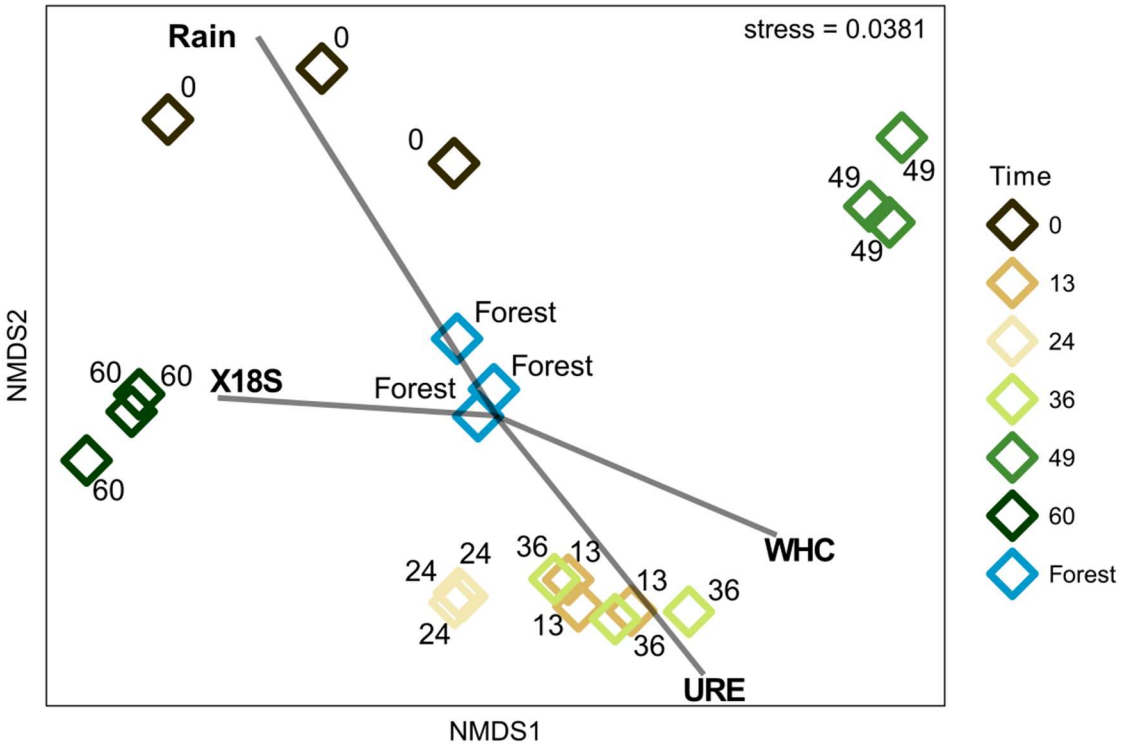

Figure 3.4. *NMDS ordination of bacterial diversity profiles from the mining site soils during time after restoration. Significant environmental variables (p<0.05) are represented by vectors fitted to the NMDS ordination that indicate the direction and magnitude of the change of the variable. (WHC: water holding capacity, URE: urease enzyme activity, 18S: fungi 18S gene qPCR).*

3.1.5. Discussion

3.1.5.1. Reduction of particle and contaminant exports after restoration at the watershed scale

Although subject to variability because of spatial differences in slope and extent of vegetation cover, an estimation of particle export from the gold mining flat can be provided. When reported at the scale of the mined area, annual fine particle specific fluxes represent 191 ± 82 $t.km^{-2}.yr^{-1}$ at T0 just after restoration. This is much higher than what was observed in a formerly gold-mined watershed (50 km²) in French Guiana (10-70 $t.km^{-2}.yr^{-1}$ (Hellal et al. 2020)). After two years (T49), the specific particle fluxes were greatly reduced (200 fold, to 1.1 ± 1.2 $t.km^{-2}.yr^{-1}$).

Annual THg specific fluxes showed the same trend in temporal evolution as particle fluxes and represented 31 ± 15 $\mu gHg.m^{-2}.yr^{-1}$ at T0, which is more important than what was observed on a small pristine watershed (1.6 km²) in the Brazilian Amazon (3-9 $\mu gHg.m^{-2}.yr^{-1}$ (Fostier et al. 2000)), but lower than a small (1 km²) formerly gold mined watershed in French Guiana (93 ± 37 $\mu gHg.m^{-2}.yr^{-1}$ (Guédron et al. 2011)). The reduction in particle fluxes over time results in a reduction of THg fluxes which reached 0.17 ± 0.16 $\mu gHg.m^{-2}.yr^{-1}$ two years after restoration. This is even lower than the fluxes observed in a small (5 km²) formerly gold-mined watershed in French Guiana during the dry season (0.584 $\mu gHg.m^{-2}.yr^{-1}$ (Hellal et al. 2020)). The annual Hg influx from rainfall amounts to 8 $\mu gHg.m^{-2}.yr^{-1}$, hinting towards a net gain of Hg on the mining site, two years after rehabilitation. Hence, the mine soil has evolved from being a source of particulate Hg for downstream rivers during the first year, to becoming a sink able to trap and immobilise Hg, as the particles are stabilised and erosion is reduced. However, in these downslope mining soils depleted in iron oxides and dominated by kaolinite, which is known to be a minor carrier phase for Hg in tropical soils (Guédron et al. 2009, Gurjão et al. 2010), organic matter is the main carrier phase for Hg. Hence, a decrease in carbon concentration over time, as observed in these soils, might also reduce the capacity of the soil to act as a sustainable sink for Hg. Similarly, the reduction of particle exports also induced a reduction in specific yearly Pb and As export from 1500 at T0 down to 17 $\mu g.m^{-2}.yr^{-1}$ at T49, and from 121 down to 1.2 $\mu g.m^{-2}.yr^{-1}$ respectively. To the best of our knowledge, no other studies have assessed the export of neither of these two metal(loid)s in the Amazon region during the mining operations or after the restoration process. The depletion in iron oxides in the downslope mined soils will possibly also affect the retention capacity of the soils for these elements, as both Pb and As are known to show a strong affinity for iron oxides and organic matter (da Silva Junior et al. 2019, Rocha and Mahler 2023).

The reduction in particle export over time after restoration is mainly due to the colonisation of the mining site by herbaceous plants, which provides multiple positive feedback on the soil stabilization (Figure 3.5). This induces a stabilisation of the soil through the increase in root density, which increases

the soils' shear strength (Katuwal et al. 2013), with herbaceous plants being particularly efficient in soil stabilisation due to their great density of very fine roots (Tufekcioglu et al. 1998, Trükmann et al. 2009). In addition, the presence of above-ground plant biomass (AGB) plays a role in rain interception and reducing splash erosion due to the impact of raindrops (Yao et al. 2018), which can be a major component of erosion (Angulo-Martínez et al. 2012). The increase in above-ground biomass is also linked to a reduction in total water exported during a rain event, which can be explained by a reduction of the overland flow velocity, and thus a better water infiltration in the soil. Furthermore, the appearance of a biological soil crust observed on the surface of the soil might have contributed to the prevention of soil erosion, in combination with herbaceous plants and their roots. These "soil biocrusts" are known to help stabilise soils and can play a role in restarting the C and N cycles (Antoninka et al. 2020), and while they are known to develop preferentially in dry climates, biocrusts have been studied in tropical regions as well (Seitz et al. 2017, Oliveira and Maciel-Silva 2022).

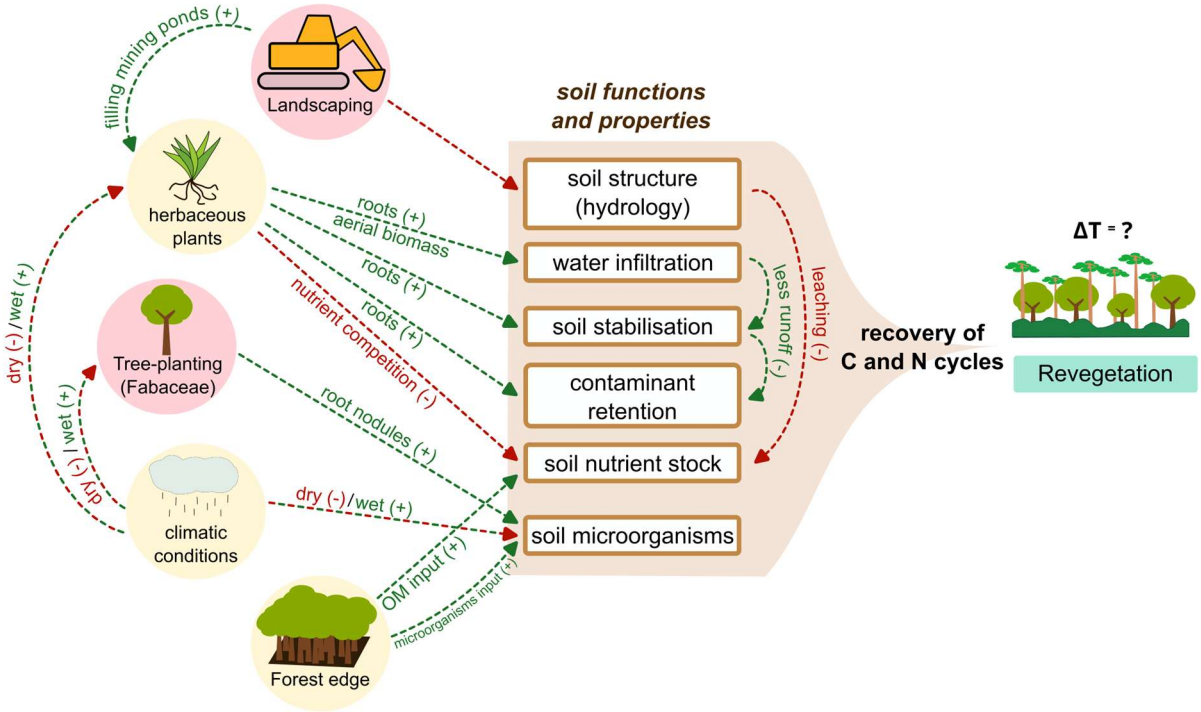

Figure 3.5. *Synthesis of parameters impacting the restoration of a gold mined soil. Natural parameters are depicted in yellow circles, and human intervention is in red circles. Red arrows represent negative impact and green arrows positive impact.*

3.1.5.2. Potential barriers and drivers for the recovery of soil functions

The lack of evolution in the indicators other than arylsulfatase activity could hint towards a lack of sensitivity of these parameters, but more likely the gold mining flat does not undergo a significant change in soil structure and activity over this timespan. The recovery of soil functions is, however, dependent on other parameters such as access to water (climate) and to nutrients (C and N), and the

presence of plant-microbial consortia that may regulate the re-establishment of soil functions on the restored mining flat.

Rainfall participates in microbial community changes on the gold mining site (NMDS, Figure 3.4), and has an impact on microbial biomass and communities (Ren et al. 2018). The two first years (until May 2023) of this study were dominated by stronger rainfall (average: 237 ± 135 mm/month) typical of "La Niña" events, whereas the last year (2023-2024) was drier (average: 146 ± 106 mm/month) and typical of an "El Niño" episode, resulting in a drop of 40 % of the previous year's rainfall. Consequently, a significant percentage of planted trees were lost in this last year, and this might also have hampered soil microorganism activity and development.

The decrease of soil C and N content over the studied period can be attributed to the strong development of pioneer herbaceous plants, which have likely consumed the few available resources initially present in the soils. Indeed, of the herbaceous plants identified on the mining site, none were part of the Fabaceae family (Table S 3.4) and are thus not known to be able to fix nitrogen through symbiosis with bacteria. This might lead to a competition for resources in the soil, and this depletion of nitrogen by the herbaceous plants could inhibit the efficient recovery of microbial communities, and thus of soil functions performed by these communities. To assess whether the nitrogen pools are transferred from the soil towards the plant biomass, the total soil N budget in the soil's first 20 cm was compared to the plant (root + above-ground biomass) on that same surface. N concentrations in plants are estimated to be ~ 1 % (Nardoto et al. 2008, Xiong et al. 2021). Considering the increase of biomass over time, the proportion of N transferred into the biomass through time should not exceed 10-15 % (Figure S 3.6), pointing towards a stagnant total pool of nitrogen, with rapid recycling of fresh organic matter by the herbaceous plants. It is worth mentioning that only the herbaceous biomass was taken into account in this budget calculation. Hence, on the tree-covered site, a significant proportion of nutrients is stored in the planted trees, meaning that the N budget in plants is underestimated on that site. If this lack of nutrients induces the observed stagnation of microbial activity, it is likely that at a later stage of tree development, the addition of litter will feed the soil microbial biomass with nutrients, and restore the carbon and nitrogen cycle (as well as other nutrients). It was only at the last time point (T60) that litter began to accumulate under the planted trees, with no visible impact yet on soil nutrients or soil functions. Litter decomposition has been shown to be slower in young secondary forests than in Amazonian primary forests, but with around 30 % loss of litter biomass occurring in the first month after litter-fall (da Silva et al. 2018). However, the quantity and diversity of microorganisms and soil fauna are known to affect the rate of litter decomposition (Krishna and Mohan 2017), so a lack of the appropriate microorganisms might also explain the absence of litter-fall impact on soil functions. Another possible explanation for the depletion of C and N in soils is the loss through downward or lateral leaching. Indeed, landscaping during the restoration phase of a gold mine does not restore the

soils' initial structure, and results in the creation of a sometimes heterogeneous anthroposol, which no longer benefits from its initial hydric properties regulating water infiltration and retention. As the alluvial mining sites are located in lowland areas, they are prone to undergo major water table oscillations, which can result in the downward or lateral translocation of nutrients, and also possibly the dissolution of their carrier phases (clay minerals), which would otherwise be able to form clay-humic complexes (Fritsch et al. 2011). The loss of these carrier phases might then lead to the loss of the elements/nutrients that would be essential for tree growth and microbial communities.

Leguminous trees of the Fabaceae family, known to form nodules for symbiosis with nitrogen-fixing bacteria (diazotrophs), have been planted during the restoration of the gold mining flat. However, this does not result in a significant input of nitrogen in the soils as discussed above. This might be due to the fact that all the nitrogen is rapidly up-taken into the biomass, but another explanation can be the sheer absence of diazotrophs in these soils. To estimate the presence of N-fixing diazotrophs in the restored mined-soil, the microorganisms detected in the soil were compared to a database of organisms containing the gene responsible for N-fixation (*nifH*) on KEGG. Databases were only compared at the genus level because the sequences in the restored mined-soils were not determined until the species level. This might lead to an overestimation of the presence of N-fixing organisms, as the presence of a N-fixing species does not mean that all the species in the genus are capable of N-fixation. However, this overestimation should be similar between all samples, allowing us to follow a potential evolution over time. An increase of diazotroph presence was observed at T49 and T60 (Figure S 3.9), mostly due to *Paludibacter* and *Methylocystis*. Even when those genii are removed, the increase is still visible, albeit less substantial. The mining site restoration thus seems to be accompanied by a return of N-fixing species, especially as the planted trees are from the Fabaceae family, and are able to form root nodules and symbiotic relationships with diazotrophs. In contrast, a lower percentage of N-fixing bacteria is observed in the forest soils, which could be explained by more abundant N in these soils, and by other sources of available nitrogen (e.g., decomposed OM). As a result, N-fixation does not give a competitive advantage compared to other genii in a functional primary or secondary forest.

The forest edge effect observed on the landscaped site led to a differential revegetation on the three erosion plots, due to an input of nutrients, microorganisms, and seeds from the forest, which also had a visible impact on different soil function indicators (ARS, DNA, genes linked to the nitrogen cycle, Figure S 3.2). The facilitation of the closure of mines by the forest edge effect has been investigated in more detail in the Amazon and elsewhere (Parrotta and Knowles 2001, Martínez-Ruiz et al. 2021, Garate-Quispe et al. 2023).

3.1.5.3. Recommendations and perspectives for goldmining sites restoration

Using the data presented here, a timeline for the restoration of an alluvial gold mining site can be proposed. Indeed, after landscaping and replanting, rapid soil colonization by herbaceous plants and soil biocrust, occurs within the first year and leads to a sharp decline in particle and metal(loid) export. The planted trees then grow to 3–5-meter height leading to a tree-cover succession stage within 3 years. However, even 5 years after restoration, no clear recovery of soil functions was observed. This can be attributed to the depletion of soil nutrients by the herbaceous plant growth and to nutrient leaching which hinders the completion of the next succession stage where a secondary forest would appear. In order to promote an efficient rehabilitation and closure of the mining site, the importance of rapid landscaping after the exploitation phase is paramount. Indeed, if there is little time between the exploitation of the mining site and its restoration, the organic layer stored by the miners will be less susceptible to leaching and losses of nutrients, microorganisms, and seeds, all of which are essential for the adequate closure of a mining site. Hence, rehabilitation integrated into the progress of extraction activities seems to be the best strategy. A fast and efficient recolonisation by herbaceous plants leading to reduced particle and metal(loid) and more specifically Hg export is in line with the Minamata convention on mercury, which states that national action plans (NAPs) should include "Strategies for promoting the reduction of emissions and releases of, and exposure to mercury in artisanal and small-scale gold mining and processing" (Minamata_Convention_on_Mercury 2023). Several organisations work across the world and more specifically in the Amazon region to raise awareness in gold-miner communities and to limit the impact of gold-mining on the environment (planetGOLD 2023).

In addition, many mines in French Guiana use leguminous plants to help restart the nitrogen cycle through symbiotic nitrogen-fixing microorganisms (Couic et al. 2022). These leguminous trees appear to have an impact on the soil microbial communities as it was observed that more N-fixing microorganisms are present on the tree-covered site. However, these microorganisms appear only 4 to 5 years after restoration, which was also coupled with an increase in litterfall and a decrease in herbaceous cover after 5 years. Possibly, at this succession stage, the planted trees provide shade, which reduces the ability of herbaceous plants to grow and also impacts the soil microbial communities. This reflects a start in adaptation to the changing environment of the rehabilitated mining site and gives promising perspectives for the future recovery of soil functions and microbial communities in mining site soils. Additional inoculation of the tree shoots with N-fixing bacteria could improve restoration and the recovery of the N-cycle. Finally, the variability over the whole mining site needs to be better assessed, as differential parameters (physicochemical, slope, edge effect, …) have the possibility to influence the development of microbial communities creating patches of diversity and "efficient rehabilitation" but only on specific locations on the mining site. Taking advantage of the

positive influence of the edge effect could include focusing the rehabilitation effort on punctual niches as “hotspots” for microbial dispersion, or also conducting mine work over narrower widths in order to achieve a larger forest edge over mined area ratio.

The time frame of this study appeared to be too short to detect any significant increase in soil functions, possibly because some of the parameters discussed here are hindering the refunctionalisation of the soils. Further studies thus need to perform monitoring of a mining site over a longer period of time (in the decade time frame), to document the transition towards the restarting of the carbon and nitrogen cycles through the input of organic matter from litter-fall back to the soils. This tipping point is essential for the recovery of a secondary forest and appears to lie in the decades’ timespan. On an even larger timescale, climate change is believed to lead to lower rainfall in tropical regions (Neelin et al. 2006), which might add to the difficulty of restoring efficiently a mining site.

The application of mining site restoration to illegal gold mines has to be studied, as in the case of illegal gold mining, Hg is used for Au amalgamation and leads to contamination of the surrounding water and the soils. It is thus not trivial to decide whether an illegal mining site should be restored and how, as restoration might lead to the remobilisation of the anthropogenic Hg in soils during the landscaping process.

3.1.6. Conclusion

This chapter provides an estimation of the rapid reduction of both particle and metal(loid) export on a gold mining flat after its restoration. Within one year, the particle export is already reduced 3-fold, and up to 2000-fold after 4 years. This decreased erosion, coupled to a reduction of overland flow induces a decrease in metal(loid) (Hg, Pb, As) export. The soil stabilisation was observed to be primarily due to the spontaneous colonisation by herbaceous plants.

Biological soil functions however did not recover in the same time span. There is no evolution observed for the majority of parameters followed. This lack of recovery might be due to the depletion of the soil nutrient stocks by the strong herbaceous growth as described above. Nevertheless, microbial communities were shown to vary significantly during the 5 years after restoration, underlining their adaptability to climatic conditions and a changing environment. This is promising in terms of restoration of microbial diversity and the carbon and nitrogen cycles eventually but the time span for such restoration could not be determined in this study.

While the rapid reduction of mining flat erosion is encouraging concerning restoration practices, it needs to be assessed whether this is sufficient to limit the export of particles to the river. The next chapter will focus on the impact of the gold mining flat on particle and metal(loid) exports at the scale of the watershed.

Graphical abstract

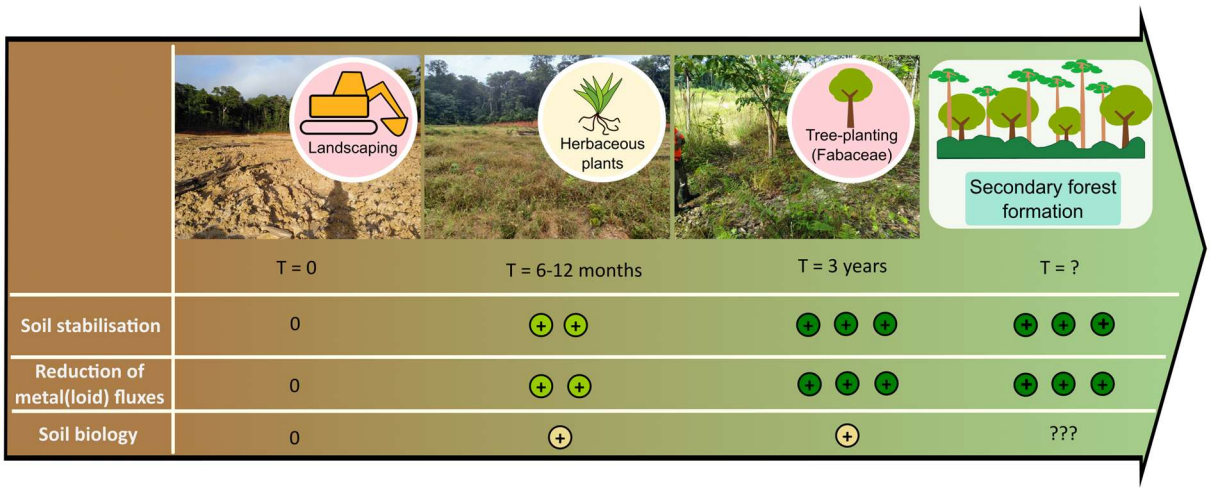

3.1.7. Supplementary Information

3.1.7.1. Study area and chemical and biological analyses

3.1.7.1.1. Details of the gold mining exploitation and restoration phases.

During exploitation, deviation of the river prevents contact to the mining site which works in closed circuit. Gold separation and extraction is done only by gravimetry on site, separating the fine particles which are left to sediment in mining ponds versus heavier auriferous particles. The mining ponds are only emptied into the river once the particulate matter has sedimented and the water is clear

3.1.7.1.2. Chemical analysis.

Total Hg on solid coarse samples was analysed by atomic absorption spectroscopy after pyrolysis and gold amalgamation (AMA 254, Altec) with a relative precision of ± 5 % determined from triplicates, consistently with typical relative errors reported for this analyser (Roos-Barraclough et al. 2002, Guédron et al. 2009). The total mercury concentration measurements were validated with the certified reference materials (ERM CC141 loam soil) and were always within the published range (0.083 ± 0.017 $\mu g.g^{-1}$). The detection limit (defined as three times the standard deviation (SD) of the blank) was at maximum 0.005 $\mu g.g^{-1}$.

THg speciation in suspended particulate matter (SPM) collected on filter samples was extracted by acid digestion with 3 mL (HNO_3 6 N, INSTRA-ANALYZED, J.T.Baker), following the standard operating protocols described elsewhere.(Stoichev et al. 2016) Filtered water samples were acidified with HCl (Optima purity grade) 0.2 %. All samples were analysed following established methods using SS-ID GC-ICP-MS (Rodriguez Martin-Doimeadios et al. 2002, Monperrus et al. 2005, Monperrus et al. 2008, Kleindienst et al. 2023). For data validation, the same protocol was used for Hg speciation analyses on 3 blank filters, 3 blank HNO_3 6 N, and one CRM in triplicate (IAEA-456) digested in 3, 4 and 4 mL of HNO_3 6N respectively.

Multi-elemental analysis of major and trace elements was performed by inductively coupled plasma-atomic emission spectrometry (ICP-AES) (Agilent, Varian 720-ES) and by inductively coupled plasma mass spectrometry (ICP-MS) (Agilent 7900 coupled to an ESI PrepFast IC module) respectively. The following elements were analysed by ICP-AES : Al, Ca, Fe, K, Mg, Mn, S, Si, Sr, Ti, and Zn. The other elements were analysed by ICP-MS : Cr, Co, Ni, Cu, As, Se, Cd, Tl, Pb, Th, U.

The filtered water samples were analysed directly and the filter samples solutions were analysed after microwave (ultra-WAVE, Milestone) assisted acid digestion (HNO3) at 220 °C. The accuracy of the measurements was evaluated based on the analysis of certified reference materials (NIST 1944 and IAEA-405 for solid samples and SLRS-6 for water samples).

3.1.7.1.3. Soil erosion measurements.

Soil erodibility and critical erosion shear-stress were measured using an EROMES device as described elsewhere (Schünemann and Kühl 1991, Lanuru et al. 2007, Joensuu et al. 2017, Haddad 2022). Briefly, a 10 cm diametre cylinder is placed above the soil, filled with clear water, and a helix placed 3 cm above the soil rotates at increasing velocities to induce soil erosion. The rotation velocities of the helix are calibrated to relate to bed shear stress. The erosion rate is deduced by turbidity measurements which are calibrated to relate to particle concentration. The experiment was stopped at saturation of the turbidity sensor or after 20 shear stress increments, to a maximum force of 4.67 Pa. The critical erosion threshold (τ_c) was determined as the shear stress at which the erosion rate (ER) exceeded 0.1 $g.m^{-2}.s^{-1}$. The erosion rate (m_e; $g.m^{-2}.s^{-1}.Pa^{-1}$) was determined as the slope of the erosion rate versus the shear stress (at shear stress $\geq \tau_c$). A high erosion rate m_e associated to a small critical erosion threshold (τ_c) represents a higher soil "erodibility" while low values of m_e associated to high values of τ_c indicate a more stable soil.

3.1.7.1.4. Soil physico-chemical characterisation.

Soil Water Holding Capacity (WHC): 20g of soil is placed on a filter and saturated with H_2O mQ. The saturated soil is weighed, dried 24h at 105°C and weighed again. WHC (g H_2O / $g_{dry\ soil}$) = water mass / dry soil mass

Soil pH: Soils were freeze-dried and sieved at 2 mm. 5g of soil were weighed in 25 mL H_2O mQ, shaken for 3 minutes and let to rest for 2 minutes. The pH was measured in the suspension.

Grain size measurements: Soils were freeze-dried 48h and sieved at 1.25 mm. Particle size distributions (PSD) were measured with a laser diffraction sizer (Malvern, Mastersizer 2000) following the protocol detailed in Grangeon et al. (2012). For each sample, clay (<2µm), silt (2-63µm) and sand (>63µm) fractions were extracted.

Carbon and Nitrogen : Soils were freeze-dried, sieved at 2 mm and ground at <63µm to measure total C and N contents using a Flash Smart elemental analyser (ThermoFisher Scientific)(Piton et al. 2020).

Soil density: Soil cubes of 10×10×10 cm were extracted from each site. The total volume of soil removed was measured by filling the hole (covered with a plastic foil) with water. The total amount of soil was weighed, and an aliquot was taken to be dried and weighed again, to measure the soil apparent density (DA).

Plant biomass: The aerial part of the plants was separated, washed with H_2O mQ, dried, and the above ground biomass (AGB) was calculated by dividing the plant weight by the total soil volume. Roots were separated manually, washed with H_2O mQ, dried and weighed. The root density (RD) was calculated by dividing the weight of dried roots by the total soil volume.

3.1.7.1.5. Soil DNA and qPCR.

Soil DNA were extracted from 0.6 to 0.7 g of soil (dry weight), previously frozen at -20°C, using the FastDNA® SPIN Kit for soil (MP Biomedicals, Illkirch, France) and the FastPrep R-24 classic Instrument used per the manufacturer's instructions. Soil DNA extract concentrations were measured with the Quantus fluorimeter and the QuantiFluor™ dsDNA System, according to the manufacturer's instructions (Promega, Madison, WI, USA). Real-time quantitative polymerase chain reaction (qPCR) was performed to assess gene abundances as a measure of bacterial and archeal abundance (16S rRNA), fungi abundance (18S rRNA) and abundance of genes linked to the nitrogen cycle (*narG*, *amoA*, *nosZ, nifH*, *nirS*). Primers sets of the genes used in the qPCR are described in Table S 3.1.

Table S 3.1*.Functional genes linked to N-cycling in soils with primers, base sequences and targets(Vainio and Hantula 2000, Throback et al. 2004, Gaby and Buckley 2012, Fikri et al. 2021)*

Genes	Primers	Base sequences	Target
16S	341F	5'-CCT ACG GGA GGC AGCAG-3'	bacteria + archea
	515R	5'-ATT ACC GCG GCT GCT GGC A-3'	
18S	*FR1*	AIC CAT TCA ATC GGT AIT	fungi
	FF390	CGA TAA CGA ACG AGA CCT	
narG	*narG-F*	5'-TCGCCSATYCCGGCSATGTC-3'	Nitrate reductase
	narG-R	5'-GAGTTGTACCAGTCRGCSGAYTCSG-3'	
nosZ	*nosZ-1F*	5'-WCSYTGTTCMTCGACAGCCAG-3'	Nitrous oxide reductase
	nosZ-1R	5'-ATGTCGATCARCTGVKCRTTYTC-3'	
amoA	*amoA-1F*	5'-GGGGTTTCTACTGGTGGT-3'	Bacterial ammonia mono-oxygenase
	amoA-2R	5'-CCCCTCKGSAAAGCCTTCTTC-3'	
nifH	*Pol-F*	5'-TGCGAYCCSAARGCBGACTC-3'	Nitrogenase
	Pol-R	5'-ATSGCCATCATYTCRCCGGA-3'	
nirS	nirSCd3aF	5'-GT(C/G)AACGT(C/G)AAGGA(A/G)AC(C/G)GG-3'	Nitrite reductase
	nirSR3Cd	5'-GA(C/G)TTCGG(A/G)TG(C/G)GTCTTGA-3'	

qPCR reactions were carried out for each gene, using 2 ng of soil DNA, 10 µL of SsoAdvanced Universal SYBR Green Supermix (Bio-rad), each primer at 0.16 µL (0.4 µM for 16S rRNA, 50 µM for *narG*, *amoA*, *nosZ, nifH, nirS* genes), and 0.2 µL of T4 GP32 (500 ng.µL^{-1} only for 16S rRNA and *narG*) (Fikri et al. 2021, Michel et al. 2021).

Programmes for qPCR were run in a CFX Connect (Bio-Rad) and consisted of an initial denaturation at 95°C for 3 min before 35 cycles of 95°C for 30 s, 60 °C for 30 s, 72°C for 30 s (16S rRNA gene), 5 min at 95°C before 6 cycles of 30 s at 95°C and 30 s at 63°C with a point at –1°C by cycle and 30 s at 72°C, and 34 cycles consisting of 30 s at 95°C, 30 s at 58°C, 30 s at 72°C (*narG* gene), 2 min at 95°C before 40 cycles of 15 s at 95°C, 15 s at 62°C, 30 s at 72°C (*nosZ* gene), 5 min at 95°C before 40 cycles of 15 s at 95°C, 30 s at 55°C, and 30 s at 72°C, and 30 s at 80°C (*amoA* gene), 3 min at 95°C before 35 cycles of 30 s at 95°C, 30 s at 55°C, and 30 s at 72°C, followed by 30 s at 72°C (*nifH* gene), 2 min at 95°C before 40 cycles of 30 s at 95°C, 30 s at 62°C, and 30 s at 72°C, followed by 5 min at 72°C, (*nirS* gene), and finally a data acquisition step at 80 °C for 30 s at each cycle.

Sequencing: bacterial and archaeal diversity were determined by 16S rRNA gene metabarcoding. A portion of the 16S rRNA gene (V4-V5 region) was amplified using the barcoded, universal primer set (515WF/918WR) (Wang et al. 2009). PCR reactions were performed using the AccuStart II PCR ToughMix kit, followed by cleaning (HighPrep PCR beads, Mokascience). Pooled triplicates were submitted for sequencing on Illumina MiSeq instrument at GeT-PlaGe (Auzeville, France).

Sequences were processed on the Galaxy platform using FROGS (Escudie et al. 2018) based on the Galaxy analysis platform (Galaxy 2022). Sequences were removed from the data set if they exhibited ambiguous bases or did not match expectations in amplicon size. Remaining sequences were clustered into ASVs (amplicon sequence variant) based on the iterative Swarm algorithm, then chimeras and singletons (PCR artefacts and ASVs containing only one sequence) were removed. Bacterial double affiliation was performed by blasting ASVs against SILVA database 138.1 (Quast et al. 2013). ASVs with affiliation <100 % at the phylum level were removed from the data set.

Table S 3.2. *Major and trace element concentration in the filtered (A) and the particulate (B) fraction.*

A - Filtered	T0 n=8	± SD µg.L^{-1}	T8 n=3	± SD µg.L^{-1}	T13 n=11	± SD µg.L^{-1}	T36 n=6	± SD µg.L^{-1}	T44 n=2	± SD µg.L^{-1}	T49 n=9	± SD µg.L^{-1}
Cr	0.31	0.18	0.40	0.19	0.36	0.13	0.22	0.04	0.19	0.04	0.38	0.16
Co	0.06	0.03	0.09	0.05	0.03	0.01	0.50	0.26	0.27	0.06	0.19	0.12
Ni	0.19	0.05	0.23	0.03	0.14	0.07	0.25	0.07	0.76	0.38	0.55	0.32
Cu	0.40	0.56	0.49	0.29	0.40	0.17	0.65	0.27	1.51	0.07	1.78	1.10
As	0.038	0.004	0.05	0.01	0.03	0.02	0.03	0.01	0.04	0.01	0.05	0.02
Se	0.18	0.03	0.18	0.03	0.14	0.05	0.12	0.05	0.09	0.01	0.09	0.05
Cd	0.007	0.005	0.087	0.079	0.015	0.010	0.002	0.001	0.02	0.00	0.02	0.01
Tl	0.038	0.008	0.05	0.02	0.01	0.00	0.03	0.03	0.01	0.01	0.01	0.00
Pb	0.084	0.083	0.01	0.00	0.10	0.11	0.04	0.03	0.02	0.02	0.12	0.12
Th	0.026	0.019	0.04	0.03	0.04	0.03	0.03	0.01	0.01	0.00	0.03	0.01
U	0.018	0.010	0.02	0.01	0.02	0.01	0.03	0.00	0.01	0.00	0.03	0.02
Al	0.02	0.01	0.09	0.06	0.10	0.11	0.04	0.01	nd	nd	0.05	0.02
Ca	0.31	0.11	0.45	0.20	0.29	0.18	0.45	0.09	0.72	0.06	0.98	0.56
Fe	0.007	0.008	0.029	0.007	0.04	0.06	0.008	0.007	nd	nd	0.04	0.02
K	0.55	0.24	1.8	0.2	1.19	0.49	1.55	0.65	1.38	0.42	1.67	1.11
Mg	0.13	0.03	0.30	0.16	0.14	0.08	0.20	0.05	0.20	0.04	0.28	0.10
Mn	0.009	0.002	0.04	0.04	0.010	0.004	0.05	0.02	0.0495	0.0005	0.03	0.02
S	0.39	0.11	0.66	0.35	0.32	0.12	0.47	0.21	0.25	0.14	0.31	0.14
Si	0.29	0.07	0.90	0.09	0.47	0.23	0.86	0.25	0.72	0.14	1.50	0.73
Sr	0.0019	0.0008	0.002	0.001	0.002	0.001	0.0021	0.0004	0.0010	0.0006	0.003	0.002
Zn	0.01	0.01	0.02	0.03	0.005	0.004	0.003	0.001	0.008	0.006	0.013	0.013
		ng.L^{-1}		ng.L^{-1}		ng.L^{-1}		ng.L^{-1}		ng.L^{-1}		ng.L^{-1}
THg	0.72	0.50	1.98	0.45	1.78	0.76	1.62	0.51	1.02	0.04	1.80	0.41
MeHg	0.012	0.004	0.038	0.023	0.036	0.009	0.008	0.002	0.032	0.001	0.056	0.024

B – Particulate	T0 n=2	± SD µg.g^{-1}	T8 n=2	± SD µg.g^{-1}	T13 n=11	± SD µg.g^{-1}	T36 n=5	± SD µg.g^{-1}	T44 n=2	± SD µg.g^{-1}	T49 n=6	± SD µg.g^{-1}
Cr	107	5	83	7	95	7	122	33	50	21	95	23
Co	10.3	0.1	9	1	10	1	16	4	8	3	11	2
Ni	55.1	0.1	41	4	48	4	53	15	21	4	42	13
Cu	18.2	0.1	17	1	19	3	34	8	24	3	32	3
As	3.4	0.4	1.6	0.3	3	1	1.5	0.5	1.1	0.1	1.5	0.4
Se	1.9	0.5	1.0	0.5	1.8	0.3	1.2	0.4	1.3	0.4	0.9	0.1
Cd	0.031	0.001	0.13	0.01	0.2	0.1	0.06	0.04	0.06	0.08	0.2	0.2
Tl	0.35	0.05	0.284	0.002	0.29	0.02	0.5	0.2	0.17	0.09	0.30	0.08
Pb	10	2	9.2	0.1	12	6	12	4	7	2	15	10
Th	8.9	0.5	7.7	0.2	7.5	0.4	8	2	3	1	4.9	1.0
U	1.5	0.2	1.112	0.001	1.3	0.1	1.8	0.4	0.9	0.2	1.2	0.1
Al	149	14	140	12	232	13	179	33	84	35	193	50
Ca	1.0	0.3	0.9	0.1	2.2	1.3	2.5	2.1	2.6	1.8	5.0	2.5
Fe	39	6	51	6	60	5	39	8	30	11	47	7
K	1.5	0.1	1.0	0.1	1.5	0.1	3.9	0.9	2.2	0.5	3.4	0.6
Mg	0.70	0.08	0.66	0.06	1.20	0.17	1.31	0.36	1.15	0.30	1.77	0.12
Mn	0.07	0.01	0.10	0.02	0.12	0.01	0.20	0.05	0.39	0.05	0.35	0.13
S	0.38	0.08	0.34	0.05	1.07	0.79	0.84	0.54	2.24	1.91	2.57	1.17
Sr	0.012	0.002	0.013	0.001	0.016	0.003	nd	nd	0.012	0.003	0.009	0.003
Ti	0.56	0.11	0.37	0.07	1.95	1.13	1.11	0.62	1.08	0.84	3.02	0.97
		ng.g^{-1}		ng.g^{-1}		ng.g^{-1}		ng.g^{-1}		ng.g^{-1}		ng.g^{-1}
THg	163	30	262	9	178	47	98	22	228	7	178	47
MeHg	0.43	0.15	0.24	0.04	0.75	0.44	0.73	0.32	1.40	0.72	2.79	1.49

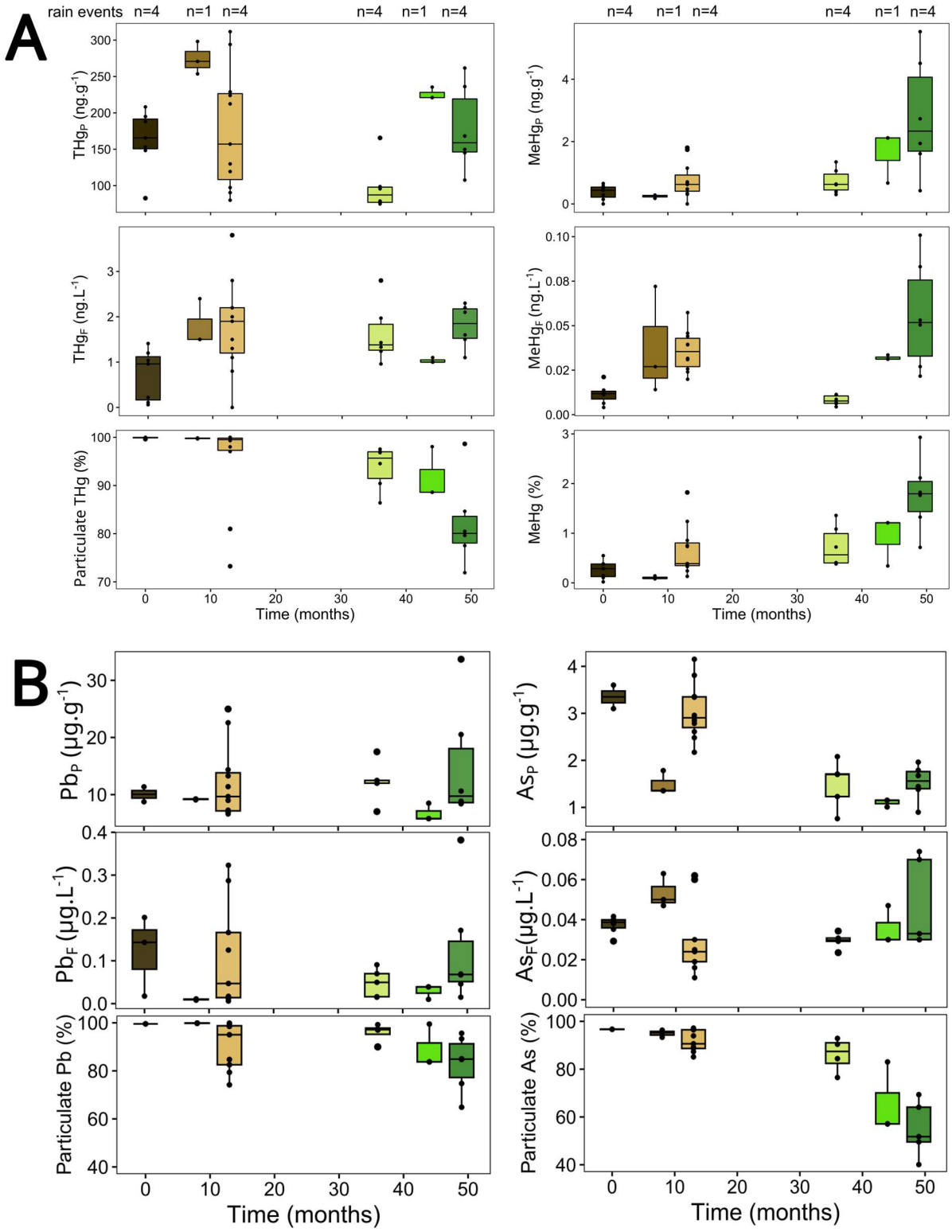

Figure S 3.1. *Synthesis of A) THg and MeHg fluxes in the particulate (xHg_P) and filtered (xHg_F) fractions as well as the percentage of total Hg present in the particulate fraction, and present as MeHg; B) TPb and TAs fluxes in the particulate (X_P) and filtered (X_F) fractions as well as the percentage of total Pb or As present in the particulate fraction.*

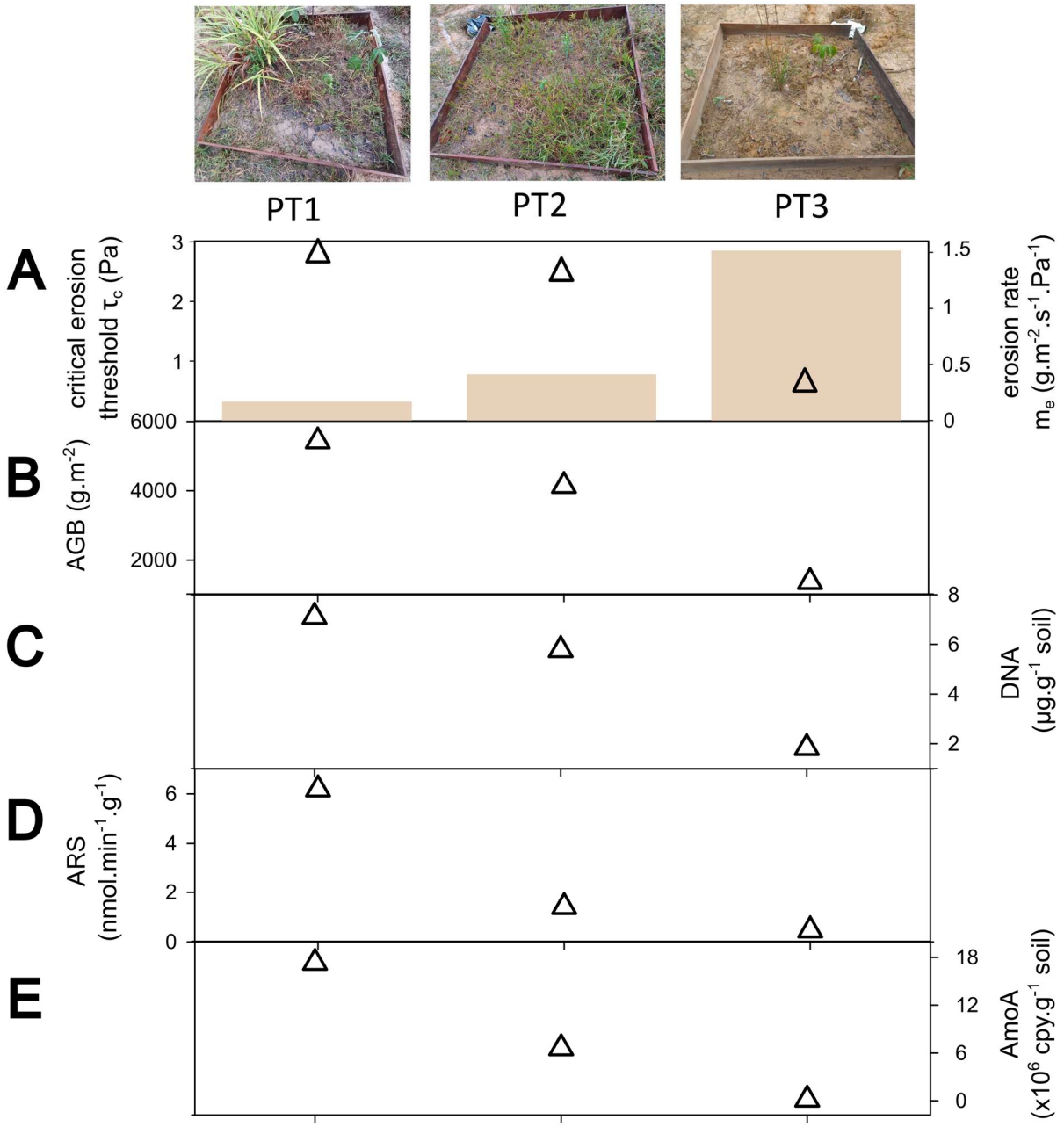

Figure S 3.2. *Spatial difference due to the forest edge effect on revegetation on the landscaped site replicates at T = 13 months with A) erodability constants (critical threshold τ_c black triangles, left and erosion rate m_e, brown histograms, right), B) above-ground biomass (AGB), C) DNA, D) arylsulfatase activity (ARS), and E) copies of the AmoA gene measured on these three sites. PT1 is the site closest to the forest edge, and undergoes the most efficient revegetation leading to lower soil erodability, and shows the highest values for biological indicators (DNA, ARS, AmoA), probably due to input in organic matter and microorganisms from the nearby forest.*



Figure S 3.3. *Biological soil crust in part responsible for soil stabilisation.*

Table S 3.3. *Soil characteristics and soil function parameters.*

			Enzyme activity			qPCR								Biomass				Grain size						
ID	**Site**	**Time**	**ARS**	**PHOS**	**URE**	**18S**	**16S**	**amoA**	**narG**	**nifH**	**nirS**	**nosZ**	**DNA**	**RD**	**AGB**	**pH**	**WHC**	**Clay**	**Silt**	**Sand**	**N**	**C**	**C_N**	**Rain**
		month	nmol/min/g	nmol/min/g	nmol/min/g	$X10^6$ copies/g soil	$X10^8$ copies/g soil	$X10^6$ copies/g soil	$X10^8$ copies/g soil	$X10^8$ copies/g soil	$X10^7$ copies/g soil	$X10^7$ copies/g soil	µg/g soil	g/m^3	g/m_2		$g_{H2O}/g_{dry\ soil}$	%	%	%	%	%		mm
G1-PT-1	Landscaped	0	0	29.84	0.17	6.40	18.18	0.94	4.48	3.34	1.85	3.95	5.72	0	0	5.00	0.235	4.7	29.5	65.8	0.074	1.04	14.0	3153
G1-PT-2	Landscaped	0	0	24.34	<DL	4.61	17.47	2.01	6.46	4.00	1.38	4.02	2.64	0	0	4.53	0.317	5.7	30.0	64.3	0.055	0.76	13.8	3153
G1-PT-3	Landscaped	0	1.76	42.26	<DL	2.82	16.76	3.09	8.44	4.66	0.91	4.10	5.36	0	0	4.93	0.359	4.5	28.7	66.8	0.070	1.02	14.6	3153
G3-PT-1	Landscaped	13	6.18	30.52	0.89	6.14	21.54	17.30	22.61	8.55	3.48	9.00	7.11	2475	396	5.39	0.539	4.1	27.9	67.9	0.09	1.36	15.1	2544
G3-PT-2	Landscaped	13	1.41	49.00	0.90	4.79	13.95	6.59	11.03	4.40	2.01	5.36	5.77	257	220	5.15	0.596	5.1	30.5	64.5	0.072	1.06	14.7	2544
G3-PT-3	Landscaped	13	0.47	23.07	0.71	0.75	3.03	0.15	0.79	0.46	0.06	0.30	1.83	507	67	5.23	0.581	5.7	28.6	65.7	0.055	0.77	13.9	2544
G4-PT-1	Landscaped	24	2.36	32.91	0.85	1.37	4.37	0.66	1.73	0.68	0.22	0.57	1.46	2811	n.d.	5.00	0.468	5.6	25.8	68.6	0.041	0.60	14.7	1751
G4-PT-2	Landscaped	24	1.79	20.49	1.01	0.75	5.45	0.64	1.23	0.60	0.08	0.39	1.68	820	2782	5.18	0.442	6.5	28.8	64.7	0.044	0.55	12.6	1751
G4-PT-3	Landscaped	24	0.60	15.26	0.62	1.06	3.28	0.65	0.06	0.13	0.15	0.01	1.06	84	968	4.93	0.422	6.0	26.5	67.5	0.039	0.60	15.3	1751
G1-PV-1	Tree-cover	36	2.62	30.54	<DL	43.64	28.25	10.80	18.09	6.63	2.81	6.07	5.08	5243	243	5.10	0.460	9.7	47.0	43.3	0.034	0.32	9.3	3153
G1-PV-2	Tree-cover	36	2.76	44.36	<DL	12.96	12.24	3.82	7.37	3.73	0.98	2.54	2.79	1817	128	5.03	0.447	6.1	33.3	60.6	0.036	0.45	12.5	3153
G1-PV-3	Tree-cover	36	2.24	31.96	<DL	46.48	29.82	6.80	14.20	6.10	3.09	4.44	2.65	1433	84	5.23	0.370	7.9	39.8	52.3	0.030	0.30	10.0	3153
G3-PV-1	Tree-cover	49	7.29	35.60	1.15	15.18	14.14	8.50	10.86	5.34	2.41	4.74	4.16	2989	538	4.91	0.595	6.6	43.6	49.8	0.048	0.51	10.7	2544
G3-PV-2	Tree-cover	49	9.22	28.02	1.09	14.58	7.73	8.47	9.60	4.72	1.64	4.94	4.87	13063	516	4.95	0.602	7.4	44.1	48.5	0.052	0.66	12.7	2544
G3-PV-3	Tree-cover	49	5.46	25.67	1.09	17.02	7.20	8.24	13.55	4.72	1.74	5.18	4.20	1056	931	5.06	0.602	8.5	46.8	44.6	0.054	0.72	13.3	2544
G4-PV-1	Tree-cover	60	4.14	15.82	1.13	5.03	5.95	3.02	2.99	1.82	0.67	1.91	1.99	2610	116	5.00	0.485	8.4	42.5	49.1	0.048	0.50	10.4	1751
G4-PV-2	Tree-cover	60	5.58	30.13	1.26	9.69	7.56	4.01	5.31	2.54	1.05	2.46	2.19	3620	404	5.04	0.473	8.4	42.1	49.5	0.043	0.48	11.1	1751
G4-PV-3	Tree-cover	60	4.13	12.82	1.13	2.32	2.54	1.74	2.38	1.10	0.39	1.19	0.76	1928	416	5.00	0.498	8.4	40.9	50.7	0.035	0.34	9.8	1751
G4-REF-1	Forest	Forest	19.39	89.26	4.32	8.16	43.03	33.76	40.38	17.63	4.44	21.94	12.06	16895	384	4.93	0.523	3.3	36.5	60.2	0.14	1.93	13.8	1751
G4-REF-2	Forest	Forest	19.36	79.72	3.82	4.86	36.74	29.40	36.16	15.42	3.88	22.07	10.14	12520	795	4.97	0.545	3.6	37.6	58.9	0.135	1.85	13.7	1751
G4-REF-3	Forest	Forest	20.81	95.45	4.16	4.48	31.21	25.82	36.73	14.68	3.34	17.73	8.69	5935	445	4.86	0.528	3.8	39.6	56.6	0.146	1.99	13.6	1751

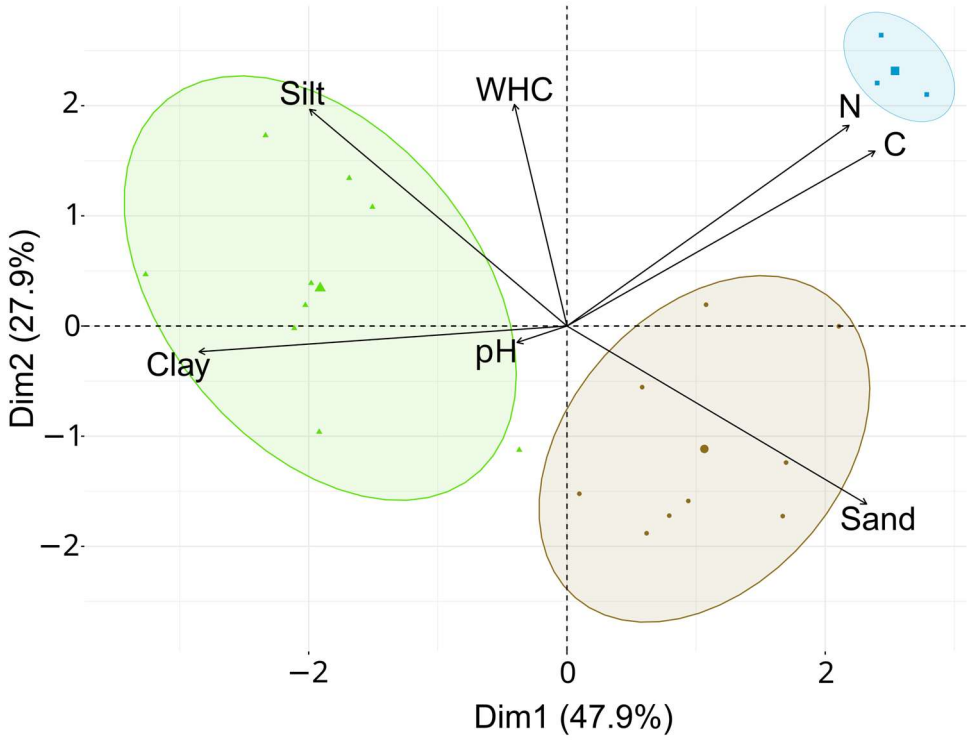

Figure S 3.4. *PCA for soil characteristics. Brown = landscaped site, green = tree-cover site, blue = forested site.*

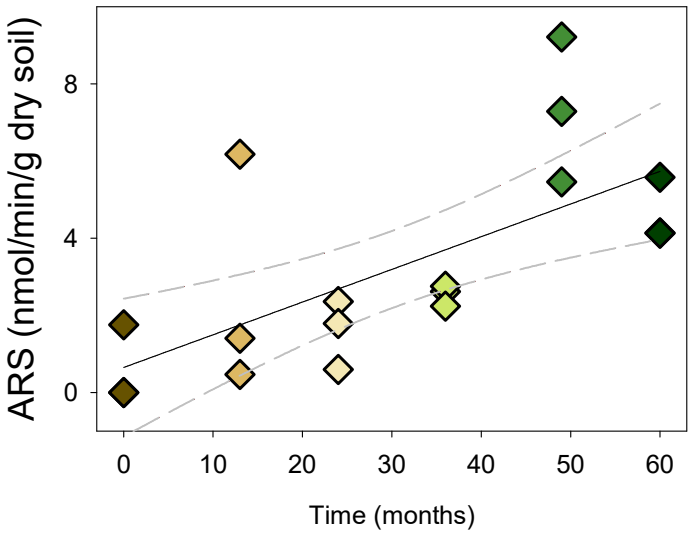

Figure S 3.5. *ARS activity versus time after rehabilitation on the mining flat.*

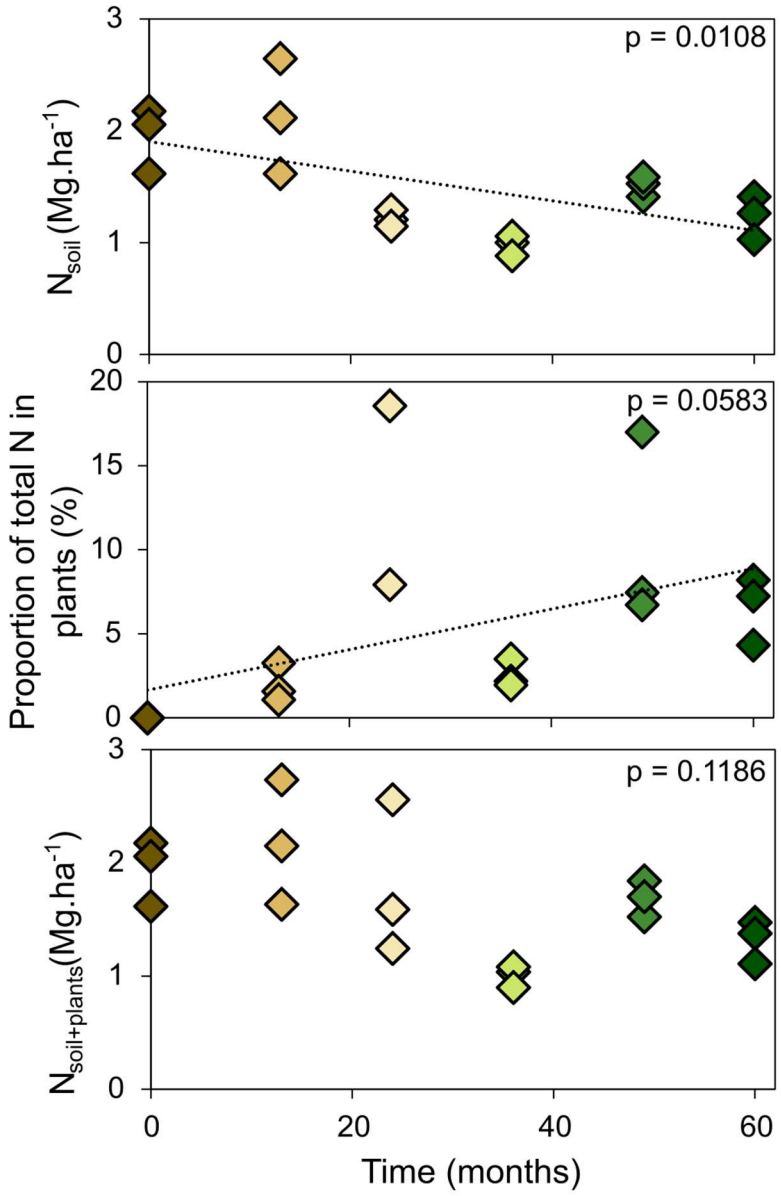

Figure S 3.6. *Nitrogen budget and partition between the soil and the plants evolution over time after restoration.*

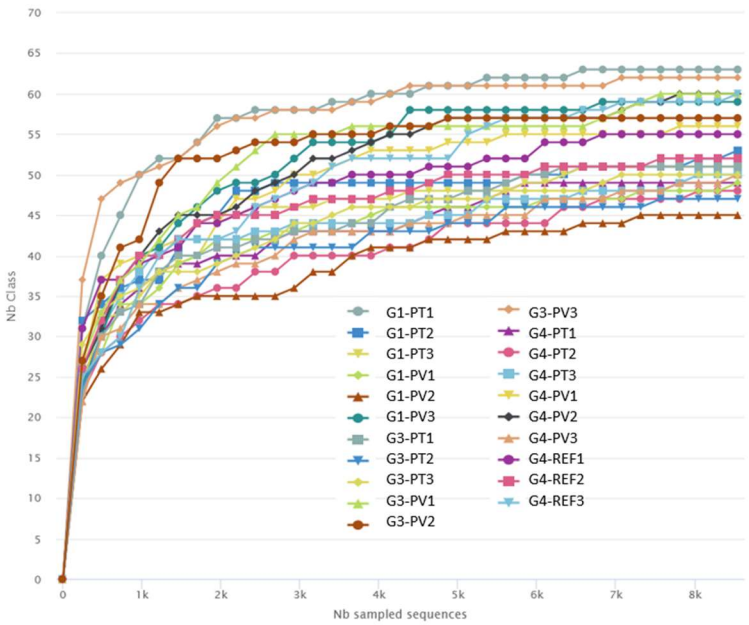

Figure S 3.7. *Rarefaction curves.*

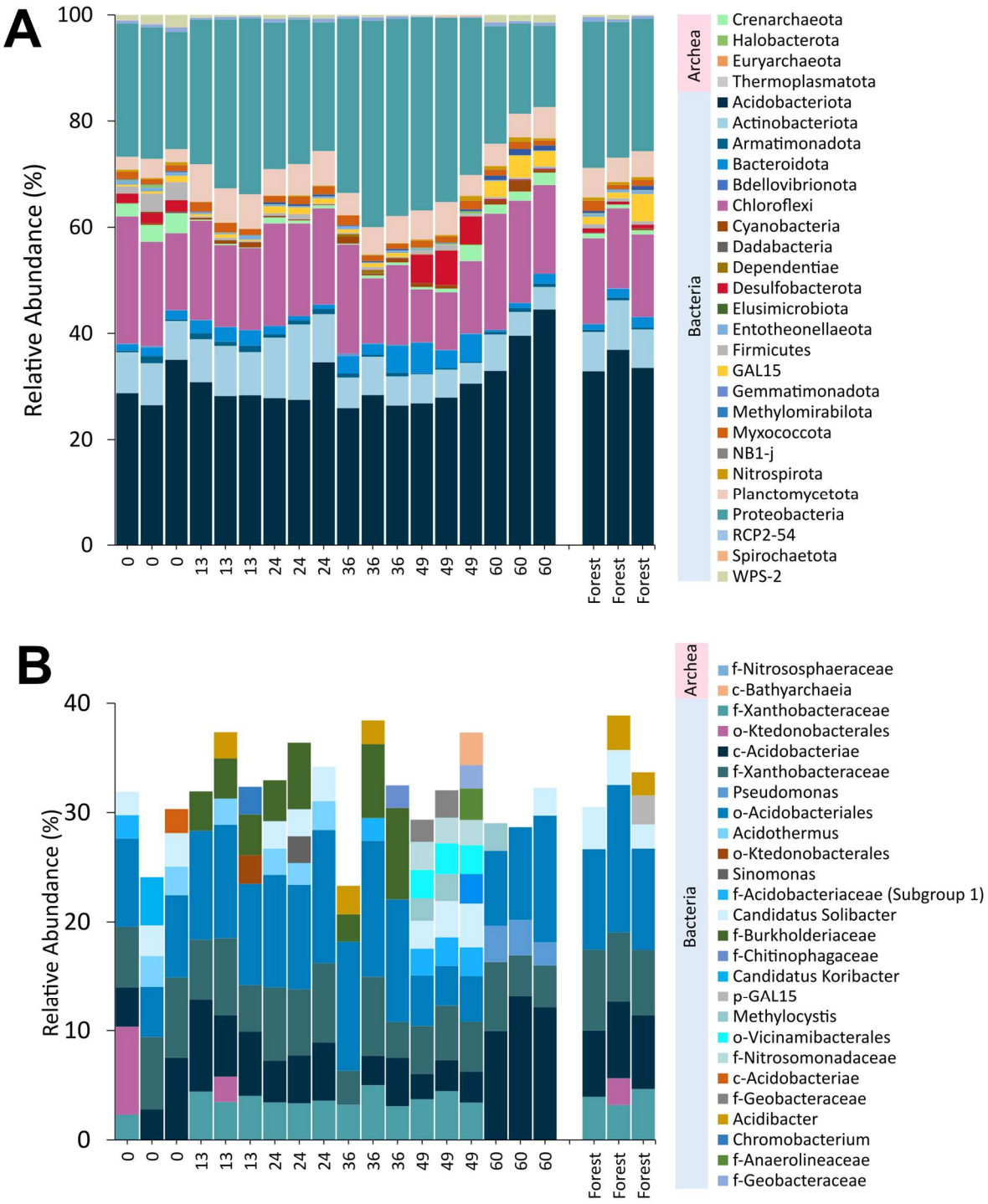

Figure S 3.8. *Bacterial and archea community barplot with relative abundances of different bacterial phyla of (A) all ASVs and (B) genus of the major ASVs (>2 %).*

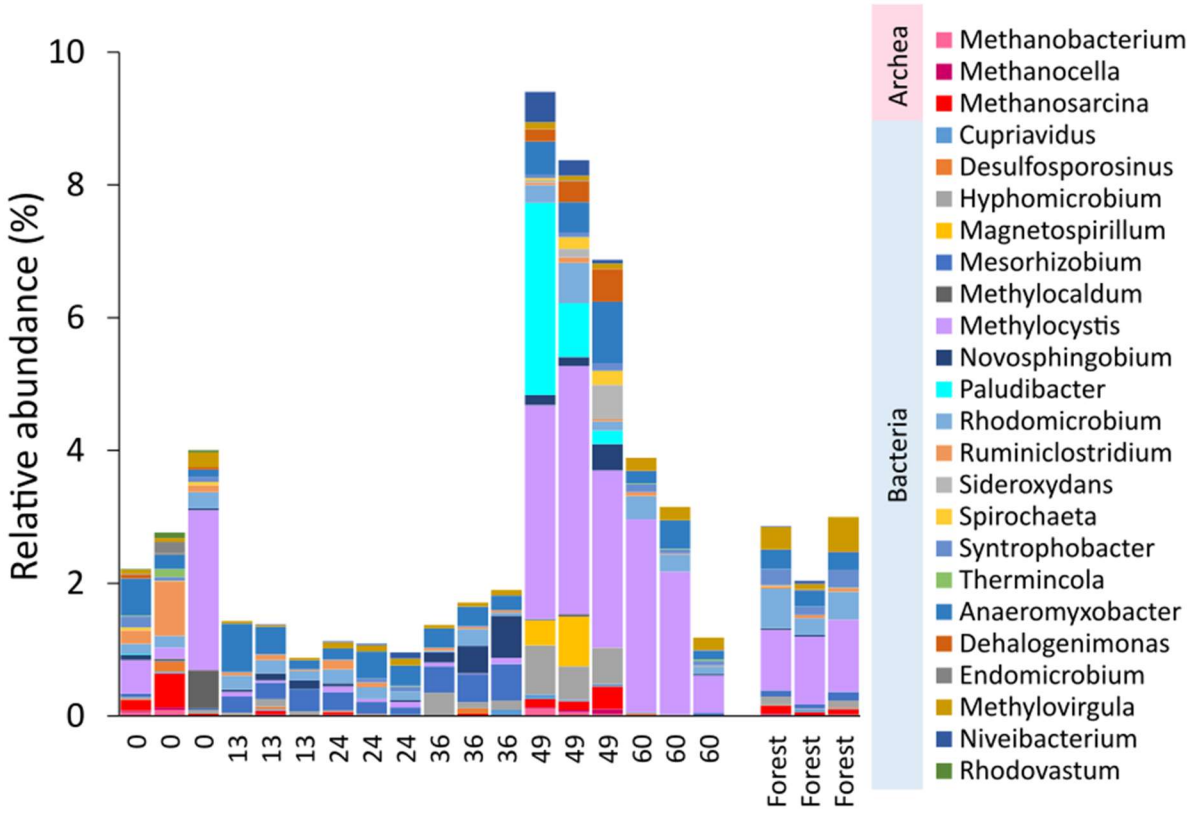

Figure S 3.9. *Bacterial and archea community barplot with relative abundances of geni with potential N-fixing capacity (diazotrophs) at different time points after restoration, and in a forest soil.*

Table S 3.4. *Herbaceous plants on the mining site identified at the family level.*

Lamiaceae	
Cyperaceae	  
Poaceae	

Chapter 4.

Impact of a gold mining site on the export of particles and metal(loid)s at the watershed scale

Introduction

The previous chapter assessed the temporal evolution of the mining flat after restoration and discussed the amount of material and metal(loid)s removed from the mining area during rain events. Erosion can have deleterious effect on the mining flat itself, by possibly preventing revegetation through the removal of soil organic matter and seeds. However, this eroded material can then be transported to the adjacent river, where siltation also negatively impacts ecosystems (Mol and Ouboter 2004, Wantzen and Mol 2013). The following chapter changes the scale of study and aims at assessing the impact of the restored gold mining flat on the extent of particle and metal(loid) export at the watershed scale. To do so, hydrological monitoring was performed on the gold mined river, upstream and downstream of the mining flat. This chapter is divided into two parts. The first article focuses on the understanding of the hydrological functioning of the watershed and aims at determining the source(s) of suspended particles in the gold-mined river. It aims at providing a mass balance of particle and carbon export from the gold mined watershed. The second article builds on the conclusions provided by the first article, and determines metal(loid) fluxes upstream and downstream of the mining flat.

4.1. Article II –

Restored gold mine in an Amazonian catchment (French Guiana): source tracking and hydro-sedimentary mass balance of carbon and particulate emissions

Naomi NITSCHKE[a,d,e,f], Stéphane GUÉDRON[a], Cedric LEGOUT[b], Antonio MARTINEZ-CORTIZAS[c] , Stanislav JELAVIC[a], Jennifer HARRIS[d], Emmanuel TESSIER[e], Sylvain CAMPILLO[a], Stéphane TARAVELLA[f], and David AMOUROUX[e]

[a] Univ. Grenoble Alpes, Univ. Savoie Mont Blanc, CNRS, IRD, IFSTTAR, ISTerre, 38000 Grenoble, France

[b] Université Grenoble Alpes, CNRS, IRD, IGE, 38000 Grenoble, France

[c] CRETUS, EcoPast (GI-1553), Facultade de Bioloxía, Universidade de Santiago de Compostela, 15782 Santiago de Compostela, Spain

[d] BRGM, F-45071 Orléans, France

[e] Université de Pau et des Pays de l'Adour, CNRS, IPREM, Institut des Sciences Analytiques et de Physico-chimie pour l'Environnement et les Matériaux, Pau, France

[f] GAIA SAS, Cayenne, France

*email : naomi.nitschke@univ-grenoble-alpes.fr

Acknowledgments

We thank Cindy Arnoldi (LECA, UGA), for analytical support in particulate carbon measurements, and Akram Ali (SAS GAIA) for field assistance.

4.1.1. Abstract

Artisanal and small-scale gold mining (ASGM) is prevalent in South America and the Amazon. It involves soil reworking, leading to an increase in downstream turbidity and ecosystem degradation. In French Guiana, restoration, including landscaping and tree-replanting, is mandatory for legal gold mines. To investigate the extent of particle export originating from a restored gold mining flat, high frequency suspended solid concentrations (SSC) and discharge measurements were performed upstream and downstream of a restored mining site. Additionally, two flood events were followed with geochemical tracers involving multielemental concentrations and Fourier-transformed infrared spectroscopy (FTIR) data in the particulate and filtered fractions, in order to unravel the origin of water (overland flow and groundwater), and particles (forest topsoil, mine topsoil, or river bed sediments) within the watershed. Results show that within the year following landscaping, the mining flat is still a significant source of particles and carbon to the river, with an excess 100-300 $kg.km^{-2}$ of particles exported due to the presence of the mining flat, and specific carbon exports amounting to 9.8 $t\ C.yr^{-1}.km^{-2}$ which is comparable to exports observed in larger watersheds in the Amazon region. However, this increase cannot be explained by an exacerbated overland flow, as the hydrological functioning is not fundamentally affected downstream of the mining flat compared to upstream. Multielemental and FTIR data in the particulate fraction point towards the main source of suspended particles being riverbank erosion and riverbed sediment remobilisation rather than mining flat remobilisation, underlining the importance of riverbed recreation and stabilisation in the restoration process of a gold mine.

Keywords Gold mining; Amazon; mine restoration; hydrology; carbon; SPM

Highlights

- The particle and water sources and exports of a restored goldmine were studied.
- The restored mining flat is still a source of particles, one year after landscaping.
- The mining flat does not affect the hydrological behaviour at the watershed-scale.
- The major source of suspended particles likely originates from riverbank erosion.

4.1.2. Introduction

Artisanal and small-scale gold mining (ASGM) is, after agriculture, a major cause of deforestation in the Amazon region (Hänggli et al. 2023). Alluvial gold mining includes the removal and destructuration of the topsoil layer by high-pressure water hoses so as to access the gold-bearing gravel layer, leading to an increase in particle export to the surrounding rivers (Gallay et al. 2018, Dethier et al. 2019) and carbon storage loss (Csillik and Asner 2020). This rise in river turbidity can be harmful for downstream ecosystems (Mol and Ouboter 2004, Tudesque et al. 2012). In addition, these particle are often rich in metals, such as mercury (Hg) and lead (Pb), and their remobilization results in important exports of metal(loid)s in these rivers (Roulet and Grimaldi 2001, Diringer et al. 2020).

In the Amazon region, numerous studies have documented carbon and particle export and hydrosedimentary budget of large river systems like the Amazon river and its main tributaries (Moreira-Turcq et al. 2003, Montanher et al. 2018, Armijos et al. 2020), or other major rivers in the region (Laraque et al. 2009, Sondag et al. 2010, Gallay et al. 2017, Rousseau et al. 2019). These studies involve watershed sizes above 10,000 km², and punctual (monthly) sampling over years or decades, which allows the examination of integrated large-scale seasonal trends. On a global scale, tropical rivers account for 60 % of total organic carbon exports to the ocean (Huang et al. 2012), however these budgets might be subject to changes, as deforestation in the Amazon region also leads to a loss of carbon stocks (Nogueira et al. 2015). Several carbon export budgets performed on the Amazon river show that it represents up to 10 % of total carbon exports to the oceans (Richey et al. 1990, Moreira-Turcq et al. 2003) but the specific impact of ASGM on carbon export is not clear (Gallay et al. 2017). Yet, little data is available on small-scale hydrological processes (Grimaldi et al. 2003), which would help to understand the impact of gold-mining activities on these processes.

Gold mining in French Guiana is unique in the Amazon region due to the presence of semi-industrial alluvial ASGM activity supervised and regulated by the authorities, existing in parallel with illegal ASGM activities (Jébrak et al. 2021). In the case of legal gold mines, measures to limit their impact on the surrounding environment include i) gold extraction in closed circuit and settling of washed particles in ponds, followed by ii) landscaping after exploitation (drainage of the ponds and soil reconstruction with remaining fine materials and organic matter), and revegetation of the mining site by tree plantations (Marquis 2015). However, the co-existence of legal and illegal (or historical) ASGM practices adds complexity to source tracing and hampers the straightforward determination of legal ASGM impact on particle fluxes. Small-scale (1-50 km² watershed) studies in French Guiana aimed at determining the impact of ASGM during the set up and exploitation phases (Grimaldi et al. 2015), observing a stark increase (1000 to 10,000 fold) in particulate export during the mining site opening compared to before. Additionally, the impact of historical ASGM sites on contaminant (mercury)

exports has also been investigated (Guédron et al. 2011, Hellal et al. 2020), with historical anthropogenic mercury being remobilised by more recent exploitations. Up until now, little to no studies attempted to understand the evolution of particle and carbon export after exploitation of a mining site, during restoration, in the Amazon region. It is not clear how long the mining sites continue to be a significant source of particles after exploitation, as well as whether and to what extent the rehabilitation of a gold mining site is efficient in decreasing particle export to the river.

Hydrological processes involved in the remobilisation of these particles include the extent of overland flow compared to groundwater input during a flood event. Chemical tracers have been used previously in Amazonian catchments to trace water sources to the river in pristine and agricultural catchments (Grimaldi et al. 2003, Chaves et al. 2008, Neill et al. 2011), but not in the context of a mine exploitation or rehabilitation. At the scale of large river systems, isotopic compositions of different elements (i.e., Fe, Sr, Nd, Pb) have been used to distinguish between various sources of particles and weathering mechanisms involved (dos Santos Pinheiro et al. 2014, Höppner et al. 2018). However, the assessment of exact particle sources at the scale of a mining flat is challenging because the mineralogical composition of gold-mined lowlands is relatively homogeneous (dominated by quartz and kaolinite), and the distinction between particles emissions from illegal ASGM, legal mines and the natural sources requires the identification of new and specific tracers.

The aim of this study was to understand the hydrological processes taking place on a gold-mined watershed, and quantify the contribution of the gold-mined flat to particle and carbon export during its rehabilitation. In addition, tracers were used to assess to what extent chemical and mineralogical analysis enabled to distinguish whether pristine or alluvial gold-mined flats were the main sources of particles and carbon export towards the main stream.

4.1.3. Materials and Methods

Study area. French Guiana (87,500 km²) is part of the Guiana shield located in the north-eastern region of South America between Brazil and Surinam (2-6°N and 51°30'-54°30'W). It experiences an equatorial humid climate with average annual rainfall of around 4000 mm and 96 % of the territory is covered by tropical rainforest. The study was conducted on the Awa site, an alluvial gold mine (54°20'34"W, 4°19'8"N) of the mining company SAS GAIA (Figure 4.1). The Awa River is part of the bigger Maroni river watershed, the largest river of French Guiana (66 814 km²), which is densely gold-mined (Gallay et al. 2018) and has a long history of gold mining dating back to the 1900s (Jébrak et al. 2021). The Awa watershed area is 32 km². Alluvial gold mining exploitation was performed below a riverbed, to extract gold from gravel deposits resulting from the weathering of auriferous quartz veins (Thomassin, Urien et al. 2017). These downslope valleys typically consist of sandy hydromorphic soils exhibiting reducing conditions due to the presence of water flowing slowly (Guédron, Grangeon et al. 2009). The mineralogy of these soils is dominated by quartz and kaolinite, with some goethite. Exploitation and production was conducted on the site from downstream to upstream between September 2017 and April 2021. The first restoration operations were conducted between May and July 2019, and full restoration was then performed between May 2021 and August 2022. Restoration consists in filling the mining ponds with the gravel and clay removed during exploitation, performing landscaping respecting as much as possible initial soil stratification, then replanting trees grown in on-site nurseries, at a three-meter interval. It has to be noted that illegal gold mining had been taking place upstream of this site before and during the study.

Three sampling campaigns were conducted over one year (from 2022 to 2023): G1 (04/22), G2 (12/22) and G3 (05/23), on two different sites on the gold-mined river (Figure 4.1). The first being located at the entrance, upstream of the mining site and the second one further down on the mining site. These two sites are termed here "upstream" and "downstream", respectively. The downstream site could not be located further downstream, at the exit from the gold mine, due to accessibility and practical issues.

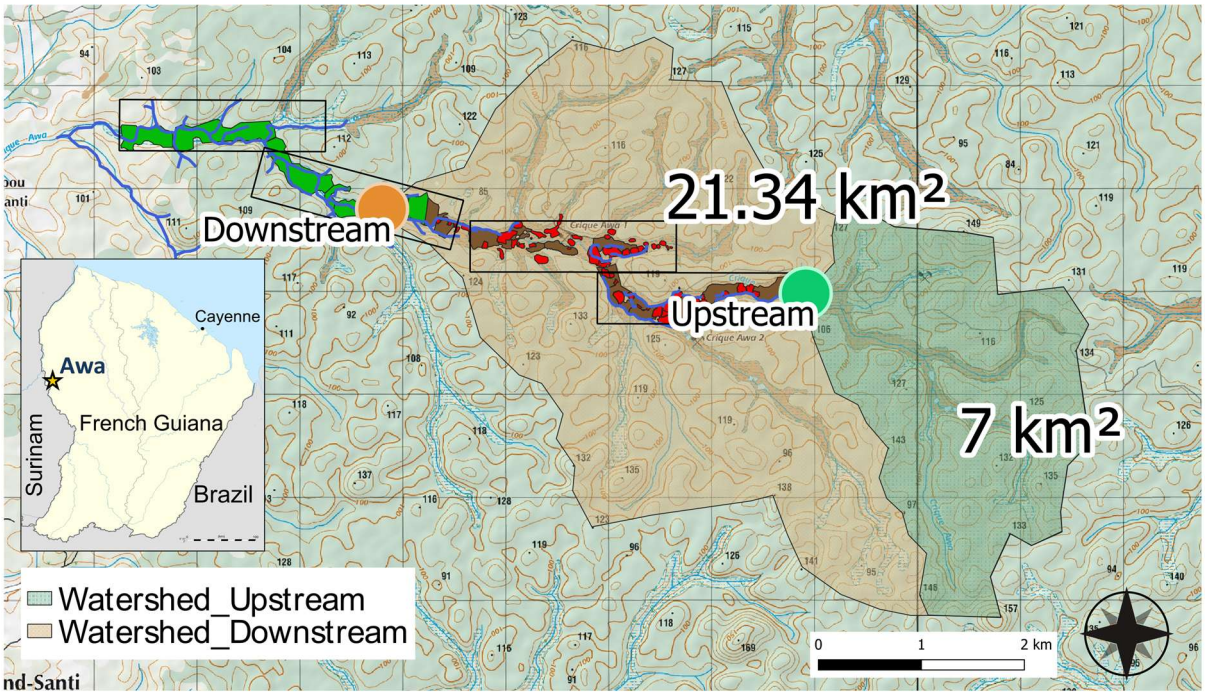

Figure 4.1. *Study site with the two monitoring and sampling stations on the Awa gold-mined river.*

Monitoring and sampling. A monitoring station was installed at both the upstream and downstream sites, measuring water level using a pressure level sensor (OTT-PLS) and turbidity (Hydrolab HL4) at 1h time intervals. A stage discharge rating curve was constructed at different water levels using two devices (an impeller current meter, OTT and a hand-held surface velocity radar, Viatronics) to calculate discharges based on the water level measurements. These two sensors stayed on site, even outside of the sampling campaigns. Unfortunately, there is no overlap between the upstream and downstream long-term monitoring data, due to sensor failure and theft. For long-term trends, hourly rain data was recovered from a national meteorological station in Grand-Santi, 7 km away from the mining site. For specific events, a rain gauge located in the central part of the mining flat was used to quantify wet deposition for major rainfall events and the total duration of the rainfall events was also noted.
An automated water sampler (ISCO) was installed at each station and programmed to collect river samples every two hours (or longer during water level recession) during the 3 sampling campaigns.

Overland flow water and eroded particle samples were collected as described in section 3.1.3. Briefly, erosion plots were installed to recover the overland flow water and eroded material from a defined area during a rain event. Each plot consisted of wood panels (2 m × 2 m, 4 m²) inserted 10 cm into the soil and extending 15 cm above the soil, and was connected to an 80L bucket installed at the lowest point of the slope and buried in the soil. After each rain event, the total volume of water was measured, and a 250 mL aliquot of the suspension was sampled in an FEP bottle, to measure suspended solid concentration (SSC) and major and trace elements in the filtered and particulate fractions.

All river and overland flow water samples were collected in pre-cleaned vials following ultra-clean technique protocols (Stoichev et al. 2006). A 250 mL aliquot of the water sample was filtered on an acid-washed and pre-weighed 0.45 µm PVDF filter, which was air-dried in a laminar flow hood 48 h and weighed to determine the SSC (Stoichev et al. 2016). The filtrate was collected in trace grade falcon tubes acidified with HNO_3 2 % for multi-elemental analyses, in pre-burnt borosilicate vials acidified with HCl 0.2 % for dissolved organic carbon (DOC) analyses and in 2 mL Eppendorf tubes and frozen for anion analyses. Another 250-300 mL aliquot was filtered on a pre-burnt (450°C) and pre-weighed GF/F filter for total carbon, FTIR and XRD analyses.

In addition to the river samples, soil samples on and around the mining site were sampled using a manual auger. These soils were homogenised, freeze-dried, sieved at 2 mm and ground to a powder <63 µm for further analysis. Freeze-dried soils were sieved at 1.25 mm for grain size measurements. Particle size distributions (PSD) were measured with a laser diffraction sizer (Malver, Mastersizer 2000) following the protocol of Grangeon et al. (2012). For each sample, the proportions of clay (<2 µm), silt (2-63 µm) and sand (>63 µm) fractions were extracted.

Soil erosion measurements. Soil erosion rates and critical erosion shear-stress were measured using an EROMES device as described elsewhere (Schünemann and Kühl 1991, Lanuru et al. 2007, Joensuu et al. 2017, Haddad 2022). Briefly, a 10 cm diameter cylinder is placed above the soil, filled with water, and a helix placed 3 cm above the soil rotates at increasing velocities to induce soil erosion. The erosion flux is deduced from turbidity measurements that are calibrated to relate to suspended particle concentration. The experiment was stopped at saturation of the turbidity sensor or after 20 shear stress increments, to a maximum force of 4.67 Pa. The erosion threshold (τ_c) was determined as the critical shear stress at which the erosion flux (ER) reached 0.1 $g.m^{-2}.s^{-1}$. The erosion rate (m_e; $g.m^{-2}.s^{-1}.Pa^{-1}$) was determined as the slope of the erosion flux versus the shear stress (at shear stress ≥ τ_c). A high erosion rate m_e associated to a small critical shear stress τ_c represents a high soil "erodibility" while low m_e values with high values of τ_c indicate a more stable soil.

Chemical analyses. Multi-elemental analysis of major and trace elements was performed by inductively coupled plasma-atomic emission spectrometry (ICP-AES) (Agilent, Varian 720-ES) and by inductively coupled plasma mass spectrometry (ICP-MS) (Agilent 7900 coupled to an ESI PrefFast IC module) respectively. The filtered water samples were analysed directly and the filter and soil sample solutions were analysed after microwave (ultra-WAVE, Milestone) assisted acid digestion (HNO_3) at 220 °C. The accuracy of the measurements was evaluated based on the analysis of certified reference materials (NIST 1944 and IAEA-405 for solid samples and SLRS-6 for water samples).

Dissolved Organic Carbon. Filtered and acidified water samples were analysed in pre-burnt borosilicate vials using a TOC-VCSN analyser from Shimadzu associated to an ASI-V autosampler as described in (Tisserand et al. 2024)

Carbon and Nitrogen. Total carbon and nitrogen contents were measured on ground soils using a Flash Smart elemental analyser (ThermoFisher Scientific). (Piton et al. 2020)

Total organic carbon (TOC) content and isotopic composition ($\delta^{13}C_{org}$) of suspended sediments on GF/F filters were measured by Cavity Ring-Down Spectrometer (Picarro, Inc.) coupled with Combustion Module (Costech, Inc.) (CM-CRDS) using previously reported analytical methods, calibration, and sample preparation (Balslev-Clausen et al. 2013, Guédron et al. 2019).

Spectral analyses. Samples were analysed by attenuated total reflectance Fourier transformed infrared spectroscopy (ATR-FTIR) using a Nicolet iS50 FT-IR equipment (Thermo Fisher Scientific). Spectra were collected in the mid infrared (MIR) range, 4000-400 cm^{-1}, with a resolution of 4 cm^{-1} and performing 64 scans per sample. A background was obtained before samples' spectra collection. Spectral pre-processing, peak location (using the second derivative spectrum), average and standard deviation spectra and figures of the spectra were done with Orange v3.38.1 (Demsar et al. 2013).

X-ray diffraction analyses.

Sample preparation protocol for bulk powders: To achieve a final particle size ~1 µm necessary for optimal mineral quantification, a slurry of ~1 g of sample and 15 ml of 99 % ethanol was ground in the McCrone micronizing mill for 10 minutes and then dried at 45 °C overnight. To quantify the amorphous fraction of the sample, 20 % of corundum (CR-1, Baikowski) was added and the difference between the weight percentage of added and refined standard was recalculated to actual weight percentage of the amorphous fraction. To minimise particle orientation during the analysis, the powder was then front-loaded to sample holders by sieving it through a 50 µm stainless steel sieve and gently pressed.

Analysis: The filters were directly placed on low XRD background Si wafers, bulk powders were analysed in Bragg-Brentano geometry. Both were analysed using a Bruker D8 instrument equipped with either a Co or Cu tube and either a SolX (filters) or Vortex (bulk) detector. The opening of primary and secondary Soller slits was 2.5°, and of divergence and receiving slit 0.4° (filters) or 0.3° (bulk). The sample was spun at 40 rpm during acquisition to improve the counting statistics. The step of tube and detector was 0.013°, counting time was 24 s (filters) or 8 s (bulk) per step and the data was collected between 5 and 60 °2Θ for filters, and between 5 and 90 °2Θ for bulk samples.

Data processing: The Rietveld analysis was done using BGMN software and the PROFEX interface using accompanying and in-house crystal structure database. The theoretical instrumental peak broadening was calculated using the raytracing procedure embedded within the BGMN.

Data analyses. Principal components analysis was performed on whole spectra, i.e., using the transposed data matrix (tPCA): wavenumbers in rows and samples in columns, with varimax rotation and on the correlation matrix. This approach enables to decompose the samples' spectra into a limited number of components' scores spectra related to the compounds contributing to the MIR spectral signal of the samples. The loading of a component in a sample is thus related to the proportion of spectral variance of the sample accounted by the compound reflected by the scores' spectrum of the component – which is correlated to the amount of the compound in the sample. This approach has been successfully applied in investigations of organic and inorganic matrices (Martínez Cortizas et al. 2021, Kylander et al. 2023, Martínez Cortizas et al. 2024).

A binary end-member mixing model was performed using different geochemical tracers, with two sources (overland flow and groundwater). Tracers were selected based on i) an observable temporal variation in concentrations during the rain event, ii) significant ($p<0.01$) differences in concentration between overland flow and groundwater, and iii) a concentration range in the river standing between on of the respective endmembers.

$$X_R = X_{GW} \times f + X_{OF} \times (1 - f)$$

Where X_R is the tracer concentration in the river, X_{GW} in groundwater, and X_{OF} in overland flow, and f the fraction of groundwater. To account for temporal changes in groundwater concentrations due to renewal over time, the groundwater concentration was considered equivalent to the endmember river concentration at baseflow for each event, as no overland flow contribution is assumed at baseflow. Then, this value was adapted linearly during the flood event to match the baseflow concentration after the event and to consider at best the change in groundwater concentrations as it is recharged during the event. As the mixing models were in good agreement, the average overland flow contribution of all models was used in further calculations. The total flow coefficient (C_{TF}) and overland flow coefficient (C_{OF}) were calculated as follows:

$$C_{TF} = \frac{(V_{tot} - V_{BF})/S}{R}$$

$$C_{OF} = \frac{(V_{OF})/S}{R}$$

Were V_{tot} is the total water volume flowing through the river during the flood event, V_{BF} is the water volume attributed to baseflow, S the surface of the watershed (7 km² upstream and 21 km² downstream), and R the amount of rainfall during the flood event, in mm.

All statistical analyses were performed using R. The Student's t-test was performed when the data was normally distributed and the variances between the two studied groups were equal. When this was not the case, the Wilcoxon test was performed. Regressions are shown only if the p-value is below 0.01.

4.1.4. Results and discussion

4.1.4.1. Interseasonal hydrosedimentary dynamics of two nested watersheds

Turbidity and water discharge were measured between April 2022 and May 2023 upstream and downstream of the studied mining site, which had undergone landscaping restoration work until May 2022. Additionally, illegal ASGM activities had taken place previously on and upstream from the mining flats. The Awa River water discharges downstream from the gold-mined flat averaged 0.7 ± 0.3 $m^3\ s^{-1}$ during low water level, and rose up to 2 ± 1 $m^3\ s^{-1}$ during flood events (Figure 4.2). Upstream of the mining flat, the water discharges were 0.4 ± 0.1 $m^3\ s^{-1}$ at baseflow, and peaked at 1.2 ± 0.6 $m^3\ s^{-1}$. Unfortunately, there is no overlap between the upstream and downstream chronicles because of sensor defects and theft.

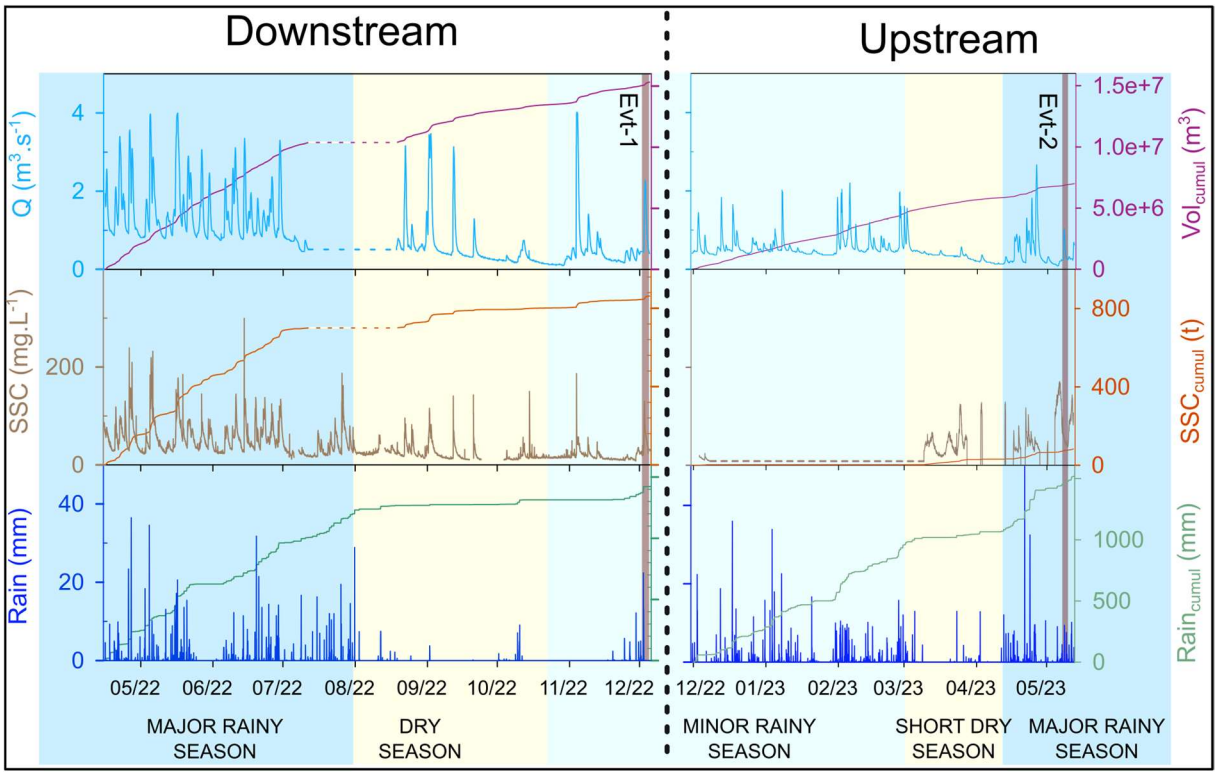

Figure 4.2. *Chronicles of discharge (Q), suspended solid concentrations (SSC) and rainfall at two monitoring stations located downstream and upstream of a mining flat. The positions of the two flood events studied subsequently (Evt-1 and -2) are depicted as vertical bands.*

Nevertheless, the hydrological descriptors calculated by season show that the main water and particle export per day as well as per event (Table 4.1) occurs during the major rainy season (MaR, i.e., April to June). This major rainy season is followed by a dry season (August-November) and a minor rainy season (December-February) both exhibiting smaller rainfall amounts, flow and suspended sediment fluxes.

Table 4.1. *Main hydrological parameters integrated at the seasonal scale. miR = minor rainy season, MaR = major rainy season, DS = dry season, SSC = suspended solid concentrations.*

Site	Season	Event number	Rainfall .day^{-1}	Rainfall. evt^{-1}	Specific flow vol.day^{-1}	Specific flow vol.evt^{-1}	specific SSC day^{-1}	specific SSC event^{-1}
		n	mm	mm	mm	mm	kg km^{-2}	kg km^{-2}
Upstream	miR	26	11	38	7	6	*no sensor*	*no sensor*
	DS	3	2	24	4	2	105	300
	MaR	6	14	67	6	12	245	751
Downstream	MaR	20	12	46	6	8	424	1023
	DS	11	3	33	2	5	65	335
	miR	7	3	18	2	5	69	200

The comparison between the upstream and downstream sites for the MaR, which were measured during two different years but with comparable daily rainfall during the respective periods, shows that the exported volumes per day normalised by the watershed area were comparable (6 mm), whereas the exported particles per day were increased downstream by 1.7-fold. This hints towards an increased erosion within the mining flats compared to the upstream area covered with forest.

Because there was no overlap between the upstream and downstream records, the temporal evolution of the exports due to the mining flats was assessed by observing the change in ratios of particle and water volumes exported during different events over time. A notable decrease in the particle/water ratio was observed over time (Figure S 4.1). This decrease could either be due to seasonal variations, with a higher ratio observed during the major rainy season followed by lower ratios during the dry season, or it could be attributed to a decrease in particle export, as the mining flat was starting to grow a plant cover and the soils were more stabilised. Eight months after landscaping (in December 2022), the particle/water ratios reached values in the range of the ratios observed upstream from the mining flats (0.06 ± 0.02), where these ratios are stable over time. Consistently, restored mine flat-soils were shown to be stabilised rapidly, within 12 months after the landscaping of the mining flats, mostly due to the spontaneous colonisation of herbaceous plants (chapter 3).

4.1.4.2. Particulate emission from a restored gold mined flat over one year after landscaping

In order to explore in further detail the increase in particle export downstream from the mining flat observed at the seasonal scale, two flood events were fully recorded simultaneously upstream and downstream of the mining flats, allowing to reconstruct a hydrosedimentary budget (Figure 4.3). The first event ("event-1") was recorded in December 2022 after the dry season, at the beginning of the minor rainy season (miR, i.e., from December to February), and 8 months after landscaping, whereas

the second event ("event-2") was monitored in May 2023 during the major rainy season (MaR, i.e.; from April to July), and 13 months after landscaping. Both events were relatively similar in rainfall amounts (44 and 34 mm, respectively), and intensities (0.55 and 0.68 mm.min^{-1}, respectively).

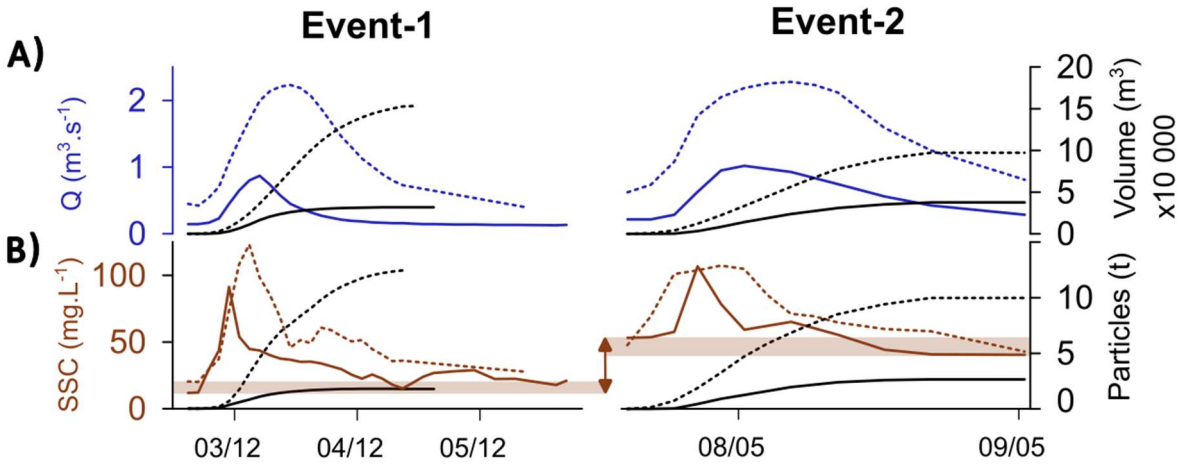

Figure 4.3. *A) Discharge (Q, blue) and cumulated volume (black), B) SSC (brown) and cumulated particles (black) on two rain events upstream (full line) and downstream (dotted line) of the mining site.*

A decrease in both volume and particle export on the downstream site in the event-2 compared to event-1 was observed (Table 4.2) and could be attributed to the somewhat lower rainfall at the second event (25 % lower).

Table 4.2. *Hydrosedimentary budget upstream and downstream of the gold-mined flats for two events recorded during different seasons (event-1 in the minor rainy season, miR, and event-2 in the major rainy season, MaR).*

	Event-1 (miR)		**Event-2 (MaR)**	
	Upstream	Downstream	Upstream	Downstream
Vol_cumul (mm)	4.5	7.3	5.4	4.6
SSC/area (kg.km^{-2})	252	594	381	476
SSC/vol (mg.L^{-1})	56	81	71	103

On the contrary, the upstream site displays an increase in particle export during event-2, even though the rainfall was lower. This increase is mainly due to an increase in baseflow SSC at event-2 (47 ± 6 mg.L^{-1}) compared to event-1 (15 ± 4 mg.L^{-1}). This difference in baseflow SSC could be explained by the difference in seasonality of these two events, as event-1 occurred after the dry season, where lower SSC are expected, and event-2 occurred during the major rainy season. However, additional measurements taken one year before event-2 during the same season showed much lower baseflow SSCs (25 ± 3 mg.L^{-1}, Figure S 4.3, p= 0.0008). Another explanation, supported by field observations, is the presence of illegal gold-mining operations taking place upstream from the legal mine. After event-2, a drastic increase in turbidity was recorded, not correlated to any significant increase in water

height, which also points towards the presence of illegal operations creating artificial particle export to the river. This presence of illegal ASGM potentially masks the impact of the legal mine in event-2.
Concerning the impact of the mining flats, during the first event, the specific water volume exported was 1.6-fold higher downstream compared to upstream, and the amount of particles was 2.4-fold higher (Table 4.2). In the second event, however, the differences between upstream and downstream were greatly reduced, with comparable water volume exports. Albeit less important than in the first event, an increase in particle export downstream from the mining flats was still observed, with a 1.2-fold increase during event-2. To clarify the processes involved in the observed increase in particulate matter exports downstream from the mining flats, sourcing of river water and suspended particles was performed using chemical and mineralogical tracers.

4.1.4.3. Hydrological processes: groundwater and overland flow contributions during two events

Water tracing using geochemical indicators has already been documented in French Guiana, with Cl and H_4SiO_4 characterizing the residence time of water in the soil or subsurface groundwater, K originating from throughfall, and Ca, Na, and Mg supplied by the leaching of the litter (Grimaldi et al. 2003). A similar approach with geochemical indicators was used for the quantification of water originating from overland flow and subsurface groundwater during the two studied flood events in the Awa watershed using an binary mixing model (BMM). Hydrogeochemical tracers used as endmembers for the BMM were re-evaluated in the context of this study and selected based on the significance of variations in elemental concentrations during the flood event and between overland flow and groundwater ($p<0.01$, Figure S 4.4), and with a concentration range in the river standing between one of the respective endmembers (Figure 4.4).
The elements passing these criteria and thus selected for the BMM were Si, Sr, Mg, Al, and U, with Si, Sr, and Mg decreasing with increasing discharges suggesting a dilution of groundwater by overland flow also confirmed by the increase in Al and U concentrations with increasing discharge (Figure S 4.5). To account for temporal changes in groundwater concentrations due to renewal over time, the endmember concentration at baseflow was considered equivalent to the groundwater concentration for each event. Then, this value was adapted linearly during the flood event to match the baseflow concentration after the event and to consider at best the change in groundwater concentrations as it is recharged during the event. Only the concentration variations of Si (groundwater) and U (overland flow) are depicted in Figure 4.5A, but the average of all tracers was used in the calculation of overland flow contribution, which produced similar results (SD < 15 %, Figure 4.5B). The concentrations of all tracers are presented in Figure 4.5.

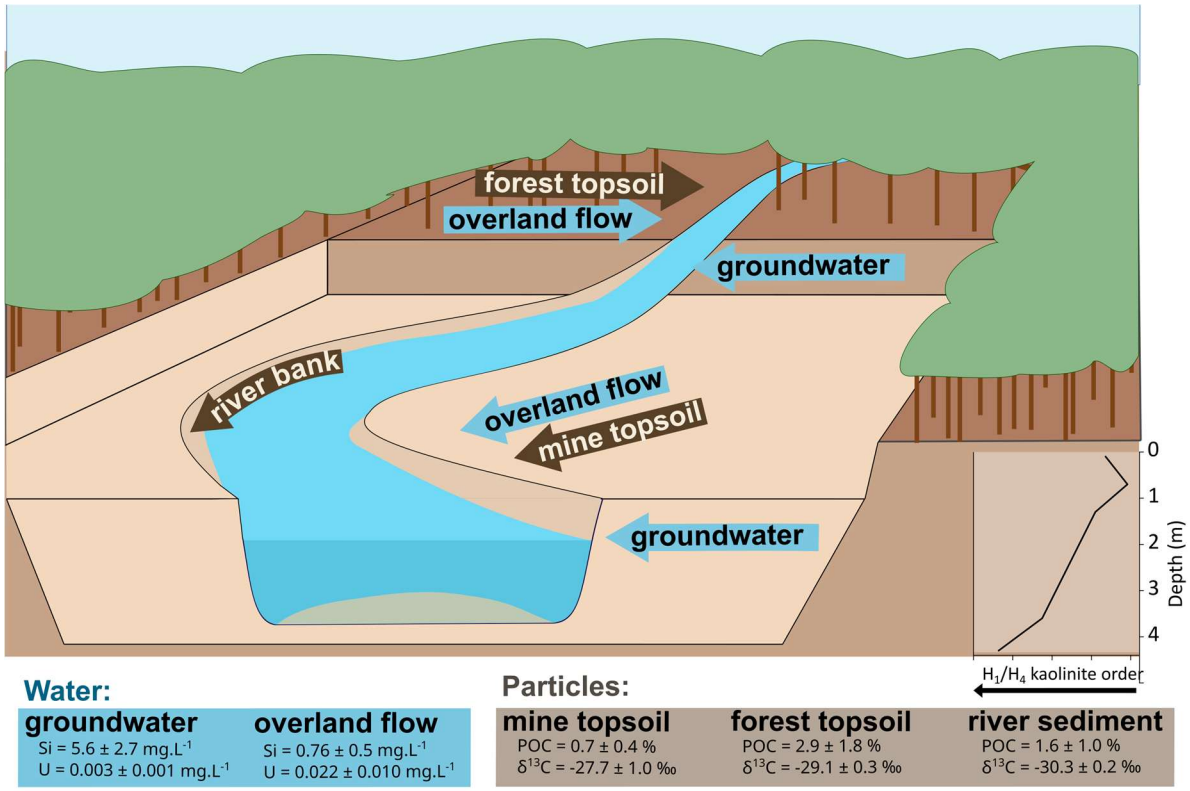

Figure 4.4. *Selected tracers in the different endmembers from the filtered fraction (Si and U, blue) and from the particulate fraction (POC and δ13C, brown) on a restored gold-mined river, as well as kaolinite order evolution along a forest soil profile.*

The total flow coefficient (C_{TF}, total specific water volume corrected by baseflow/total rain) and the overland flow coefficient (C_{OF}, total specific overland flow water volume/total rain) were determined for each event and at each site. The total flow coefficients are similar in both events and sites (14 ± 2 %, Figure 4.5C), and in the range of observed values in a small (7 000 m²) pasture-covered watershed in the Brazilian Amazon (Chaves et al. 2008). The overland flow coefficient is the same upstream and downstream of the mining flat, with values of 9 % for event-1, and 5.5 % for event-2. These values are significantly lower than those previously reported in smaller watersheds (<1 km²) but similar-sized rainfall events of French Guiana and in the Amazon region (Grimaldi et al. 2003, Chaves et al. 2008). A low amplitude event (rainfall = 18mm) was monitored two days after event-2 (MaR season), only on the downstream site, and almost no overland flow was observed (C_{OF} = 1.7 %, Figure S 4.6).

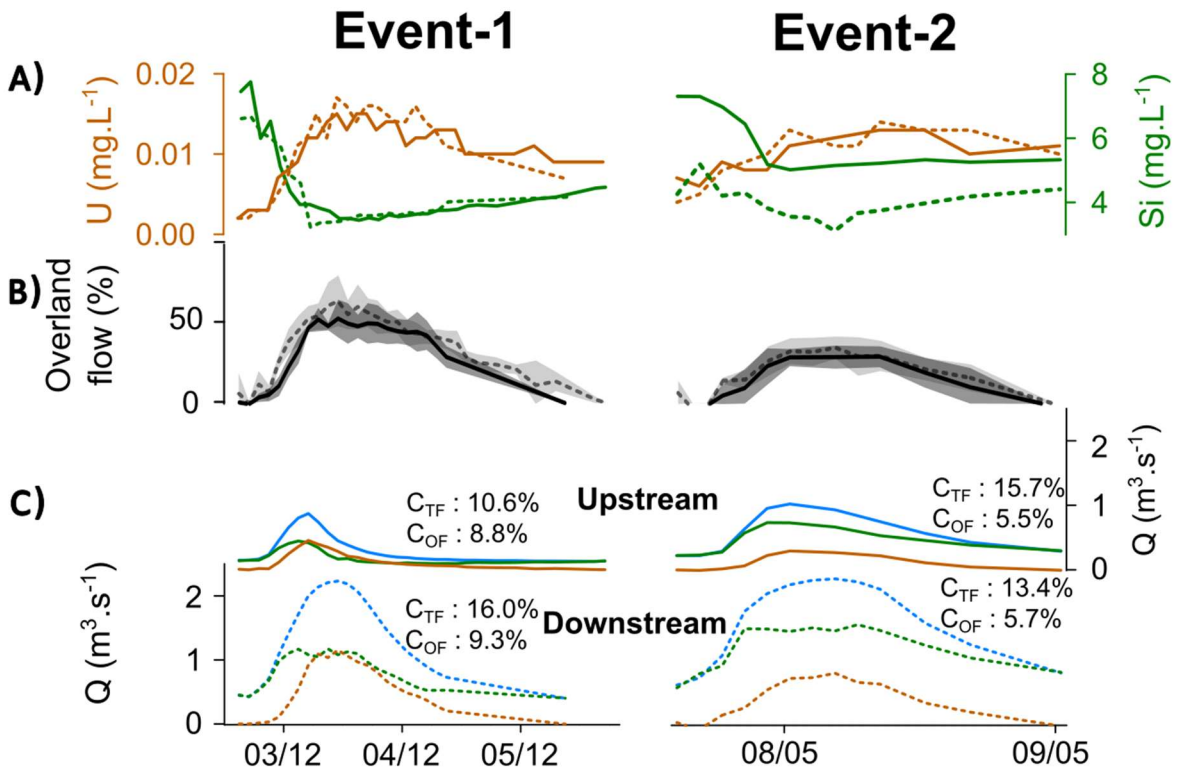

Figure 4.5. *A) Concentrations of U (brown) and Si (green), B) Contribution of overland flow and C) reconstruction of the groundwater (green) and overland flow (brown) to the total (blue) discharge during two flood events, upstream (full line) and downstream (dotted line) of the mining flat. The total flow coefficient (C_{TF}) and overland flow coefficient (C_{OF}) are inserted in the bottom panels.*

The higher overland flow coefficients observed during the miR (event-1) than during the MaR (event-2) could be attributed to differences in i) the rainfall amount or intensities (Mügler et al. 2019), or ii) the seasonal hydrological regime (Gomi et al. 2008). The rainfall amount was slightly higher during event-1 than during event-2 (44 mm and 34 mm respectively), whereas average rainfall intensities were slightly lower (0.55 mm.min^{-1} and 0.68 mm.min^{-1} respectively). Thus, the similarity of both rainfall amounts and intensities between the two events does not appear to explain the increased overland flow coefficient observed in event-1. Concerning differences in the hydrological regime, event-1 was monitored at the onset of the miR season, after a long dry season, with a cumulated rainfall over the previous 30 days of only 112 mm, which might have resulted in a small hydrological connectivity of subsurface water and a certain hydrophobicity of the organic layer at the surface of soils limiting infiltration (Burch et al. 1989, Buttle and Turcotte 1999, Scherrer et al. 2007). On the other hand, event-2 was monitored during the MaR, with the previous month's rainfall amounting to 357 mm, resulting in damper soils, and thus exhibit a good infiltration capacity and hydrological subsurface connectivity promoting efficient water infiltration and groundwater flow.

Chemical tracers in the dissolved fraction allowed a robust reconstruction of water sources and contributions on the mined watershed. No visible differences in the hydrological processes were observed upstream and downstream from the mining flats, suggesting that the exploitation site does

not significantly change the hydrological behaviour at the scale of the watershed. The observed increase in sediment export downstream from the mining flats (sections 4.1.4.1 and 4.1.4.2) is thus not due to an increase in overland flow, which might have promoted overland erosion. However, it should be noted that the mined area represents a total of 0.65 km², which amounts to only 3 % of the total watershed surface at the downstream site. These results on the hydrology of the watershed are nonetheless essential as a first step to further understand potential differences in the sedimentary regime.

4.1.4.4. Characterisation of the suspended solids and their potential sources in the watershed

In order to assess to which extent sediment tracing could help to understand the higher suspended sediment fluxes observed downstream compared to upstream, during the two studied events, and the potential influence of the mining flats on particle export, suspended particles were characterized using multiple complementary tools (i.e., multielemental analysis, carbon, as well as FTIR and XRD) and compared to potential soil and sediment sources. Potential sources to the river particles identified on the catchment were i) surface forest soil, ii) the restored mine flat anthroposol, and iii) river bank and river bed sediments (Figure 4.4). In this context, it is expected that forest and mine top-soils contribute to the particulate remobilisation through overland flow, while those emitted through river bank erosion and sediment remobilization result from the total river flow (i.e., water level fluctuations due to inputs from groundwater and overland flow).

4.1.4.4.1. Mineralogical and elemental composition of soils and suspended particles

The mineralogical composition of both mine and forest topsoils obtained by XRD were similar, with a predominance of quartz (64 ± 8 %), followed by kaolinite (23 ± 5 %), and amorphous minerals (10 ± 2 %) as well as some goethite and gibbsite (Figure S 4.7A). XRD analysis on filters, although only qualitative owing to limited amount of particulate matter and the arrangement of the filter, showed a similar mineral composition in river SPM (Figure 4.6 and Figure S 4.7).

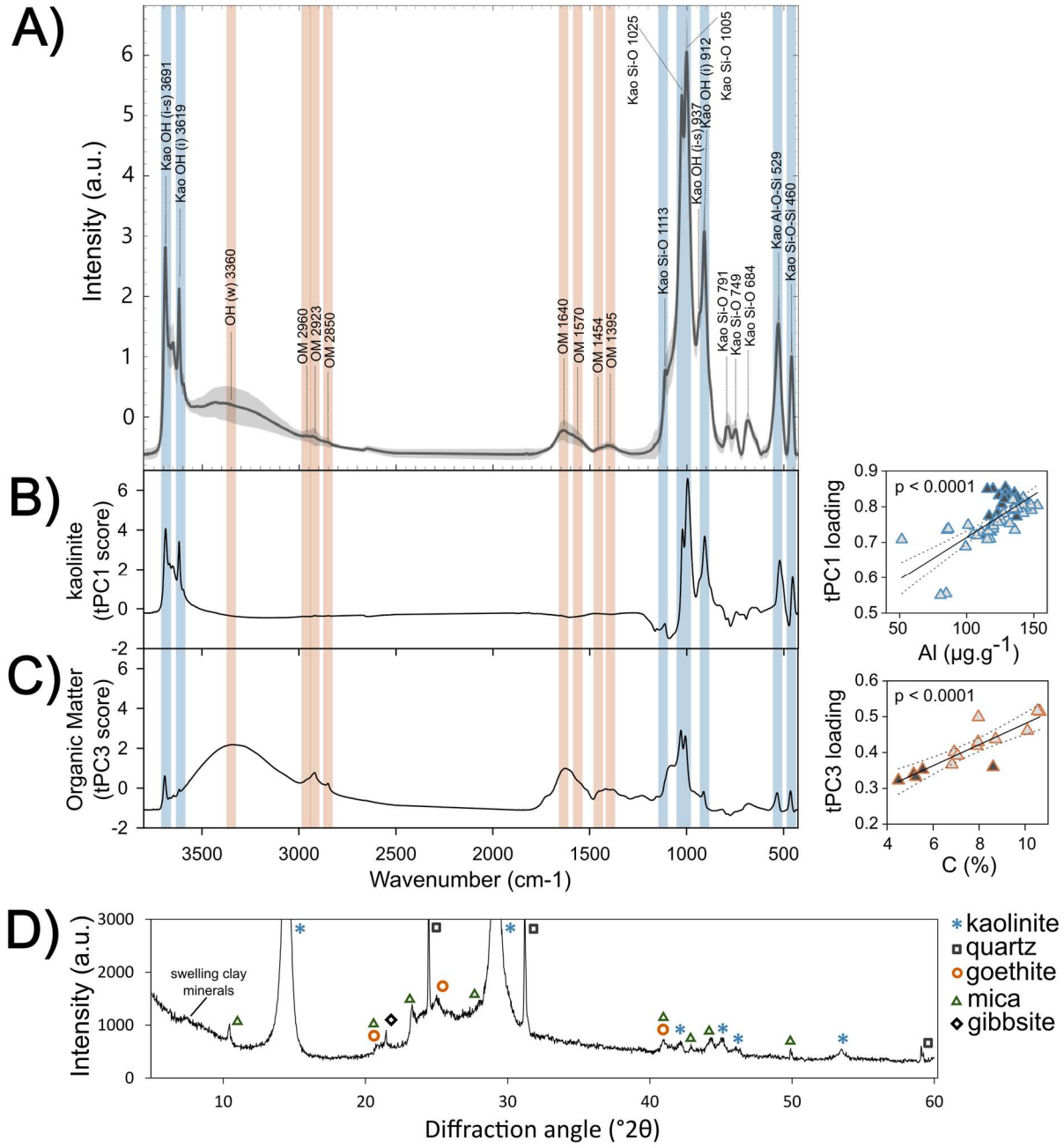

Figure 4.6. *A) FTIR averaged spectra with standard deviation. The main peaks with their corresponding wavenumber and bond type are highlighted in blue for peaks attributed to kaolinite, and in brown for peaks attributed to organic matter (OM), extracted scores for B) tPC1 and C) tPC3 as well as the relationships of their respective loadings vs Al and C respectively and D) example of an XRD diffractogram of river particulate matter.*

However, lower proportions of quartz compared to kaolinite were found in SPM, most likely due to a difference in grain size, as the finer (kaolinite) particles are preferentially eroded to the river. This is in line with reported data for particulate matter in the Maroni river, which was also shown to consist primarily of kaolinite (80-90 %), unlike in the Amazon or the Orinoco rivers, where kaolinite accounts only for 20-40 % (Rousseau et al. 2019). Consistently, elemental concentrations in SPM samples were 3 to 30-fold higher than all bulk soils and sediments, thus, multi-elemental data couldn't be used as a

source tracer in river SPM. The SPM were dominated by Al (12 ± 2 %), Fe (10 ± 3 %) and C (9 ± 3 %), in accordance with the elemental composition of eroded particles collected on mine experimental plots (section 3.1.3). FTIR spectra confirmed XRD mineralogical analyses and additionally showed changes in the abundance of organic matter (Figure 4.6). Indeed, a transposed principal component analysis (PCA) performed on all FTIR spectra enabled the extraction of different signals and the determination of the contribution of each signal in the samples. The three first principal components (tPC) scores explained 97 ± 3 % of the total FTIR signal of the samples, with the tPC1 corresponding mostly to the signal of kaolinite, tPC2 representing quartz and tPC3 organic matter (OM). In river particles FTIR tPC1 (kaolinite) was positively correlated to the Al content in the river SPM (R^2 = 0.52, p<0.01, Figure 4.6), whereas tPC3 (OM) was positively correlated to the concentration of particulate organic carbon (R^2 = 0.76, p<0.01, Figure 4.6). This latter correlation was then used to estimate the particulate carbon concentration in the remaining filter samples that have only been measured in FTIR.

4.1.4.4.2. Additional tracers for source discrimination

Because no significant difference was observed in the mineral composition of the different particle sources, complementary characterization were focused on i) the kaolinite structure using FTIR, and ii) the organic carbon abundance and isotopic composition ($\delta^{13}C_{org}$) to distinguish their potential sources. First, the structural degree of kaolinite order was studied to distinguish between the surficial and deep sources of kaolinite in the watershed, as cycles of dissolution and recrystallisation in the surface of Amazonian soils have been shown to result in the replacement of ancient highly ordered kaolinite by a more recent generation of poorly ordered kaolinite (Balan et al. 2007, Fritsch et al. 2011). The kaolinite (dis)order was thus determined using FTIR by the calculation of the peak height ratio of H_1 (3691 ± 0.8 cm^{-1}) over H_4 (3619 ± 0.3 cm^{-1}) (Drits et al. 2021). The ratio H_1/H_4 was positively correlated to the XRD "001" kaolinite peak width (full width at half maximum, FWHM) in kaolinite standards, with higher FTIR ratios and higher XRD FWHM reflecting higher disorder of the kaolinite. Consistently with literature, kaolinite order was found to increase with depth in the soil profile sampled in the vicinity of the mining site (Figure 4.4). Thus, this contrast in kaolinite order with depth could be used as an indicator to document legal sources which include deep soil reworking over several meters, and illegal or natural sources (surface erosion or remobilisation). Similar to kaolinite disorder, organic carbon (C_{org}) concentrations decreased with depth, but also decreased from forest topsoils (2.9 ± 1.8 %) to riverbed sediments (1.6 ± 1.0 %) and mine topsoils (0.7 ± 0.4 %). In addition, the carbon isotopic composition ($\delta^{13}C_{org}$) showed an increase with depth from topsoils (-28.9 ± 0.3 ‰) to deeper horizons (-26.0 ± 0.6 ‰). This change in $\delta^{13}C_{org}$ with depth could originate from i) the change in $\delta^{13}C$ between ancient deep carbon sources compared to surficial recent ones due to the combustion of fossil fuels depleted in ^{13}C (i.e., the Suess effect (Suess 1953, Körtzinger et al. 2003)), ii) diagenetic fractionation

of OM resulting in the accumulation of ^{13}C (Wynn et al. 2005, Bass et al. 2011), or iii) past changes in the superficial vegetation cover from C_4 (mostly herbaceous) to C_3 (trees) plants (Wright et al. 2021). Hence, as kaolinite (dis)order, $\delta^{13}C_{org}$ composition data in SPM might allow the distinction between recent litter OM and ancient carbon stored in deeper soil horizons.

4.1.4.5. Sourcing suspended solids in the river

4.1.4.5.1. Flood-dependent tracer variations

River particles exhibit changes in the chemical and mineralogical composition during flood events and between upstream and downstream sites. As for the dissolved phases, two main and opposite variations are observed during flood event-1, where the organic matter (i.e., FTIR tPC3 and Sulphur concentration) decreased during the flood event, whereas the mineral phase (FTIR tPC1 and Al concentration) increased and was positively correlated to SSC (Figure 4.7).

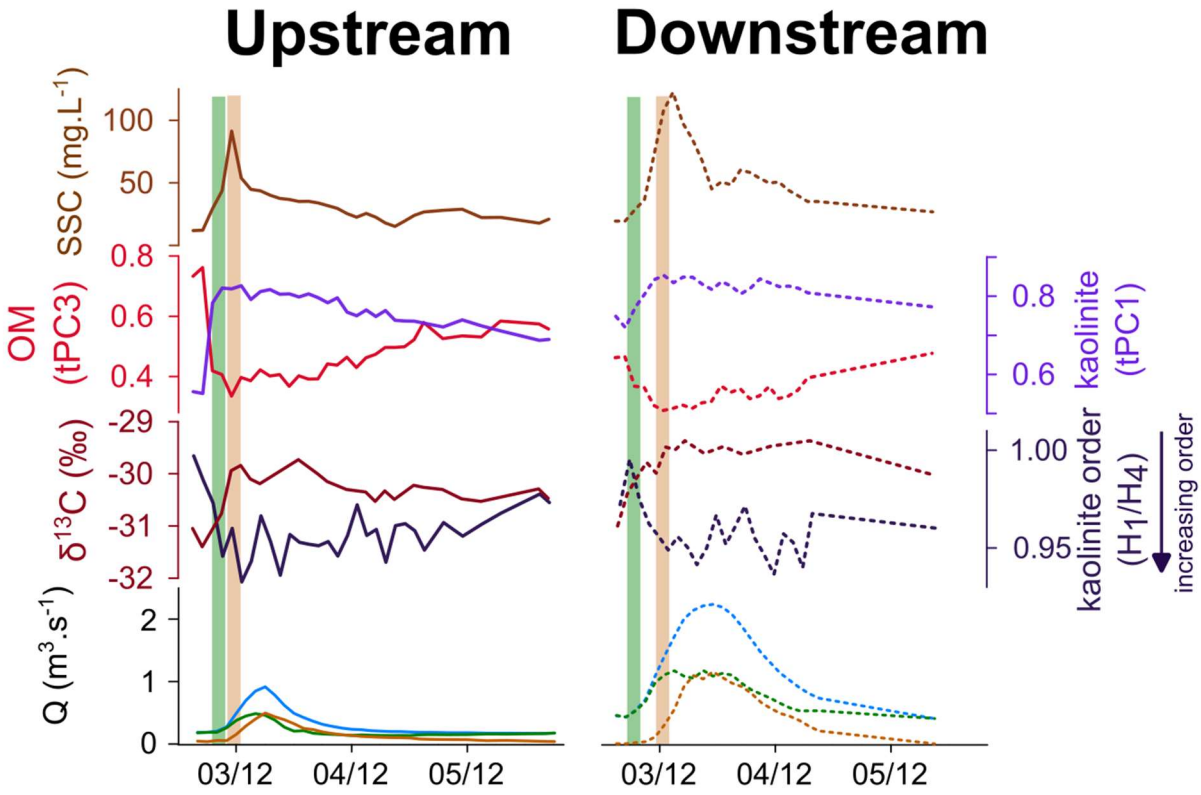

Figure 4.7. *Evolution of A) SSC, B) OM (red) and kaolinite (purple), and C) reconstruction of the hydrograph with groundwater (green) and runoff (brown) to the total (blue) discharge during a rain event (event-1).*

The amplitude in variations of all parameters is slightly higher upstream of the mining flat than downstream, where baseflow levels are closer to the eroded mining flat particles. The concentrations reached at the peak in SSC are comparable between upstream and downstream of the mining flat, hinting towards a common source of particles. Consistently, the decrease in particulate organic carbon

(POC) with increasing SSC (Figure 4.7), illustrates the dilution of the organic-rich river particles by an input of organic-poor eroded or re-suspended particles during the flood event, as observed in various rivers and contexts (Moreira-Turcq et al. 2003, Oeurng et al. 2011, Guzmán-Uria et al. 2020). This decrease in C_{org} concentration is concomitant with increases in $\delta^{13}C_{org}$ values. The low (<-31‰) values as baseflow are in agreement with values observed in forested catchments of the Amazon basin (Bird et al. 2012) and might originate from C_3 plants or litter displaying an isotopic composition close to or below 30‰ in the Amazon region (de Araújo et al. 2008, Mortillaro et al. 2011). The slight but significant increase in $\delta^{13}C_{org}$ during the flood event (up to -30‰), which mirrors the POC pattern, could originate from input from topsoil erosion (-28.9 ± 0.3 ‰) or river bed sediment remobilisation (-30.6 ± 0.2 ‰).

Additionally, increased disordered kaolinite (i.e., lower H_1/H_4 ratio, Figure 4.7) during the peak of the flood event hints towards the remobilisation of kaolinite from deeper horizons during the flood event compared to surface kaolinite present at baseflow. No difference in kaolinite order was observed between the particles upstream and downstream from the mining flat, which also supports a similar source of kaolinite for the entire watershed.

During event-2, much lower variations in the organic and the mineral phases were observed during the rain event. This is due to the fact that the SSC at baseflow is already much higher (45 ± 6 $mg.L^{-1}$) than for event-1 (18 ± 6 $mg.L^{-1}$) and as a result, the different indicators (FTIR and multi-elemental data) display values that are similar to the values at peak SSC in event-1. The variations that occurred during the flood event are thus “hidden” by the strong SSC concentration at baseflow.

4.1.4.5.2. Hypotheses for the source of suspended particles

Ultimately, an inter- and intra-flood event temporal variation of river suspended particle composition was observed. However, the tracers studied here do not highlight any significant differences in sources between upstream and downstream of the mining flat. This suggests either that i) there is no significant difference in the particle origin between the upstream and the downstream of the mining flats or ii) these techniques are not sufficiently discriminant between the different sources. Assuming that our method provides sufficient sources discrimination, the results suggest that the excess SPM export observed downstream of the mining flats compared to upstream might originate primarily from river bank erosion. This hypothesis is supported by the superposition of the organic and mineral phase variations with the decomposed hydrograph from section 4.1.4.3. Here, it appears that the particle influx coincides with groundwater influx, rather than with overland flow (Figure 4.7), also indicating the erosion of the river bank sediment (transitory/transient sediment deposits) as the main source of particles to the river rather than the forest or mine soil erosion. In line with these results, additional measurements on soil and sediment erodibility also showed that mine topsoils display an increased

critical shear stress and decreased erosion rates compared to river bank sediments (Figure S 4.11). The mine soils appear to be well stabilised, at least one year after restoration, and less prone to erosion as observed in chapter 3. It is also consistent with a specific feature that was observed on the downstream sedigrams. A sharp narrow SSC peak preceding the "main" SSC peak was identified at the onset of 70 % of flood events downstream, while it was never observed upstream. This behaviour thus appears to be characteristic of the mining flats, resulting in 8-shaped hystereses ("anticlockwise-clockwise") or in clockwise hystereses depending on the size of the first peak compared to the main SSC peak (Figure S 4.2). This type of hysteresis hints towards proximal sources of particles from the watershed outlet (e.g., from the river bed or banks). In order to understand what could influence the presence or absence of this pre-peak, different hydrological indicators have been calculated. The total volume of the previous event ($p=0.00343$, Wilcoxon), as well as the slope of the rising limb of the hydrographs ($p=0.0357$, Wilcoxon) are significantly higher in events that display this pre-peak behaviour. This suggests that the particles remobilized during this first SSC peak likely originate from riverbed sediment remobilisation, with the previous event "charging" the bed with bank collapses or with the settling of suspended particles at the end of the falling limb of hydrographs.

Finally, all of the aspects discussed above support the riverbank erosion and bed sediment remobilisation as the main source of particles to the river rather than mining flat topsoil erosion.

4.1.4.6. Hydro-sedimentary budget: SPM and carbon exports from a restored gold mined flat

Suspended particles and carbon exports due to the mining flats were assessed in more detail so as to understand the impact of the mining flats on particle and carbon storage and export. Assuming that if the gold mining flats were absent, the specific river particle export would be equal downstream compared to upstream, the theoretical downstream particle export "without a mining flat" was calculated and compared to the measured fluxes, in order to estimate the excess particle export generated by the gold mining flat. The gold-mining flat generated an excess 7.2 t of particle export during event-1, and 2.0 t during event-2. Although two isolated events are not sufficient to assess for temporal trends in the particle export, this decrease in particle export might in part be due to the restoration of the gold mining flats, as observed in section 4.1.4.1.

Seasonal specific particulate exports downstream of the restored goldmining flats are lower in the dry season (0.89 $g.s^{-1}.km^{-2}$, range: 0.07 – 18.2 $g.s^{-1}.km^{-2}$) than in the rainy season (4.86 $g.s^{-1}.km^{-2}$, range: 0.84 – 43.4 $g.s.km^{-2}$) and similar to exports observed in a comparable sized gold-mined flat in French Guiana [0.34 and 2.24 $g.s^{-1}.km^{-2}$ in the dry and rainy season respectively, (Hellal et al. 2020)]. At the scale of the Maroni River, which is substantially gold-mined and of which the Awa river is a tributary, particulate exports averaged over the year are in the lower range of what was observed here, and

amount to 0.83 ± 0.6 $g.s^{-1}.km^{-2}$ (Rousseau et al. 2019). Hence, even after restoration, goldmines are thus still a significant source of particles to the watersheds.

Concerning carbon exports, total organic carbon (TOC) concentrations were calculated as the sum of dissolved (DOC) and particulate (POC) organic carbon. Organic carbon exports could be estimated thanks i) to the relationship between FTIR data tPC3 and POC concentrations, and ii) to DOC measurements in the two events. DOC (4.1 ± 1.7 $mg.L^{-1}$) and POC (3.2 ± 0.9 $mg.L^{-1}$) concentrations were similar upstream and downstream of the mining flat. POC represented 38 ± 9 % of TOC both upstream and downstream of the mining site at event-1, but was higher (56 ± 14 %) during event-2, which can be explained by higher particle concentrations observed in the second event. These proportions are in the higher range of those previously observed in the Amazon and the Maroni rivers, where POC concentrations usually represented only 10 to 40 % of the total organic carbon (Moreira-Turcq et al. 2003, Gallay et al. 2017). Specific carbon export was higher downstream than upstream of the mining flats during event-1 (4-fold) leading to an excess 670 kg C export. During event-2 however, carbon exports were identical upstream and downstream of the mining flat.

Reported to the discharge and SSC chronicle downstream of the mining flats, TOC exports amount to 206 t $C.yr^{-1}$ for a watershed size of 21 km^2. This corresponds to a specific TOC export of 9.8 t $C.yr^{-1}.km^{-2}$, in the range of what was observed on the Maroni watershed, of which the Awa river is part [7.5 t $C.yr^{-1}.km^{-2}$, (Gallay et al. 2017)], and also similar to the carbon exports of the sum of tributaries of the Amazon [8.9 t $C.yr^{-1}.km^{-2}$, (Moreira-Turcq et al. 2003)]. Finally, over the recorded timescale (April-December, including the MaR, the dry season, and the beginning of the miR), 66 % of carbon exports occurred during the MaR season, and 23 % in the dry season, with POC representing 45 % of the total carbon exports.

4.1.5. Conclusion

Gold mining flats are still a source for particulate matter export, even one year after the restoration work has been performed. This excess in particulate export does not appear to originate from the erosion of the restored gold mining flat, as topsoils are rapidly stabilized by herbaceous plants. Thus, the major source of the particulate export appears to originate from riverbank erosion and riverbed sediment remobilisation. Therefore, specific attention should be given to riverbank stabilisation during the restoration process. During this study (1 year), the excess particle export downstream from the mining flats appeared to decrease, but did not allow for a clear determination of longer temporal trends.

In addition, illegal ASGM operations upstream from the mining flats add variability to the data and the assessment of the influence of the legal gold mine can be affected or masked by these illegal operations. Illegal ASGM operations are not controllable and are thus a parameter which needs to be taken into account when attempting to perform a hydrosedimentary budget of a legal gold mining flat.

The following article in this chapter will aim to determine whether the observed increase in particle export induces an increase in metal(loid) export, and to what extent.

4.1.6. Supplementary Information

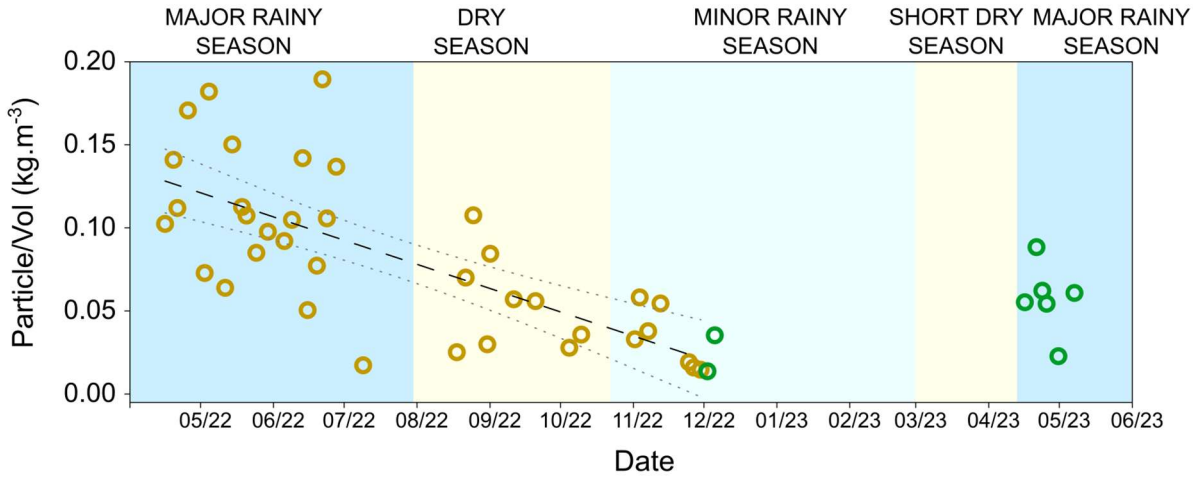

Figure S 4.1 *Temporal evolution of particle export normalised by water export upstream (green) and downstream (orange) of the mining flat.The regression for the downstream site is significant (p<0.0001), whereas the regression for the upstream site is not depicted because it was not significant (p=0.11).*

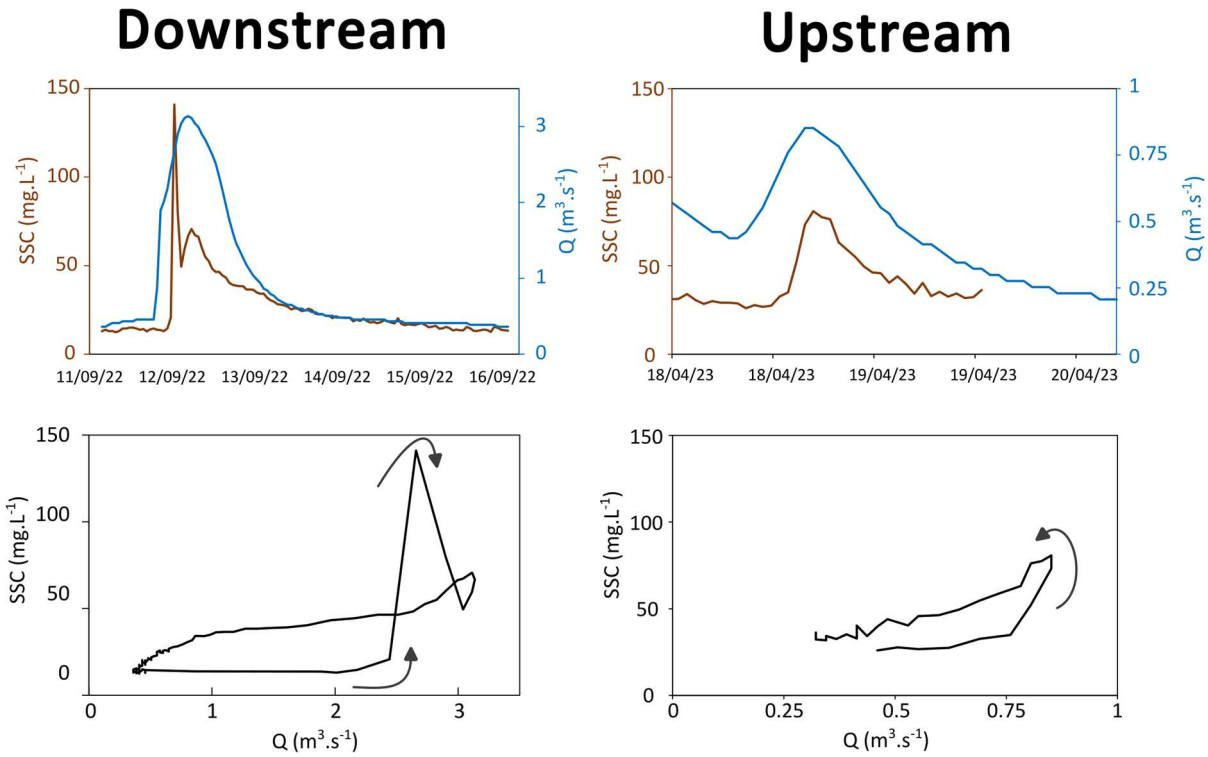

Figure S 4.2. *Turbidity-Discharge relationships Upstream and Downstream of the mining flat.*

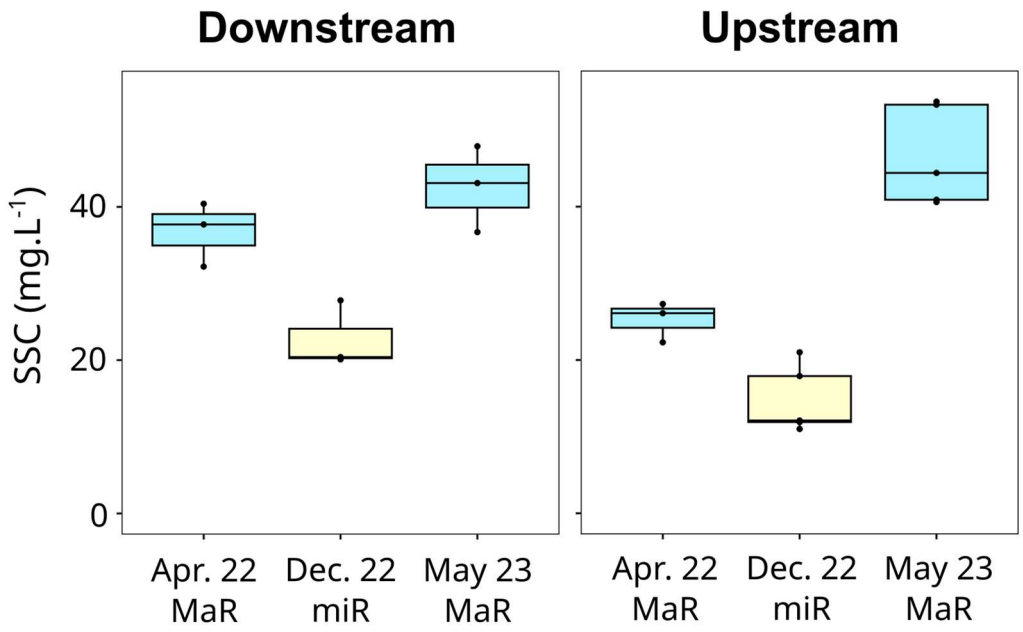

Figure S 4.3. *SSC concentrations at baseflow for the different sampling campaigns spanning different seasons (Major rainy season = MaR, minor rainy season = miR).*

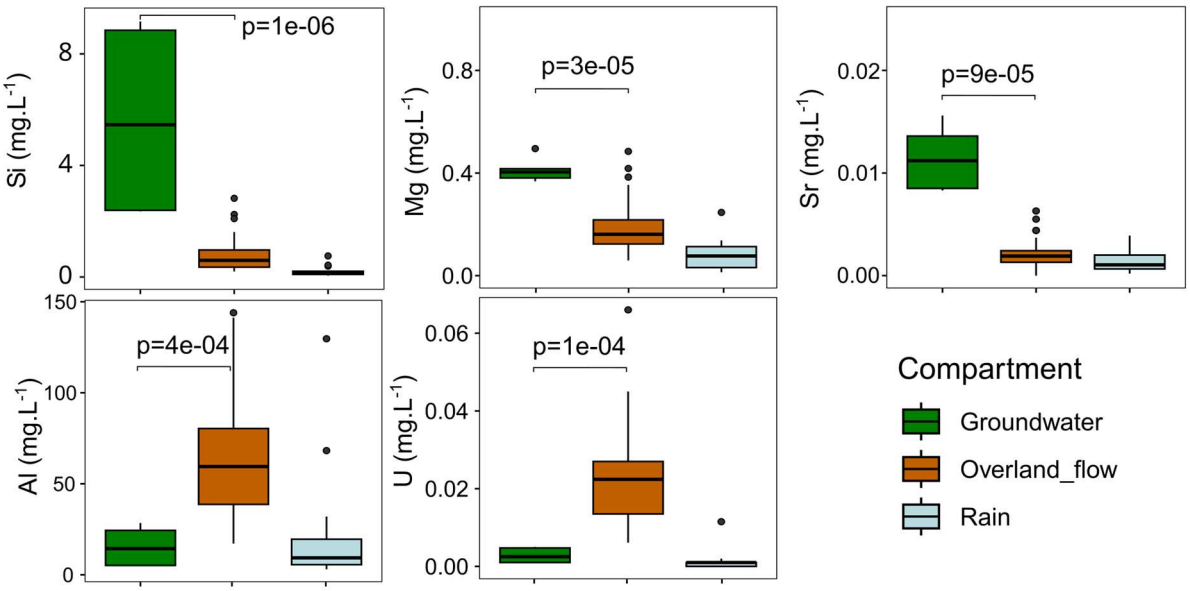

Figure S 4.4. *Endmembers (groundwater and overland flow) for the elements selected in the end-member mixing analysis. Concentrations in the rain samples are shown for comparison with overland flow values.*

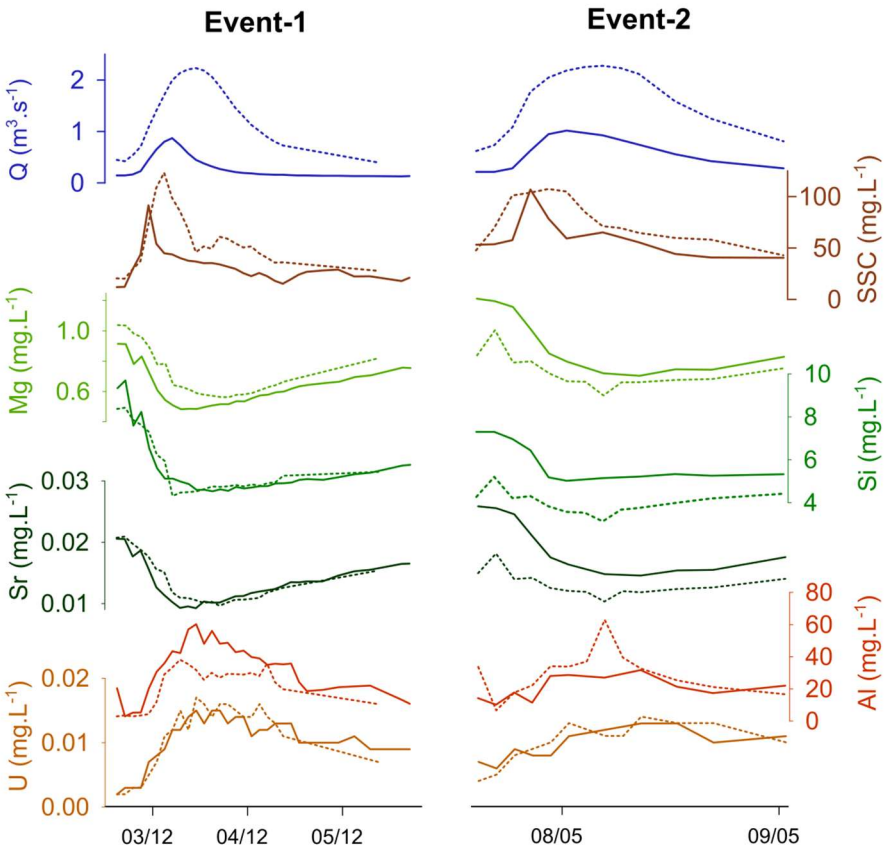

Figure S 4.5. *Evolution of discharge, SSC, and selected tracers (Mg, Si, Sr, Al, U) in the filtered fraction during a flood event, for two events upstream and downstream of the mining flat.*

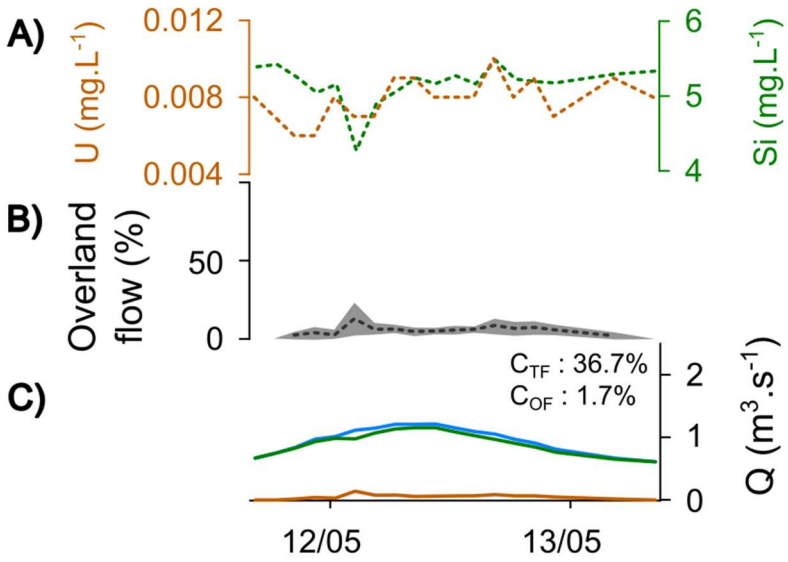

Figure S 4.6. *A) Concentrations of U (orange) and Si (green); B) Contribution of overland flow and C) reconstruction of the groundwater (green), overland flow (brown) to the total (blue) discharge during a rain event, downstream of the mining flat. The total flow coefficient (C_{TF}) and overland flow coefficient (C_{OF}) are inserted in the bottom pannel.*

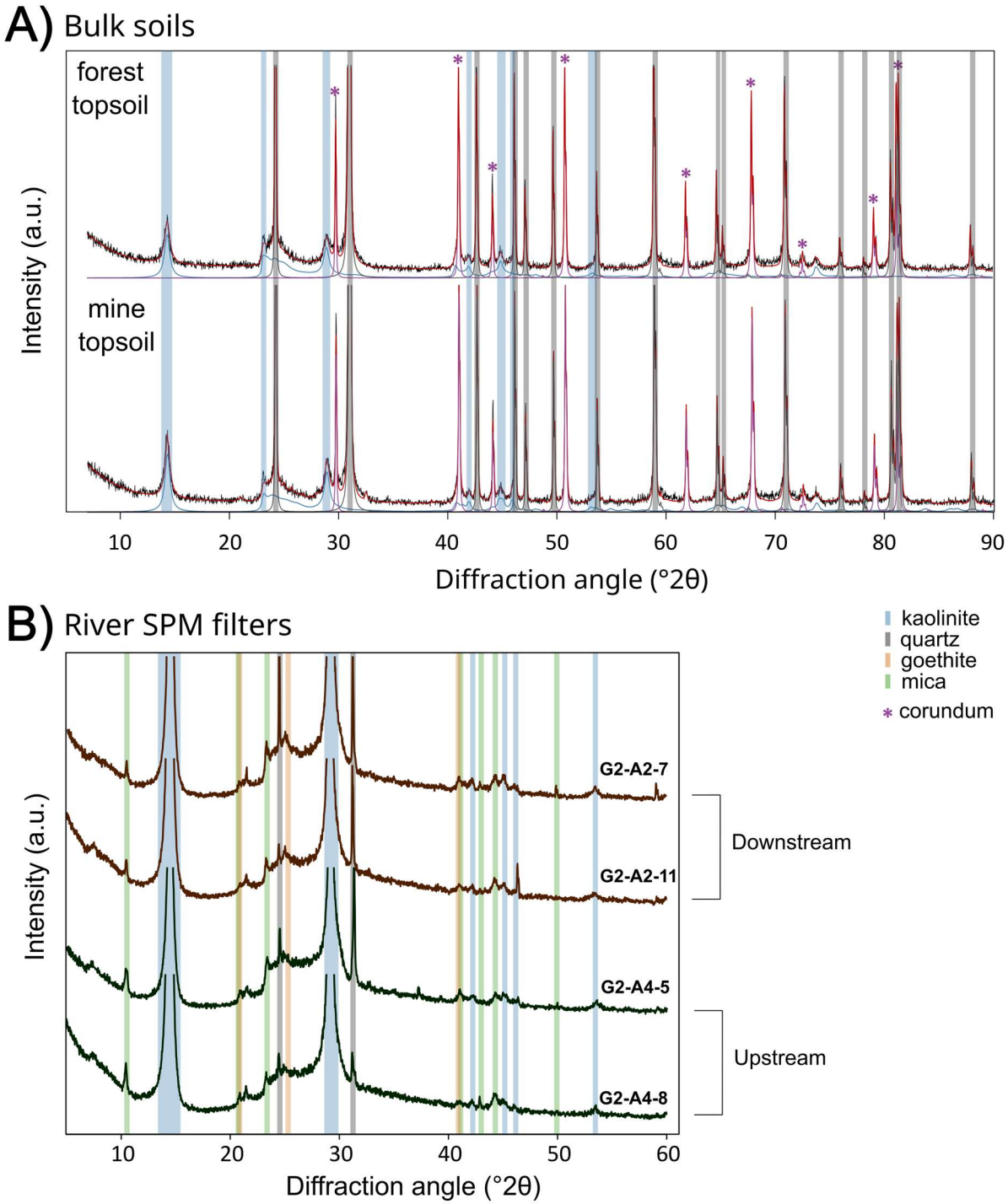

Figure S 4.7. *Example of an XRD diffractograms of A) bulk soils, and B) river particulate matter. The main mineral peaks are highlighted : kaolinite (blue), quartz (grey), goethite (orange) and mica (green). The refined standard corundum added to bulk soils to quantify the amorphous phase is shown with purple stars.*

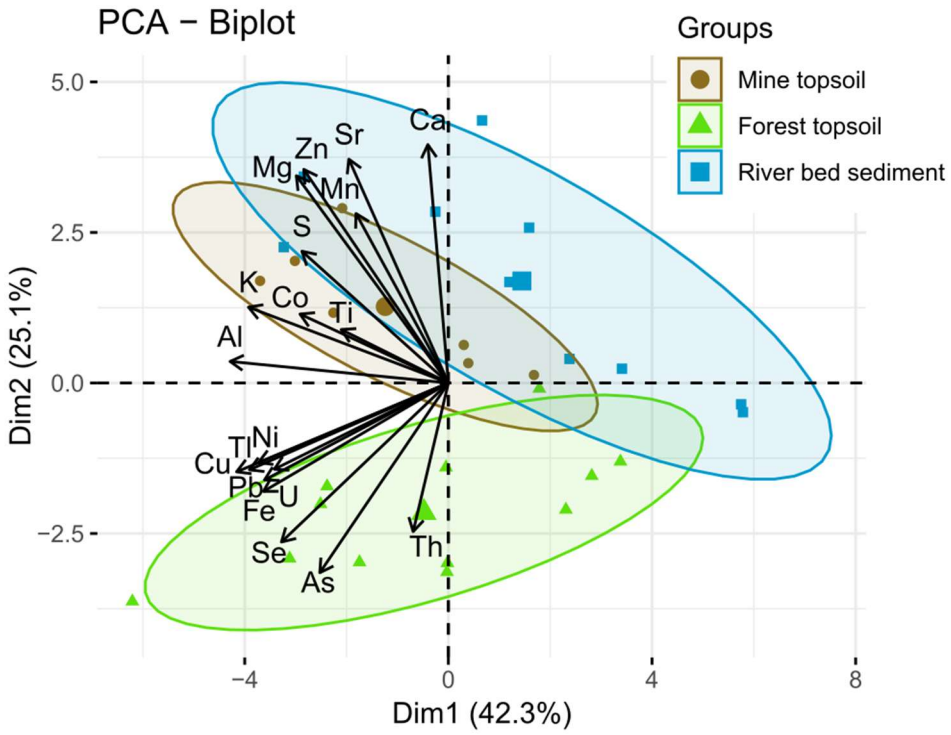

Figure S 4.8. *PCA of multielemental data in the potential particle sources.*

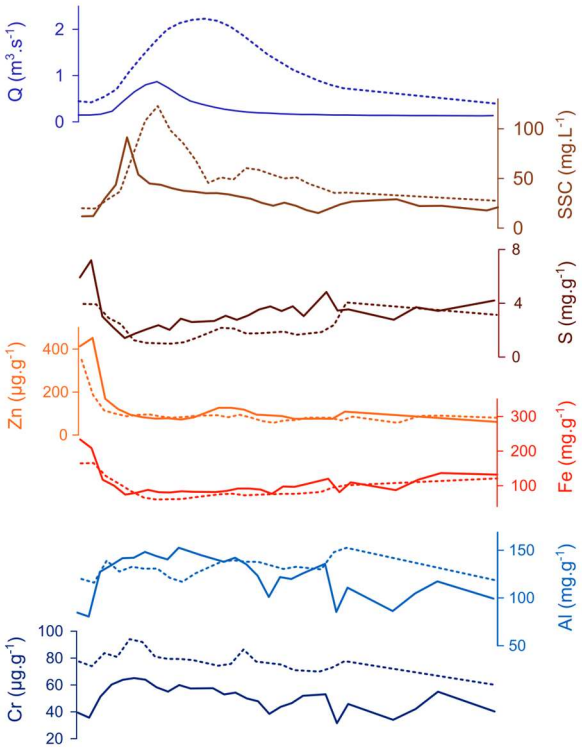

Figure S 4.9. *Evolution of discharge, SPM, and selected tracers in the particulate fraction during a rain event (event-1).*

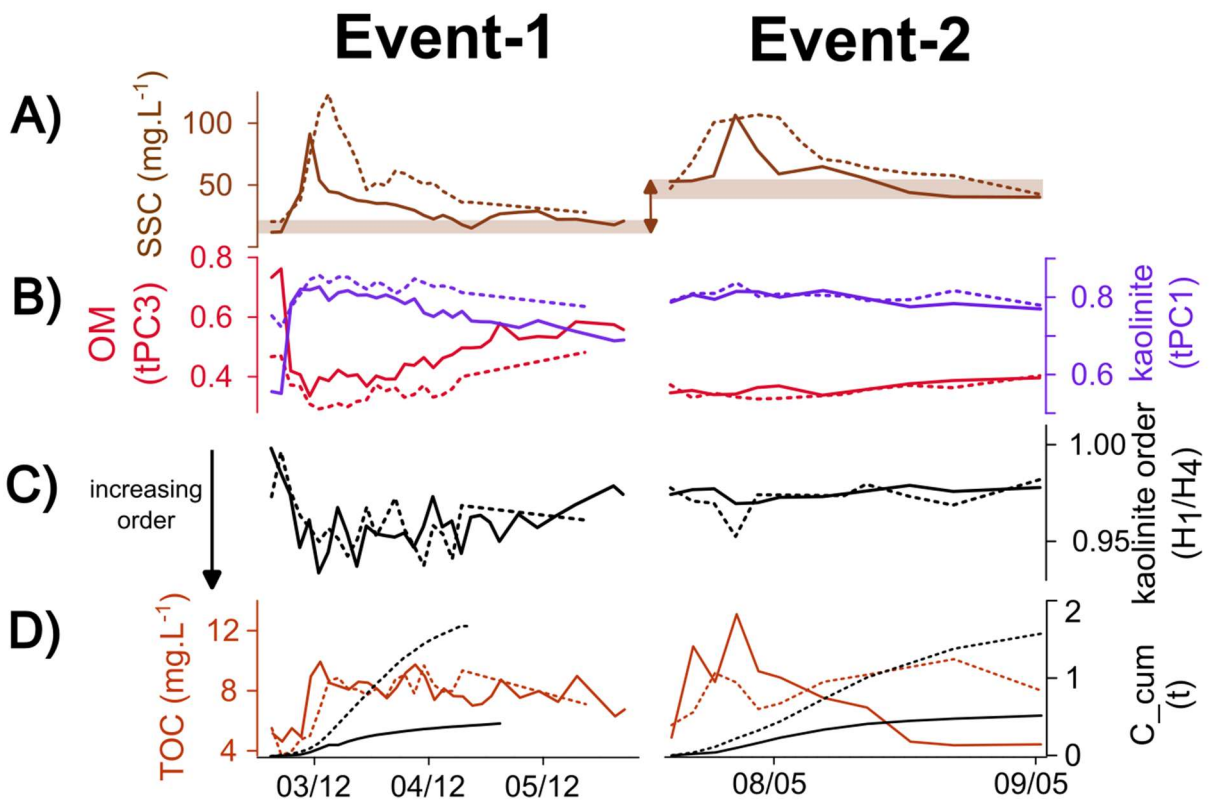

Figure S 4.10. *Evolution of A) SSC, B) selected tracers C) kaolinite order (H_1/H_4), and D) total organic carbon (TOC, red) and cumulated carbon (black) in the particulate fraction during a rain event, during two events upstream (dashed line) and downstream (dotted line) of the mining flat.*

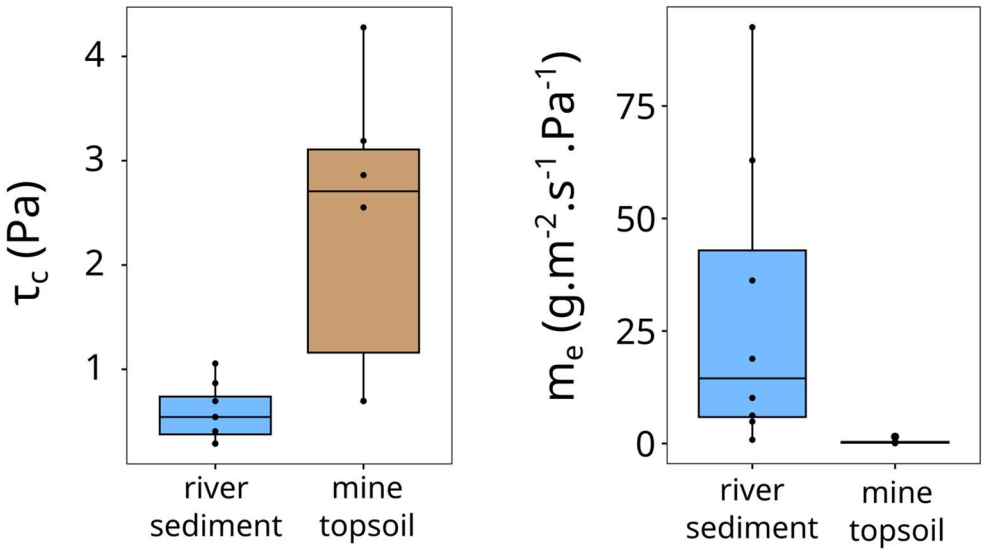

Figure S 4.11. *Critical shear stress (τ_c), and erosion rate (m_e) of river banks sediments (blue) and mine topsoil (brown).*

4.2. Article III –

Distribution and exports of mercury and metal(loid)s in a restored gold-mined Amazonian watershed (French Guiana)

Naomi NITSCHKE[a,b,,e], David AMOUROUX[b], Jennifer HARRIS[c], Emmanuel TESSIER[b], Océane ASENSIO[b], Sylvain CAMPILLO[a], and Stéphane GUÉDRON[a]

[a] Univ. Grenoble Alpes, Univ. Savoie Mont Blanc, CNRS, IRD, IFSTTAR, ISTerre, 38000 Grenoble, France

[b] Université de Pau et des Pays de l'Adour, CNRS, IPREM, Institut des Sciences Analytiques et de Physico-chimie pour l'Environnement et les Matériaux, Pau, France

[c] BRGM, F-45071 Orléans, France

*email : naomi.nitschke@univ-grenoble-alpes.fr

Acknowledgments

We thank Océane Asensio (UPPA-Tech, IPREM UPPA/CNRS) and Cindy Arnoldi (LECA, UGA) for analytical support in the laboratory. Thanks to Akram Ali (SAS GAIA) for field assistance.

4.2.1. Abstract

Artisanal and small-scale gold mining (ASGM) involves downstream river system contamination through the use of liquid Hg for gold amalgamation but also leads to the release of geogenic metal(loid)s because of soil reworking and particle export. The restoration of legal gold mines is mandatory in French Guiana and involves landscaping and tree-replanting. In order to unravel the distribution of metal(loid)s (mercury, lead, arsenic), the speciation of mercury (total mercury, methylmercury and dissolved gaseous mercury), and the impact of the restored gold mining flat on their exports, high resolution discrete sampling of flood events during different seasons was coupled to hourly suspended sediment concentration and discharge data upstream and downstream of a gold-mined river. Particulate total mercury was shown to originate from mining flat erosion while particulate methylmercury (MeHg) concentrations decreased during the flood event, due to dilution with MeHg-poor particles emanating from river bed sediment remobilisation. The restored gold-mining flat induced a 2-fold increase in metal(loid) export 8 months after restoration, but no significant increase 12 months after restoration. The estimation of annual metal(loid) export shows that the major rainy season is responsible for the majority of export for all metal(loid)s (66 ± 6 %). However, the metal(loid)s which displayed equal proportions in the particulate and dissolved fraction (MeHg and As) show slightly more evenly distributed exports, with lower percentages during the MaR season and higher during the dry seasons compared to the metal(loid)s that are primarily associated to the particulate phase (THg and Pb). These results show that the metal(loid) export from gold-mining practices and restoration can be followed and that seasonality plays an important role in these exports in the Amazon region, emphasising the need for continuous measurement rather than discrete sampling campaigns.

Keywords Gold mining; Amazon; mine restoration; hydrology; mercury; arsenic; lead

Highlights

- The export of metal(loid)s was studied in a restored gold-mined river.
- The restored mining flat is still a source of metal(loid)s, one year after landscaping.
- The majority of metal(loid)s are exported during the rainy season.
- Metal(loid) fluxes can be estimated by continuous discharge and turbidity monitoring.

4.2.2. Introduction

Artisanal and small-scale gold mining (ASGM) is widespread and increasing across the Amazon basin, partly fuelled by high gold prices and unemployment (Lobo et al. 2016, Veit and Quijano Vallejos 2020). As it involves deforestation and extensive topsoil destructuration in order to access the gold bearing layer, ASGM is associated to a strong environmental impact including increased topsoil erosion leading to river siltation (de Lucia Lobo et al. 2019), which can be harmful for downstream ecosystems (Mol and Ouboter 2004, Tudesque et al. 2012). This increase in particle export also leads to the remobilisation of geogenic metal(loid)s associated to these particles, like mercury (Hg), which is naturally accumulated in the soils from atmospheric Hg taken up by the vegetation over millions of years (Guédron et al. 2006, Fostier et al. 2015). In addition, although banned by the Minamata Convention on Hg, informal miners use liquid elemental (i.e., anthropogenic Hg) for gold amalgamation, and the burning of amalgams leads to the contamination of the surrounding environment. Once released to the river, the methylation of Hg, and its bioaccumulation and biomagnification in food webs, results in high Hg concentrations in piscivorous fish, which poses a health threat for the indigenous communities whose diet mostly relies on fish consumption (Maury-Brachet et al. 2006, Pignoux et al. 2019).

In addition to Hg contamination, an alarming distribution of lead (Pb) poisoning was recently discovered in children in French Guiana (Rimbaud et al. 2017), and in artisanal gold miners (Douine et al. 2025). In response, the regional health agency created a working group focused on understanding the potential contamination sources and mechanisms for heavy metals and metalloids in French Guiana (“Stratégie Métaux Lourds”, StraMeLo). Recently, high blood Pb levels observed in French Guiana riverine population were proposed to be linked to manioc consumption, and possibly to exposure to lead from bullets used in hunting activities (Andrieu et al. 2020, Maurice et al. 2021). Although little is known about arsenic (As) levels in French Guiana, hotspots in groundwater have been measured elsewhere in the Amazon basin, in Peru and Brazil, where levels were found to exceed the WHO guidelines in a significant number of floodplain lakes and groundwater (de Meyer et al. 2017). Background levels concerning Pb and As are still scarce in soils and water systems in the Amazon region and more specifically in French Guiana.

To limit the environmental impact of ASGM in French Guiana, the government imposes legal mines to work in a closed circuit separated from the adjacent river and let the washed particles settle in mining ponds before releasing the water back to the river. In addition, after the exploitation phase, the gold mining site is landscaped, the mining ponds are filled again, and the site is replanted (Marquis 2015). These laws and regulations in place in F. Guiana should be applicable to the large majority of gold mines in South America and elsewhere, which operate in similar ecosystems, and initiatives to

implement such regulations are taking place in a number of countries supported by organisations like planetGOLD (planetGOLD 2023). Yet, the majority of studies have focused on the impact of active mines on particle and metal(loid) export of active gold mines, with for example a 10-fold increase in particulate Hg export observed during a simulated set up and exploitation phase in a small watershed in French Guiana (Grimaldi et al. 2015). Although the majority of exports are expected during the exploitation phase, it is also important to understand the fate of gold mining sites once extractive operations are over, and restorations has been performed. In this context, it is essential to document the extent of particle and metal(loid) exports as well as the timescale in the reduction of such export. Additionally, baseline concentrations and speciation of critical metals and metalloids are crucial to decipher the effective impact of gold mining (legal and illegal) on downstream environments and watersheds. More studies and robust databases are thus necessary to provide accurate environmental risk assessments to help environmental policy implementation and avoid contradictory or controversial conclusions.

To fulfil this knowledge gap, this study builds on the previous finding that the gold mining site is still a source of particulate export one year after restoration, originating from river bank erosion and riverbed sediment remobilisation (article 4.1), and provides a complete dataset of background levels of metal(loid)s (Hg, Pb, As) to assess the impact of a restored gold mining flat on these metal(loid) fluxes at the watershed scale. To do so, the concentrations of Hg, Pb and As as well as Hg speciation were followed at high resolution in the particulate and filtered fraction upstream and downstream of a mining flat during flood events located in different seasons in order to provide an estimate of yearly metal(loid) exports from the restored mining flat.

4.2.3. Materials and Methods

Study area. French Guiana (87,500 km²) is part of the Guiana shield located in the north-eastern region of South America between Brazil and Surinam (2-6°N and 51°30'-54°30'W). It experiences an equatorial humid climate with average annual rainfall of around 4000 mm and 96 % of the territory is covered by tropical rainforest. The study was conducted on the Awa site, an alluvial gold mine (54°20'34"W, 4°19'8"N) of the mining company SAS GAIA (Figure S 4.12). The Awa River is part of the Maroni river watershed, the largest river of French Guiana (66 814 km²), which is densely gold-mined (Gallay et al. 2018) and has a long history of gold mining dating back to the 1900s (Jébrak et al. 2021). The Awa watershed area is 32 km². Alluvial gold mining exploitation was performed below a riverbed, to extract gold from gravel deposits resulting from the weathering of auriferous quartz veins (Thomassin et al. 2017). These downslope valleys typically consist of sandy hydromorphic soils exhibiting reducing conditions due to the presence of water flowing slowly (Guédron et al. 2009). The mineralogy of these soils is dominated by quartz and kaolinite, with some goethite. Exploitation and production was conducted on the site from downstream to upstream between September 2017 and April 2021. The first restoration operations were conducted between May and July 2019, and full restoration was then performed between May 2021 and August 2022. Restoration consists in filling the mining ponds with the gravel and clay removed during exploitation, performing landscaping respecting as much as possible initial soil stratification, then replanting trees grown in on-site nurseries, following a grid with three-meter intervals. It has to be noted that illegal gold mining had been taking place upstream of this site before and during the study.

Three sampling campaigns were conducted over one year (from 2022 to 2023): G1 (04/22), G2 (12/22) and G3 (05/23), on two different sites on the gold-mined river (Figure S 4.12). The first being located at the entrance, upstream of the mining site and the second one further down on the mining site. These two sites are termed "upstream" and "downstream", respectively. The downstream site could not be located further downstream, at the exit from the gold mine, due to accessibility and practical issues.

Monitoring and sampling. A monitoring station was installed at both the upstream and downstream sites, measuring water level using a pressure level sensor (OTT-PLS) and turbidity (Hydrolab HL4) at a 1h time step. Discharge and suspended sediment concentration were calculated as described in section 4.1.3. For long-term trends, hourly rain data was recovered from a national meteorological station in Grand-Santi, 7 km away from the mining site. For specific events, a rain gauge located in the central part of the mining flat was used to quantify wet deposition for major rainfall events and the total duration of the rainfall events was also noted.

An automated water sampler (ISCO 3700, Teledyne) was installed at each station and programmed to collect river samples every two hours (or longer during water level recession) during the 3 sampling campaigns.

Overland flow water and eroded particle samples were collected as described in section 3.1.3. Briefly, erosion plots were installed to recover the overland flow water and eroded material from a defined area during a rain event. Each plot consisted of wood panels (2 m × 2 m, 4 m²) inserted 10 cm into the soil and extending 15 cm above the soil, and was connected to an 80L bucket installed at the lowest point of the slope and buried in the soil. After each rain event, the total volume of water was measured, and a 250 mL aliquot of the suspension was sampled in an FEP bottle, to measure suspended solid concentration (SSC), and major and trace elements in the filtered and particulate fractions.

All river and overland flow water samples were collected in pre-cleaned vials following ultra-clean technique protocols (Stoichev et al. 2006, Bravo et al. 2018). A 250 mL aliquot of the river water sample was filtered on an acid-washed and pre-weighed 0.45µm PVDF filter, which was air-dried in a laminar flow hood 48h and weighed to determine the SSC (Stoichev et al. 2016). The filtrate was collected in trace grade falcon tubes acidified to ultrapure HNO_3 2 % for multi-elemental analyses, and to ultrapure HCl 0.2 % for mercury analyses.

In addition to the river samples, soil samples on and around the mining site were sampled using a manual auger. These soils were homogenised, freeze-dried, sieved at 2mm and ground to a powder <63 µm for further analysis. Freeze-dried soils were sieved at 1.25 mm for grain size measurements. Particle size distributions (PSD) were measured with a laser diffraction sizer (Malver, Mastersizer 2000) following the protocol of Grangeon et al. (2012). For each sample, the proportions of clay (<2µm), silt (2-63µm) and sand (>63µm) fractions were extracted.

Chemical analyses. Multi-elemental analysis of major and trace elements was performed by inductively coupled plasma-atomic emission spectrometry (ICP-AES) (Agilent, Varian 720-ES) and by inductively coupled plasma mass spectrometry (ICP-MS) (Agilent 7900 coupled to an ESI PrepFast IC module), respectively. The filtered water samples were analysed directly and the filter and soil sample solutions were analysed after microwave (ultra-WAVE, Milestone) assisted acid digestion (HNO_3) at 220 °C and 110 bar. The accuracy of the measurements was evaluated based on the analysis of certified reference materials (NIST 1944 and IAEA-405 for solid samples and SLRS-6 for water samples).

Dissolved Organic Carbon. Filtered and acidified water samples were analysed in pre-burnt borosilicate vials using a TOC-VCSN analyzer from Shimadzu associated to an ASI-V autosampler as described in (Tisserand et al. 2024).

Mercury analyses. Hg speciation in filtered water and on suspended particulate matter (SPM) collected on filter samples was analysed following established methods using species specific isotope dilution

analysis by gas chromatography – inductively coupled plasma mass spectrometry [SS-ID GC-ICP-MS (Monperrus et al. 2005, Monperrus et al. 2008, Sharif et al. 2014, Cavalheiro et al. 2016)].

Dissolved gaseous mercury (DGM) represents all volatile Hg species (i.e. elemental Hg^0 and dimethylmercury DMHg) in water samples, and was collected manually in PTFE bottles leaving no headspace. The samples were then purged within ~0.5 h after sampling and collected on a gold-coated sand trap. DGM was analyzed by thermodesorption (600 °C) and CV-AFS detection using a Tekran® (Model 2500). The system was calibrated by gas phase Hg (Hg^0) as described elsewhere (Duval et al. 2023, Kleindienst et al. 2023).

It is assumed here that the majority of DGM is lost through degassing during the sampling and filtering procedure of THg analysis. Indeed, considering the atmospheric Hg concentrations (7.5 ± 6.3 $ng.m^{-3}$, average concentration over one year measured by passive sampling on the mining as described in chapter 5), and Henry's law constant of 0.36 at 28°C (Andersson et al. 2008), the DGM concentrations expected at equilibrium would be around 4 $ng.m^{-3}$, which corresponds to 10 – 50 % of the initial DGM still present after equilibration. The "real" THg is thus assumed to be the sum of iHg, MeHg and DGM. However, because DGM is not the predominant Hg species in river water (< 10 %), the THg value does not vary significantly if DGM is taken into account or not (p=0.71, Wilcoxon).

Statistical analyses. All statistical analyses were performed using R. The Student's t-test was performed when the data was normally distributed and the variances between the two studied groups were equal. When this was not the case, the Wilcoxon test was performed. Regressions are shown only if the p-value is below 0.01.

4.2.4. Results and Discussion

4.2.4.1. Metal(loid) levels, speciation and partitionning in river water

4.2.4.1.1. Distribution of the selected metal(loid)s: As, Pb and Hg compounds

Concentration levels averaged at 1.2 ± 0.7 ng.L^{-1}, 0.04 ± 0.01 µg.L^{-1}, and 0.015 ± 0.015 µg.L^{-1} in the filtered fraction and at 16 ± 8 ng.L^{-1}, 0.08 ± 0.05 µg.L^{-1}, and 0.6 ± 0.3 µg.L^{-1} in the particulate fraction for mercury, arsenic and lead respectively (Figure 4.8). No significant differences in concentrations were observed between upstream and downstream of the mining flat nor between the sampling seasons (minor rainy season in December versus major rainy season in May).

Both Hg and Pb were present primarily in the particulate fraction (91 ± 9 % and 96 ± 5 % respectively, Figure S 4.13A), whereas MeHg displayed a similar distribution to As, with almost equal proportions present in the particulate and filtered fractions (56 ± 10 % and 64 ± 17 % respectively).

Both filtered and particulate Hg concentrations were in the range of widely documented values observed in French Guiana (Roulet and Grimaldi 2001, Guédron et al. 2006, Goix et al. 2019, Hellal et al. 2020). Total (filtered and particulate) lead concentrations were low (0.62 ± 0.36 µg.L^{-1}), and in the range of values observed in two anthropised watersheds in Brazil [0.5 – 1.1 µg.L^{-1}, (Salomão et al. 2018)], but largely below concentrations observed in a gold-mine river basin in Ecuador [34 – 9200 µg.L^{-1} (Tarras-Wahlberg et al. 2001)]. Similarly, total arsenic concentrations observed in the Awa river were 0.12 ± 0.06 µg.L^{-1}. This is comparable to values observed in the northern tributaries of the Amazon river (0.1 – 0.3 µg.L^{-1}), but lower than the tributaries draining the Andes (0.9 – 19.5 µg.L^{-1}) which are known to be a significant source of dissolved and particulate As to the Amazon (Scarpelli 2005). The As distribution in the main Amazon tributaries (51 ± 25 %) followed a similar partitioning as observed on the Awa river. Although extensive data is lacking in the Amazon concerning As and Pb in water, the metal(loid)s investigated here displayed concentrations closer to estimated background levels than concentrations in contaminated mining areas (Moulatlet et al. 2023). These results are in line with the similar concentrations observed upstream and downstream of the mining flat and point towards a limited remobilisation of geogenic metal(loid)s downstream of the restored post-mining flat.

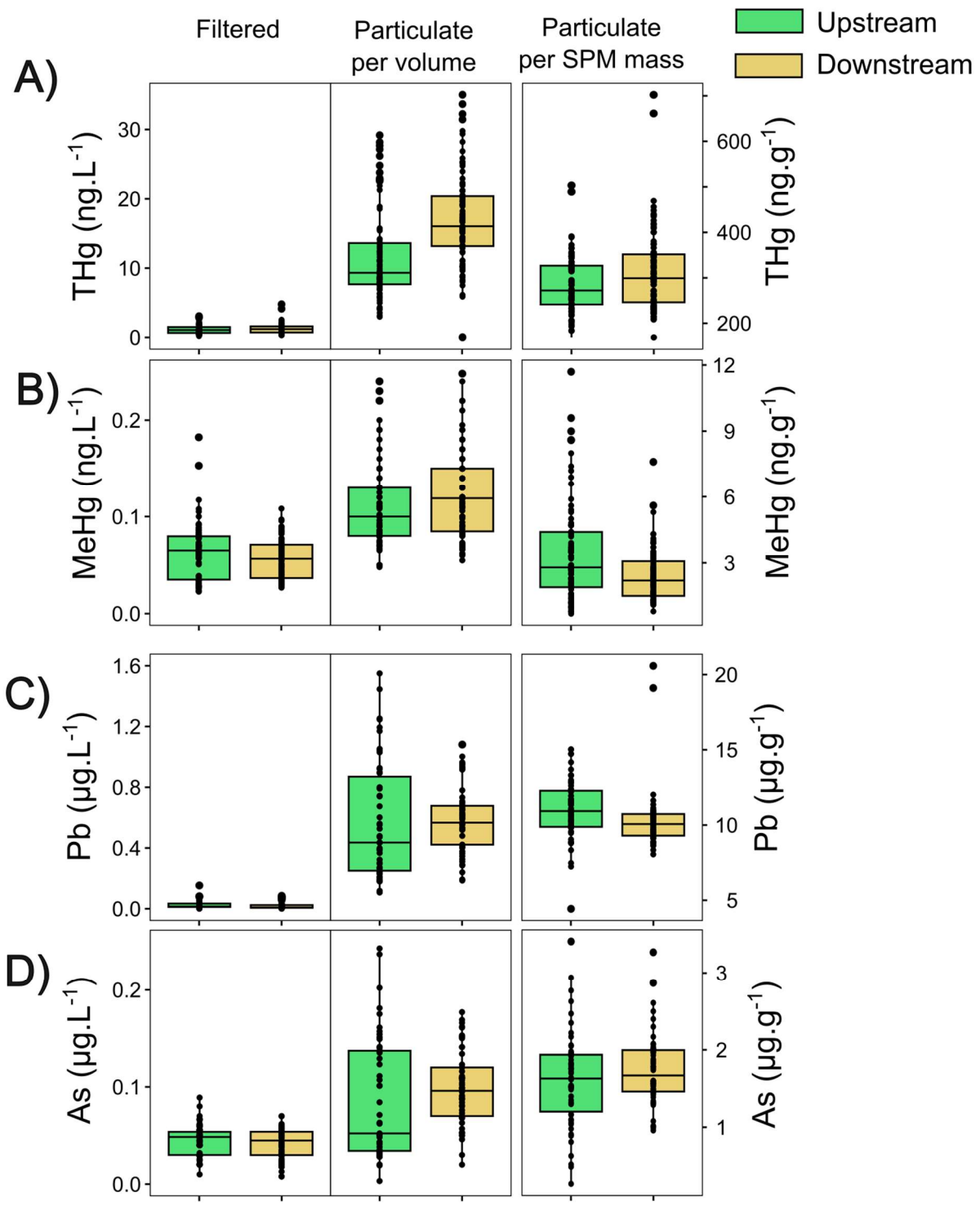

Figure 4.8. *Concentration in the filtered and particulate (per volume and per SPM mass) fractions of A) THg, B) MeHg, C) Pb and D) As in river water downstream (yellow) and upstream (green) of the mining flat pooled from sampling campaigns G2-G3.*

4.2.4.1.2. Mercury speciation

Mercury speciation, i.e., methylmercury and inorganic mercury in the particulate and filtered fractions and dissolved gaseous mercury (DGM) for a limited number of samples, provides different distribution and partitioning than for total concentrations. Filtered MeHg concentrations are 70 ± 20 pg.L^{-1}, and

particulate MeHg amounts to 90 ± 30 pg.L^{-1}. Although displaying flood-dependent variations, MeHg accounts globally for 7 ± 4 % (median: 6 %, range: 1 – 22 %) in the filtered fraction, and only 0.7 ± 0.4 % (median: 0.6 %, range: 0.2 – 2.7 %) in the particulate fraction. DGM levels are 48 ± 30 pg.L^{-1}, significantly lower than concentrations observed in a heavily gold mined river in French Guiana at 570 pg.L^{-1} (Amouroux et al. 1999), and in the range of river water of the rio Negro [12 – 96 pg.L^{-1}, (Jardim et al. 2009)], and an artificial lake in French Guiana [46 – 96 pg.L^{-1} (Muresan et al. 2007)]. DGM accounts for 5 ± 4 % of filtered THg (median: 4 %, range : 0.6 – 15 %).

As a result, the distribution of the metal(loid)s is highly element- and speciation-dependent, with THg and Pb mainly associated to the particulate phase, while MeHg and As appear more evenly distributed between the particulate and filtered fractions. Additionally, the presence of the mining flat does not impact the concentrations of any metal(loid) within the gold-mined river.

4.2.4.2. Main carrier phases and sources of Hg and its compounds, Pb, and As

In the filtered fraction, $MeHg_F$, Pb_F and As_F displayed very stable concentrations during flood events and between seasons and sites. THg_F was weakly correlated to Al, DOC and Fe (Table S 4.1), similarly to what was observed in the Amazon river (Maia et al. 2009), emphasizing the role of organic matter (OM) and iron in the transport and speciation of mercury (Ravichandran 2004, Chadwick et al. 2006). Additionally, filtered THg concentrations were also negatively correlated to elements defined as originating from groundwater (Mg, Si, Sr) and positively correlated to elements originating from overland flow (Al, U) (article 4.1), which is a first hint towards Hg_F input in the river arising from overland flow.

THg in the particulate fraction displayed very little variations in concentrations (in ng.g^{-1}), and no significant correlation was observed to any geochemical indicator, supporting kaolinite as the main carrier for THg. In contrast, MeHg was strongly correlated to particulate organic carbon (POC, $R^2 = 0.58$, $p < 0.0001$), as observed in a small catchment in French Guiana (Guédron et al. 2011), and also to particulate iron and sulfur. This points towards OM being the major carrier phase for MeHg in the particulate fraction. Concerning particulate Pb and As, few correlations were observed, mostly to refractory elements (Ti, Rb, Tl, Th, U, Table S 4.1B). Consistently, Pb in lateritic duricrusts in Brazil was found primarily associated to residual minerals (Iza et al. 2018).

Organic matter is thus an important carrier phases for Hg, with differences between the filtered and particulate phase, as THg was found to be related to DOC while MeHg was associated to POC.

4.2.4.3. Metal(loid)s concentrations, partitioning and exports during two flood events

In order to unravel the behaviour and sources of the different metal(loid)s during a flood event, as well as the impact of the mining flat on metal(loid) export, filtered and particulate concentrations were followed during two flood events recorded simultaneously upstream and downstream of the mining flat. The first event ("event-1") was recorded in December 2022 after the dry season, at the beginning of the minor rainy season (miR, i.e., from December to February), and 8 months after landscaping, whereas the second event ("event-2") was monitored in May 2023 during the major rainy season (MaR, i.e.; from April to July), and 13 months after landscaping. Both events were relatively similar in rainfall amounts (44 and 34 mm, respectively), and intensities (0.55 and 0.68 $mm.min^{-1}$, respectively). The concentrations of filtered Pb and As were stable and independent of water discharge (Figure S 4.14), while THg_F concentrations increased with increasing discharge. When superimposing the THg_F concentrations with the decomposed hydrograph of overland flow and groundwater input (article 4.1), the variation of THg during event-1 coincides with the arrival of overland flow (Figure 4.10). This is in agreement with higher THg concentrations observed in wet deposition (3.0 ± 1.2 $ng.L^{-1}$) and throughfall (6.3 ± 2.2 $ng.L^{-1}$), than in porewater (0.9 ± 0.4 $ng.L^{-1}$) on the mining site. $MeHg_F$ concentrations however stayed stable during the flood event, and as a result, the percentage of MeHg in the filtered fraction decreased during the flood event, and was anticorrelated to discharge.

Although only a limited amount of data is available on DGM during the rain events, it appears that DGM concentrations rise during the flood events (Figure 4.9). However, because the rise is DGM is less extensive than the rise in THg, during event-1, the proportion of DGM on THg appears highest at baseflow before the flood event, and decreases during the peak of the flood. This proportion of DGM does not increase again right after the flood event because THg concentrations stay high, while DGM falls sharply after the discharge peak. A better time resolution of DGM during the flood event would be needed to unravel its dynamics with respect to discharge.

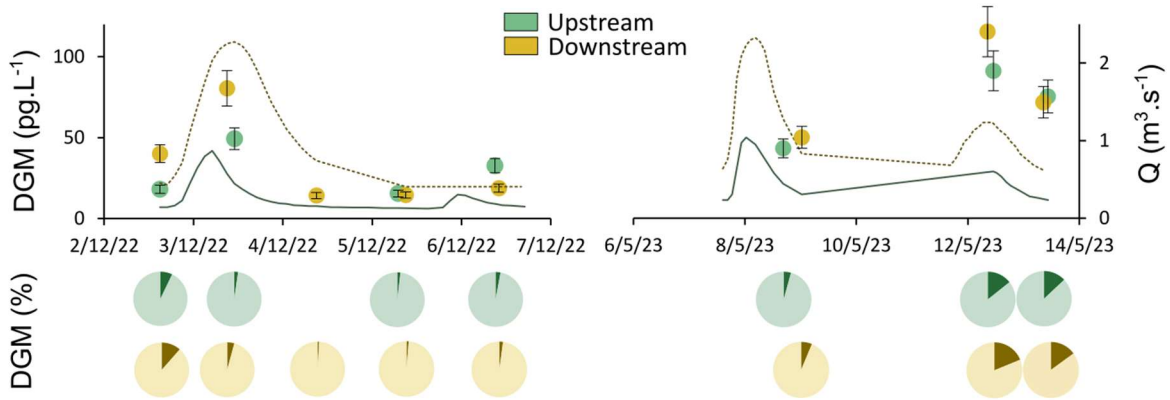

Figure 4.9. *Dissolved Gaseous Mercury (DGM, circles) and discharge (Q, lines) during flood events upstream (green) and downstream (yellow) of the mining flat.*

In the particulate fraction, Pb and As concentrations were stable and consistently followed SPM concentrations. THg_P concentrations increased slightly during the flood event, in line with the arrival of overland flow, suggesting the erosion of the forest and mining topsoils as the predominant input of THg_P. Particulate MeHg on the other hand decreased significantly during the flood event, following the behaviour of POC, indicating a dilution by MeHg-poor particles input during the flood event, most likely originating from river bed and riverbank sediment remobilisation.

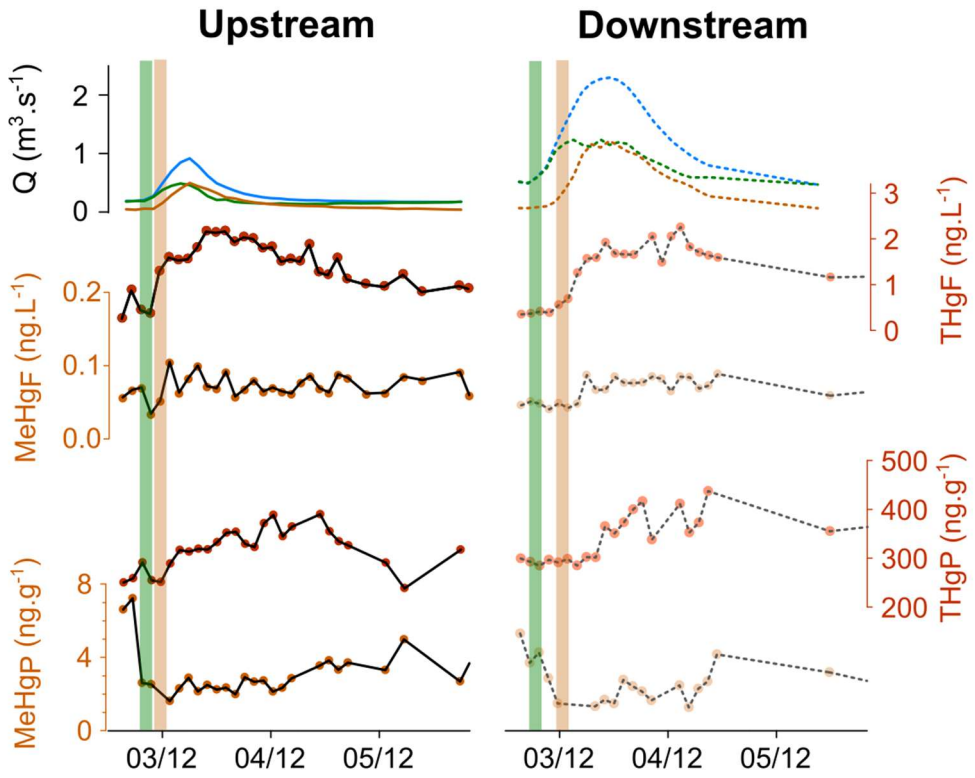

Figure 4.10. *Superposition of the decomposed hydrograph (overland flow, brown; groundwater, green; total, blue from article 4.1) with concentrations of filtered THg and MeHg, as well as particulate THg and MeHg. The arrival of groundwater and overland flow are depicted as green and brown bands respectively.*

Table 4.3. *Mass budget of THg, MeHg, Pb and As upstream and downstream of the gold-mined flats for two events recorded during different seasons (event-1 in the minor rainy season, miR, and event-2 in the major rainy season, MaR).*

	Event-1 (miR)				**Event-2 (MaR)**			
	Upstream	filtered (%)	Downstream	filtered (%)	Upstream	filtered (%)	Downstream	filtered (%)
Vol_cumul (mm)	4.5		7.3		5.4		4.6	
SSC/area (kg.km^{-2})	252		594		381		476	
THg/area (mg.km^{-2})	113	(12%)	254	(7%)	204	(6%)	234	(6%)
MeHg/area (mg.km^{-2})	1.3	(48%)	2.2	(40%)	1.7	(51%)	1.7	(41%)
Pb/area (g.km^{-2})	3.4		7.0		7.9	(3%)	5.8	(2%)
As/area (g.km^{-2})	0.6	(49%)	1.7	(31%)	1.9	(28%)	1.3	(19%)

The mass budget of metal(loid) export during the two events shows that during event-1 in the minor rainy season (miR), the gold mining flat contributes to an increase in specific flux of all metal(loid)s by approximately 2-fold. During event-2 however, the differences are much less pronounced and specific export even appears lower downstream of the mining flat compared to upstream for Pb and As. This might be explained by slightly higher particulate concentrations of Pb (and to a lesser extent As) upstream of the mining flat during the second event, as well as an increased specific particle export even though the rainfall amounts were similar and somewhat lower during the second event. Such increase in upstream particle export is likely due to illegal gold mining upstream of the legal gold mining site, thereby potentially masking the impact of the mining flat during the second event (article 4.1).

The input of particulate THg originates from mining flat erosion while the particulate MeHg in the river is diluted by MeHg-poor particles, mainly originating from river bed sediment remobilisation. Additionally, the restored mining flat is a source of metal(loid)s (Hg, Pb, As) 8 months, but less so one year after restoration.

4.2.4.4. Hg, Pb, and As seasonal fluxes at watershed level

Using the data from the discrete sampling presented above, relations are observed between i) filtered metal(loid) fluxes and discharge and ii) particulate concentrations and SSC upstream and downstream of the mining flat (Figure S 4.15). These relations are identical in the MaR and miR, as well as between sampling years in the MaR, and between upstream and downstream of the mining flat providing a reliable estimate for metal(loid) fluxes during the chronicle of Q and SSC (Figure 4.11).

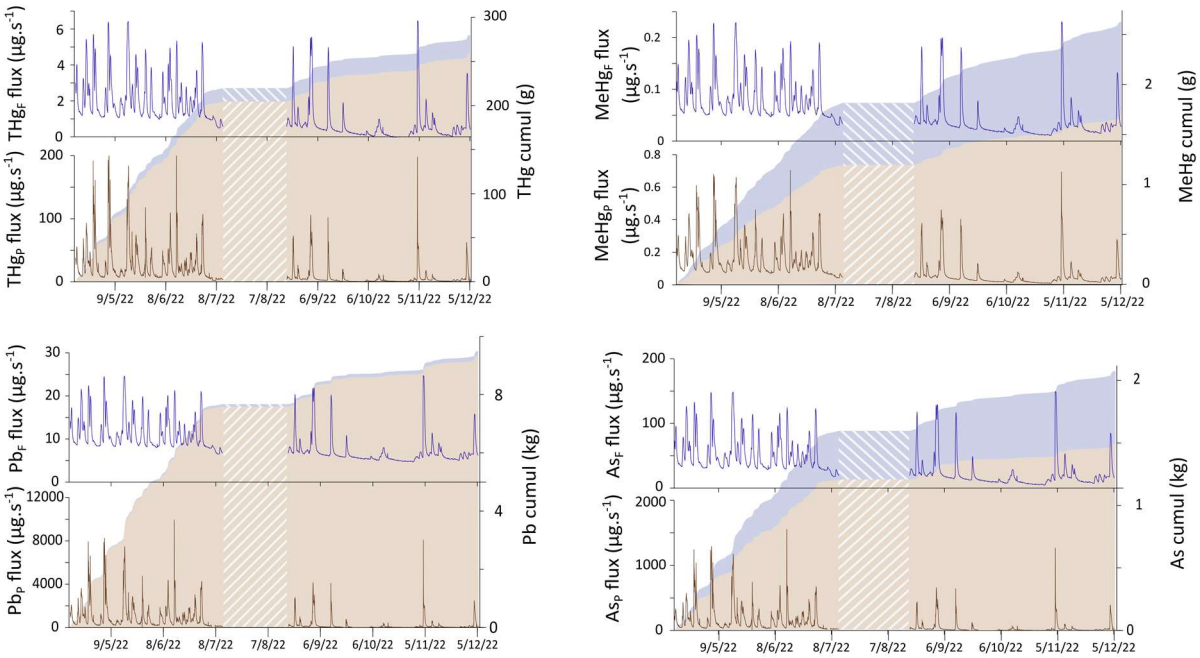

Figure 4.11. *Estimation of seasonal filtered (blue lines and areas) and particulate (brown lines and areas) metal(loid)s exports downstream of the mining flat. Dashed areas represent a period during which discharge data was lacking.*

Albeit some gaps in the discharge and SSC data, all three major seasons were sampled in the chronicle presented, allowing for comparison of seasonal exports of the different metal(loid)s. The strongest export occurs, predictably, during the major rainy season, with a specific daily export 3-5 times more important compared to the dry season (Table 2A). The average daily fluxes for the different seasons allow to extrapolate metal(loid) exports during the period where data is lacking and calculate an annual export of the different metal(loid)s over a full hydrological year (Table 2B). The MaR accounts for the majority (66 ± 6 %) of annual metal(loid) exports, with 12 ± 2 % and 19 ± 3 % exported during the dry season and the miR respectively, and only 4 % during the small rainy season ("March little summer").

Table 4.4. *Specific seasonal fluxes of THg, MeHg, Pb and As, and estimation of the cumulated downstream export for each season, as well as the percentage of total export between brackets. miR: minor rainy season, MaR: major rainy season, DS: dry season, SSC: suspended solid concentrations.*

Season	A) Average daily exports							
	Event number	Rainfall	flow vol	SSC	THg	MeHg	Pb	As
	n	mm .day^{-1}	mm .day^{-1}	kg.km^{-2} .day^{-1}	mg.km^{-2} .day^{-1}	mg.km^{-2} .day^{-1}	g.km^{-2} .day^{-1}	g.km^{-2} .day^{-1}
MaR	20	12	6	424	119	0.983	4.154	0.866
DS	11	3	2	65	25	0.338	0.746	0.198
miR	7	3	2	69	31	0.397	0.932	0.240
	B) Extrapolation to seasonal exports							
	Duration (days)				mg.km^{-2}	mg.km^{-2}	g.km^{-2}	g.km^{-2}
MaR	122				14525 (68%)	120 (57%)	507 (71%)	106 (66%)
DS	92				2275 (11%)	31 (15%)	69 (10%)	18 (11%)
miR	120				3673 (17%)	48 (23%)	112 (16%)	29 (18%)
March summer	30				742 (3%)	10 (5%)	22 (3%)	6 (4%)
Yearly export	365				21215	209	710	159

Averaged over the whole year, THg fluxes amount to 0.67 µg.s^{-1}.km^{-2}, which is comparable to exports observed on a similar sized (56 km²) gold-mined watershed in French Guiana at 0.70 µg.s^{-1}.km^{-2} (Hellal et al. 2020), but also to a pristine small (1 km²) watershed (Guédron et al. 2011).

The average daily As exports are 0.4 g.day^{-1}.km^{-2}, which are much lower than exports from a watershed impacted by gold mining in Brazil at 8-87 g.day^{-1}.km^{-2} (Bidone et al. 2018). However the soils in these watersheds display high contents of arsenopyrite, which explains these exacerbated exports. When comparing to an adjacent pristine watershed, the daily As exports (0.05 – 1 g.day^{-1}.km^{-2}) are much closer to what was observed in this study.

Dissolved (<0.2 µm) Pb export at the Solimões river, part of the Amazon watershed, amounts to 0.2 g.km^{-2}.yr^{-1} (Viers et al. 2005), which is significantly lower than the filtered (<0.45 µm) Pb fluxes observed here (14 g.km^{-2}.yr^{-1}).

The data showed that the majority of export of all metal(loid)s occurs during the major rainy season, however the metal(loid)s which displayed equal proportions in the particulate and dissolved fraction (MeHg and As) show slightly more evenly distributed exports, with lower percentages during the MaR season and higher during the dry seasons compared to the metal(loid)s that are primarily associated to the particulate phase (THg and Pb).

The calibration of the river system by discrete metal(loid) concentrations measurements as well as discharge and SSC during several flood events and during different seasons allowed for a subsequent estimation of the exports of these cont metal(loid)s aminants all year round. This is especially beneficial in tropical remote sites like gold-mining sites, which can only be accessed through expensive helicopter flights or time-consuming boat rides. Turbidity and discharge probes are robust, can be deployed in the long term, and need only minimal care. Although they cannot totally replace discrete monitoring, such use of probes can provide a cost-effective alternative to river monitoring in remote places. They could be used by the gold mining companies themselves, or by the state agencies supervising their work to monitor the impact of the mining site on metal(loid) fluxes.

4.2.5. Conclusion

The gold mining site appears to be a significant source of metal(loid)s 8 months after restoration, with a 2-fold increased specific export for all metal(loid)s downstream of the restored gold-mining flat.

The calibration of the river system to estimate annual metal(loid) fluxes showed that Hg and Pb, which were primarily associated to the particulate fraction (> 90 %), were mainly exported during the major rainy season (MaR, 70 % of annual exports), while for MeHg and As, which were more evenly distributed between the filtered and particulate fractions (56 and 64 % respectively), the MaR season accounted for slightly lower annual exports (57-66 %).

However, the upscaling towards larger watersheds might prove challenging as an increasing number and diversity of particle and metal(loid) sources might add complexity to the relations observed here. Additionally, no discrete sampling was performed during either extreme flood event, nor the dry season, where the observed relations may not hold true. Concerning the data during the dry seasons, this should not strongly affect the annual export assessment, as these seasons were estimated to represent only around 15 % of annual exports.

4.2.6. Supplementary Information

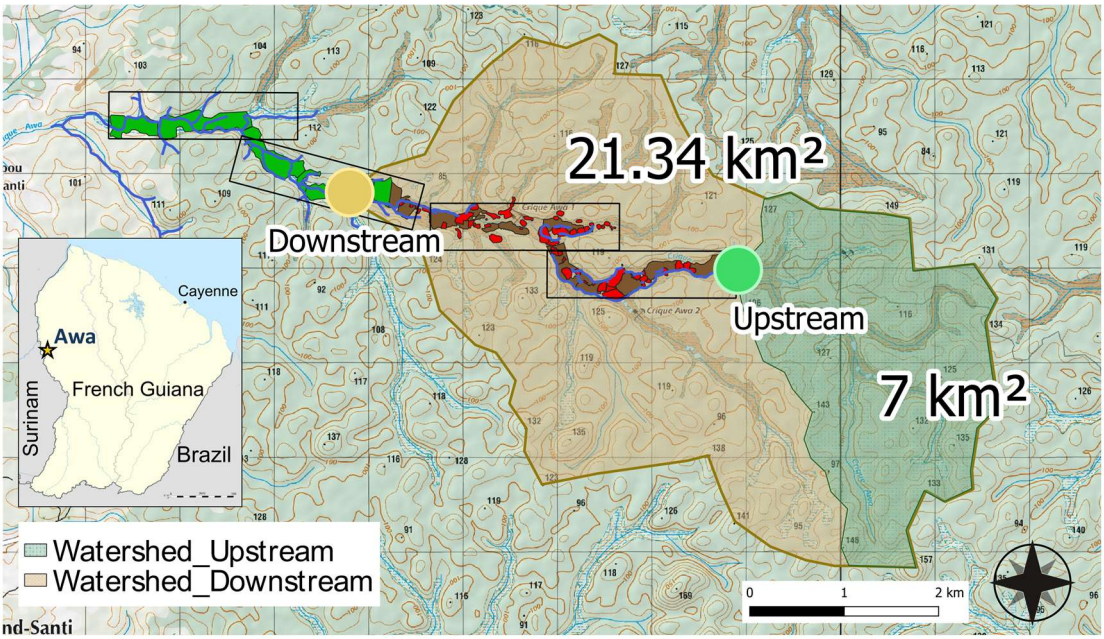

Figure S 4.12. *Study site with the two monitoring and sampling stations on the Awa gold-mined river.*

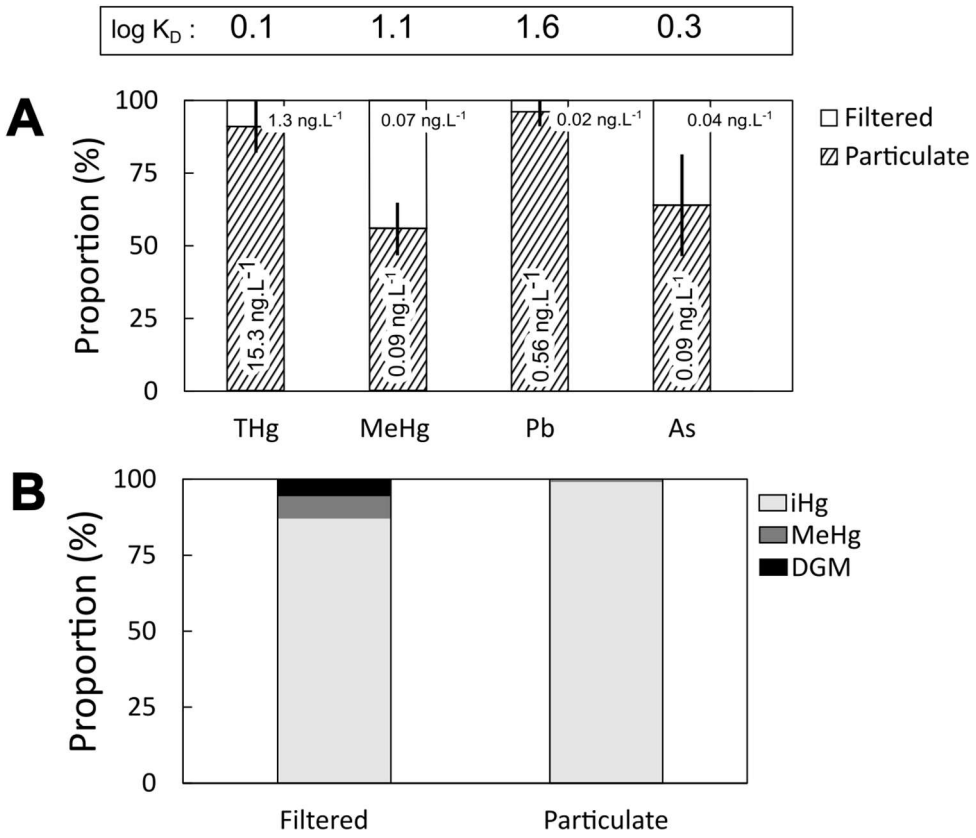

Figure S 4.13. *A) Proportion of the different metal(loid)s (THg, MeHg, Pb, As) present in the particulate and the filtered fraction in the river water, and B) proportion of Hg as iHg, MeHg and dissolved gaseous mercury (DGM) in the filtered and as iHg and MeHg in the particulate fractions.*

Table S 4.1. *Pearson's correlation matrix of particulate THg, MeHg, Pb and As concentrations in A) the filtered and B) the particulate fractions, versus major and trace element concentrations and FTIR data (kaolinite, quartz and particulate organic carbon - POC).*

A	Filtered fraction																							
	Ca	Fe	K	Mg	Mn	Na	S	Si	Sr	Zn	Al	Ti	Cr	Co	Ni	Cu	Zn	Se	Rb	Sr	Mo	Tl	Th	U	DOC
THg	-0.58	0.39	0.40	-0.57	-0.23	-0.54	0.50	-0.45	-0.60	-0.09	0.58	0.26	0.33	0.04	-0.03	0.54	-0.02	0.33	0.24	-0.59	0.36	0.31	0.62	0.55	0.50
MeHg	-0.02	0.56	0.33	-0.05	-0.01	0.10	0.15	-0.16	-0.03	0.03	0.11	0.08	0.06	-0.02	-0.06	0.16	0.07	0.02	0.15	-0.07	0.15	0.06	0.25	0.33	0.31
Pb	-0.02	0.28	0.12	-0.12	-0.11	-0.03	0.16	0.03	-0.04	0.31	0.29	0.44	0.05	0.00	-0.06	0.17	0.22	-0.10	0.24	-0.01	0.14	0.23	0.19	0.09	0.06
As	-0.21	0.20	0.37	-0.21	-0.17	-0.10	0.25	-0.06	-0.18	-0.07	0.20	0.09	0.25	-0.06	-0.08	0.14	-0.07	0.04	0.27	-0.17	0.15	0.25	0.32	0.29	0.21

B	Particulate fraction																							
	kaol	qtz	POC	Al	Ca	Fe	K	Mg	Mn	Na	S	Ti	Cr	Co	Ni	Cu	Zn	Se	Rb	Sr	Sn	Tl	Th	U
THg	-0.05	-0.05	0.11	-0.08	0.23	0.23	-0.06	0.33	0.06	0.11	0.23	-0.11	0.11	0.03	0.07	0.25	-0.14	0.13	-0.09	0.13	-0.09	-0.01	-0.18	-0.14
MeHg	-0.75	-0.42	0.80	-0.67	0.50	0.74	-0.55	0.32	0.38	0.74	0.87	-0.39	-0.46	-0.01	-0.25	-0.10	0.31	0.43	-0.63	0.57	-0.19	-0.48	-0.53	-0.60
Pb	0.25	0.21	-0.30	0.70	0.21	-0.01	0.34	0.27	-0.06	-0.06	-0.21	0.52	0.43	0.27	0.27	0.14	0.21	0.05	0.63	0.18	0.54	0.66	0.84	0.81
As	0.17	0.26	-0.21	0.44	0.16	-0.07	0.25	0.11	-0.12	-0.09	-0.17	0.36	0.46	0.08	0.12	0.11	0.00	-0.09	0.42	0.00	0.28	0.43	0.53	0.48

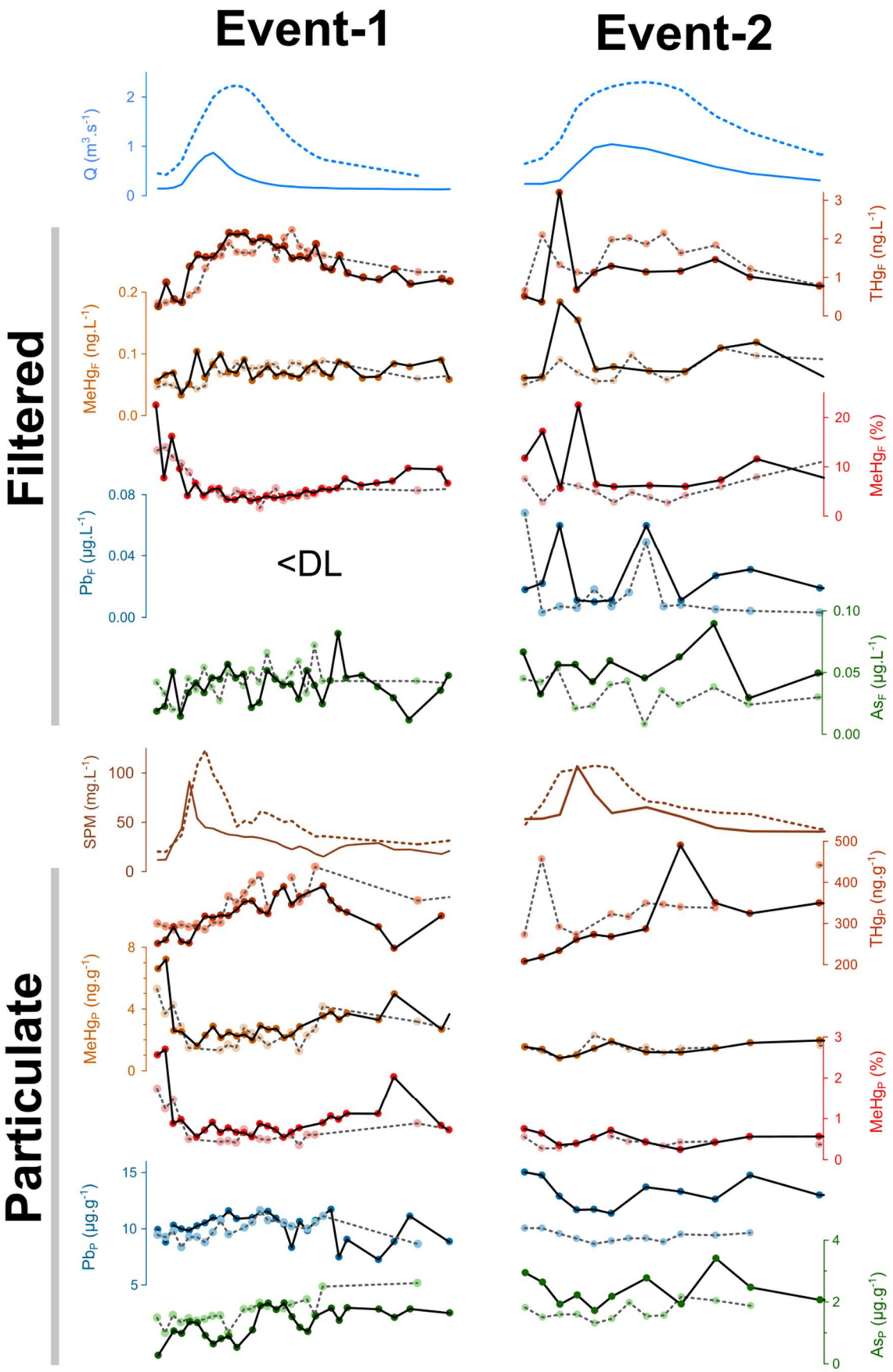

Figure S 4.14. *concentration variations of metal(loid)s (THg, MeHg, Pb, As) in the filtered and the particulate fraction for two flood events.*

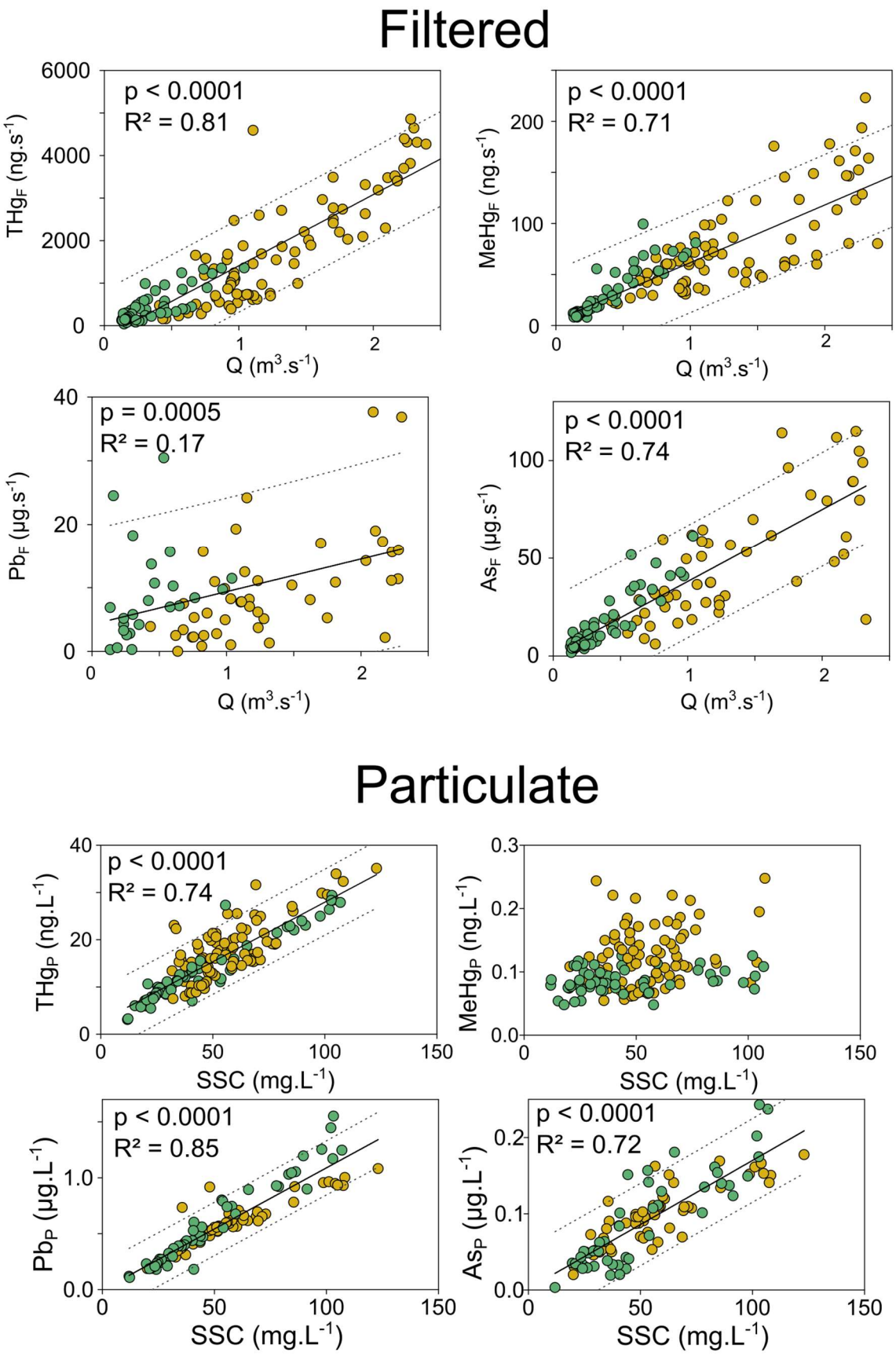

Figure S 4.15. *Relations of metal(loid)s in the dissolved and particulate fractions versus discharge (Q) and suspended sediment concentration (SSC) respectively.*

Chapter 5.

Distribution and transfers of mercury species in a “mine ecosystem”

Introduction

The two previous chapters assessed the impact of gold mining on the exports of particles and metal(loids) at different scales. The distribution of Hg, Pb and As was assessed in eroded material, overland flow, and river water. The following chapter focuses on Hg, and on its distribution in different compartments on and around the mining site. Indeed, Hg is particular compared to Pb and As, as it is used by illegal miners to extract the gold, leading to a contamination with anthropogenic Hg, in addition to the exports of "natural" Hg.

This chapter aims at:

- Providing an understanding concerning the stocks of Hg on the mining site;
- Assessing the impact of illegal gold mining on Hg concentrations and speciation, and tracing anthropogenic Hg compared to natural Hg;
- Comparing this Hg distribution in different "mining environments"

To do so, Hg concentrations, speciation and isotopic composition were determined in various ecological compartments on and around two legal mining sites with different amounts or types of past illegal mining practices.

5.1. Article IV –

Legal and illegal gold mining in the Amazon: distribution of mercury species and isotopes in a "mine ecosystem"

Naomi NITSCHKE*[a,b,c,e], Emmanuel TESSIER[b], Stéphane GUÉDRON[a], Océane ASENSIO[b] , Oumou KABA[b], Jennifer HARRIS[c], Arnauld HEURET[d] , Stéphane TARAVELLA[e], and David AMOUROUX*[b]

[a] Univ. Grenoble Alpes, Univ. Savoie Mont Blanc, CNRS, IRD, IFSTTAR, ISTerre, 38000 Grenoble, France

[b] Université de Pau et des Pays de l'Adour, CNRS, IPREM, Institut des Sciences Analytiques et de Physico-chimie pour l'Environnement et les Matériaux, Pau, France

[c] BRGM, F-45071 Orléans, France

[d] Université de Guyane, Cayenne, France

[e] Gaïa SAS, Cayenne, France

*email : naomi.nitschke@univ-grenoble-alpes.fr

david.amouroux@univ-pau.fr

Acknowledgments

We thank Océane Asensio (UPPA-Tech, IPREM UPPA/CNRS) and Camille Serbutoviez-Verville (ISTerre, UGA) for analytical support in the laboratory. We thank the GMOS program, and especially Francesca Sprovieri, Nicola Pirrone, Antonella Tassone and Attilio Naccarato (CNR-Institute of Atmospheric Pollution Research, Rende Division, UNICAL, Italy) for providing atmospheric Hg passive samplers (MerPAS) as well as analysing them. We thank Benoît Burban (UMR EcoFoG, Cirad/INRAE) for installing and retrieving these MerPAS samplers on the Guyaflux tower. Finally, we thank Akram Ali (SAS GAIA) for field assistance.

5.1.1. Abstract

Artisanal and small-scale gold mining (ASGM) in the Amazon region leads to the contamination of surrounding ecosystems with both anthropogenic and geogenic mercury (Hg) originating from gold amalgamation and soil destructuration (slurry) respectively. To investigate the storage and transfer of Hg between compartments on a restored gold mining site, as well as the suitability of indicators in assessing sources and transfers, Hg concentrations and speciation were measured in various compartments (river and mining pond water, soil, sediments, atmosphere, vegetation) on and around two mining sites. Additonally, Hg stable isotope compositions were measured in soils, sediments and vegetation. The Hg stable isotope compositions highlighted an important dissemination of anthropogenic Hg in mining pond sediment and soil in illegal mining areas (3 – 82 %), as well as its incorporation in the surrounding vegetation (roots and leaves). Anthropogenic Hg contamination was restricted to illegal mining areas, with no visible impacts on legally mined soils. However, Hg isotopic composition showed an increase of anthropogenic Hg contribution in river sediments downstream of the mining site which hints towards their potential use to follow past illegal gold mining exploitation. Atmospheric Hg concentrations directly measured during the sampling campaigns by active sampling were 7.5 ± 6.3 $ng.m^{-3}$, slightly above levels observed in remote areas. Three months integrative measurements using passive samplers showed a seasonal trend, with increasing concentrations during the dry season. High concentrations of dissolved gaseous mercury (DGM) found in some mining ponds (30-7000 $ng.m^{-3}$, median 1300 $ng.m^{-3}$), supports stagnant water as a source of elemental Hg to the atmosphere through volatilisation, while Hg reemissions from soils and reworked mining environments are still to be characterised.

Keywords Gold mining; Amazon; mine restoration; mercury; mercury stable isotopes; DGM, TGM

Highlights

- The concentration, speciation and isotopic composition of Hg in several mining site compartments were studied.
- Anthropogenic Hg contamination is localised around illegal mining ponds.
- Mining ponds are a potential source of gaseous mercury to the atmosphere.

5.1.2. Introduction

The use of mercury (Hg) in artisanal and small-scale gold mining (ASGM) was banned by the Minamata Convention on Mercury, but its use is still widespread across the Amazon region despite many countries having signed this convention (ACTO/OTCA 2018, Minamata_Convention_on_Mercury 2023). ASGM is thought to be the major source worldwide of Hg pollution to the atmosphere and to hydrosystems (AMAP/UNEP 2019). In ASGM, the amalgamation process and subsequent burning of the Hg-gold amalgam to retrieve gold leads to Hg losses, directly to the rivers as liquid Hg, as well as gaseous elemental mercury (GEM) to the atmosphere where dry or wet deposition can occur on the surrounding ecosystem. In French Guiana, no Hg is used by legal gold mines due to its prohibition in 2006, but illegal gold mining using Hg amalgamation is prevalent on the territory, with an estimated 5-10 times higher annual gold production compared to legal mines which produce around 1 ton of gold annually (Escat 2015, Le Tourneau 2021, Camino [last accessed 10 April 2025]). Due to the increasing price of gold, gold mining (both legal and illegal) is likely to remain high in French Guiana and the Amazon region (Hammond et al. 2007, Qian et al. 2019).

All alluvial gold mining practices (legal and illegal) involve the disaggregation of soils and remobilisation of suspended material and particles with high pressure water hoses in order to access the gold-bearing gravel layer, leading to an increase in turbidity in the downstream rivers with negative impacts on the ecosystems (Mol and Ouboter 2004, Tudesque et al. 2012, de Lucia Lobo et al. 2019). This particle export results in the remobilisation of Hg naturally associated to these soils due to the accumulation of atmospheric Hg up-taken by the vegetation and incorporated into the soils through litterfall (Guédron et al. 2006, Fostier et al. 2015). The long-term fate of post-exploitation mining sites in the absence of restoration practices, and their impact on the export of particles and thus of Hg is not clear. Once released to the hydrosystems, Hg is susceptible to undergo methylation, bioaccumulation and biomagnification along the food webs, posing a threat for local populations through the consumption of Hg-rich piscivorous fish (Maury-Brachet et al. 2006, Pignoux et al. 2019). Hg concentrations and speciation in regional ASGM contexts are already documented in water and soil compartments (Telmer et al. 2006, Guédron et al. 2009, Guédron et al. 2011, Laperche et al. 2014), as well as in fish communities (Durrieu et al. 2005, Martinez et al. 2018, Maury-Brachet et al. 2019). On the other hand, this remains less documented in the case of Hg uptake and recycling by tropical vegetation (Casagrande et al. 2023), and atmospheric compartments (Amouroux et al. 1999, Guédron et al. 2018, Gerson et al. 2022, Szponar et al. 2025), where Hg baselines and the impact of ASGM remain elusive.

An alternative tool to Hg concentration and speciation analyses is the use of Hg stable isotopes as tracers of sources and processes. The large ranges of mass-dependent fractionation (δ^{XXX}Hg, MDF) and mass-independent fractionation (Δ^{XXX}Hg, MIF) in natural samples allows the use of Hg isotopic data in

the identification of contamination sources (Barre et al. 2018, Tsui et al. 2020). In the context of ASGM in the Amazon, stable isotopes have been used in sediments, soils and the atmosphere to distinguish between anthropogenic and natural Hg sources (Adler Miserendino et al. 2018, Guédron et al. 2018, Goix et al. 2019, Nitschke et al. 2024, Szponar et al. 2025).

The objective of this study was to provide a fine understanding of the sinks, sources and potential transfers of Hg between compartments on legal gold mining sites with influence of illegal gold mining and to assess the relevance of different indicators in following these sources and transfers. This increased understanding aims at better predicting the long term fate of gold mining sites by unraveling Hg mobility and reallocation or export within the mining ecosystem. To do so, Hg concentrations and speciation were measured in different compartments (water, soil, sediments, atmosphere, vegetation), as well as Hg stable isotopes in soils, sediments and vegetation on two mining sites and their nearby forests.

5.1.3. Materials and Methods

Study area. French Guiana (87,500 km²) is part of the Guiana Shield located in the north-eastern region of South America between Brazil and Surinam (2-6°N and 51°30'-54°30'W). It experiences an equatorial humid climate with an average annual rainfall of around 4000 mm and 96 % of the territory is covered by tropical rainforest.

The study was conducted on two mining sites of the mining company SAS GAIA (Figure 5.1); the "Awa" site (54°20'34"W, 4°19'8"N), and the "Sophie" site (53°24'59"W, 3°51'17"N). The Awa site (watershed area 32 km²), an alluvial gold mine, is drained by the Awa river, which is part of the Maroni watershed [i.e., the largest river of French Guiana (66 814 km²)], which is densely gold-mined (Gallay et al. 2018) and has a long history of gold mining dating back to the 1900s (Jébrak et al. 2021). Alluvial gold mining exploitation was performed below a riverbed, to extract gold from gravel deposits resulting from the weathering of auriferous quartz veins (Thomassin et al. 2017). These downslope valleys typically consist of sandy hydromorphic soils exhibiting reducing conditions due to the presence of slow-flowing water (Guédron et al. 2009). The mineralogy of these soils is dominated by quartz and kaolinite, with some goethite. Exploitation and production was conducted on the site from downstream to upstream between September 2017 and April 2021. The first restoration operations were conducted between May and July 2019, and full restoration was then performed between May 2021 and August 2022. Restoration consists in filling the mining ponds with the gravel and clay removed during exploitation, performing landscaping respecting as much as possible initial soil stratification, then replanting trees grown in on-site nurseries, at a three-meter interval. It has to be noted that illegal gold mining had been taking place upstream of this site before and during the study. The second mining site is called Sophie and is located in the upstream part of the Mana watershed (12 208 km²). During the time of the study, this site was under prospection by the mining company for primary gold exploitation (i.e. gold associated to quartz veins). Core drilling was performed to estimate the location and the amount of gold present, and evaluate the feasability of the subsequent exploitation. No known historical gold mining has been taking place on this site, but there is evidence of extensive illegal gold mining taking place on many locations on and around the mining site since approximately 20 years, mostly in vertical tunnels to access the gold-bearing quartz veins.

The differences between the Awa and the Sophie mining sites are the type of deposit, as well as the illegal mining history. On the Awa site, only alluvial gold mining took place, whereas on the Sophie site, the majority of exploitations are primary, with some past alluvial gold mining. Additionally, on the Awa site, illegal gold mining had taken place in the past, before the arrival of the legal mining company, and the mining ponds were more than 15 years old, whereas on Sophie, illegal gold mining was extensive in the region for the past 20 years. In the second section of the results and discussion (section 5.1.4.2)

focusing on the comparison between the two mining sites, the Awa and Sophie sites will be called "alluvial" and "primary" sites respectively for the sake of simplicity.

Four sampling campaigns were conducted over one year (from 2022 to 2023): G0 (01/22), G1 (04/22), G2 (12/22) and G3 (05/23), where the Awa site was sampled on all four campaigns, and the Sophie site was sampled during G0 and G2. A synthesis of the locations of the different compartments sampled on each site can be found in Figure 5.1.

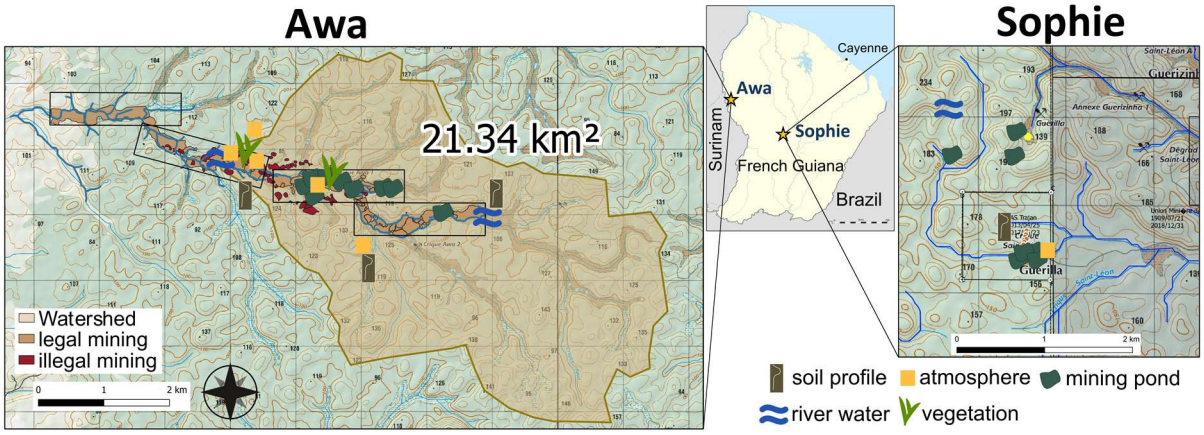

Figure 5.1. *Maps with location and sample type on the two studied mining sites Awa and Sophie.*

Monitoring and sampling. For long-term trends, hourly rain data was recovered from a national meteorological station in Grand-Santi, (7 km away from the Awa mining site), and in Saül (38 km away from the Sophie mining site).

Solids sampling. Soil samples on and around the mining sites were sampled using a manual auger. Surface sediment samples were collected at the edge of mining ponds and in the Awa river in 50 mL PP falcon tubes. All solids were then homogenised, freeze-dried, sieved at 2mm, and this latter fraction was ground to a powder <63 µm for further analysis.

Water sampling. On the Awa site, a monitoring station was installed on the river, upstream and downstream of the mining site, where an automated water sampler (ISCO) was installed at each station and programmed to collect river samples every two hours, or longer during water level recession (section 4.1.3).

Overland flow water and eroded particle samples were collected on the Awa site as described in section 3.1.3. Briefly, erosion plots were installed to recover the overland flow water and eroded material from a defined area during a rain event. Each plot consisted of wood panels (2 m × 2 m, 4 m²) inserted 10 cm into the soil and extending 15 cm above the soil, and was connected to an 80L bucket installed at the lowest point of the slope and buried in the soil. After each rain event, the total volume of water was measured, and a 250 mL aliquot of the suspension was sampled in an FEP bottle.

All river and overland flow water samples were collected in pre-cleaned vials following ultra-clean technique protocols (Stoichev et al. 2006). A 250 mL aliquot of the water sample was filtered on a acid-

washed and pre-weighed 0.45µm PVDF filter, which was air-dried in a laminar flow hood 48h and weighed to determine the SSC (Stoichev et al. 2016). The filtrate was collected in PTFE acidified to HCl 0.2 %.

Wet deposition samples were collected in an open area of the mining site and throughfall samples were collected under forest cover in the vicinity of the mining site. Both sample types were collected in PP bottles and retrieved after each important rain event or when the collected volume exceeded 200 mL.

Soil subsurface pore water was collected using microporous polymer tube samplers (Rhizon® SMS, Rhizosphere Research Products) in acid-washed 50 mL syringes.

Rain and porewater samples were then transferred to PTFE bottles and acidified to HCl 0.2 %.

Chemical analyses. *Total mercury* (THg) on solid samples was analyzed by atomic absorption spectroscopy after pyrolysis and gold amalgamation (AMA 254, Altec) with a relative precision of ± 5 % determined from triplicates, consistently with typical relative errors reported for this analyser (Roos-Barraclough et al. 2002, Guédron et al. 2006). The total mercury concentration measurements were validated with the certified reference materials (ERM CC141 loam soil, IAEA-336 lichen) and were always within the published range (0.083 ± 0.017 and 0.2 ± 0.04 $\mu g \cdot g^{-1}$, respectively). The detection limit (defined as 3 times the standard deviation (SD) of the blank) was at a maximum of 0.005 $\mu g \cdot g^{-1}$.

Mercury speciation. Inorganic (iHg) and methylated (MeHg) mercury concentrations in filtered water and on suspended particulate matter (SPM) collected on filter samples was analysed following established methods using single-spike isotope dilution analysis by gas chromatography – inductively coupled plasma mass spectrometry [SS-ID GC-ICP-MS (Monperrus et al. 2005, Monperrus et al. 2008, Sharif et al. 2014, Cavalheiro et al. 2016)]. Total Hg in water samples was considered as iHg + MeHg. It is assumed here that the majority of DGM is lost through degassing during the sampling and filtering procedure of THg analysis. Indeed, considering the atmospheric Hg concentration on the mining site measured over more than one year using passive sampling detailled above (7.5 ± 6.3 $ng.m^{-3}$), and a dimensionless Henry's law constant of 0.34 at 27°C (Andersson et al. 2008), the DGM concentrations expected at equilibrium would be around 20 $ng.m^{-3}$, which corresponds to 2 – 50 % of the initial DGM still present after equilibration in mining ponds and rivers respectively. The "real" THg should thus be the sum of iHg, MeHg and DGM. However, because DGM is not the predominant Hg species in river water (< 10 %), the THg value does not vary significantly if DGM is taken into account or not (p=0.71, Wilcoxon).

Dissolved gaseous mercury (DGM) represents all volatile Hg species (i.e. elemental Hg^0 and dimethylmercury DMHg) in water samples, and was collected manually in PTFE bottles leaving no headspace. The samples were then purged within ~0.5 h after sampling and collected on a gold-coated

sand trap. DGM was analyzed by thermodesorption (600 °C) and CV-AFS detection using a Tekran® (Model 2500). The system was calibrated by gas phase Hg (Hg^0) as described elsewhere (Duval et al. 2023, Kleindienst et al. 2023).

Total gaseous mercury (TGM). Active sampling of atmospheric Hg was conducted at 1.5 m above the ground. Air was pumped for 20 min through a teflon tubing line to goldcoated quartz sand Hg-traps. Air-pumping flow rate ranged from 0.1 to 0.5 L min^{-1} and was controlled at the beginning and the end of every sampling period. For 22 samples (15 % of all samples), a second gold-trap was added to control for loss of Hg through lack of retention on the first gold-trap due to elevated relative humidity. The average Hg loss was 30 ± 10 % which was added as a correction to samples collected with a single gold trap. Before and after collection, gold traps were stored in double sealed plastic bags until analysis.

The analysis of gaseous Hg species (DGM and active sampling TGM) was done by double amalgamation on gold-AFS Tekran-2500 (DA/Au-AFS). Thermodesorption efficiency was controlled by carrying out two consecutive analyses of the gold-coated sand trap. Gaseous Hg quantification was done by external calibration of the DA/Au-AFS device using a controlled Hg^0 source.

Passive sampling of atmospheric Hg was conducted using the *Mer*PAS® consisting of sulfur-impregnated activated carbon sorbent developed at the university of Toronto and commercialised by Tekran Instrumen Corp. (McLagan et al. 2017). The PAS were installed on poles at a height of ~1.5 m for three months on i) the open mining site, ii) in the nearby forest under tree cover, iii) near illegal mining ponds, and iv) on a tower above the canopy, at 23 and 54 m height. At all locations, three PAS were deployed, with two serving as sample replicates while the third was kept closed and served as a field blank. Meteorological data was used to correct the sampling rate SR of the PAS according to the following equation:

$$SR_{exp} = SR_{cal} + 0.0009 \times \left(T_{exp} - 9.89°C\right) + 0.003 \times (ws_{exp} - 3.41)$$

With T_{exp} and ws_{exp} being the average temperature and windspeed, respectively, recorded during the deployment time. The Hg atmospheric concentration is then calculated as:

$$TGM = \frac{m}{SR_{exp} \times t}$$

With *m* the mass of Hg sorbed on the sampler, and *t* the duration of deployment.

Vegetation. Herbaceous plants were sampled in the vicinity of illegal mining ponds, and on the legally worked mining flat. The plants were unearthed, the above ground biomass was separated from the roots, stored in sealed plastic bags and kept at 4°C. The above-ground biomass was rinsed with several (2-4) baths of milli-Q water, the roots were subjected to 2-3 alternating baths of milli-Q and Na_2EDTA 40 mM for 15 min to remove any soil particles and elements potentially stuck to the roots surface. All vegetation samples were then freeze-dried, and ground to a fine powder for further analyses.

Mercury stable isotopes analysis. For each sample, appropriate amounts (between 0.1 to 0.5 g) were weighed in discardable glass vessels and digested in 4 mL HNO_3 using the Milestone ultraWAVE digestion system using the following parameters: 110 bar, 240 °C, 40 min for sediment samples; and 110 bar, 230°C, 15 min for vegetation samples. Then, 1 mL H_2O_2 was added to the samples which were heated at 85°C overnight. All sample extracts were then centrifuged 3 min at 3400 rpm and the supernatant was collected and diluted for isotopic measurements to a final Hg concentration of 0.5 ng.mL^{-1} in 10 % HNO_3, 2 % HCl. The sample digestion protocol was validated by the digestion of soil and sediment reference materials used in previous studies for "matrix matching" secondary standards: NIST-SRM-1944, IAEA-405, NIST-1575a and BCR-482, under equivalent conditions. The isotopic data of these reference materials measured in this study is in agreement with previously published values (Sherman and Blum 2013, Janssen et al. 2015, Bérail et al. 2017, Guédron et al. 2018, Yamakawa et al. 2021).

Hg isotope analyses were performed using cold vapour generation with $SnCl_2$ reduction coupled to an MC-ICP-MS instrument (Nu Plasma, Nu Instrument) following similar protocols as previously published (Jiménez-Moreno et al. 2016, Guédron et al. 2018). Briefly, the instrumental mass bias was corrected using a Tl internal standard (NIST SRM 997 $^{205}Tl/^{203}Tl$ = 2.38714) as well as sample-standard bracketing using the NIST 3133 standard solution. All samples and standards were analysed at 0.5 ppb of Hg.

Hg isotopic ratios are reported as δ relative to the ratio measured in the NIST 3133 :

$$\delta^{XXX}\mathrm{Hg}\ (‰) = \left(^{xxx/198}\mathrm{Hg}_{\mathrm{sample}}/^{xxx/198}\mathrm{Hg}_{\mathrm{NIST\ 3133}} - 1\right) \times 1000$$

Where xxx is the studied mercury isotope between ^{199}Hg and ^{204}Hg. The MIF, reported as Δ, is the difference between the theoretical value predicted by the MDF of δ^{xxx}Hg and the measured values.

$$\Delta^{xxx}\mathrm{Hg}\ (‰) = \delta^{xxx}\mathrm{Hg} - \delta^{202}\mathrm{Hg} \times \beta_{xxx}$$

Where the β_{xxx} corresponds to 0.2520, 0.5024, 0.7520 and 1.493 for ^{199}Hg, ^{200}Hg, ^{201}Hg and ^{204}Hg isotopes respectively. The analytical uncertainty was evaluated by multiple measurements (n=39) of the NIST RM 8610 reference material, certified for Hg isotopes. The analytical methods have been validated with several primary and secondary standards (NIST 3133, NIST RM 8610) certified for Hg isotopes and reference materials not certified for Hg isotopes but with published reference values.

Extraction recoveries were estimated based on the multicollector signal of the sample and compared to the total Hg measured by AMA-254 before digestion (av. recovery = 94 %).

The external reproducibility (2SE) of all samples was determined by measuring replicates of selected samples (n=6). The analytical uncertainty (2SD) determined using the NIST RM 8610 (n=29) was always higher than the external reproducibility (2SE) of measured samples (n=14), so the analytical uncertainty was used to describe variability of measured samples.

Data analyses.

Hg^0 gaseous fluxes at the air-water interface. The flux density (ng.m^{-2}.day^{-1}) of gaseous Hg from the surface water compartments to the atmosphere can be estimated using the following formula derived from Fick's law for water-air exchange :

$$Flux\ Density = k_{Hg}\left(Hg_{DGM} - \frac{Hg_{TGM}}{H'}\right)$$

Where k_{Hg} is the Hg^0 mass transfer velocity (m.day^{-1}), and *H'* is the dimensionless Henry's law constant corrected for water temperature and salinity (Andersson et al. 2008). At 27°C (the average temperature measured in both river water and mining ponds), *H'* is 0.335.

The mass transfer velocity can be calculated based on the CO_2 mass transfer velocity and the ratio of Hg and CO_2 Schmidt numbers, and with the exponent n varying between 0.5 and 1 depending on which process dominates diffusion (Jähne et al. 1987, Cole and Caraco 1998):

$$k_{Hg} = k_{CO_2}\left(\frac{Sc_{Hg}}{Sc_{CO_2}}\right)^{-n}$$

For the k_{Hg} in mining ponds, a volatilisation model for sheltered lakes was used (Cole and Caraco 1998, Duval et al. 2023), with an average wind speed of 1 m.s^{-1} as measured during daytime hours on the mining site, and a n value of 0.5, resulting in a k_{Hg} of 0.54 m.day^{-1}. For river – atmosphere exchanges, a k_{CO2} of 1.2 m.day^{-1} was empirically estimated in the main tributaries of the Amazon basin (Richey et al. 2002), and using a n value of 0.68 for moderate turbulences (Striegl et al. 2012), the k_{Hg} amounts to 1.18 m.day^{-1}.

Statistical analyses. All statistical analyses were performed using R. The Student's t-test was performed when the data was normally distributed and the variances between the two studied groups were equal. When this was not the case, the Wilcoxon test was performed. Regressions are shown only if the p-value is below 0.01.

5.1.4. Results and Discussion

5.1.4.1. Baseline levels, stocks and potential transfers on the alluvial Awa mining site

5.1.4.1.1. Hg content and speciation in soils and sediments

Three pristine soil profiles were sampled around the mining site, and even though they were sampled at different heights on the hills surrounding the mining site (on a hilltop, in the valley, and at midslope), all profiles display very homogeneous THg concentration variations with depths. Surface soil concentrations were 152 ± 33 ng.g^{-1}, increased to 200-250 ng.g^{-1} at 80 cm depth, and then decreased again below 50 ng.g^{-1} below 2m depth (Figure 5.2A), following the same trend as iron concentrations in these soils. This emphasises the association of Hg to iron oxides as has been evidenced in French Guiana and in the Amazon (Roulet et al. 1998, Guédron et al. 2009, Harris-Hellal et al. 2011, Figueiredo et al. 2018).

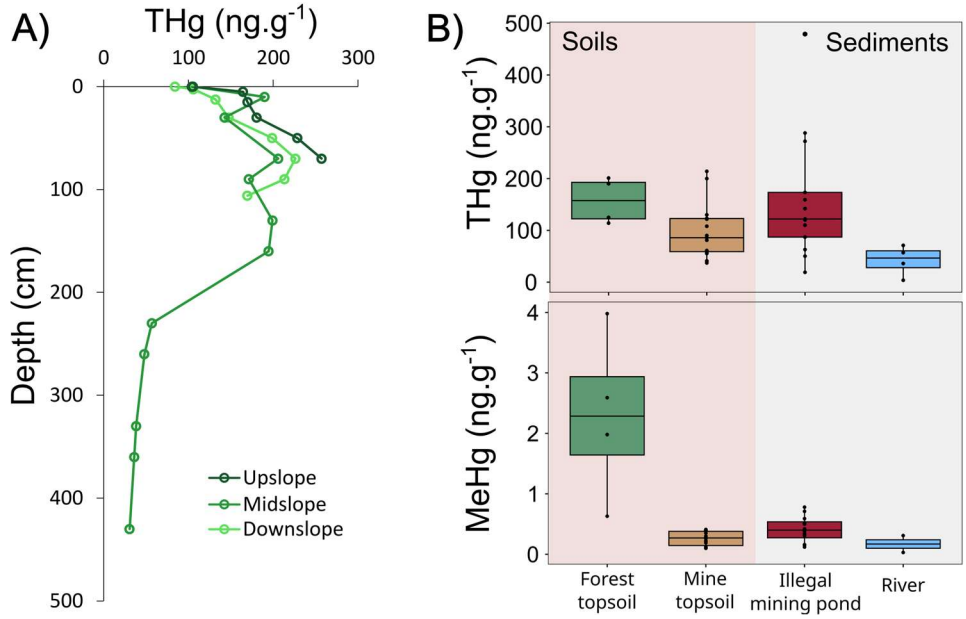

Figure 5.2. *A) Total Hg in three soil profiles around the mining site and B) THg and MeHg in surface soils and sediments.*

When comparing surface soils and sediments on and around the mining site, no significant difference in THg concentrations was observed between any compartment (ANOVA p=0.04, Figure 5.2B). THg concentrations were in the range of undisturbed soils and sediments in F. Guiana (Roulet and Lucotte 1995, Guédron et al. 2009, Laperche et al. 2014). However, significantly higher MeHg concentrations were found in forest surface soils than in mine soils and river and mining pond sediments (Kruskal-Wallis = 0.0032). The MeHg concentrations in forest topsoils around the mining site (2.3 ± 1.4 ng.g^{-1}) were only slightly higher than those observed in the Brazilian Amazon [0.93 ± 0.01 ng.g^{-1} (Fostier et al. 2023)]. The presence of MeHg in the forest soils might originate from atmospheric deposition on tree leaves and incorporation through litterfall as observed in boreal and temperate forests (Graydon et al. 2009, Tsui et al. 2012), or from throughfall (Gerson et al. 2022). It might also arise from methylation of

iHg directly in the soils by anaerobic bacteria (Kronberg et al. 2016, Eklof et al. 2018), but this has not been shown to occur in Amazonian soils until now.

The use of liquid Hg in illegal gold mining practices was not visible in the sediments of illegal mining ponds as the THg concentrations were similar to mine soils. This might in part be due to the fact that sediment sampling was done on the edges of the ponds due to accessibility issues to access deep unconsolidated sediment where Hg contamination might be more conserved. Sediments from mining ponds in F. Guiana (with and without use of liquid Hg) displayed concentrations in the same range [100 – 200 $ng.g^{-1}$ (Hellal et al. 2020)]. In order to investigate in further detail the sources of mercury (anthropogenic or geogenic), mercury stable isotopes were measured on soils and sediments, as well as vegetation.

5.1.4.1.2. Stable isotopes for Hg source tracing in soils and vegetation

Anthropogenic and geogenic Hg in soils and sediments. When displaying the $\delta^{202}Hg$ versus the $\Delta^{199}Hg$, all soil and sediment samples are distributed between two poles (Figure 5.3). These two poles represent anthropogenic and geogenic mercury and were constructed using literature data as described in Nitschke et al. (2024), chapter 6. The anthropogenic endmember was estimated using isotopic data of liquid Hg used by gold miners in French Guiana and Bolivia (Laffont et al. 2011, Goix et al. 2019), as well as highly contaminated (> $1 \mu g.g^{-1}$) soils in French Guiana and Ecuador (Guédron et al. 2018, Schudel et al. 2018), resulting in a signature of $\delta^{202}Hg = -0.42 \pm 0.20‰$ and $\Delta^{199}Hg = -0.01 \pm 0.07‰$. The geogenic endmember was estimated using deep undisturbed soils (>0.5 m) in French Guiana (Guédron et al. 2018, Goix et al. 2019), resulting in a signature of $\delta^{202}Hg = -2.53 \pm 0.23‰$ and $\Delta^{199}Hg = -0.62 \pm 0.10‰$.

Illegal mining pond sediments and mining soils in the vicinity of these ponds displayed isotopic compositions that are less negative than mine soils and river sediments, and closer to the anthropogenic mercury endmember (Figure 5.3). Using a binary mixing model with the endmembers presented in Nitschke et al. (2024), the proportion of anthropogenic Hg was estimated based on the $\Delta^{199}Hg$ isotopic composition of the soil or sediment sample. Soils in the legally mined areas and sediments upstream of the mining site displayed no evidence of anthropogenic Hg contribution (-16 to 11 %, median -8 %), while mining ponds sediments and soils in the vicinity of these ponds exhibited a much larger contribution (3 – 82 %, median 21 %). This highlights the use of liquid Hg by illegal gold miners in their operations. Interestingly, mining pond sediments did not display significantly higher THg concentrations than mine soils and river sediments, emphasizing the importance of using Hg stable isotopes in source tracing at the scale of a mining site, in comparison with the information provided by total concentration measurements.

The comparatively more negative isotopic composition of legal mine soils indicated that no liquid Hg was used in legal operations, and showed that anthropogenic contamination remains localised in and around mining ponds, without a strong repercussion on sites that have been mined legally after exploitation. It might also be that anthropogenic Hg contamination was prevalent on the whole mining site (legal and illegal sections), but that during the exploitation process by the gold mining company, this anthropogenic Hg has been remobilised and lost to the downstream hydrosystem. The sections worked previously by illegal miners are usually not reworked and restored by the mining company and would thus have retained this anthropogenic Hg contamination.

Although Hg isotopic data is available only for three river sediment samples, the sediments collected upstream of the mining site and on a tributary river that has never been goldmined showed very negative δ^{202}Hg and Δ^{199}Hg (−2.12‰ and -0.67‰, respectively), whereas the sediment collected downstream of the mining site displays a somewhat less negative δ^{202}Hg and Δ^{199}Hg (−1.84‰ and -0.48‰, respectively), overlapping with the compositions of illegal mining pond sediments. The amount of data is insufficient for an unequivocal assessment, but this might indicate some downstream contamination of the hydrosystem with anthropogenic Hg originating from the illegal mining ponds. If this is confirmed, it would suggest that thanks to Hg isotopes, it is possible to track the influence of illegal mining activity involving liquid Hg use even years after the exploitation is over.

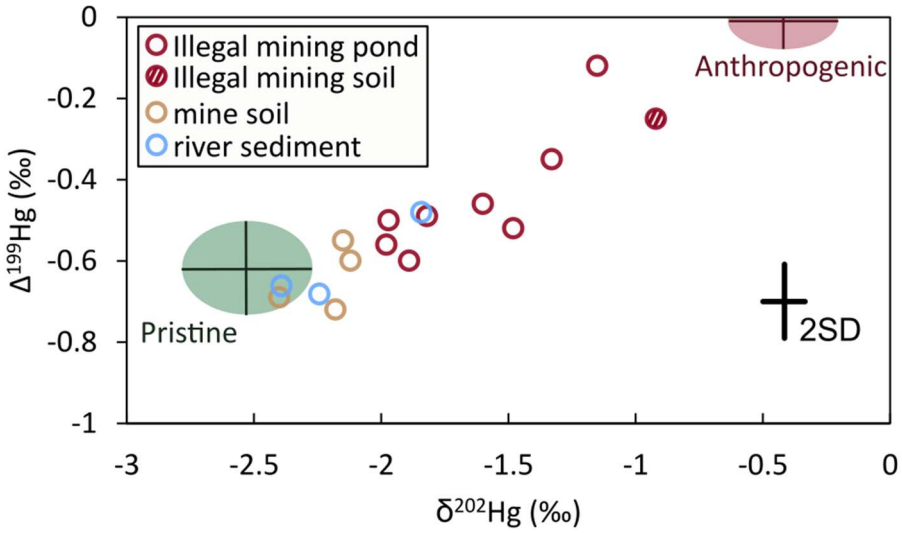

Figure 5.3. *Δ^{199}Hg vs δ^{202}Hg in soil and sediment samples on the mining site. The isotopic signatures for anthropogenic and pristine (geogenic) Hg are estimated from literature data (Laffont et al. 2011, Guédron et al. 2018, Schudel et al. 2018, Goix et al. 2019).*

Hg sources and transfers in the vegetation. In order to investigate the potential transfer of Hg from soils to the vegetation, THg concentration and Hg stable isotopes were measured in herbaceous plants in legal sections of the mining site, and in the vicinity of illegal mining ponds. Higher Hg concentrations were observed in roots compared to above-ground biomass (Figure 5.4A), pointing towards the main source of Hg in these herbaceous plants being the soil in opposition to atmospheric uptake by the

aerial parts. Only little translocation occurs, as the aerial parts contain very low concentrations of Hg. The extent of uptake and translocation is highly dependent on the plant species but the soil was also found to be the primary source of Hg in herbaceous plants and shrubs on tropical soils in the Brazilian Amazon (de Freitas et al. 2024). Plants sampled close to illegal mining ponds displayed higher THg concentrations in the roots hinting towards anthropogenic Hg contamination. Consistently, the isotopic data in plants showed that samples around illegal mining sites always displayed a less negative (i.e. more anthropogenic) Δ^{199}Hg compared to samples on the legal mining sections (Figure 5.4B).

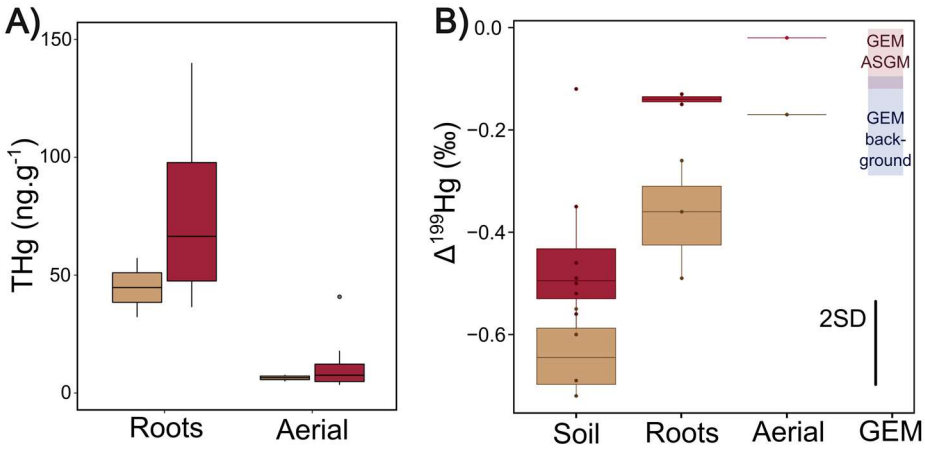

Figure 5.4. *A) THg and B) MIF (Δ^{199}Hg) in plants compartments on the legal mine (brown) or close to illegal mining ponds (red). Isotopic data for gaseous elemental mercury (GEM) is from the Peruvian Amazon (Szponar et al. 2025).*

Additionally, plants exhibited a Δ^{199}Hg that was in between the compositions of soil (or sediment) and gaseous elemental mercury from the Peruvian Amazon (Szponar et al. 2025), with a distinction observed between the roots and the aerial parts. Indeed the roots showed Δ^{199}Hg values closer to the soil isotopic composition, while the aerial parts resembled the GEM isotopic composition. This might be the result of source mixing between soil Hg and atmospheric Hg, as has been observed in rice plants in China (Yin et al. 2013), with a potential influence here of atmospheric Hg down to plant roots for herbaceous species. It has to be noted that all plant species sampled here were herbaceous plants with superficial roots (<10 cm depth), and the translocation of atmospheric Hg to the roots might not be visible in trees or not to the same extent. Again, these findings are preliminary, as the low number of samples does not allow for a statistical analysis of the differences observed, but showed the potential of the isotopic tool in refining the origin and transfer of Hg in and between different compartments.

5.1.4.1.3. Mercury distribution and speciation in water compartments

In all water samples, the majority of mercury was associated to the particulate fraction (> 80 %). In the filtered fraction, similar concentrations of THg were observed in mine soil runoff, illegal mining ponds and river water, while wet deposition samples displayed significantly higher THg concentrations at 2.9 ± 1.2 ng.L^{-1} (Figure 5.5A), in line with concentrations observed previously in F. Guiana

[4.6 ± 0.7 ng.L^{-1} (Guédron et al. 2011)]. Throughfall exhibited even higher THg concentrations, at 6.3 ± 2.1 ng.L^{-1}, including both the atmospheric Hg and the one previously adsorbed on tree leaves (Wright et al. 2016). Thus, the lower THg concentrations observed in runoff water compared to wet deposition hint towards Hg sorption and scavenging onto soil particles during a rain event, with the soil acting as a Hg filter. Additionally, illegal mining ponds displayed significantly higher MeHg on the particles, which might reflect an increased methylation activity, as was observed in other mining ponds in French Guiana (Guédron et al. 2011).

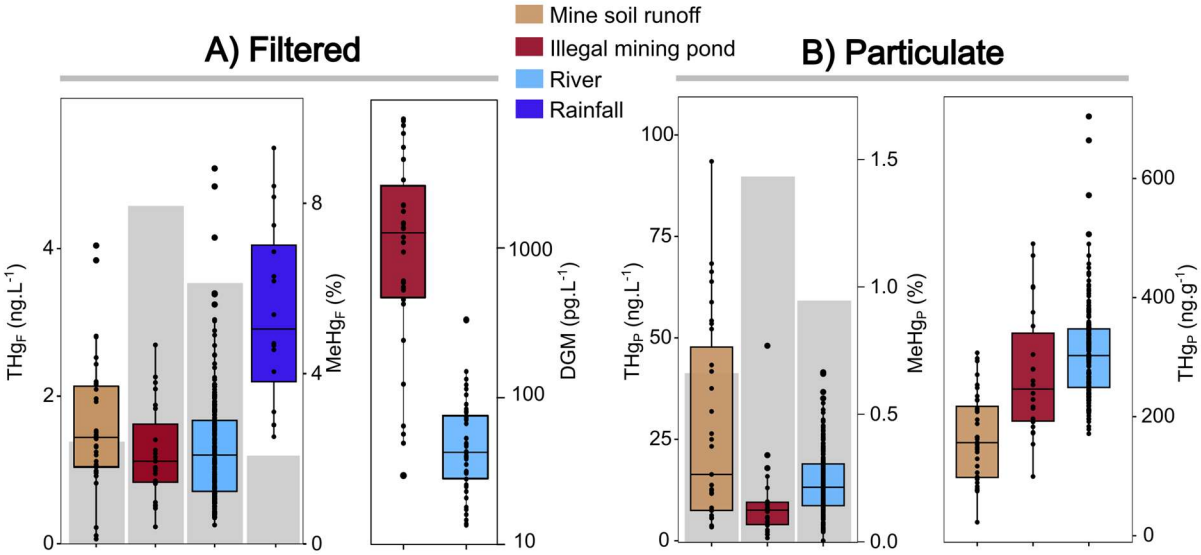

Figure 5.5. *A) Hg in the filtered (or dissolved) fraction. Total Hg (THg) as boxplots and the proportion of MeHg as gray bar charts, as well as dissolved gaseous mercury (DGM). B) Hg in the particulate fraction. THg as boxplots (expressed as ng per L and ng per g of particulate matter) and the proportion of MeHg as gray barcharts.*

Significantly higher concentrations of dissolved gaseous mercury (DGM) were recorded in illegal mining pond sediments (2025 ± 2000 pg.L^{-1}) than in the river water (60 ± 55 pg.L^{-1}), making DGM the most abundant Hg species in some mining ponds' filtered water whereas it accounted for less than 15 % in river water (Figure 5.5A). In F. Guiana, such high concentrations have only been recorded in a heavily gold mined river (Petit Inini river, 570 pg.L^{-1}) (Amouroux et al. 1999). Additionally in some occasions, water samples from the same mining ponds but sampled during two different days displayed drastically different DGM concentrations. The presence of high DGM concentrations in the absence of elevated THg concentrations, neither in the particulate, nor in the filtered fraction, points towards a specific source of Hg contamination, probably through the input of liquid Hg^0 during the gold amalgamation process.

Evidence of this point source of Hg leading to hotspots remarkably localised in time and space in several mining ponds was also observed in filtered THg. Indeed, two outliers (not included in Figure 5.5) displayed filtered iHg concentrations of 354 and 206 ng.L^{-1} when the average is 1.2 ± 0.7 ng.L^{-1}. Both these ponds were sampled again during preceding or following sampling campaigns and displayed

concentrations below 1 ng.L^{-1}, indicating that the high concentrations observed possibly originate from point sources of Hg like for example the release of Hg-rich pockets trapped within the mining pond floor. It is important to characterise these potential hotspots that might act as sources of Hg to the rest of the mine and the adjacent river.

5.1.4.1.4. Atmospheric Hg

Total gaseous mercury (TGM) in the atmosphere was investigated using active and passive sampling during different seasons on different locations on and around the mining site.

TGM Baselines

Active sampling was performed during the field campaigns, in daytime hours in order to measure background concentrations and potential differences between the atmosphere over the legal sections of the mining site, the vicinity of illegal mining ponds, and under the adjacent forest cover. The average TGM measured by active sampling was 7.5 ± 6.3 ng.m^{-3}, with significantly ($p = 0.0001$, Kruskal-Wallis) lower concentrations during the minor rainy seasons than during the major rainy seasons, but no significant difference in TGM was observed between the sites (Figure 5.6A, $p=0.56$). No samples were collected during the dry season using active sampling.

Passive sampling on the other hand provided an estimation of the integrated level of TGM over a season (3 months sampling), and was performed on the same sites as active sampling, and additionally in the atmospheric boundary layer (54 m height, i.e., above the forest canopy). The values observed on the mining site were similar to those observed under the adjacent forest canopy, and in the atmospheric boundary layer with an average concentration between all samples of 1.4 ± 0.6 ng.m^{-3} for passive sampling. There appears to be a seasonal variation in TGM, with significantly ($p<0.001$, ANOVA) higher concentrations measured during the dry season and lower concentrations observed during high rain periods (Figure 5.6B). This is the opposite trend to what is usually observed in temperate ecosystems where lowest TGM concentrations are observed during the summer (Sprovieri et al. 2016). No seasonal variation was observed with passive sampling near a Brazilian city in the Amazon (Manaus) but far from any anthropogenic influence (Sprovieri et al. 2016).

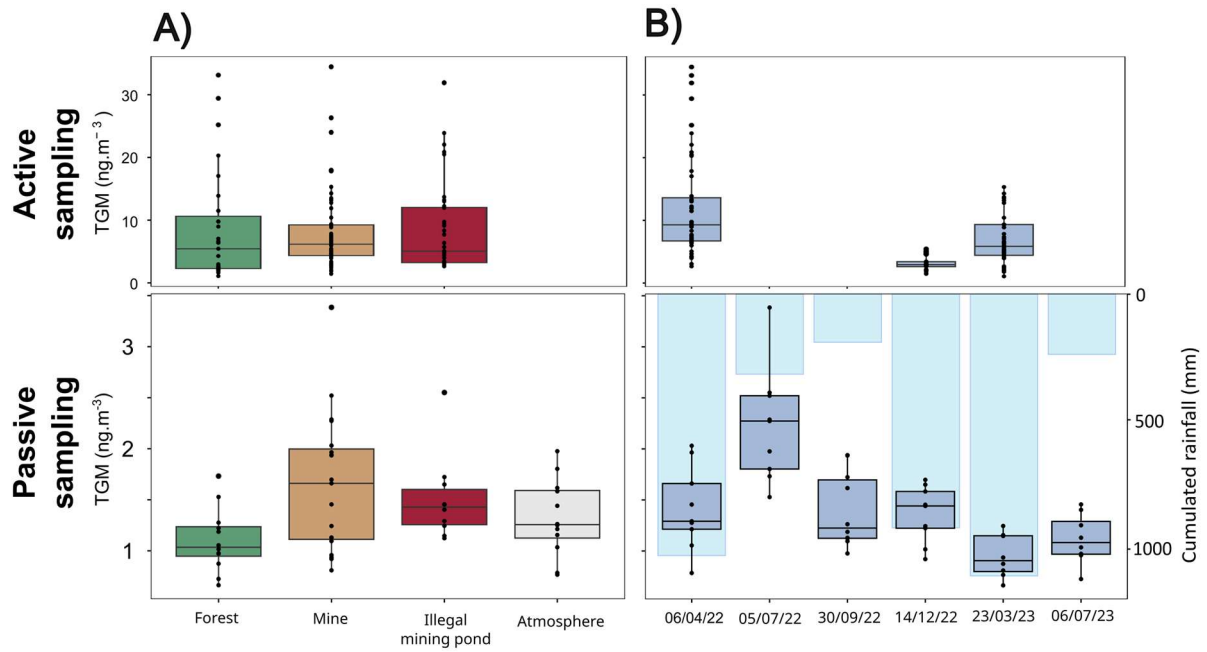

Figure 5.6. *Total gaseous mercury (TGM) concentrations by site (A), and seasonal evolution (B) measured using active (up) or passive (down) sampling.*

The average TGM measured by active sampling was 5-fold higher than the average TGM measured by passive sampling. This might be in part explained by the fact that all active sampling were carried out during the day, when TGM concentrations are known to be higher (Amouroux et al. 1999, Muresan et al. 2007). Additionnally, the passive samplers were calibrated in temperate environments and the diffusion rate of Hg in the carbon sorbent might be affected in a very humid environment. Indeed, only temperature and windspeed are taken in account in the Hg diffusion rate, but nor humidity. The accuracy of passive samplers (among which the one used in this study) was shown to be dependent on the sampling location and affected by adverse meteorological conditions (Naccarato et al. 2021).

Estimation of Hg^0 fluxes at the air-water interface

When comparing dissolved gaseous Hg (DGM) concentrations in water compartments with Hg concentrations in the atmosphere, it appears that surface waters were always supersaturated with Hg^0 in mining ponds (146 – 35 000 %, median = 6 100 %), and most of the time in rivers (68 – 700 %, median 200 %), supporting water compartments as a potential source of gaseous Hg to the atmosphere. The flux density (FD) of gaseous Hg from the surface water compartments to the atmosphere was calculated using a different model for the mining ponds and the river system, yielding a mass transfer velocity k_{Hg} of 0.54 and 1.18 $m.day^{-1}$ respectively. Although the k_{Hg} is more important in river water due to increased turbulences and water flow, the large DGM concentrations in mining ponds resulted in an increased FD (4-4000 $ng.m^{-2}.day^{-1}$, median 680 $ng.m^{-2}.day^{-1}$), compared to the river water (0 – 150 $ng.m^{-2}.day^{-1}$, median 24 $ng.m^{-2}.day^{-1}$). The flux density of elemental Hg in illegal mining ponds

was thus at least 10- fold higher compared to rivers. When taking into account the surface taken up by mining ponds over the whole mining site (0.14 km², 11 % of the whole mined area), the average daily export of Hg from mining ponds was 95 mg, which is still higher than the average daily input of Hg from the atmosphere to the mining site through wet deposition (28 mg).

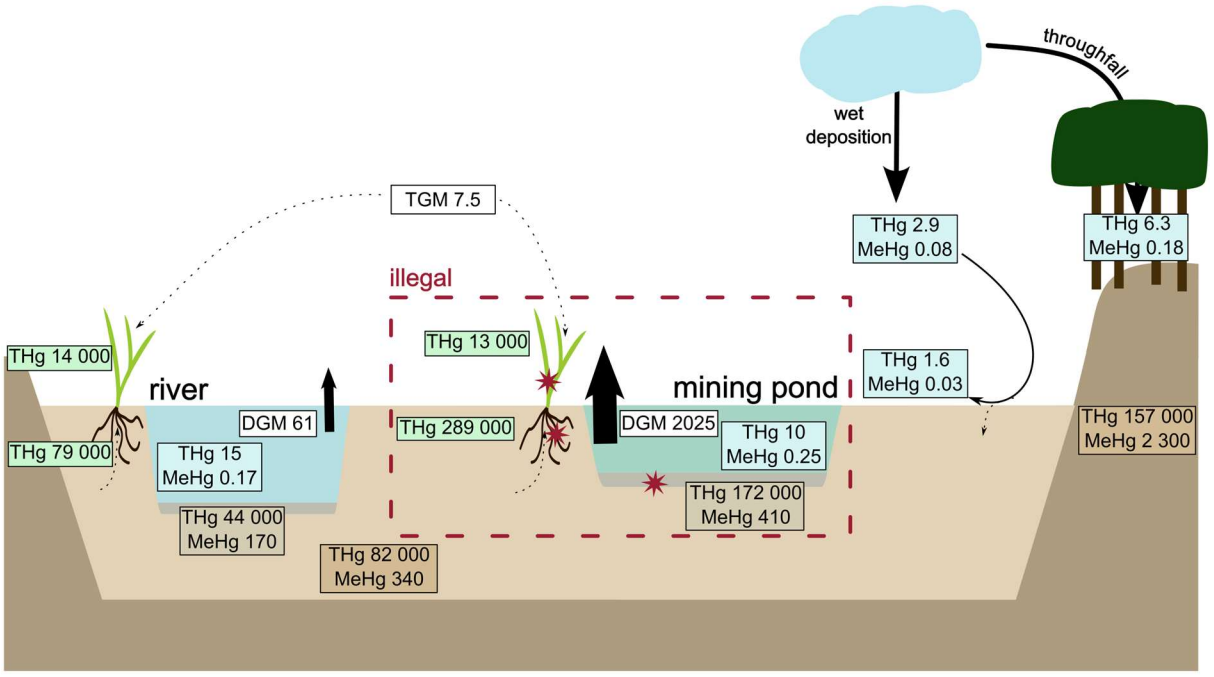

Figure 5.7. *Synthesis of mercury pools and speciation on an alluvial mining site in French Guiana. The compartments displayed are the vegetation (green), water (blue), sediments and soils (brown), and gaseous Hg (white). THg and MeHg are average concentration values expressed in ng.kg^{-1}, Hg^0 in TGM and DGM are in ng.m^{-3}, in the water compartment, values correspond to the sum of the particulate and filtered fractions except for wet deposition, throughfall and runoff where only the filtered fraction is displayed. The red dashed square represents an illegally mined section of the mining site, and red stars represent compartments where the presence of anthropogenic Hg was witnessed using Hg stable isotopes.*

5.1.4.2. Comparison of Hg contamination extent in different exploitation sites: impact of gold mining history, practices and progress state on Hg contamination

The following section compares Hg distribution in compartments on the Awa and Sophie mining sites, which are termed “alluvial” and “primary” mining sites hereafter.

5.1.4.2.1. Soil

As detailled in section 5.1.4.1.1, all profiles on the alluvial site displayed very similar THg concentration patterns, which were similar to oxisol profiles in the Tapajos (Roulet et al. 1998) and French Guiana (Guédron et al. 2009, Guédron et al. 2018). The profile at the primary site has similar THg at depths below 30 cm, but displayed an increased THg on the surface, which might indicate anthropogenic

contamination. However, when normalising the THg concentrations by the iron content in these soils, the differences between the alluvial and primary sites were greatly reduced (

Figure S **5.1**). This indicates that the higher surface concentration might not (only) be due to anthropogenic contamination, but rather to the presence of iron oxide carrier phases as was observed in other pristine hilltop oxisols in F. Guiana with THg concentrations above 400 $ng.g^{-1}$ (Guédron et al. 2009).

5.1.4.2.2. Mining ponds as Hg contamination archives.

Total filtered Hg in the mining ponds was similar on both mining sites, but filtered MeHg concentrations were significantly higher (p=0.00039 Kruskal-Wallis) on the primary site (0.43 ± 0.26 $ng.L^{-1}$), with a 4-fold increase in $MeHg_F$ concentrations compared to the alluvial site (0.10 ± 0.09 $ng.L^{-1}$). In the particulate fraction, on average, both THg and MeHg concentrations were higher on the primary site with a 4-fold increase in $MeHg_P$ concentrations, and a 9-fold increase in THg_P concentrations (Table S 5.2) compared to the alluvial site. As a result, the partition coefficient for THg (K_D = THg_P/THg_F) is 4 times higher on the primary site (29.2) compared to the alluvial site (7.8). However, because the MeHg concentrations increased by the same factor of four in the particulate and in the filtered fractions on the primary site, the K_D for MeHg is similar in both sites (K_D ~ 1).

The higher THg and MeHg on the primary site cannot be explained by a higher suspended particle concentration which are similarly low on both sites (27 ± 18 $mg.L^{-1}$ and 16 ± 7 $mg.L^{-1}$ on the alluvial and primary sites respectively). Instead, the higher HgP concentrations in the primary site are due to suspended particles that are enriched in both THg and MeHg compared to the alluvial site (Table S 5.2). This enrichment of the particles on the primary compared to the alluvial site might be due to an input of more contaminated particles originating from sediment resuspension. In addition, differences in particle properties including organic matter content or particle size distribution might explain the higher adsorption capacity of particles in the mining ponds on the primary site. No organic carbon (C_{org}) measurements have been performed on the particles, and particle size distribution measurements performed on a limited number of sediment samples (n= 2 and 3 on the alluvial and primary sites respectively) displayed large variabilites and no significant differences between the two sites.

The mining ponds sediments displayed significant differences in Hg concentrations, with both THg (290 – 4798, median 1550 $ng.g^{-1}$) and MeHg (1 - 4 $ng.g^{-1}$, median 2.4 $ng.g^{-1}$) being elevated on the primary site, resulting in a 13-fold and 6-fold increase compared to the alluvial site respectively (Figure 5.8B). As a comparison, the background THg concentration in river sediment was estimated to be 100 ± 50 $ng.g^{-1}$ in F. Guiana (Laperche et al. 2014). This might support the hypothesis of the enrichment of Hg in the particulate phase on the primary site originating from the resuspension of contaminated sediments, but further geochemical analyses would need to be performed on the sediments and

suspended particles to understand the geochemical control on Hg adsorption on particles. The difference in sediment contamination by anthropogenic Hg between both mining sites might be explained by differences in exploitation practices and history. On both sites, mining ponds have been worked by illegal gold miners using mercury in the process. On the alluvial site the illegal gold mining had taken place many years before (>15 years), whereas on the primary site, the mining activity was more recent and extensive.

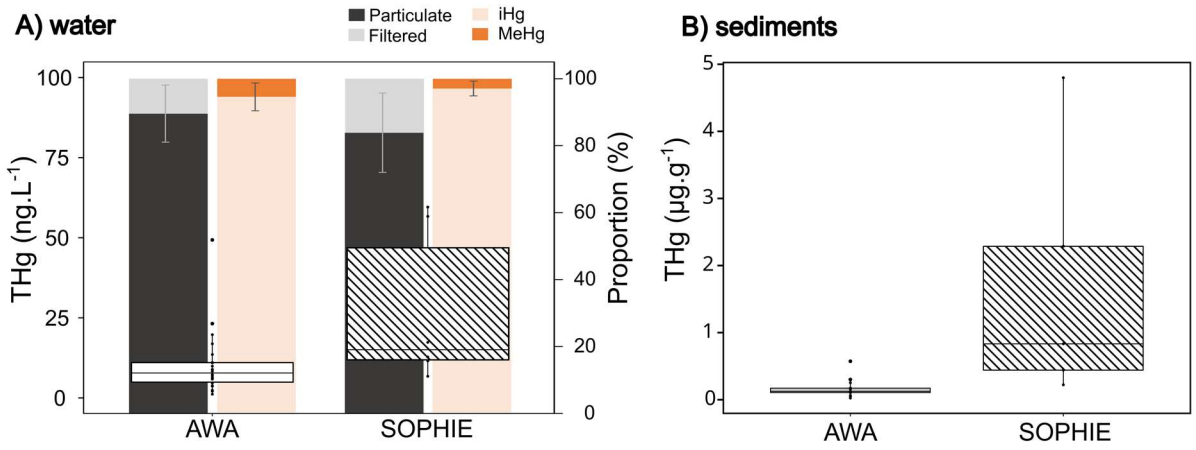

Figure 5.8. *Mercury concentration and speciation in mining pond A) water and B) sediments.*

5.1.4.2.3. Atmospheric Hg on and around mining sites.

TGM measured by active sampling on the primary mining site (4.1 ± 0.5 ng.m^{-3}) was in the same range as on the alluvial site during the same season (3.2 ± 1.1 ng.m^{-3}) and other forested or mining areas in French Guiana (Table 5.1). Passive TGM sampling from the alluvial mining site (1.4 ± 0.6 ng.m^{-3}) is similar to values in remote forests in Peru (0.70 ± 0.1 ng.m^{-3}) and Brazil (0.94 – 1.18 ng.m^{-3}), where significantly higher concentrations were measured in forests near active ASGM sites (1 – 25 ng.m^{-3}) and even higher in urban areas close to gold shops (4-500 ng.m^{-3}) (Sprovieri et al. 2016, Gerson et al. 2022, Szponar et al. 2025). Similarly, active sampling has also shown elevated TGM concentrations in and around gold shops (Hacon et al. 1995, Hachiya et al. 1998). The atmospheric compartment is thus probably a suitable indicator of anthropogenic Hg contamination only in highly active and contaminated mining/urban sites, and is not suitable to detect subtle differences close to the baseline levels (Amouroux et al. 1999).

Concerning volatilisation of Hg^0 from mining ponds to the atmosphere, the high DGM concentrations observed lead to an estimated Hg volatilisation flux density on the alluvial site (median 680 ng.m^{-2}.day^{-1}) that is above the fluxes estimated above an artificial lake in French Guiana [50 – 250 ng.m^{-2}.day^{-1}, (Amouroux et al. 1999, Muresan et al. 2007)]. These flux densities are closer to fluxes measured at the soil/atmosphere interface in French Guiana (Tessier et al. 2003) on a non-contaminated soil (240 ng.m^{-2}.day^{-1}) than a contaminated soil (24000 ng.m^{-2}.day^{-1}).

5.1.5. Conclusion

High DGM concentrations in mining ponds resulting from hotspot anthropogenic Hg^0 contamination, and/or from enhanced Hg reduction causes them to be a significant source of elemental Hg to the atmosphere.

The increased particulate Hg concentrations in the suspended particles and the sediments on the mining site with recent illegal exploitation compared to the site of past exploitation can be explained by the extent of illegal mining activity having occurred on this site in the past years, but geochemical factors like the C_{org} content might also play a role in the Hg adsorption capacity of the particles.

Hg stable isotopes demonstrated anthropogenic contamination localised primarily in and around illegal mining ponds, with legal soils displaying a pristine Hg isotopic composition. However, preliminary results hint towards a contamination of downstream sediments with anthropogenic Hg, highlighting the potential of Hg isotopes in sediments as a tool to track past illegal activities.

The isotopic data presented in plants is preliminary and more data would be necessary in order to unravel the differences in Hg sources in the parts of the plants (roots or aerial parts), the impact of anthropogenic Hg contamination in soil and atmosphere on plant Hg concentrations, and the potential translocation of atmospheric Hg from the aerial parts to the roots.

The following chapter will use the Hg isotopic composition in river sediments across the main watersheds of French Guiana to assess its potential as a tool to follow illegal gold mining.

Table 5.1. *Comparison of reported values in French Guiana of gaseous Hg in the water (DGM), in the atmosphere (TGM) and the volatilisation fluxes when available. Values are expressed as mean±SD (median).*

	Location	Sampling method	DGM	TGM	Hg volatilisation flux	reference
			$ng.m^{-3}$	$ng.m^{-3}$	$ng.m^{-2}.day^{-1}$	
Mining ponds	F. Guiana	active	2025±2000 (1276)	7.5±6.3 (5.9)	1080±1210 (680)	This study
River	F. Guiana	active	61±55 (43)	7.5±6.3 (5.9)	38±40 (24)	This study
Mining site	F. Guiana	active	–	5.4±1.6		(Amouroux et al. 1999)
Lake	F. Guiana	active	196±10	2.8±1.4	266	(Amouroux et al. 1999)
Gold mined river	F. Guiana	active	573±18	15±7	95	(Amouroux et al. 1999)
Lake	F. Guiana	active	70±40	2.4±0.4	49±24	(Muresan et al. 2007)
Soil/Air interface (non-contaminated soil)	F. Guiana	active	–	6±2	240	(Tessier et al. 2003)
Soil/Air interface (contaminated soil)	F. Guiana	active		41±30	24 000	(Tessier et al. 2003)
Forest cover	F. Guiana	active	–	4.6±2.9	–	(Guédron et al. 2018)
Remote forest	Peru	passive		0.70±0.1		(Szponar et al. 2025)
Forest near ASGM	Peru	passive		4.9±6.6		(Szponar et al. 2025)
Legal mining site	F. Guiana	passive		1.4±0.6		This study

5.1.6. Supplementary Information

Table S 5.1. *THg, MeHg and iHg concentrations (ng.g^{-1}) and proportion of MeHg (%) in soils and sediments. The results are presented as average ± standard deviation, with the median between parentheses.*

	n	THg ng.g^{-1}	MeHg ng.g^{-1}	iHg ng.g^{-1}	MeHg %
Forest topsoil	3	157±44 (128)	2.29±1.39 (2.28)	193±165(125)	1.5±1.1 (1.21)
Mine soil	22	82±60 (71)	0.34±0.40 (0.27)	82±60 (71)	0.4±0.2 (0.33)
Illegal pond sediment	13	172±168 (116)	0.41±0.22 (0.40)	171±168 (116)	0.4±0.2 (0.27)
River sediment	4	44±34 (45)	0.17±0.20 (0.17)	44±34 (45)	0.8±0.3 (0.76)

Table S 5.2. *THg, MeHg and iHg concentrations (ng.L^{-1}) and proportion of MeHg (%) in water samples. The results are presented as average ± standard deviation.*

Mining site			*Filtered*			*Particulate*				
		n	THg ng.L^{-1}	MeHg ng.L^{-1}	MeHg %	THg ng.L^{-1}	THg ng.g^{-1}	MeHg ng.L^{-1}	MeHg ng.g^{-1}	MeHg %
Awa ("alluvial")	River	218	1.3±0.8	0.06±0.02	8.1±7.9	14±8	308±78	0.11±0.05	3±2	1.1±0.9
	Illegal pond	25	1.15±0.7	0.10±0.09	8.1±8.0	9±10	276±109	0.15±0.12	5±3	2.5±2.8
	Mine runoff	38	1.6±0.9	0.03±0.02	2.4±2.4	53±70	164±25	0.13±0.08	1.1±1.2	0.71±0.7
	Wet deposition	13	2.86±1.2	0.08±0.09	3.3±3.8					
	Throughfall	10	6.3±2.8	0.18±0.2	2.8±3.3					
Sophie ("primary")	mining pond	8	2.88±3.63	0.43±0.26	26.7±15.3	84±160	7996±17474	0.56±0.21	39±17	3.4±2.6

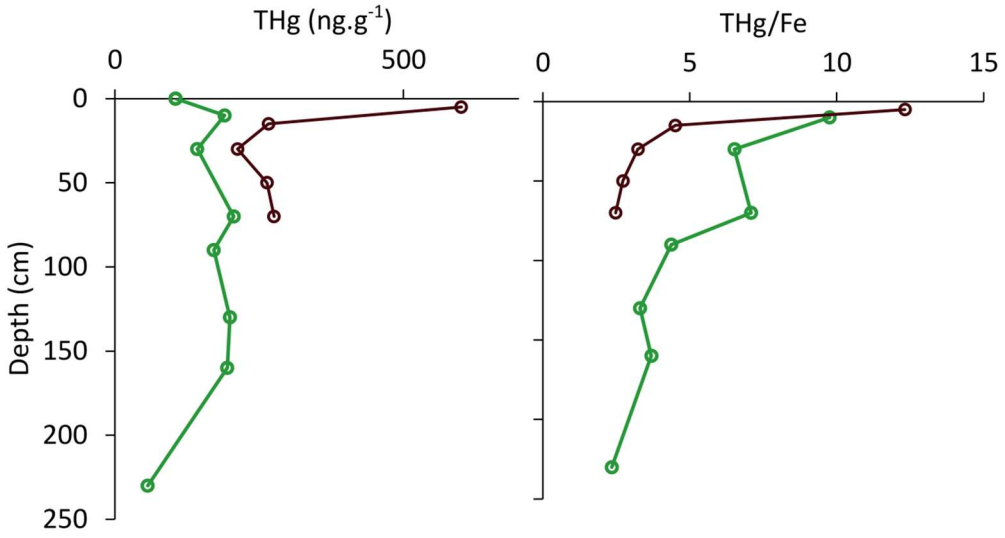

Figure S 5.1. *THg and Hg/Fe ratio for two selected soil profiles close to the Awa (green) and the Sophie (black) mining site.*

Chapter 6.

Evaluation of the Hg contamination from goldmining in French Guiana at the watershed scale using Hg isotopic composition in river sediments

Introduction

The previous chapter assessed the distribution of Hg on legal gold mining sites under the influence of past illegal activities. Preliminary results on the Awa mining site showed that the river sediment downstream of the mining site displays a less negative (i.e. more anthropogenic) Hg isotopic composition than the upstream river sediment and sediment sampled on a non-gold-mined river. However, the data presented in the previous chapter however, is not sufficient for unequivocal assessment of the impact of illegal activites on the anthropogenic Hg contribution in the river sediments. This chapter aims to take this result a step further and investigate the impact of illegal gold mining activities on anthropogenic Hg contamination in riverbed sediments at the scale of the whole territory of French Guiana. To do so, Hg isotopic composition coupled to geochemical data was measured in archive riverbed sediments across the main watersheds of French Guiana.

This chapter is based on : Nitschke, N., S. Guédron, E. Tessier, D. Tisserand, S. Campillo and D. Amouroux (2024). "Evaluation of the Hg Contamination from Gold Mining in French Guiana at the Watershed Scale Using Hg Isotopic Composition in River Sediments." ACS ES&T Water 4(8): 3443-3452. doi : 10.1021/acsestwater.4c00270

6.1. Article V – Evaluation of the Hg contamination from goldmining in French Guiana at the watershed scale using Hg isotopic composition in river sediments

Naomi NITSCHKE [a,b], Stéphane GUÉDRON [a], Emmanuel TESSIER [b], Delphine TISSERAND [a] Sylvain CAMPILLO [a], David AMOUROUX [b]**

[a] Univ. Grenoble Alpes, Univ. Savoie Mont Blanc, CNRS, IRD, IFSTTAR, ISTerre, Grenoble 38000, France

[b] Universite de Pau et des Pays de l'Adour, E2S UPPA, CNRS, IPREM, Institut des Sciences Analytiques et de Physico-chimie pour l'Environnement et les Matériaux, Pau 64000, France

*email: naomi.nitschke@univ-grenoble-alpes.fr

*email: david.amouroux@univ-pau.fr

6.1.1. Abstract

Artisanal and small-scale gold mining (ASGM) is a major source of mercury (Hg) contamination in Amazonian ecosystems, due to remobilisation of geogenic Hg from mined soil, and anthropogenic Hg used for gold amalgamation. To assess these two relative contributions, Hg stable isotope composition together with geochemical variables were determined in sediment samples collected in the early 2000s across the main watersheds of French Guiana. Mercury in sediment was found associated to organic matter and Fe/Al-oxides. Total Hg concentrations were correlated ($p < 0.001$) to both mass-dependent ($\delta^{202}Hg$) and odd-mass-independent fractionation ($\Delta^{199}Hg$) indicating that the Hg isotopic composition of river sediments reflects the extent of contamination, with two isotopic endmembers for pristine or geogenic ($\delta^{202}Hg$ = -2.53 ± 0.23 ‰, $\Delta^{199}Hg$ = -0.62 ± 0.10 ‰) and for ASGM contaminated ($\delta^{202}Hg$ = -0.42 ± 0.20 ‰, $\Delta^{199}Hg$ = -0.01 ± 0.07 ‰) sediments. A binary mixing model showed that the contribution of anthropogenic Hg in river sediments varied widely (ca. 0 to 100 %) and reflected the geographical and historical monitoring of ASGM activities in French Guiana. These results highlight that Hg isotopic measurements in archived sediments allows retrospective assessment of Hg pollution in ASGM impacted regions, and evaluation of its temporal evolution.

Keywords Artisanal and Small-scale Gold Mining; Amazon; mercury stable isotopes; river sediment; geochemistry; sources apportionment

Highlights

- Mercury isotopic composition in French Guiana's main watersheds river sediments was studied.
- Mercury in river sediments is associated to iron oxides and organic matter.
- A binary mixing model allowed the apportionment of "pristine" and "anthropogenic" Hg in river sediments.
- The contribution of anthropogenic mercury was related to the geographical extent of illegal gold mining activities in the watersheds.

6.1.2. Introduction

Mercury (Hg) use in artisanal and small-scale gold mining (ASGM) is still widespread across the Amazon basin, despite many regional countries having signed the Minamata Convention on Mercury, which bans the use of Hg due to its high toxicity (ACTO/OTCA 2018, Minamata_Convention_on_Mercury 2023). Once released in rivers, Hg can be methylated, bioaccumulated and biomagnified in food webs and methylmercury (MeHg) neurotoxicity is a risk for indigenous communities in the Amazon basin through the consumption of Hg-rich piscivorous fish (Maury-Brachet et al. 2006, Pignoux et al. 2019). The recent increase in gold prices has fuelled the expansion of ASGM activities across the Amazon basin (Hammond et al. 2007). Over the last decades, research investigations have shown that anthropogenic activities, i.e., mainly ASGM and deforestation, are involved in Hg pollution of downstream ecosystems (Telmer et al. 2006, Diringer et al. 2015, Martinez et al. 2018, AMAP/UNEP 2019). ASGM is estimated to account for around 40 % of global atmospheric Hg emissions. This number rises up to 83 % at the regional scale, in South America (AMAP/UNEP 2019), where ASGM is thought to make up to 94 % of anthropogenic Hg release to land and water (AMAP/UNEP 2019). The exact extent of contamination to terrestrial and aquatic ecosystems is however difficult to assess due to a lack of measurements in the area and the informal nature of ASGM. An evaluation method to estimate the large scale impact of ASGM pollution is thus needed.

In French Guiana, gold mining started in the 1850's and was followed by two main gold rushes peaking in the early 1900's (1870-1920 CE) and in the late 1990's (1990-2010 CE) (Hammond et al. 2007, Jébrak et al. 2021). Today, although Hg use is prohibited since 2006, the majority of ASGM activities are alluvial, and performed by illegal miners, namely "garimpeiros"(Jébrak et al. 2021) who use liquid Hg in the gold mining process. Gold (Au) is recovered after the disaggregation of alluvial deposits with high-pressure water jets creating slurries that flow over a carpeted table to preconcentrate Au gravimetrically. This practice leads to the remobilisation of fine particles naturally enriched in geogenic Hg, resulting from the accumulation in soil of atmospheric Hg taken up by vegetation over millions of years (Guédron et al. 2006, Fostier et al. 2015). Au is then separated on-site by amalgamation with Hg, which results in the contamination of the surrounding environment from direct liquid Hg losses or from the recondensation of gaseous elemental Hg emitted during the burning of the amalgam. Current ASGM also reworks historical gold mining sites, which leads to remobilisation of inherited Hg pollution and further contamination of downstream rivers, even though Hg is not used any more on the mining site (Guédron et al. 2009). Downstream, river sediments receive part of the suspended particles emitted from anthropogenic and natural erosion (Moreno-Brush et al. 2016, Lino et al. 2019). Reported background concentration in river sediment of F. Guiana (100 ± 50 $ng.g^{-1}$) (Laperche et al. 2014) are generally lower than their sourcing soil, which can reach concentrations up to hundreds of $ng.g^{-1}$

(Guédron et al. 2006, Grimaldi et al. 2008, Guédron et al. 2009, Grimaldi et al. 2015). Governmental research programs in the 2000's have used Hg levels in sediment, fish, and human hair samples for the mapping of Hg contamination and human exposure across French Guiana (Laperche et al. 2014, Maury-Brachet et al. 2019). River sediment maps are unique as they provide a large scale vision of Hg distribution between pristine and gold-mined areas. However, the use of total Hg concentration as a contamination tracer displays limitations as the local Hg level variability is often biased by high natural Hg in soils and potentially by historical ASGM (Guédron et al. 2009, Laperche et al. 2014).

An alternative to THg concentration mapping is the use of Hg isotope composition to refine Hg sources. Mercury stable isotopes display large ranges of mass dependent fractionation (δ^{XXX}Hg, MDF) and mass independent fractionation (Δ^{XXX}Hg, MIF) in natural samples (Blum and Bergquist 2007, Blum et al. 2014), and the combination of MDF and MIF enables the use of Hg isotopic data to identify contamination sources in different environments (Tsui et al. 2012, Barre et al. 2018, Goix et al. 2019). A recent study using Hg isotopes has attributed the peculiar negative MDF (δ^{202}Hg = −2.53 ± 0.23 ‰) and MIF (Δ^{199}Hg = −0.62 ± 0.10 ‰) values observed in deep pristine Amazonian soil profiles (below 0.2 m) compared to surface soils to million-years processes such as abiotic reduction and complexation to Fe/Al oxides, and potentially to a different pre-anthropogenic gaseous elemental mercury (GEM) signature compared to its modern signature (Guédron et al. 2018). The contrast between the isotopically lighter signature of pristine soils versus the heavier ones of soils contaminated by anthropogenic Hg used in ASGM allowed the use of Hg isotopes to apportion the respective contribution of these two sources of Hg in river sediment close to illegal ASGM sites and in a pristine region (Goix et al. 2019). On the other hand, the Hg contamination downstream of ASGM sites in a smaller watershed in the Brazilian Amazon was hypothesised to result mainly from remobilised Hg from soil erosion as the isotopic signatures of downstream sediments were consistent with those of deforested soils (δ^{202}Hg = −1.73 ± 0.14 ‰) (Adler Miserendino et al. 2018). Yet, it is thus not clear whether Hg isotopic data can be used universally to trace anthropogenic Hg contamination sources.

In this study, we determined the Hg stable isotope composition together with geochemistry of archived sediment samples from the 2000's, spanning across the main rivers of F. Guiana including samples collected from pristine and ASGM sites impacted by Hg contamination. The aim is to establish whether the Hg isotopic composition can be used as a monitoring tool for discrimination between geogenic and pristine Hg in sediments, and thus assess the degree of anthropogenic Hg contamination not only at the local scale, but also at the watershed scale. To do so, δ^{202}Hg and Δ^{199}Hg isotopic values with sediment geochemistry and watershed sub-basin ASGM geographical extent were further investigated.

6.1.3. Materials and Methods

Research area and sample collection. French Guiana (87,500 km²) is part of the Guiana shield located in the north-eastern region of South America between Brazil and Surinam (2-6°N and 51°30'-54°30'W). The main rivers of French Guiana are the Maroni, Oyapock, Mana, Sinnamary, Comté (by watershed size). It experiences an equatorial humid climate with average annual rainfall of around 4000 mm and 96 % of the territory is covered by a tropical rainforest.

In French Guiana, the majority of historical and current gold-mining sites are located on and around the northern and southern greenstone belts (Figure 6.1). These rocks were formed during the Trans-Amazonian Orogeny between 2.26 and 1.98 Ga and typically contain gold deposits associated with pyrite or arsenopyrite minerals (Kroonenberg et al. 2019).

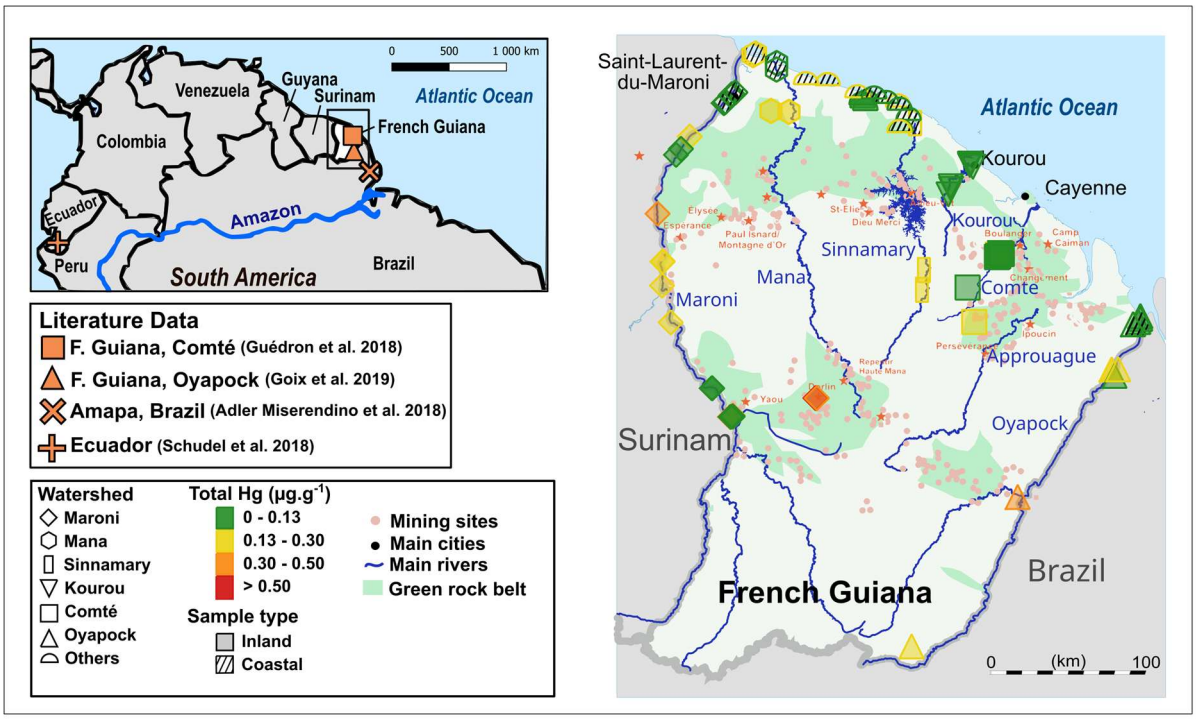

Figure 6.1. *Map of South America (Top left) with location of published mercury isotopic data in tropical sites (Adler Miserendino et al. 2018, Guédron et al. 2018, Schudel et al. 2018, Goix et al. 2019). Map of French Guiana (right) with the location of sediment sampling points (2003-2005). Symbol colours indicate the range of total Hg concentration in sediment and symbol shapes indicate the watershed it was sampled on.*

Mercury in French Guiana is monitored since the 1990s through different research programs (Carmouze and Lucotte 2001, Grimaldi et al. 2002). Sixty-two samples were retrieved from a sediment sample archive from the "Mercury in French Guiana program", which combined scientific field trips and participative science (i.e., local fishermen and schools). Selected sediment samples were collected between 2002 and 2005, and include sediment from the Maroni, Oyapock, Comté rivers and coastal ones collected a few kilometres above their connection to the Atlantic sea (Figure 6.1). The samples were collected on river banks, focussing on meanders, where fine particles tend to accumulate.

Collected samples were then freeze-dried, and ground at a size <63 µm before being stored at room temperature at ISTerre (Grenoble, France).

Chemical analysis. Total mercury (THg) analyses had been performed on the sediment samples in the year after sampling (2003-2005), and to ensure the quality of preservation of these samples, THg concentration was re-analysed on the entire set of selected samples in 2021. THg was analysed by atomic absorption spectroscopy after pyrolysis and gold amalgamation (AMA 254, Altec) with a relative precision of ± 5 % determined from triplicates, consistently with typical relative errors reported for this analyser (Roos-Barraclough et al. 2002, Guédron et al. 2009). The total mercury concentrations measurements were validated with the certified reference materials (IAEA-456 coastal sediment, ERM CC141 loam soil) and were always within the published range (0.077 ± 0.005 $\mu g.g^{-1}$ and 0.083 ± 0.017 $\mu g.g^{-1}$ respectively). The detection limit (defined as three times the standard deviation (SD) of the blank) was at maximum 0.005 $\mu g\ g^{-1}$. The sediment samples show good THg concentration conservation, within the analytical error, 10 years after sampling (Figure S 6.1).

The concentration of trace (i.e. As and Zn) and major (Al, Fe, Mg, Mn, S, Ti, and Ca) elements was measured by ICP-AES (Agilent, Varian 720-ES) after microwave (ultraWAVE, Milestone) assisted acid digestion (HNO_3, H_2O_2) at 85°C. Accuracy of the measurements was evaluated based on the analysis of certified reference materials (NIST 1944 and IAEA-405) for sediment samples.

Total organic carbon (TOC) content and isotopic composition (δ^{13}Corg) of sediment were measured by Cavity Ring-Down Spectrometer (Picarro, Inc.®) coupled with Combustion Module (Costech, Inc.®) (CM-CRDS) using previously reported analytical methods, calibration, and sample preparation (Balslev-Clausen et al. 2013, Guédron et al. 2019).

Mercury Stable Isotopes Analysis. For each sample, appropriate amounts (between 0.1 to 0.5 g) were weighed in discardable glass vessels and digested in 4 mL HNO_3 using the Milestone ultraWAVE digestion system using the following parameters : 110 bar, 240 °C, 40 min for sediment samples. Then, 1 mL H_2O_2 was added to the sediment samples which were heated at 85°C overnight. All sample extracts were then centrifuged 3 min at 3400 rpm and the supernatant was collected and diluted for isotopic measurements to a final Hg concentration of 0.5 $ng.mL^{-1}$ in 10 % HNO_3, 2 % HCl. The sample digestion protocol was validated by the digestion of soil and sediment reference materials used in previous studies for "matrix matching" secondary standards : NIST-SRM-1944, IAEA-405), under equivalent conditions. The isotopic data of these reference materials measured in this study is in agreement with previously published values (Sherman and Blum 2013, Janssen et al. 2015, Bérail et al. 2017, Guédron et al. 2018)

Hg isotope analyses were performed using cold vapour generation with $SnCl_2$ reduction coupled to an MC-ICP-MS instrument (Nu Plasma, Nu Instrument) following similar protocols as previously published (Jiménez-Moreno et al. 2016, Guédron et al. 2018). Briefly, the instrumental mass bias was corrected

using a Tl internal standard (NIST SRM 997 $^{205}Tl/^{203}Tl$ = 2.38714) as well as sample-standard bracketing using the NIST 3133 standard solution. Most of the samples and standards were analysed at 0.5 ppb of Hg, except for sediment samples S57-S67, which were analysed and bracketed at 1 ppb. All isotopic data is provided in Table S 6.2.

Hg isotopic ratios are reported as δ relative to the ratio measured in the NIST 3133 :

$$\delta^{XXX}\mathrm{Hg}\ (‰) = \left(^{xxx/198}\mathrm{Hg}_{\mathrm{sample}}/^{xxx/198}\mathrm{Hg}_{\mathrm{NIST\ 3133}} - 1\right) \times 1000$$

Where xxx is the studied mercury isotope between ^{199}Hg and ^{204}Hg. The MIF, reported as Δ, is the difference between the theoretical value predicted by the MDF of δ^{xxx}Hg and the measured values.

$$\Delta^{xxx}\mathrm{Hg}\ (‰) = \delta^{xxx}\mathrm{Hg} - \delta^{202}\mathrm{Hg} \times \beta_{xxx}$$

Where the β_{xxx} corresponds to 0.2520, 0.5024, 0.7520 and 1.493 for ^{199}Hg, ^{200}Hg, ^{201}Hg and ^{204}Hg isotopes respectively. The analytical uncertainty was evaluated by multiple measurements (n=39) of the NIST RM 8610 reference material, certified for Hg isotopes (Table S 6.3). The analytical methods have been validated with several primary and secondary standards (NIST 3133, NIST RM 8610) certified for Hg isotopes and reference materials not certified for Hg isotopes but with published reference values. Isotopic data results for CRMs (i.e. CRM NIST RM 8610, NIST-SRM-1944, IAEA 405) are given in Table S 6.4 and compared with previously published results.

Extraction recoveries were estimated based on the multicollector signal of the sample and compared to the total Hg measured by AMA-254 before digestion (av. recovery = 110 ± 16 %).

The external reproducibility (2SE) of all samples was determined by measuring replicates of selected samples (n=14). The analytical uncertainty (2SD) determined using the NIST RM 8610 (n=39) was always higher than the external reproducibility (2SE) of measured samples (n=14), so the analytical uncertainty was used to describe variability of measured samples.

Statistical analysis. Statistical analyses were performed using R. Data was assessed for normal distribution using a Shapiro-Wilk test and for homoscedasticity. When the results were not normally distributed, non-parametric Kruskal-wallis and Mann-Whitney-Wilcoxon tests were used to compare sets of data. Linear regressions were performed and correlation coefficient (R) and p-values are reported.

6.1.4. Results and Discussion

6.1.4.1. Legacy of gold mining in French Guiana and Hg carrier phases in sediment

The average THg concentration in river sediments (av. ± SD = 0.40 ± 0.82 $\mu g.g^{-1}$, median = 0.150 $\mu g.g^{-1}$) is in the range of reported values measured in river sediments from French Guiana (0.10 ± 0.05 $\mu g.g^{-1}$) (Laperche et al. 2014, Goix et al. 2019), Surinam (0.07 – 0.22 $\mu g.g^{-1}$) (Ouboter et al. 2012), and in the Amazon basin (Tapajos, Brazil, 0.02 – 0.155 $\mu g.g^{-1}$) (Lino et al. 2019). The high variability of these concentrations is due to the presence of sediments from well-known major historical mining sites, such as Dorlin on the Maroni watershed (2.17 $\mu g.g^{-1}$) and Camopi on the Oyapock watershed (0.45 $\mu g.g^{-1}$), which display concentrations 4- to 22-fold above the average background concentration in sediments determined for F. Guiana of 0.10 ± 0.05 $\mu g.g^{-1}$ (Figure 6.1) (Laperche et al. 2014). However, no significant difference in THg concentration between any of the different watersheds is observed (Kruskal-Wallis, p = 0.08). This highlights that the distribution of THg concentration does not allow the differentiation of the main anthropogenic impact due to gold mining between the different watersheds of French Guiana. Such variability could result both from point sources Hg contamination due to ASGM and from variable THg geochemical background along the watershed.

To determine Hg carrier phases in sediments, we performed a principal component analysis (PCA) of THg with major elements concentrations and total organic carbon (TOC). PCA of all the major elements emphasizes the geochemical distinction between coastal sediment samples and the other samples (inland samples). The coastal samples display significantly higher concentrations of Zn, Mg, Mn, S, Ca and Fe (Figure S 6.2 and

Figure S **6.3**), possibly due to marine inputs or sedimentary inputs from the Amazon River, as river sediment from the Amazon was found to display significantly higher Mg and Zn concentrations than on the Maroni river, and in comparable concentrations with those measured here in coastal samples (Bouchez et al. 2011, Rousseau et al. 2019).

When focusing on the inland data of the main watersheds, THg concentration was found positively correlated with TOC (R^2=0.65 and 0.79, p=0.03 and p=0.001 respectively) and sulfur (R^2=0.94 and p<0.01 for both watersheds) concentrations for both the Oyapock and the Comté watersheds. Total sulfur concentrations have been shown to display strong correlations to organic matter and to organic sulfur in tropical soils of South American soils (David et al. 1982, Figueiredo et al. 2018, Vanolli et al. 2024). This corroborates previous regional studies, which reported OM, and more specifically its sulfur functional groups, as a major carrier phase of Hg in F. Guiana soils (Grimaldi et al. 2008).

THg concentrations were also found correlated to Al (R^2=0.59 and 0.97, p=0.02 and $1x10^{-5}$ for Oyapock and Comté watersheds respectively), and to a lesser extent to Fe (R^2=0.52 and p=0.03 only for the Comté watershed). This can be explained by the fact that Hg has a strong affinity to iron oxides, and Al

substitutions can occur in amorphous or poorly crystallised oxides. The Hg binding capacity of these Fe-oxides is thus increased when Al substitutions occur due to the larger surface area of the oxide and atomic ordering defects (Grimaldi et al. 2008, Guédron et al. 2009). Hg has also been found to be associated with Al minerals in F. Guiana and Surinam such as gibbsite (Guédron et al. 2009, Kroonenberg et al. 2022), which can explain this strong correlation.

The affinity of Hg to carrier phases and the sediment geochemical characteristics are variable in French Guiana watersheds due to large changes in the hydrological regimes, sediment transport, and disparate extent of human activities such a ASGM. As a consequence, the determination of Hg sources based solely on geochemical parameters and Hg associations is challenging, and other parameters needs to be taken into account such as Hg stable isotopes composition.

6.1.4.2. Spatial variability and significance of isotopic signatures

The mass-dependent isotopic fractionation (MDF) of Hg in sediments across French Guiana watersheds exhibits a large range of negative values for δ^{202}Hg (-2.82 to -0.43‰). Odd mass independent isotopic fractionation of Hg (odd-MIF) display a lower variability with similar results on the Δ^{199}Hg (-0.70 to 0.13 ‰) and Δ^{201}Hg (-0.69 to 0.00 ‰). For all sediment samples, the Δ^{201}Hg vs. Δ^{199}Hg plot follows a linear relation with a slope of 1.00 (Figure S 6.4) consistent with reported fractionation during photochemical reduction of inorganic mercury in aquatic systems (Bergquist and Blum 2007). For several investigated sites (n=5), replicates were sampled in the geographical zone within a radius below 2km. The intra-site variability, i.e., the average standard deviation (SD) of both δ^{202}Hg (0.16‰) and Δ^{199}Hg (0.10 ‰) of samples within one site was close to the analytical uncertainty (2SD of NIST RM 8610 = 0.13 and 0.09 ‰, for δ^{202}Hg and Δ^{199}Hg respectively), indicating that each site exhibits a well constrained isotopic composition. On the other hand, the inter-site variability of δ^{202}Hg and Δ^{199}Hg was much larger (3.6 and 2-fold respectively) than their intra-site variability, indicating that in most cases different sampled sites display distinct isotopic compositions of Hg between sites (Table S 6.3).

MIF of even isotopes (Δ^{200}Hg and Δ^{204}Hg) is not different from zero considering the analytical uncertainty (0.08‰ and 0.39‰ respectively) with Δ^{200}Hg = -0.04 ± 0.04 ‰ and Δ^{204}Hg = 0.07 ± 0.09 ‰. No statistical difference in Δ^{200}Hg was observed between samples with high THg concentrations (> 300 ng.g^{-1}) and low THg (< 300 ng.g^{-1}) ($p = 0.167$). Δ^{200}Hg values are in agreement with isotopic values in tropical forest soils and litter in French Guiana, Brazil and China (Guédron et al. 2018, Xia et al. 2022, Richter et al. 2023), and with those of atmospheric Hg^0 on a forested site (Yuan et al. 2021), further supporting the finding that globally, soil Hg mainly originates from atmospheric Hg incorporation into leaves and subsequent litterfall (Jiskra et al. 2015).

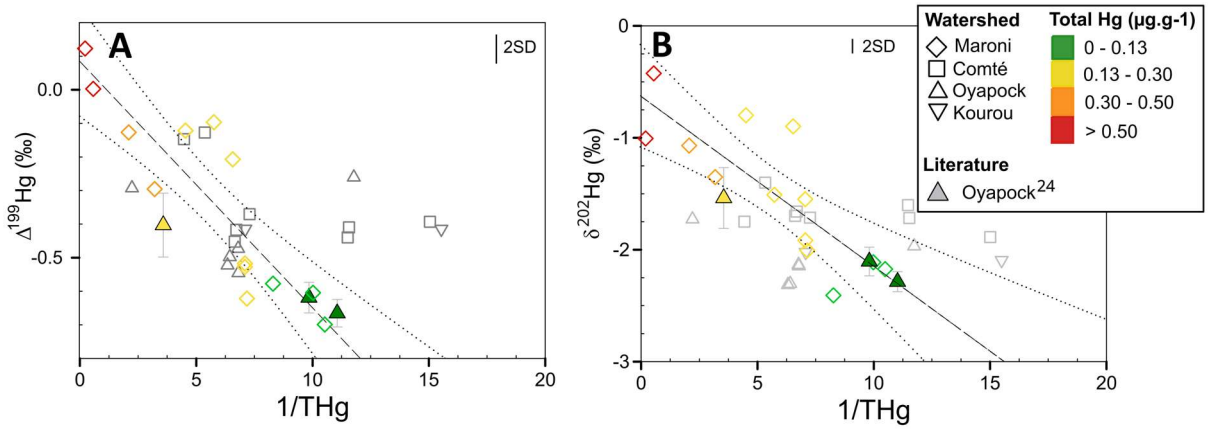

Figure 6.2. *Mass-independent fractionation ($\Delta^{199}Hg$) (A) and mass-dependent fractionation ($\delta^{202}Hg$) (B) vs the inverse of the total mercury concentration. The symbol colour represents the total Hg concentration of the sample and the symbol shape represents the watershed it was sampled on. Empty symbols represent data from this study with coloured for the Maroni river, and grey for data from other watersheds. Datapoints with fill and black border represent data from the literature on the Oyapock watershed, F. Guiana (Goix et al. 2019). Regression line (dashed line) only considers samples from the Maroni River with R^2 of 0.78 and 0.67 for $\Delta^{199}Hg$ and $\delta^{202}Hg$, respectively, and the 95 % confidence interval is represented by dotted lines.*

To apportion Hg sources, Hg isotopic composition was plotted against the inverse of the THg concentration. The Maroni river, which has the largest watershed in French Guiana, was first considered as most of the sediments were sampled (n=13) over a wide geographical area. Two groups of samples can be distinguished, i.e., i) samples with low THg concentrations, which display negative isotopic composition both for $\delta^{202}Hg$ and $\Delta^{199}Hg$, and ii) contaminated samples from known mining sites (e.g. Dorlin), which have both $\delta^{202}Hg$ and $\Delta^{199}Hg$ close to 0 (Figure 6.2). Extrapolation of the linear regressions allows the estimation of the isotopic composition of the contamination source on the Maroni watershed ($\delta^{202}Hg$ = -0.42 ± 0.20 ‰ and $\Delta^{199}Hg$ = 0.08 ± 0.07 ‰), which displays similar isotopic compositions to the one reported for liquid elemental Hg used by illegal gold miners (Laffont et al. 2011, Goix et al. 2019). This relationship between THg isotopic composition and concentration was not observed for other watersheds, possibly due to the limited amount of sampling sites and geographical data available on these rivers.

The biplot of $\delta^{202}Hg$ versus $\Delta^{199}Hg$ (Figure 6.3) shows that almost all isotopic compositions of sediment samples can be plotted along a linear trend and separated in two pools, i.e., i) pristine sediments displaying negative $\delta^{202}Hg$ and $\Delta^{199}Hg$ values, and ii) sediments contaminated with anthropogenic Hg displaying $\delta^{202}Hg$ and $\Delta^{199}Hg$ values closer to the anthropogenic Hg composition determined for the Maroni watershed in the previous section. A pristine sample collected at Trois Saut on the Oyapock watershed, on a river branch upstream of any ASGM activity displays the lowest isotopic composition ($\delta^{202}Hg$ =-2.31‰ and $\Delta^{199}Hg$=-0.49‰), whereas samples at the Dorlin mining site on the Maroni watershed have a higher isotopic signature closer to anthropogenic Hg ($\delta^{202}Hg$ = -0.84 ± 0.36 ‰ and $\Delta^{199}Hg$ = -0.00 ± 0.12 ‰). All other samples are distributed between these two end-members while

total Hg concentrations are not always correlated. On the Comté watershed, isotopic values are consistent with those of previous studies in the area, which reported very low isotopic composition (δ^{202}Hg = -2.43 ± 0.28 ‰ and Δ^{199}Hg = - 0.55 ± 0.11 ‰) in pristine soils compared to former and contaminated ASGM impacted soils that have isotopic composition similar to liquid Hg samples (δ^{202}Hg = -0.43 ± 0.32 ‰ and Δ^{199}Hg = -0.07 ± 0.08 ‰) (Guédron et al. 2018). In the eastern part of F. Guiana, Hg isotopic composition of the Oyapock River sediments also follows the same trend, with pristine sediments characterized by lower isotopic signatures (δ^{202}Hg = -2.29 ± 0.09 ‰ and Δ^{199}Hg = -0.66 ± 0.04 ‰), and sediments collected downstream of active ASGM with a higher isotopic signature (δ^{202}Hg = -1.54 ± 0.27 ‰ and Δ^{199}Hg = -0.40 ± 0.10 ‰) (Goix et al. 2019).

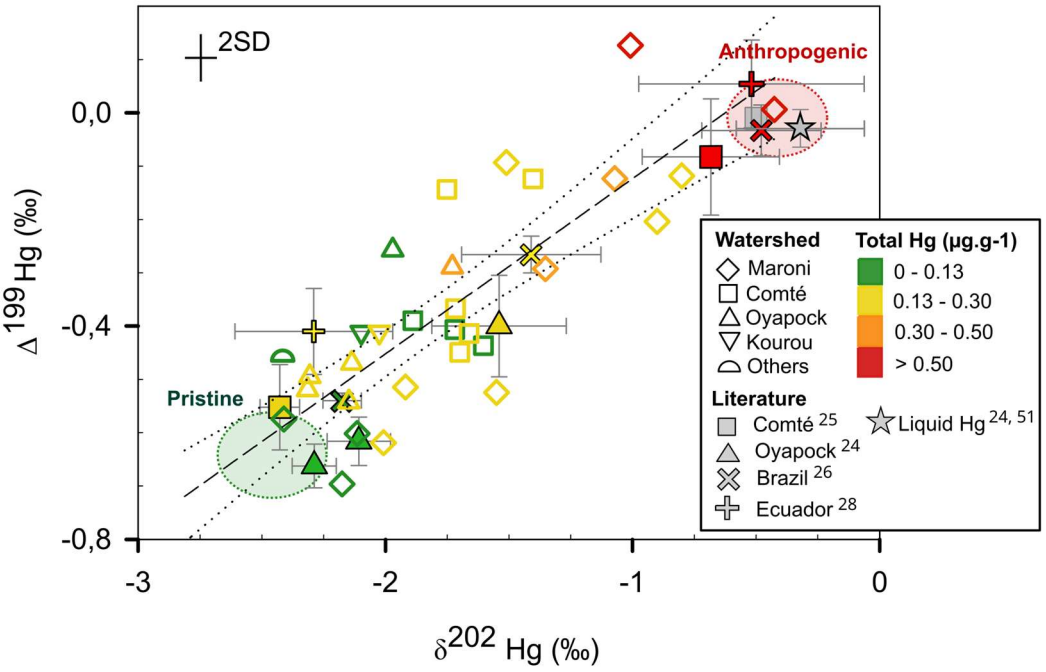

Figure 6.3. *Mass-independent fractionation (Δ^{199}Hg) vs mass-dependent fractionation (δ^{202}Hg) in sediment samples from this study (empty symbols) and comparison with literature data (filled symbols) in Amazonian regions of South America (Laffont et al. 2011, Adler Miserendino et al. 2018, Guédron et al. 2018, Schudel et al. 2018, Goix et al. 2019). The equation of the regression (dashed line, this study) is $\Delta^{199}Hg = 0.33 * \delta^{202}Hg + 0.23$, with the 95 % confidence interval in dotted lines. The symbol colour represents the total Hg concentration of the sample and the symbol shape represents the watershed it was sampled on. The pristine endmember (green circle) was determined using literature data of deep-soils in French Guiana (Guédron et al. 2018, Goix et al. 2019) and the anthropogenic (red circle) was determined using literature data of liquid Hg used in ASGM (Laffont et al. 2011, Goix et al. 2019) and highly contaminated soils in F. Guiana (Guédron et al. 2018) and Ecuador (Schudel et al. 2018).*

On a larger scale, this French Guiana dataset bears similarities with Hg isotope data from other countries from the Amazon region. Pristine forest soils generally display similar values, with very negative MDF and MIF, in agreement with pristine soils and sediments in F. Guiana (Guédron et al. 2018, Goix et al. 2019), in Amapá (northern Brazil, δ^{202}Hg = -2.18 ± 0.08 ‰ and Δ^{199}Hg = -

0.54 ± 0.01 ‰) (Adler Miserendino et al. 2018), southern Brazil (δ^{202}Hg = -1.86 ± 0.27 ‰ and Δ^{199}Hg = -0.57 ± 0.06 ‰) (Richter et al. 2023) or Ecuador (δ^{202}Hg = -2.29 ± 0.13 ‰ and Δ^{199}Hg = -0.41 ± 0.16 ‰) (Schudel et al. 2018). In contrast, mine tailing samples from Ecuador (δ^{202}Hg = -0.52 ± 0.24 ‰ and Δ^{199}Hg = 0.05 ± 0.05 ‰) (Schudel et al. 2018) and Amapá (δ^{202}Hg =-0.48 ± 0.28 ‰ and Δ^{199}Hg = -0.03 ± 0.03 ‰) (Adler Miserendino et al. 2018) have isotopic compositions (MDF and MIF) close to zero, and similar to contaminated sediments (this study) and contaminated soils in F. Guiana (Guédron et al. 2018). The Hg isotopic composition of sediment samples downstream of ASGM sites in the amazonian region of Amapá, Brazil are distributed in-between these two poles (δ^{202}Hg = -1.41 ± 0.19 ‰ and Δ^{199}Hg = -0.27 ± 0.04 ‰) (Adler Miserendino et al. 2018) suggesting some extent of anthropogenic Hg contamination in these sites. All these data in South America appear to show that the isotopic composition of Hg in sediment or soil is dictated by the extent of anthropogenic Hg contamination, leading to increase the δ^{202}Hg and Δ^{199}Hg to values closer to zero (i.e. less negative).

6.1.4.3. Assessment of anthropogenic and geogenic Hg contribution in F. Guiana watersheds.

In order to evaluate the contribution of anthropogenic Hg in each sample, a binary mixing model was established based on the Hg isotopic composition of the two poles(pristine and contaminated) previously described. These poles are subsequently defined as pristine and anthropogenic "endmembers" and were determined using published literature data. The pristine endmember signature was defined using Hg isotopic data of pristine soils sampled in French Guiana. Surface organic soil samples (including litter) were excluded to avoid possible impact of anthropogenic Hg contribution from recent atmospheric Hg deposition mainly via litterfall. The data includes pristine B and C soil horizons (below 0.5 m) collected close to the Oyapock (Goix et al. 2019) and Comté (Guédron et al. 2018) rivers in F. Guiana. This results in a pristine isotopic signature for both MDF and MIF respectively, of δ^{202}Hg = -2.53 ± 0.23 ‰, Δ^{199}Hg = -0.62 ± 0.10 ‰ and Δ^{201}Hg = -0.59 ± 0.07 ‰. This pristine endmember value is similar, albeit significantly more negative (0.43 ‰ average shift for δ^{202}Hg and 0.15 ‰ for Δ^{199}Hg) than values obtained in Ecuador (Schudel et al. 2018) and Brazil (Adler Miserendino et al. 2018, Richter et al. 2023) forest soils. This is probably due to the fact that all the soils measured in these studies were topsoils (0-10 cm or less). A shift of isotopic composition to more negative values from surface to deeper horizons has been documented in F. Guiana soils (Guédron et al. 2018). The shift in MIF Δ^{199}Hg values was hypothesised to be due to a change in atmospheric gaseous elemental mercury (GEM) isotopic signature or due to non-photochemical abiotic reduction of inorganic Hg by dissolved organic matter (DOM) (Zheng and Hintelmann 2010) while the change in δ^{202}Hg might result from fractionation of Hg when binding to OM and iron oxides, enriching the mineral horizons in lighter

isotopes (Gray et al. 2013, Enrico et al. 2017). A similar trend in Δ^{199}Hg isotopic composition with depth was also observed in tropical latosols in China (Gao et al. 2023).

The anthropogenic endmember was determined by compiling data of the signature of liquid elemental mercury from Amazonian ASGM sites in F. Guiana and Bolivia (Laffont et al. 2011, Goix et al. 2019), as well as highly contaminated soils (above 1 ppm) on South American ASGM sites (Guédron et al. 2018, Schudel et al. 2018), including French Guiana. The resulting signature of the anthropogenic endmember was δ^{202}Hg = -0.42 ± 0.20 ‰, Δ^{199}Hg = -0.01 ± 0.07 ‰ and Δ^{201}Hg = -0.01 ± 0.07 ‰, in close agreement with Hg isotopic data of sediments in Brazilian active mining tailing ponds as well as Hg ores in Europe (Gray et al. 2013, Jiménez-Moreno et al. 2016, Adler Miserendino et al. 2018) and commercial liquid Hg (Sun et al. 2016).

From these two end-members, a binary mixing model was established to evaluate the percentage of Hg originating from anthropogenic contamination on each sampling site. The model was performed both with δ^{202}Hg and Δ^{199}Hg values. δ^{202}Hg data display the broadest range of values, allowing to better discriminate between sampling location signatures. However, Hg isotopes might be subject to a variety of processes inducing MDF, which could induce a bias in the calculation of anthropogenic Hg contribution. Processes inducing MDF of Hg isotopes in river sediments include, for instance, geochemical changes in mercury speciation and carrier phase or microbial reduction and methylation (Fu et al. 2007, Kritee et al. 2007, Wiederhold et al. 2010, Jiskra et al. 2012, Reinfelder and Janssen 2019). In contrast, Δ^{199}Hg data show a narrower range of values, and the differences observed are closer to the analytical uncertainty. The main process known to produce significant mass independent fractionation is the photochemical reduction of Hg^{2+} to Hg^0, observed in river systems (Bergquist and Blum 2007, Carignan et al. 2009, Clarke et al. 2023), and to a lesser extent dark abiotic reduction by DOM (Zheng and Hintelmann 2010). The limited extent of these processes makes the calculations of contamination apportionment using the Δ^{199}Hg in the binary mixing model more accurate, even if the associated precision might be lower. The equations used for the binary mixing model are the following :

$$\Delta^{199}Hg_s = \Delta^{199}Hg_{anth} * f + \Delta^{199}Hg_{nat} * (1 - f)$$

$$\delta^{202}Hg_s = \delta^{202}Hg_{anth} * f + \delta^{202}Hg_{nat} * (1 - f)$$

Where Hg_s is the isotopic signature of the considered sample, Hg_{anth} is the signature of anthropogenic Hg used in illegal gold mining, and Hg_{nat} the natural or pristine signature of Hg in soils as previously defined. The fraction of anthropogenic Hg was derived from these equations and its distribution was compared where enough data was available (i.e. 3 watersheds : Maroni, Oyapock and Comté rivers). The trends observed are in agreement using either Δ^{199}Hg data or δ^{202}Hg, enabling the visualisation of the extent of ASGM impact on Hg contamination in rivers at the watershed scale as well as the sub-watershed scale (Figure 6.4 and Figure S 6.5). Results show that the contribution of anthropogenic Hg

in river sediment vary within and in-between the different studied watersheds. Major differences are observed along the Maroni river, which shows evidence of highly impacted sediments close to ASGM sites (i.e. Dorlin) with anthropogenic Hg contribution ranging between 80 to 100 %. In contrast, an upstream site on the Maroni river (Papaïchton) displays only limited or close to zero anthropogenic Hg contribution during the sampling period (< 20 %).

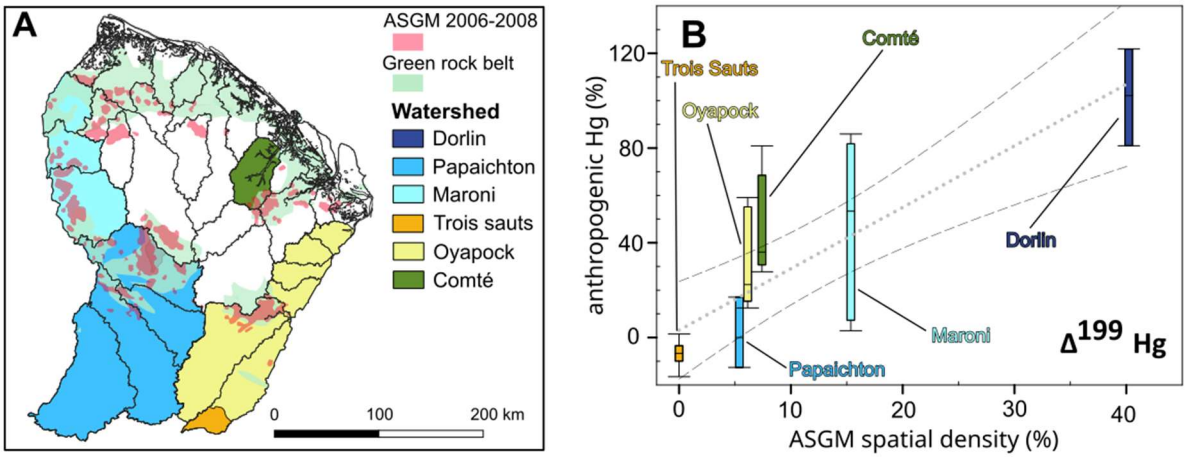

Figure 6.4. *Map of French Guiana coloured by watershed and surface of ASGM in light red (A) and theoretical contribution of anthropogenic mercury in sediment samples using a binary mixing model, with the MIF Δ^{199}Hg data from this study and from the literature (Goix et al. 2019) (anthropogenic Hg (%)) versus the ASGM spatial density as derived from the map (B). The regression Hg_{anth} = 3.49 + 2.60*ASGM-density, R^2 = 0.91, p = 0.0031, with the 95 % confidence interval in dashed lines.*

Interestingly, the ASGM spatial density was estimated right after the period of sediments collection (2006-2008) for each watershed or sub-watershed using an ASGM geographic database obtained from satellite observations (Blancodini 2019). The median anthropogenic Hg contribution for each territory estimated from the model appears to be correlated to the ASGM spatial density in each watershed or portion of a watershed, whether using Δ^{199}Hg (Figure 6.4, R^2 = 0.91, p = 0.0031) or δ^{202}Hg (Figure S 6.5, R^2 = 0.88, p = 0.0057) isotopic signature, thus giving an independent validation to the isotopic apportionment model.

6.1.5. Conclusion

Our results demonstrate that the regional spatialisation of Hg isotopic signatures in river sediment enables an estimation of the extent of ASGM impact at the scale of a site or territory, and to compensate bias of concentration maps, i.e., from abnormally high levels due to the contribution of Hg-rich geogenic particles remobilised during ASGM operations. Limitations still exist as the remobilisation of ancient anthropogenic Hg in ongoing ASGM cannot yet be distinguished, and little information is available about the stocks of anthropogenic Hg buried in soils as a heritage of historical and recent ASGM activities. Further investigation should therefore focus on the isotopic composition of ancient and modern anthropogenic Hg to test the possibility of a change in source or signatures with time. Replicating such "isotope mapping" exercise over time will enable us to assess the impact of these activities in recent decades. Knowledge on the residence time of sediments in rivers is also still partial, and refining this parameter will improve the temporal representativity of sediments.

In the intertropical region (i.e., mainly Africa and South America), the contributions of ASGM to global Hg emissions (Esdaile and Chalker 2018, AMAP/UNEP 2019) is poorly constrained due to the difficulty of accessing sites (i.e., remote areas in tropical forests) and to insecurity problems inherent in these predominantly illegal activities, which do not allow for long- or medium-term monitoring of operations. Our results also demonstrate that available Hg isotope data (i.e., δ^{202}Hg and Δ^{199}Hg) from rivers sediments over the Amazon, all align between an anthropogenic endmember defined as the signature of liquid elemental mercury and a pristine endmember with the most negative isotopic values. This supports the possibility to extend this approach to the Amazon region scale and refine the assessment of ASGM Hg contribution to the contamination of terrestrial and aquatic environments. This would have further implications for monitoring the large scale impact of ASGM on Hg pollution as the use of archive samples to perform retrospective investigations allows to enhance the value of these samples which often result from remote locations and expensive field campaigns.

Graphical Abstract

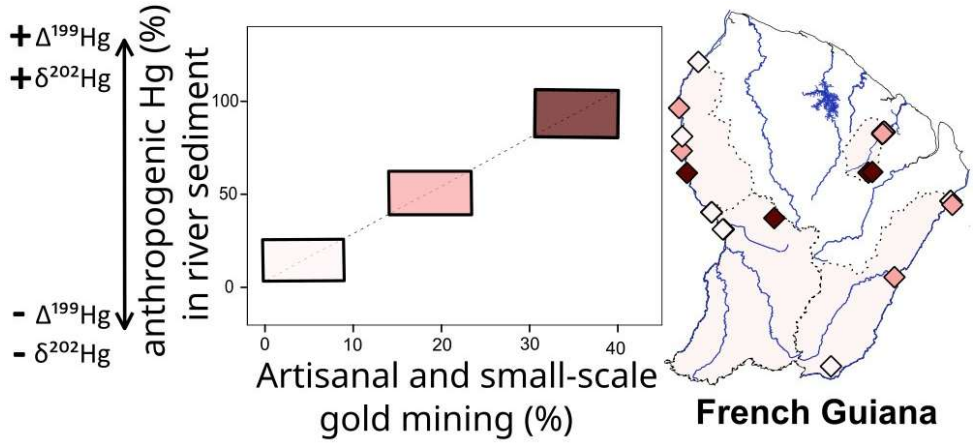

6.1.6. Supplementary Information

Table S 6.1. *Raw data for sediment samples : Total mercury (Hg), major elements (Al, As, Ca, Fe, Mg, Mn, S, Ti, Zn), carbon (C), and $\delta^{13}C$ isotopic data ($\delta^{13}C$-VPDB).*

	Watershed	Site	Latitude	Longitude	Hg	Al	As	Ca	Fe	Mg	Mn	S	Ti	Zn	C	d13C-VPDB
					µg.g-1	mg.g-1	mg.g-1	mg.g-1	mg.g-1	mg.g-1	mg.g-1	mg.g-1	mg.g-1	mg.g-1	%	‰
S-19	Comte	Cacao	-52.663	4.389	0.177	N/A	<LD	0.38	16.6	0.26	0.08	0.56	0.14	0.02	3.38	-29.94
S-33	Comte	Cacao	-52.488	4.579	0.137	71.6	<LD	1.34	31.3	0.98	0.24	0.48	0.08	0.07	3.92	-30.09
S-45	Comte	Cacao	-52.465	4.583	0.086	53.7	<LD	1.22	22.4	0.73	0.16	0.33	0.06	0.05	2.35	-30.11
S-48	Comte	Cacao	-52.485	4.572	0.066	43.0	<LD	1.21	19.0	0.73	0.16	0.31	0.06	0.04	1.46	-29.91
S-64	Comte	Cacao	-52.474	4.588	0.149	75.7	<LD	1.82	35.7	1.02	0.21	0.47	0.08	0.07	3.35	-30.16
S-65	Comte	Cacao	-52.493	4.565	0.150	88.9	<LD	1.40	30.1	0.92	0.12	0.54	0.08	0.08	3.51	-30.03
S-66	Comte	Cacao	-52.487	4.568	0.087	48.1	<LD	1.46	20.2	0.65	0.19	0.33	0.07	0.04	1.95	-29.92
S-17	Comte	Cacao_Up	-52.625	4.190	0.186	93.0	<LD	1.25	60.2	1.82	0.52	0.69	0.11	0.10	3.71	-30.04
S-67	Comte	Cacao_Up	-52.587	4.196	0.223	113.7	<LD	1.92	54.2	1.48	0.48	0.67	0.13	0.10	3.99	-30.09
S-31	Kourou	Kourou	-52.633	5.087	0.140	57.3	<LD	0.53	17.2	0.82	0.04	0.79	0.10	0.04	7.73	-29.35
S-38	Kourou	Kourou	-52.651	5.106	0.109	25.1	<LD	0.27	8.1	0.32	0.02	0.45	0.09	0.02		
S-44	Kourou	Kourou	-52.775	4.928	0.091	67.0	0.01	1.89	65.1	7.24	1.01	0.45	0.05	0.12	2.23	-28.81
S-46	Kourou	Kourou	-52.762	4.975	0.085	59.1	<LD	0.82	28.9	0.61	0.25	0.39	0.08	0.04		
S-50	Kourou	Kourou	-52.650	5.097	0.064	23.6	<LD	0.22	7.4	0.31	0.02	0.39	0.06	0.02	4.18	-29.87
S-56	Kourou	Kourou	-52.760	4.959	0.037	8.5	0.00	0.18	4.8	0.16	0.01	0.42	0.07	0.01	0.90	-29.50
S-10	Coastal	Coastal	-53.806	5.411	0.321	121.8	0.00	2.34	85.9	0.35	0.07	0.81	0.12	0.25	3.58	-28.74
S-35	Coastal	Coastal	-53.477	5.560	0.128	53.2	0.01	2.60	52.1	11.43	1.08	0.88	0.03	0.12	1.11	-26.97
S-36	Coastal	Coastal	-53.477	5.560	0.128	62.1	0.01	2.38	47.7	11.19	0.76	0.88	0.04	0.13	1.72	-28.06
S-47	Iracoubo	Iracoubo	-53.255	5.469	0.080	60.0	0.01	1.61	45.8	7.21	0.83	0.58	0.05	0.10	1.07	-27.82
S-51	Iracoubo	Iracoubo	-53.263	5.445	0.059	75.4	<LD	0.14	2.1	0.06	0.00	0.21	0.03	0.01	0.45	-29.21
S-53	Iracoubo	Iracoubo	-53.248	5.464	0.052	28.0	0.01	1.06	22.5	3.38	0.40	0.40	0.05	0.05	0.89	-27.57
S-57	Iracoubo	Iracoubo	-53.251	5.452	0.021	64.8	<LD	0.15	1.0	0.05	0.00	0.23	0.02	0.01	0.66	-30.50
S-14	Mana	Mana	-53.767	5.647	0.223	83.1	0.01	2.46	56.0	9.18	0.90	1.08	0.06	0.13	1.50	-28.05
S-30	Mana	Mana	-53.776	5.651	0.142	98.4	0.02	3.15	63.3	12.54	1.08	1.30	0.13	0.15	2.01	-27.67
S-39	Mana	Mana	-53.772	5.685	0.109	99.6	0.02	3.74	59.9	12.77	1.06	1.91	0.28	0.16	1.11	-26.67
S-21	Mana	Awala Yalimapo	-53.902	5.734	0.171	89.0	0.01	3.45	56.4	12.37	0.70	1.93	0.23	0.18		
S-22	Mana	Awala Yalimapo	-53.914	5.742	0.164	77.9	0.01	3.14	54.3	12.21	0.88	1.34	0.14	0.14		
S-1	Maroni	Dorlin	-53.547	3.749	4.323	97.2	<LD	1.01	72.6	1.32	0.86	0.00	0.00	0.00	1.50	-27.29
S-3	Maroni	Dorlin	-53.541	3.749	1.725	83.3	0.01	1.14	66.0	1.32	1.07	0.91	0.17	0.10	1.80	-28.64
S-5	Maroni	Dorlin	-53.540	3.749	0.476	84.6	0.02	0.92	73.6	0.65	0.25	0.89	0.16	0.06	1.97	-26.59
S-4	Maroni	Maripasoula	-54.028	3.647	0.543	16.7	<LD	1.46	21.6	0.26	0.16	0.71	0.22	0.07	0.28	-28.75
S-15	Maroni	Maripasoula	-54.030	3.640	0.220	41.6	<LD	10.91	46.1	4.62	0.98	0.57	0.15	0.13	3.55	-28.52
S-8	Maroni	Maripasoula	-54.044	3.640	0.399	47.7	<LD	1.40	26.2	0.86	0.35	0.72	0.32	0.08	0.41	-28.31
S-59	Maroni	Transect	-54.329	5.192	0.026	48.7	0.00	0.47	23.5	0.49	0.10	0.14	0.03	0.03		
S-20	Maroni	Transect	-54.389	4.187	0.173	71.3	<LD	1.85	20.6	0.81	0.15	0.55	0.10	0.09	1.62	-29.55
S-26	Maroni	Transect	-54.439	4.401	0.152	20.0	<LD	1.19	6.6	0.44	0.06	0.29	0.08	0.03	0.68	-28.63
S-58	Maroni	Transect	-54.435	4.541	0.141	65.6	<LD	1.96	38.3	0.78	0.34	0.40	0.07	0.07	2.35	-29.11
S-12	Maroni	Transect	-54.437	4.539	0.241	75.9	<LD	2.31	29.9	1.05	0.20	0.57	0.11	0.09	2.48	-29.43
S-11	Maroni	Transect	-54.465	4.817	0.310	30.2	<LD	1.79	17.7	0.60	0.21	0.45	0.09	0.05	1.34	-29.55
S-41	Maroni	Transect	-54.358	5.157	0.103	46.0	<LD	1.26	9.6	0.36	0.07	0.17	0.14	0.03	0.26	-30.29
S-37	Maroni	Transect	-54.278	5.263	0.120	45.2	<LD	0.18	4.9	0.26	0.03	0.27	0.09	0.02	0.33	-30.84
S-32	Maroni	St Laurent du Maroni	-54.036	5.506	0.139	83.4	0.02	3.07	63.2	13.15	1.29	0.85	0.05	0.15	0.98	-26.35
S-34	Maroni	St Laurent du Maroni	-54.033	5.506	0.136	61.5	0.01	2.16	52.6	8.28	0.84	0.76	0.04	0.15	1.10	-27.72
S-25	Maroni	St Laurent du Maroni	-54.029	5.508	0.152	79.0	0.01	2.98	54.6	10.79	1.26	1.11	0.19	0.13	1.22	-27.33
S-29	Maroni	St Laurent du Maroni	-54.080	5.456	0.142	75.7	0.01	2.86	52.8	10.41	1.21	1.02	0.07	0.13	0.37	-26.95
S-42	Maroni	Maripasoula	-54.040	3.640	0.100	71.2	<LD	1.31	32.9	1.13	0.15	0.21	0.06	0.07	0.54	-27.93
S-40	Maroni	Maripasoula	-54.029	3.642	0.107	18.8	<LD	5.58	20.6	2.76	0.23	0.21	0.09	0.07	0.54	-27.56
S-55	Maroni	Maripasoula	-54.029	3.643	0.037	16.6	<LD	2.17	9.5	0.54	0.07	0.15	0.07	0.03		
S-43	Maroni	Papaichton	-54.150	3.806	0.095	90.2	<LD	0.56	53.4	0.82	0.32	0.23	0.06	0.07	0.66	-27.22
S-61	Maroni	Papaichton	-54.149	3.806	0.141	86.9	<LD	1.44	31.6	0.94	0.14	0.25	0.09	0.09	1.06	-29.19
S-60	Maroni	Papaichton	-54.148	3.805	0.139	81.7	<LD	1.46	52.4	0.85	0.64	0.35	0.08	0.09	1.92	-29.42
S-7	Oyapock	Camopi	-52.372	3.176	0.445	119.2	<LD	3.21	46.9	0.68	1.06	1.47	0.26	0.13	11.13	-30.00
S-28	Oyapock	StGeorges	-51.825	3.915	0.147	93.2	0.00	1.22	36.7	2.62	0.18	0.53	0.12	0.07	4.96	-29.79
S-23	Oyapock	StGeorges	-51.826	3.915	0.157	82.0	0.00	1.82	40.7	2.65	0.45	0.74	0.12	0.08	8.46	-29.71
S-27	Oyapock	StGeorges	-51.826	3.915	0.147	81.4	0.00	1.68	39.7	2.08	0.32	0.74	0.12	0.07		
S-62	Oyapock	StGeorges	-51.809	3.878	0.085	41.6	<LD	0.94	13.4	2.10	0.26	0.35	0.04	0.04	5.22	-28.80
S-63	Oyapock	St-Georges	-51.787	3.916	0.126	57.8	0.01	2.92	53.3	8.18	1.34	0.45	0.03	0.13	1.91	-28.08
S-24	Oyapock	TroisSaut	-52.989	2.309	0.155	108.9	<LD	1.48	23.0	1.07	0.17	0.69	0.13	0.09	5.89	-30.00
S-49	Oyapock	Ouanary	-51.659	4.224	0.065	64.9	0.02	2.35	56.2	11.69	1.10	0.44	0.04	0.13	0.69	-25.73
S-52	Oyapock	Ouanary	-51.671	4.191	0.054	58.9	0.01	2.24	52.3	10.97	1.13	0.40	0.04	0.13		
S-13	Sinnamary	2 Roros	-52.893	4.376	0.241	126.1	<LD	2.11	39.6	0.72	0.40	1.11	0.14	0.09		
S-18	Sinnamary	Saut Dalles	-52.882	4.490	0.181	127.6	<LD	1.93	30.6	0.78	0.49	0.89	0.12	0.09		

Table S 6.2. *Total mercury (THg) and mercury isotopic composition for analysed sediment samples.*

Sample Code	Watershed	Site	[THg]	$\delta^{204}Hg$	2SD	$\delta^{202}Hg$	2SD	$\delta^{201}Hg$	2SD	$\delta^{200}Hg$	2SD	$\delta^{199}Hg$	2SD	$\Delta^{204}Hg$	2SD	$\Delta^{201}Hg$	2SD	$\Delta^{200}Hg$	2SD	$\Delta^{199}Hg$	2SD
			$\mu g.g^{-1}$	‰		‰		‰		‰		‰		‰		‰		‰		‰	
S-33	Comte	Cacao	0.137	-2.47	0.41	-1.72	0.13	-1.63	0.16	-0.88	0.13	-0.80	0.10	0.09	0.39	-0.34	0.10	-0.02	0.08	-0.37	0.09
S-45	Comte	Cacao	0.086	-2.57	0.41	-1.72	0.13	-1.77	0.16	-0.91	0.13	-0.84	0.10	-0.01	0.39	-0.48	0.10	-0.05	0.08	-0.41	0.09
S-48	Comte	Cacao	0.066	-2.78	0.41	-1.89	0.13	-1.92	0.16	-0.97	0.13	-0.87	0.10	0.04	0.39	-0.50	0.10	-0.03	0.08	-0.39	0.09
S-64	Comte	Cacao	0.149	-2.45	0.41	-1.66	0.13	-1.65	0.16	-0.91	0.13	-0.83	0.10	0.03	0.39	-0.40	0.10	-0.07	0.08	-0.41	0.09
S-65	Comte	Cacao	0.150	-2.48	0.41	-1.70	0.13	-1.66	0.16	-0.96	0.13	-0.88	0.10	0.06	0.39	-0.38	0.10	-0.10	0.08	-0.45	0.09
S-66	Comte	Cacao	0.087	-2.32	0.41	-1.60	0.13	-1.54	0.16	-0.80	0.13	-0.84	0.10	0.07	0.39	-0.33	0.10	0.01	0.08	-0.44	0.09
S-17	Comte	Cacao_Up	0.186	-2.22	0.41	-1.40	0.13	-1.35	0.16	-0.70	0.13	-0.48	0.10	-0.13	0.39	-0.29	0.10	0.00	0.08	-0.12	0.09
S-67	Comte	Cacao_Up	0.223	-2.59	0.41	-1.75	0.13	-1.61	0.16	-0.92	0.13	-0.58	0.10	0.03	0.39	-0.30	0.10	-0.04	0.08	-0.14	0.09
S-57	Iracoubo	Iracoubo	0.021	-3.72	0.41	-2.42	0.13	-2.34	0.16	-1.31	0.13	-1.07	0.10	-0.11	0.39	-0.52	0.10	-0.09	0.08	-0.46	0.09
S-31	Kourou	Kourou	0.140	-2.89	0.41	-2.02	0.13	-1.95	0.16	-1.10	0.13	-0.92	0.10	0.13	0.39	-0.43	0.10	-0.08	0.08	-0.41	0.09
S-50	Kourou	Kourou	0.064	-3.20	0.41	-2.10	0.13	-1.98	0.16	-1.12	0.13	-0.94	0.10	-0.07	0.39	-0.40	0.10	-0.06	0.08	-0.41	0.09
S-1	Maroni	Dorlin	4.323	-1.34	0.41	-1.01	0.13	-0.76	0.16	-0.49	0.13	-0.13	0.10	0.16	0.39	0.00	0.10	0.01	0.08	0.13	0.09
S-3	Maroni	Dorlin	1.725	-0.90	0.41	-0.43	0.13	-0.40	0.16	-0.23	0.13	-0.10	0.10	-0.26	0.39	-0.08	0.10	-0.02	0.08	0.01	0.09
S-5	Maroni	Dorlin	0.476	-1.52	0.41	-1.07	0.13	-1.06	0.16	-0.58	0.13	-0.39	0.10	0.08	0.39	-0.25	0.10	-0.04	0.08	-0.12	0.09
S-15	Maroni	Maripasoula	0.220	-1.07	0.41	-0.80	0.13	-0.76	0.16	-0.42	0.13	-0.32	0.10	0.12	0.39	-0.16	0.10	-0.02	0.08	-0.12	0.09
S-42	Maroni	Maripasoula	0.100	-2.83	0.41	-2.11	0.13	-2.20	0.16	-1.14	0.13	-1.13	0.10	0.33	0.39	-0.61	0.10	-0.08	0.08	-0.60	0.09
S-43	Maroni	Papaichton	0.095	-3.14	0.41	-2.18	0.13	-2.33	0.16	-1.16	0.13	-1.24	0.10	0.10	0.39	-0.69	0.10	-0.07	0.08	-0.70	0.09
S-60	Maroni	Papaichton	0.139	-3.02	0.41	-2.01	0.13	-2.07	0.16	-1.04	0.13	-1.13	0.10	-0.03	0.39	-0.56	0.10	-0.03	0.08	-0.62	0.09
S-61	Maroni	Papaichton	0.141	-2.78	0.41	-1.92	0.13	-1.98	0.16	-1.07	0.13	-1.00	0.10	0.09	0.39	-0.54	0.10	-0.10	0.08	-0.51	0.09
S-11	Maroni	Transect	0.310	-1.77	0.41	-1.35	0.13	-1.28	0.16	-0.77	0.13	-0.63	0.10	0.25	0.39	-0.26	0.10	-0.09	0.08	-0.29	0.09
S-20	Maroni	Transect	0.173	-2.17	0.41	-1.51	0.13	-1.36	0.16	-0.81	0.13	-0.47	0.10	0.09	0.39	-0.22	0.10	-0.05	0.08	-0.09	0.09
S-26	Maroni	Transect	0.152	-1.31	0.41	-0.90	0.13	-0.89	0.16	-0.42	0.13	-0.43	0.10	0.04	0.39	-0.21	0.10	0.03	0.08	-0.20	0.09
S-37	Maroni	Transect	0.120	-3.45	0.41	-2.41	0.13	-2.35	0.16	-1.28	0.13	-1.18	0.10	0.15	0.39	-0.53	0.10	-0.06	0.08	-0.57	0.09
S-58	Maroni	Transect	0.141	-2.26	0.41	-1.55	0.13	-1.64	0.16	-0.83	0.13	-0.92	0.10	0.06	0.39	-0.48	0.10	-0.05	0.08	-0.52	0.09
S-7	Oyapock	Camopi	0.445	-2.24	0.41	-1.73	0.13	-1.65	0.16	-0.88	0.13	-0.72	0.10	0.35	0.39	-0.35	0.10	-0.01	0.08	-0.29	0.09
S-23	Oyapock	StGeorges	0.157	-3.38	0.41	-2.32	0.13	-2.28	0.16	-1.23	0.13	-1.10	0.10	0.08	0.39	-0.53	0.10	-0.07	0.08	-0.52	0.09
S-27	Oyapock	StGeorges	0.147	-3.00	0.41	-2.14	0.13	-2.11	0.16	-1.06	0.13	-1.01	0.10	0.19	0.39	-0.50	0.10	0.02	0.08	-0.47	0.09
S-28	Oyapock	StGeorges	0.147	-3.16	0.41	-2.15	0.13	-2.17	0.16	-1.17	0.13	-1.08	0.10	0.05	0.39	-0.55	0.10	-0.09	0.08	-0.54	0.09
S-62	Oyapock	StGeorges	0.085	-2.82	0.41	-1.97	0.13	-1.83	0.16	-0.99	0.13	-0.75	0.10	0.12	0.39	-0.35	0.10	0.00	0.08	-0.26	0.09
S-24	Oyapock	Trois Sauts	0.155	-3.26	0.41	-2.31	0.13	-2.29	0.16	-1.32	0.13	-1.08	0.10	0.18	0.39	-0.55	0.10	-0.16	0.08	-0.49	0.09

Table S 6.3. *Evaluation of the sampling uncertainty and significance of site isotopic composition of Hg. The analytical uncertainty is based on the 2SD of secondary standard NIST RM 8610, the intra-site variability is calculated from the average of standard deviations at each site, the inter-site variability is calculated from the standard deviation of site averages.*

	n	$\delta^{204}Hg$	$\delta^{202}Hg$	$\delta^{201}Hg$	$\delta^{200}Hg$	$\delta^{199}Hg$	$\Delta^{204}Hg$	$\Delta^{201}Hg$	$\Delta^{200}Hg$	$\Delta^{199}Hg$
analytical uncertainty	39	0.41	0.13	0.16	0.13	0.10	0.39	0.10	0.08	0.09
intra-site variability		0.23	0.16	0.18	0.09	0.12	0.11	0.08	0.03	0.10
inter-site variability		0.86	0.58	0.59	0.32	0.33	0.13	0.17	0.05	0.20

Table S 6.4. *Mercury isotopic composition of certified reference material and comparison with previously published data. Bold data refers to this study, superscripts refer to published data.*

CRM	n	δ^{204}Hg	2SD	δ^{202}Hg	2SD	δ^{201}Hg	2SD	δ^{200}Hg	2SD	δ^{199}Hg	2SD	Δ^{204}Hg	2SD	Δ^{201}Hg	2SD	Δ^{200}Hg	2SD	Δ^{199}Hg	2SD
NIST RM 8610	**39**	**-0.81**	**0.41**	**-0.56**	**0.13**	**-0.45**	**0.16**	**-0.27**	**0.13**	**-0.17**	**0.10**	**0.02**	**0.39**	**-0.03**	**0.10**	**0.01**	**0.08**	**-0.03**	**0.09**
NIST RM 8610 certified value (± expanded uncertainty)	22	-0.82	0.07	-0.56	0.03	-0.46	0.02	-0.27	0.01	-0.17	0.01			-0.04	0.01	0.00	0.01	-0.03	0.02
NIST RM 8610[1]	13	-0.81	0.28	-0.53	0.16	-0.44	0.13	-0.25	0.11	-0.18	0.08	-0.01	0.20	-0.04	0.08	0.02	0.07	-0.04	0.08
NIST RM 8610[2]	61			-0.57	0.05	-0.46	0.05	-0.28	0.03	-0.16	0.04			-0.03	0.02	0.01	0.02	-0.02	0.03
NIST 1944	**11**	**-0.63**	**0.22**	**-0.43**	**0.15**	**-0.33**	**0.14**	**-0.21**	**0.12**	**-0.09**	**0.06**	**0.01**	**0.09**	**0.00**	**0.11**	**0.00**	**0.07**	**0.02**	**0.05**
NIST 1944[1]	15	-0.68	0.17	-0.44	0.14	-0.32	0.18	-0.23	0.13	-0.11	0.12	-0.02	0.16	0.01	0.12	-0.01	0.10	0.00	0.11
NIST 1944[3]	5	-0.56	0.23	-0.38	0.16	-0.34	0.11	-0.21	0.10	-0.14	0.10	0.01		-0.05		-0.02		-0.04	
NIST 1944[2]	6			-0.44	0.12	-0.34	0.08	-0.22	0.05	-0.10	0.04			-0.01	0.05	0.00	0.03	0.01	0.04
IAEA-405	**8**	**-0.61**	**0.14**	**-0.41**	**0.14**	**-0.37**	**0.15**	**-0.21**	**0.11**	**-0.14**	**0.15**	**-0.01**	**0.15**	**-0.06**	**0.06**	**-0.01**	**0.04**	**-0.03**	**0.12**
IAEA-405[1]	14	-0.50	0.17	-0.30	0.11	-0.29	0.07	-0.22	0.11	-0.17	0.15	-0.05	0.12	-0.06	0.06	-0.07	0.13	-0.10	0.15
BCR 464	**9**	**0.76**	**0.53**	**0.62**	**0.27**	**2.42**	**0.23**	**0.36**	**0.19**	**2.51**	**0.13**	**-0.17**	**0.31**	**1.95**	**0.09**	**0.05**	**0.07**	**2.35**	**0.08**
BCR 464[2]	9			0.68	0.06	2.48	0.03	0.43	0.05	2.57	0.08			1.97	0.03	0.09	0.04	2.4	0.07
BCR 464[4]	18	0.75	0.39	0.58	0.23	2.23	0.27	0.33	0.25	2.34	0.29	-0.12	0.31	1.79	0.18	0.04	0.2	2.19	0.25
			2SE		**2SE**		**2SE**		**2SE**		**2SE**		**2SE**		**2SE**		**2SE**		**2SE**
External Reproducibility	14		0.13		0.05		0.07		0.06		0.04		0.13		0.05		0.05		0.04

1. Guédron, S.; Amouroux, D.; Tessier, E.; Grimaldi, C.; Barre, J.; Berail, S.; Perrot, V.; Grimaldi, M., Mercury Isotopic Fractionation during Pedogenesis in a Tropical Forest Soil Catena (French Guiana): Deciphering the Impact of Historical Gold Mining. Environmental science & technology 2018, 52, (20), 11573–11582.

2. Sherman, L. S.; Blum, J. D., Mercury stable isotopes in sediments and largemouth bass from Florida lakes, USA. Sci Total Environ 2013, 448, 163-75.

3. Janssen, S. E.; Johnson, M. W.; Blum, J. D.; Barkay, T.; Reinfelder, J. R., Separation of monomethylmercury from estuarine sediments for mercury isotope analysis. Chemical Geology 2015, 411, 19-25.

4. Bérail, S.; Cavalheiro, J.; Tessier, E.; Barre, J. P. G.; Pedrero, Z.; Donard, O. F. X.; Amouroux, D., Determination of total Hg isotopic composition at ultra-trace levels by on line cold vapor generation and dual gold-amalgamation coupled to MC-ICP-MS. Journal of Analytical Atomic Spectrometry 2017, 32, (2), 373-384.

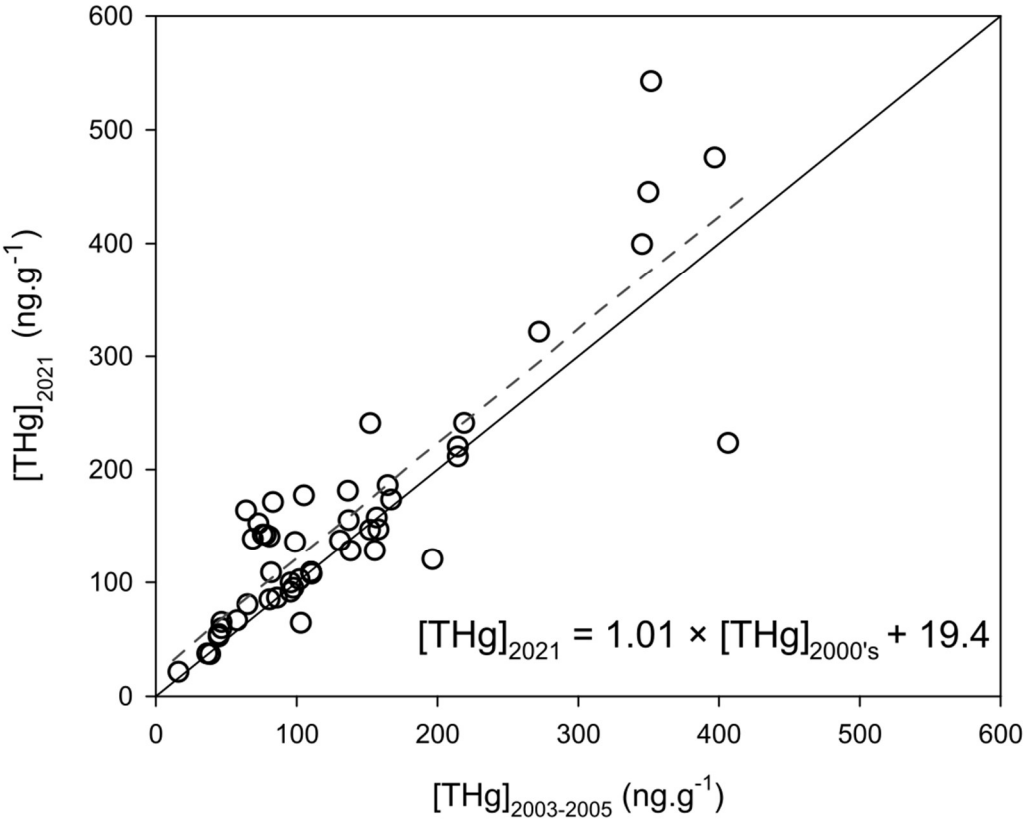

Figure S 6.1. *Comparison of total Hg concentration in sediments measured within a year after sampling (2003-2005) and recently re-analyzed before determination of the Hg stable isotope composition (2021-2022). The dashed line represents the slope of the data. The continuous black line represents the slope of 1:1 for identical concentrations.*

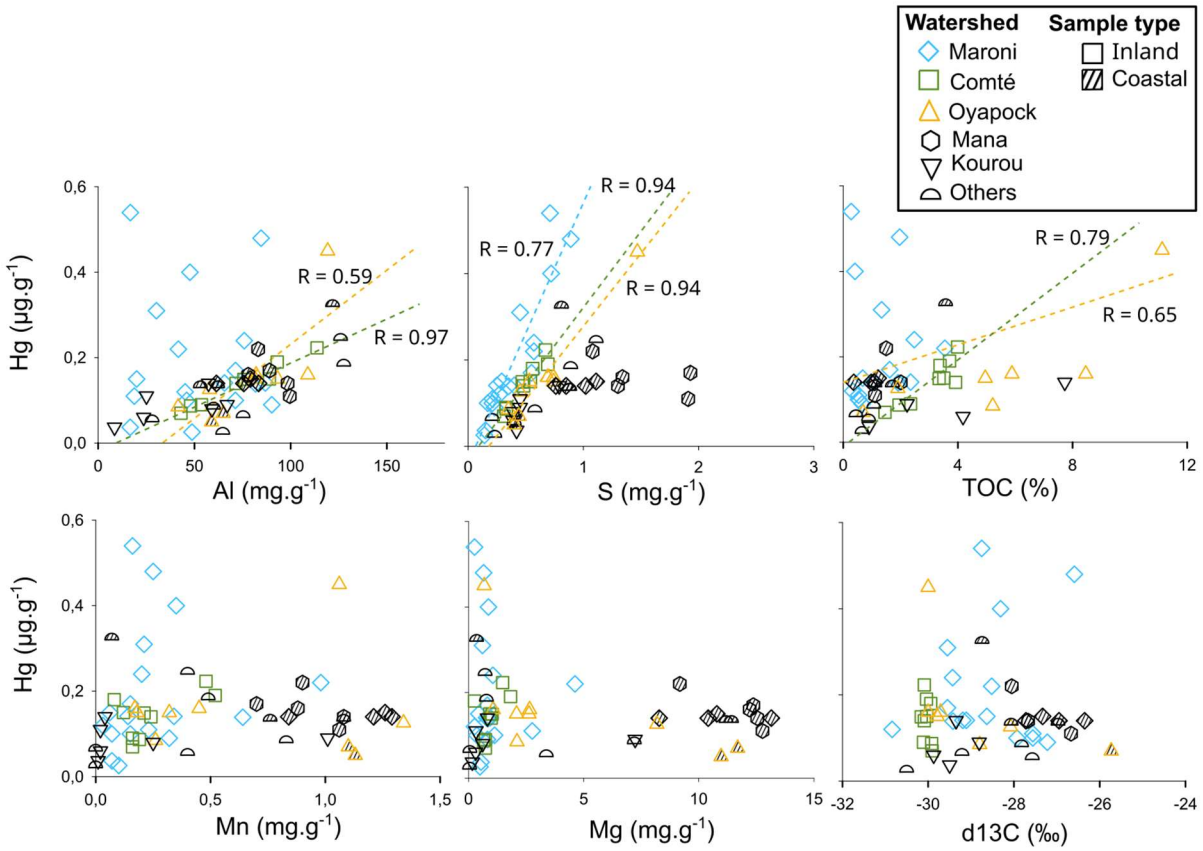

Figure S 6.2. *Plots of THg vs selected major elements in sediment samples. Regression lines are displayed for the Comté (gold), Oyapock (pink) and Maroni (blue) watersheds when p<0.05.*

Table S 6.5. *Comparison of coastal and inland sample concentrations of major elements, Hg, TOC and $\delta^{13}C$ using a Mann-Whitney-Wilcoxon test. Elements that display a statistically significant difference (p<0.05) are shown with a star *.*

Element	Hg	Al	As*	Ca*	Fe*	Mg*	Mn*	S*	Ti	Zn*	TOC	$\delta^{13}C$*
p-value	0.98	0.08	$2x10^{-8}$	$2x10^{-6}$	$3x10^{-6}$	$6x10^{-7}$	$2x10^{-5}$	$3x10^{-5}$	0.69	$4x10^{-8}$	0.21	$4x10^{-5}$

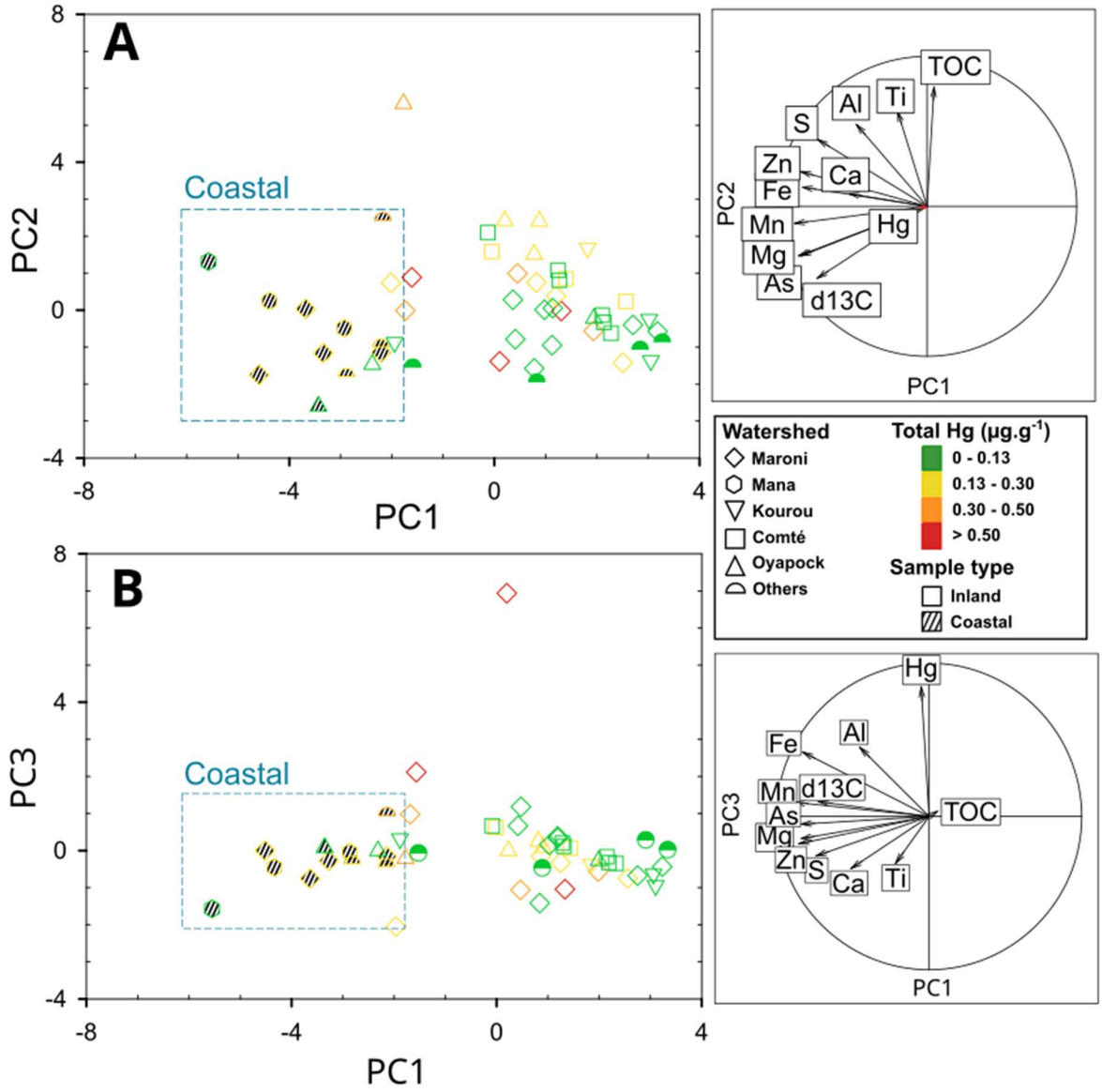

Figure S 6.3. *Principal Component Analysis of major elements, Hg and total organic carbon in F. Guiana sediments.*

Table S 6.6. *Percent of variance explained by each factor from the PCA in* ***Figure S 6.3****.*

	PC1	PC2	PC3	PC4	PC5	PC6	PC7	PC8	PC9	PC10	PC11	PC12
Variance	5.24	2.06	1.44	0.95	0.84	0.59	0.29	0.2	0.15	0.12	0.07	0.04
% of variance	43.6	17.2	12	7.9	7	4.9	2.4	1.7	1.3	1	0.6	0.4
Cumulative % of variance	43.6	60.8	72.8	80.7	87.7	92.6	95	96.7	98	99	99.6	100

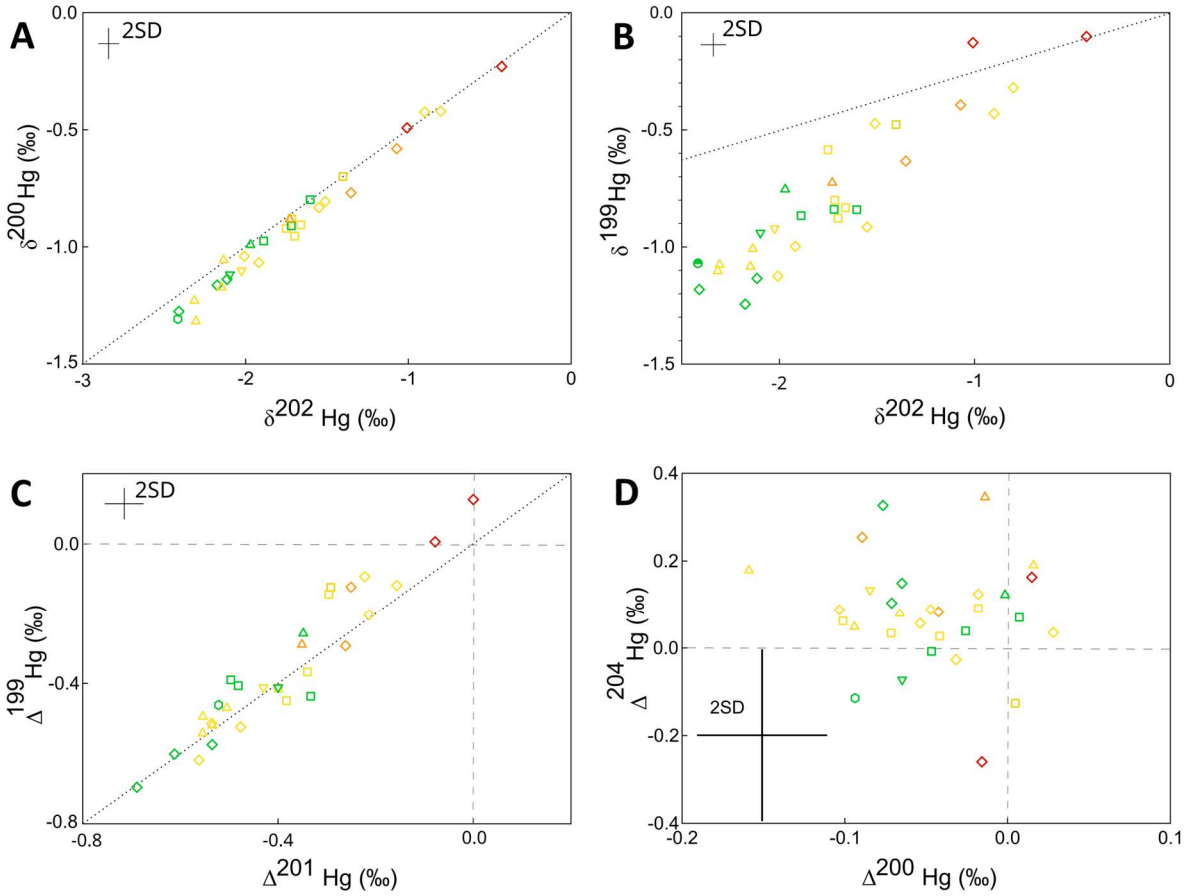

Figure S 6.4. *Plot of δ^{200}Hg and δ^{202}Hg isotopes (A), δ^{199}Hg and δ^{202}Hg isotopes (B), Δ^{201}Hg and Δ^{199}Hg isotopes (C) and Δ^{200}Hg and Δ^{204}Hg isotopes (D) for sediment samples. The dashed lines represent the slope of theoretical mass dependent fractionation of 0.5024(Blum and Bergquist 2007) in pannel A, the slope of theoretical mass dependent fractionation of 0.2520(Blum and Bergquist 2007) in pannel B and the slope of 1.0 for fractionation during photochemical reduction of iHg(II) (Bergquist and Blum 2007) in pannel C.*

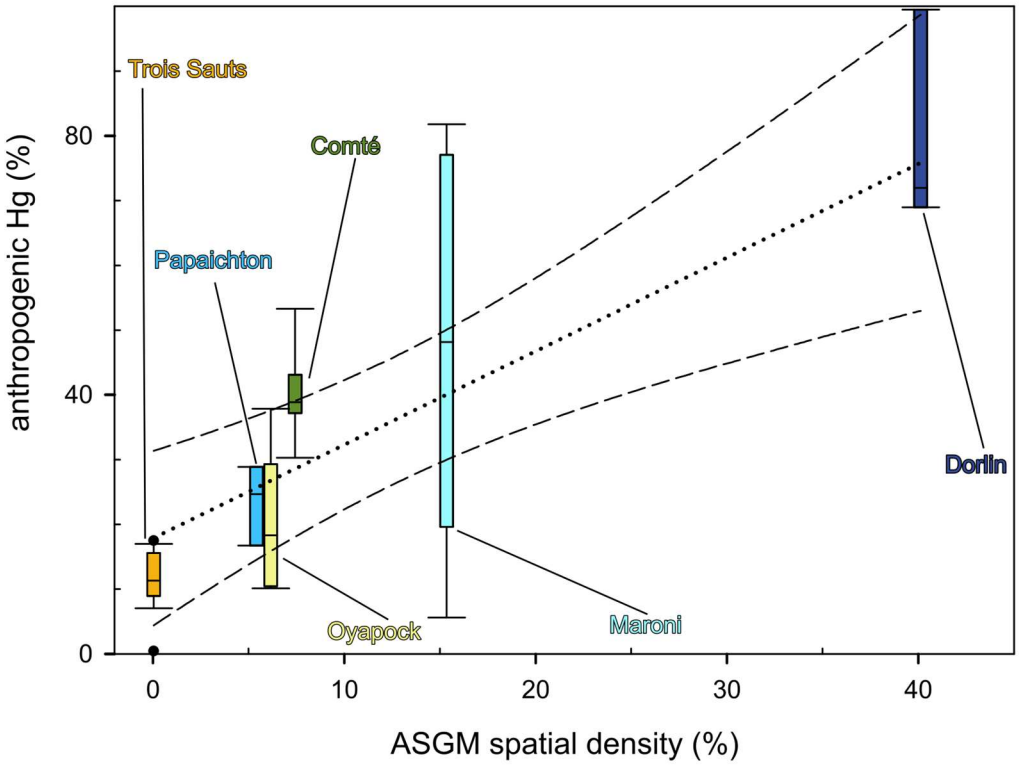

Figure S 6.5. *Theoretical contribution of anthropogenic mercury in sediment samples using a binary mixing model with the MDF δ^{202}Hg data from this study and from the literature (Goix et al. 2019) (anthropogenic Hg (%)) versus the ASGM spatial density as derived from the map (Figure 4). Black dots represent outliers. The regression is Hg_{anth} = 17.92 + 1.45 × ASGM-density, R^2 = 0.88, p = 0.0057.*

Chapter 7.

Conclusions and Outlook

7.1. Initial objectives

The global aim of this work was to investigate gold mines and their restoration in French Guiana, focusing on their impact on Hg and metal(loid) export and fate as well as the consequences for soil functioning. It was funded by the mining company SAS GAIA through a CIFRE doctoral thesis, and as such, a consequential portion of this thesis aimed at understanding the impact of legal gold mines on the export of particles and metal(loid)s, and propose operational guidelines to reduce these impacts. To do so, the majority of the studies presented here focused on one legal mining site (Awa), but the two last chapters (5 and 6) expanded the study to other mining sites and to the whole territory of French Guiana.

The initial objectives or questions of this work can be separated according to the "community" it will benefit to :

- ➔ The gold mining companies: Assess the successfulness of the restoration practice, and understanding the effects of restoration in terms of particle and metal(loid) export, and revegetation. Provide advice on where the restoration efforts should be focused and what can be improved in the current practices
- ➔ Regulatory state agencies: Propose tools and guidelines on how to evaluate the progress or success of a mining site restoration, as well as straightforward methods to assess the impact of legal and/or illegal gold mining at the watershed scale.
- ➔ Scientific community: Provide data to establish background values, which are still scarce in the area for certain metal(loid)s (e.g. Pb and As), or in certain compartments (e.g. atmospheric Hg). Building up on this, the intention was to provide an understanding on where Hg is stored on the mining site and in what form, as well as the transfers ocurring between different compartments, and understanding how Hg cycling is affected by gold mining (both legal and illegal). The second objective was to provide a deeper understanding on the recovery of soil functions after restoration, and the potential parameters impacting this recovery. Finally, this work aimed at assessing the hydrological functioning of the gold mined watershed, by tracing both water and suspended particle sources in the river.

To attempt at answering these questions, a legal mining site (Awa) was studied thoroughly, examining metal(loid) distribution and transport with a focus on Hg, from the 1 m² scale to the scale of the whole watershed, coupled to the study of soil biological activity. The impact of legal and illegal gold mines was then assessed at a more global scale, first comparing two mining sites with differences in illegal gold mining activites, and finally evaluating the consequences of illegal gold mining on anthropogenic Hg at the scale of the territory of French Guiana.

7.2. Synthesis of the main results and perspectives.

Soil erosion and metal(loid) export. This aspect was adressed in chapters 3 and 0, with first a fine examination of the temporal evolution of particle and metal(loid) export at the square meter scale thanks to erosion plots, and then a more global investigation at the scale of the whole watershed through the comparison of particle and metal(loid) fluxes upstream and downstream of the goldmined river. The erosion plots showed that the fast colonisation of the gold mining flat by herbaceous plants resulted in a rapid decrease in particle export within one year after restoration (up to 2000-fold when taking into account coarse particles). As the metal(loid)s studied here are primarily associated to the particulate fraction, and because the increase in vegetation density also induced better water infiltration capacity leading to reduced overland flow, this increase in spontaneous herbaceous vegetation colonisation was associated to a similar decrease in the export of all metal(loid)s.

At the scale of the watershed, within the year following landscaping, the mining flat was shown to still be a significant source of particles to the river, leading to an excess 100-300 $kg.km^2$ export compared to the upstream watershed. However, this increased particle export was not due to a rise in overland flow which would lead to soil erosion, as the hydrological behaviour of the downstream watershed was shown to be identical to the one upstream of the mining site. Instead, geochemical characterisation using FTIR data and multielemental composition points towards the main source of particles in the river originating from river bed sediment remobilisation and river bank erosion.

In river water, THg and Pb were shown to be mainly associated to the particulate fraction in river water (>90 %), while MeHg and As were more evenly distributed between the particulate and filtered fractions (50 – 60 % in the particulate fraction). As observed at the square meter scale, the particle export originating from the mining flat was coupled to an increase in metal(loid) export, with the majority of this export ocurring during the major rainy season (66 ± 6 %). The seasonal differences in particle export were exacerbated for the metal(loid)s which were predominantly associated to the particulate fraction (THg and Pb) compared to the ones which were more equally distributed between the particulate and filtered fractions (MeHg and As). Additionally, particulate THg was proposed to originate primarily from mining flat erosion while particulate MeHg concentrations decreased during flood events due to a dilution with MeHg-poor particles.

However, it was shown that some of the impact originating from the legal mining flat might have been masked by illegal mining activities ocurring upstream of the mining site during the second event monitored. The impact of surrounding illegal mining on legal mines is not well assessed and can lead to regulating agencies fining legal companies for a particle export that does not originate from the legal gold mine.

The significant relationships observed between the metal(loid) fluxes and river discharge and turbidity enabled the estimation of metal(loid)s exports all year round. As a result, these probes might be useful for regulatory state agencies which would want to monitor gold mining sites and their impact on metal(loid) exports. Indeed gold mining sites are usually remote, and access is challenging, usually involving expensive helicopter flights or time-consuming boat rides. Discharge and turbidity probes are robust and straightforward to handle, in comparison to discrete monitoring which requires training, as well as adequate equipment and packaging. However, these probes cannot totally replace discrete monitoring, and a calibration of the system is always necessary.

Recovery of soil biological functions. The focus on soil biological activity and diversity was presented in chapter 3, with the study of the temporal evolution of the legal gold mining site after restoration. This is an aspect that is generally overlooked by mining companies and regulation agencies in the restoration process, where the main focus is given to reducing soil erosion and particle export. Yet, the efficient recovery of soil functions is necessary in order to pass the herbaceous succession stage and recreate a secondary forest. Otherwise, the risk would be to stall at the herbaceous or shrub stage for decades or more. Here, the recovery of soil functions was assessed by analysing among others soil enzyme activity, carbon and nitrogen content and soil microbial diversity. No significant recovery of soil functions was observed within 5 years after restoration. This lack of response was in part attributed to the depletion of soil nutrient stocks by the herbaceous plant cover. Soil microbial communities displayed evolutions in the 5 years after restoration of the mining site, with the potential emergence after 4 years of nitrogen fixing bacterial communities which occupy a crucial position in the recovery of the nitrogen cycle. Studies over longer time periods (in the decades time frame or more) would be needed in order to understand the timescale that is necessary for the recovery of biological activity in the soil.

Additionally, the heterogeneity of the mining site needs to be better assessed. Indeed, tree trunks and branches are disseminated on the site to favour natural revegetation in what is called a “nucleation” restoration. This was shown to be efficient concerning tree regrowth, with the tree abundance and species richness shown to be correlated to the distance to seed sources (i.e. where the vegetation residues were deposited) (Conrado da Cruz et al. 2020). It remains to be shown whether this technique also favours the recovery of soil functions in the vicinity of these sources. The first results observed on the landscaped site which was located in the vicinity of the forest edge appear to support that hypothesis, with increased activity in the plots closest to the forest edge. The amount of data here is insufficient for unequivocal assessment and a more thorough study would be needed to assess this point.

Mercury (natural and anthropogenic) distribution and transfer. To provide a deeper understanding on Hg distribution and transfer occuring on the mining site, Hg concentration, speciation and isotopes were measured in different compartments on and around two mining sites as presented in chapters 3, 4.2, 5 and 6. The use of Hg isotopes highlighted the presence of anthropogenic Hg on portions of the mining site where illegal gold mining had taken place (illegal mining ponds), but also in the river sediments downstream of the mining site. These preliminary results with only a limited number of samples (n=3) need to be further strengthened , but if they are validated, this would support the potential of Hg isotopes as a tool to detect past illegal mining activites using Hg amalgamation for gold extraction. In these same illegal mining ponds, large concentrations of dissolved gasesous mercury (DGM) were measured resulting in significant Hg volatilisation fluxes to the atmosphere. DGM was also observed in river water where, although much less abundant than in mining ponds, it is not negligible (up to 15 % of THg). The data presented here shows that DGM appears to increase during flood events, but a better time resolution would be needed in order to fully comprehend DGM dynamics during flood events. DGM in Amazonian systems is understudied, with the majority of studies focusing on stagnant water systems like artificial or floodplain lakes (Muresan et al. 2008, Jardim et al. 2009). The studies presenting DGM data on river water (Amouroux et al. 1999) do not study its temporal evolution during a flood event.

The comparison of Hg distribution in mining ponds of two mining sites show increased concentrations of Hg in the suspended particulate matter and sediments on the site with recent illegal gold mining activities compared to the site where illegal activities ocurred more than 15 years ago, and legal exploitation was performed afterwards.

Finally, the extent of anthopogenic Hg contamination was followed in river bed sediments across the main watersheds of French Guiana using Hg stable isotope composition. Two end-members were constructed using literature data of Hg isotopes in remote and in ASGM contaminated sites. The end-members were pristine or geogenic Hg naturally present in the soils and sediments of French Guiana, and anthropogenic Hg resulting from liquid Hg used by gold miners in the amalgamation process. A binary mixing model showed that the distribution of anthropogenic Hg was very variable between sites and related to the known extent of ASGM activites in the watershed. This study was conducted using archive sediment samples collected in the 2000s, and an update of the contamination levels in the main watersheds of French Guiana would be interesting to observe their evolution. However, such extensive sampling in locations that are remote and at a large distance from one another needs strong logistical support as was provided during the program “Mercure en Guyane” in the late 1990s and early 2000s, involving participative science by local schools. A current research project focusing on the Maroni watershed (“ECLAT”) might provide such lengthy sampling. Although restricted to only one

watershed, the Maroni is where the majority of mining activities have concentrated in the past decades, and the increase in gold mining (mainly illegal), has been documented by discrete sampling coupled to remote sensing (Gallay et al. 2018).

7.3. Propositions for an efficient gold mine restoration

The following section proposes a compilation of "good practices" in the restoration of a gold mine resulting from this work. Several points have already been raised or are already implemented in the regulations but not always respected on the field.

- **Rapid restoration** after exploitation is the single most crucial and impactful parameter to be put in place. It is easy to implement and provides important benefits in the restoration sequence. Indeed, the topsoil organic layer that is stored during the gold extraction process is subject to erosion and leaching during the frequent rain events in tropical regions. As a result, the longer this layer is stored, the more it is susceptible to lose nutrients, but also microorganisms and seeds which would favour spontaneous revegetation. As observed in this work (chapter 3), it is this spontaneous revegetation that efficiently limits erosion of the mining flat, and thus export of metal(loid)s to the river. A rapid restoration in the months following the exploitation phase will lead to soil stabilisation inducing at least a reduction in particle export. In additon, the recovery of soil functions might also be accelerated as the presence of microorganisms and their diversity (nitrogen-fixing, but also others), might lead to a more efficient reestablishment of the carbon and nitrogen cycles in the soil and eventually allow the formation of a secondary forest.

  The guidelines for mine restoration in French Guiana already propose to perform restoration within 6 months after exploitation, but this is not a strict rule and is not always followed.
- **Tree planting** probably plays a secondary role in soil stabilisation but it is essential for different reasons: i) Litter input will help restarting the C and N cycle, thereby promoting the restoration of some soil functions on the site, ii) the plantation of trees from the fabaceae family (if associated with N-fixing bacteria), will also help increase soil nitrogen stocks and restore the N cycle, iii) the shade provided by these trees which are usually resistant to sunlight will help other species grow under them, thereby promoting an increase in tree diversity on the site and creating a secondary forest succession.
- The results presented in chapter 4.1 show that 8 months after restoration, the main source of particles in the rivers originates from river bank erosion. As a result, a special focus should thus be put on **river bank stabilisation**. Mining companies already attempt to recreate the original river path during the restoration phase, including meanders to slow down the water flow and limit bank erosion following existing guidelines from state agencies (Melun et al. 2021), but the presence of

refilled mining ponds with loose sediments sometimes limits the ideal reformation of the river path.

- Finally, many legal mining companies are facing the question of how to deal with **illegal mining ponds.** Indeed, legal mines frequently work on areas that have previously seen illegal mining activites (as is the case in both the Awa and Sophie sites in this study), but they are not required to restore illegally mined areas. The high DGM concentrations observed in illegal mining ponds, together with high THg and MeHg concentrations in their sediments (especially on the Sophie site) indicate that restoring them would probably lead to an important remobilisation of anthropogenic Hg stored there. On the other hand, if left as they are, they are a source of gaseous Hg to the atmosphere through volatilisation of DGM. However, the Hg exported through volatilisation is several orders of magnitude lower than the quantity of Hg that would probably be liberated to the rivers in the case of their restoration (pond emptying and soil reworking for landscaping), which plays in favour of leaving these ponds in their original state.

- An alternative restoration practice has been proposed and put in place on one gold mining site in French Guiana. There, the initial topography and slope of the site is reconstructed, and the bed of the restored river is not cut as deep (< 50 cm versus 1-2 m in traditional restoration techniques), allowing for the river to create its natural path and improving the hydrological connectivity of the site [“ResCriOr”, (Clavier et al. 2024)]. An increased aquatic habitat recovery was observed in this alternatively restored site compared to a traditionnally restored one. The authors postulate that this technique should also improve river bank stabilisation but no specific study on particle/ metal(loid) export has been performed. It would thus be interesting to compare this restoration technique with the more conventional one for particle and metal(loid) export.

Lastly, given that jewellery fabrication makes up to 40 – 50 % of total gold demands, and its use in technology amounts to less than 10 % (Lezak et al. 2022), the question of the reduction of global gold demands should be asked, and might provide the most efficient way yet of reducing the impact of both legal and illegal gold mining.

Annexe :

Synthèse en Français

Réhabilitation de mines d'or en Guyane : stabilisation et devenir du mercure et métalloïdes

8.1. Introduction

L'or (Au) est extrait des sols depuis des millénaires. L'une des plus anciennes mines d'or connues remonte au IVe ou IIIe millénaire avant notre ère (Hauptmann and Klein 2009). En 1511, le roi Ferdinand d'Espagne déclara : « Rapportez de l'or, humainement si possible, mais à tout prix, rapportez de l'or » (Bernstein 2012). Cette déclaration semble toujours d'actualité, puisque l'exploitation aurifère mondiale se poursuit aujourd'hui et tend même à s'étendre, en raison de l'augmentation des prix de l'or. Elle est responsable d'impacts environnementaux considérables, ainsi que de répercussions sur la santé des populations. À l'échelle mondiale, l'orpaillage artisanal et à petite échelle ("artisanal and small-scale gold mining" en anglais, ou "ASGM") est responsable de la production de près de 20 % de l'or mondial, et emploie environ 10 à 15 millions de mineurs (AMAP/UNEP 2019). En Amazonie, la population directement impliquée dans l'ASGM a plus que doublé au cours des 15 dernières années, atteignant 1,5 million de travailleurs. Dans certains pays d'Amérique latine, jusqu'à 80 % de l'or est produit de manière informelle ou illégale (Harlow et al. 2019).

Dans cette région, la majorité des exploitations aurifères sont alluviales : l'or est extrait de gisements secondaires situés sous ou à proximité des lits de rivières. Ce type d'exploitation (qu'elle soit légale ou illégale) est associé à la déforestation et à la remobilisation de la couche superficielle des sols pour accéder aux couches de graviers aurifères. En conséquence, les sols exploités pour l'or sont particulièrement vulnérables à l'érosion. Cela entraîne, d'une part, une perte de matière organique, de graines et de micro-organismes, ce qui freine la revégétalisation naturelle du site après l'arrêt des activités (Gomes and Luizão 2011, Veldkamp et al. 2020). D'autre part, les matériaux érodés sont transportés vers les rivières, avec un impact néfaste sur les écosystèmes aquatiques (Mol and Ouboter 2004, Tudesque et al. 2012, Wantzen and Mol 2013).

En plus de l'érosion des sols, l'exploitation aurifère engendre également une contamination de l'environnement par le mercure (Hg), utilisé dans le processus d'extraction pour amalgamer l'or. En Guyane, l'usage du Hg est interdit depuis 2006, mais reste largement répandu chez les orpailleurs illégaux. En plus de ce mercure d'origine anthropique, l'érosion accrue des sols entraîne également la remobilisation du Hg et d'autres éléments métalliques ou métalloïdes naturellement présents dans ces sols. En Amazonie, les concentrations élevées en Hg dans les sols résultent de l'accumulation du Hg atmosphérique dans les feuilles, qui s'intègre aux sols via la litière durant des millions d'années, ainsi que de la présence de phases porteuses de Hg comme les oxydes de fer et la matière organique (Roulet and Grimaldi 2001, Fostier et al. 2015, Feinberg et al. 2022). Une fois relâché dans les rivières, le Hg (naturel ou anthropique) peut être méthylé par des bactéries [majoritairement des bactéries réductrices de sulfate ou de fer (Achá et al. 2011)], donnant lieu au méthylmercure (MeHg), qui est facilement bioaccumulé et bioamplifié le long de la chaîne alimentaire (Azevedo-Silva et al. 2016). En

conséquence, de fortes concentrations de Hg sont observées chez les poissons prédateurs (Maury-Brachet et al. 2006), dont la consommation constitue la principale voie de contamination pour les populations locales (Pignoux et al. 2019).

En plus du Hg, d'autres éléments tels que le plomb (Pb) et l'arsenic (As) commencent à attirer l'attention des agences gouvernementales en Guyane. En 2011, un taux de Pb sanguin de 1700 $\mu g.L^{-1}$ a été observé chez une enfant de 3 ans en Guyane française, bien au-dessus du seuil de 50 $\mu g.L^{-1}$ fixé par l'OMS pour l'intoxication (Rorive et al. 2015, WHO 2021). Des études ultérieures ont montré que plus de 20 % des enfants guyanais et 45 % des mineurs illégaux étaient exposés au Pb (Andrieu et al. 2020, Douine et al. 2025). Résultant de ces observations, un programme de recherche soutenu par l'agence régionale de santé (ARS) a été créé (Stratégie métaux lourds, StraMeLo). Il vise à comprendre les sources potentielles de contamination de métaux et métalloïdes en Guyane, avec un accent particulier sur le Hg et le Pb. Des études ont proposé comme potentielles sources de contamination la consommation de manioc et l'exposition aux munitions de chasse (Rimbaud et al. 2017, Maurice et al. 2021).

L'arsenic est un métalloïde très toxique, particulièrement sous la forme As(III) (Moe et al. 2016). L'exposition chronique à l'As, principalement par l'eau, augmente les risques de cancers et de maladies cardiovasculaires (Kapaj et al. 2006). En Amazonie, des concentrations élevées (jusqu'à 430 $\mu g.L^{-1}$) ont été relevées dans les nappes phréatiques, surtout près des rivières, dépassant souvent le seuil OMS de 10 $\mu g.L^{-1}$ (de Meyer et al. 2023). Au Brésil, l'activité minière favorise la remobilisation géogénique de l'As et ainsi l'intoxication des populations aux alentours (Matschullat et al. 2007, Ono et al. 2012, Bueno Guerra et al. 2023). En Guyane, les données sur les concentrations naturelles d'As et les impacts potentiels de l'orpaillage restent insuffisantes.

En Guyane, la juxtaposition de sites miniers légaux, illégaux et historiques complique souvent l'identification des impacts environnementaux spécifiques à chaque type d'exploitation. Cela est d'autant plus vrai que les entreprises légales choisissent fréquemment de s'implanter sur des sites ayant déjà été exploités illégalement ou historiquement, remobilisant potentiellement le Hg anthropique stocké dans ces sols. Par ailleurs, les exploitants légaux ont l'obligation de réhabiliter les sites miniers après exploitation, notamment via des travaux de terrassement du terrain et de replantation d'arbres. L'effet de ces réhabilitations sur la réduction de l'export de particules reste cependant peu quantifié. Enfin, en raison du caractère informel de l'ASGM, l'ampleur réelle des émissions de Hg vers l'atmosphère, les sols et les milieux aquatiques est encore mal connue.

Ce travail est une thèse CIFRE co-financée par l'entreprise minière SAS GAIA. Il a été conçu pour répondre aux attentes scientifiques de plusieurs partenaires, avec pour objectif général de mieux

comprendre le devenir des sites aurifères, en mettant un accent particulier sur la phase de réhabilitation.

– L'entreprise SAS GAIA cherchait à évaluer l'efficacité de ses pratiques de réhabilitation, notamment sur l'export de particules, les contaminants et la revégétalisation, afin d'orienter ses actions futures.

– Les services de l'État impliqués dans la régulation des activités minières ont besoin d'outils pratiques pour suivre la réhabilitation des sites miniers et évaluer l'impact de l'orpaillage, légal ou non, à différentes échelles.

– Le projet répond aussi à des questions scientifiques fondamentales sur le cycle du mercure et d'autres contaminants, en apportant des données de référence rares et en étudiant les formes, stocks et transferts de Hg sur les sites miniers.

Les résultats de ce travail sont divisés en 4 parties qui sont les suivantes :

I – Etude de l'évolution temporelle sur 5 ans d'un site d'orpaillage restauré et son impact sur les flux de particules et de contaminants (Hg, Pb, As), ainsi que sur la restauration des fonctions biologiques des sols, à l'échelle de parcelles d'érosion de 2 x 2 m.

II – Export de particules et de contaminants à l'échelle du bassin versant orpaillé. Ce chapitre contient deux parties. Une première se focalise sur les exports de particules et de carbone en proposant une compréhension fine du fonctionnement hydrologique du bassin versant. La deuxième partie utilise ces résultats et les transpose aux exports de contaminants (Hg, Pb, As)

III – Evaluation de la répartition du Hg, et ses transferts dans différents compartiments sur et autour du site d'orpaillage. Analyse de l'impact de l'orpaillage illégal sur cette répartition, et comparaison de deux sites (Awa et Sophie) aux pratiques et historiques d'exploitation différents.

IV – Utilisation des isotopes du mercure pour estimer la contribution anthropique du Hg dans les sédiments des principaux bassins versants de Guyane française.

8.2. Sites d'étude

8.2.1. Description des sites miniers

8.2.1.1. Awa, site minier alluvionnaire

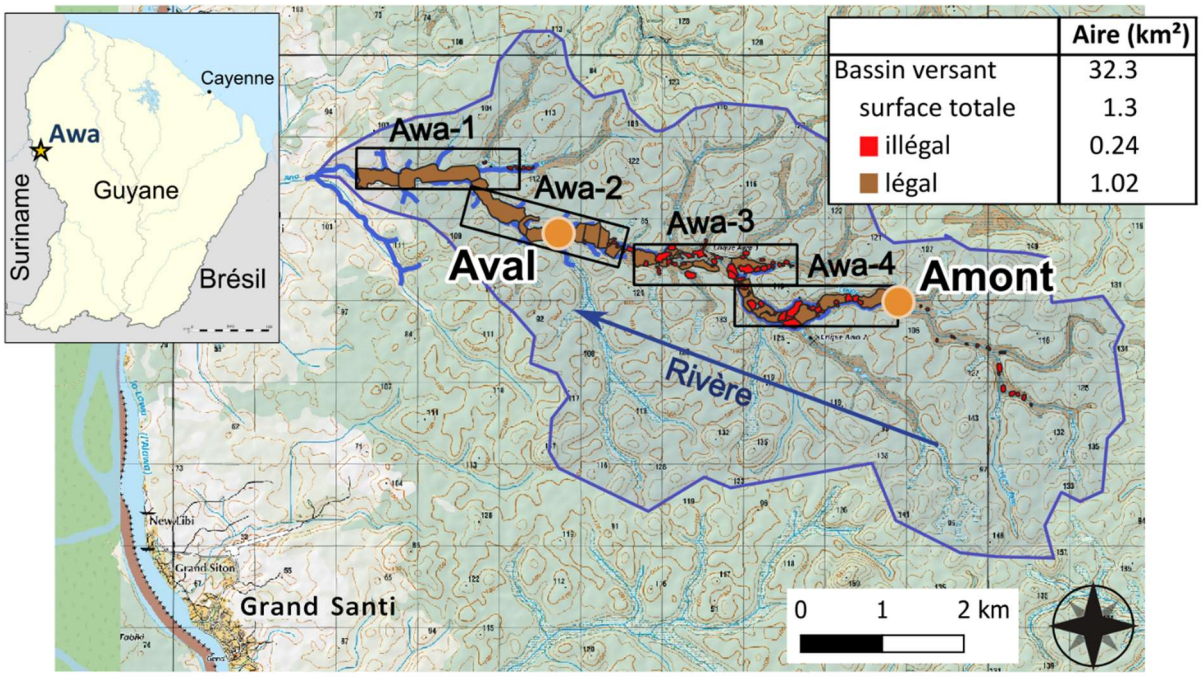

Figure 8.1. *Site d'extraction d'or d'Awa avec les zones d'exploitation légales (marron) et illégales (rouge). La localisation des stations hydrologiques en amont et en aval est représentée par des points orange.*

Le site aurifère d'Awa (54°20'34"W, 4°19'8"N) est situé sur le fleuve éponyme, à proximité de la ville de Grand-Santi. Il est situé dans le bassin versant du Maroni, fleuve qui constitue la frontière occidentale de la Guyane française avec le Suriname. Les précipitations ont été mesurées sur une station météorologique située à Grand Santi, à 7 km du site minier (meteo.data.gouv.fr [last accessed on 3rd February 2025]). La pluviométrie moyenne annuelle sur les trois années de l'étude s'élève à 2500 mm. Il s'agit d'une mine d'or alluviale, où les étapes d'exploitation et de réhabilitation ont suivi les réglementations en vigueur en Guyane. Il y a 4 AEX (zones d'exploitation de 1 km²), numérotées de 1 à 4 d'aval en amont (Figure 8.1). Awa-1 et -2 ont été exploitées entre septembre 2017 et avril 2020, suivies par Awa-3 et -4 qui ont été exploitées entre mai 2020 et avril 2021. Les premiers travaux de réhabilitation ont été réalisés localement en mai-juillet 2019. Cependant, le principal effort de réhabilitation, en commençant par l'aval (Awa-1) jusqu'à l'amont (Awa-4), a été réalisé entre mai 2021 et août 2022. La réhabilitation a consisté à remplir les bassins miniers, puis à terrasser et à replanter 100 % du site minier (légal), à intervalles de 3 mètres. Six pépinières ont été créées sur le site pour un total de 7000 jeunes arbres plantés. Les espèces d'arbres utilisées sont *Euterpe oleracea* (palmier açaí), *Inga sp.*, *Senna multijuga*, et *Hymenaea courbaril*, ces trois derniers faisant partie de la famille des *Fabaceae* (Figure 8.2).

Avant l'arrivée de la société SAS GAIA, de l'orpaillage clandestin avait eu lieu sur le site, comme en témoigne la présence de bassins de décantation, principalement dans les secteurs Awa-3 et -4. Ces zones ont été laissées dans leur état d'origine, sans exploitation ni réhabilitation de la part de la société. En ce qui concerne l'exploitation historique de l'or (avant les années 2000), peu d'informations sont disponibles sur le secteur d'Awa en particulier, mais les premiers permis d'exploitation « sur la rive droite du Maroni » peuvent être trouvés à partir de 1873, et un permis d'exploitation sur le fleuve Awa a été enregistré en 1901 (communication personnelle, Pierre Rostan, Mine et avenir).

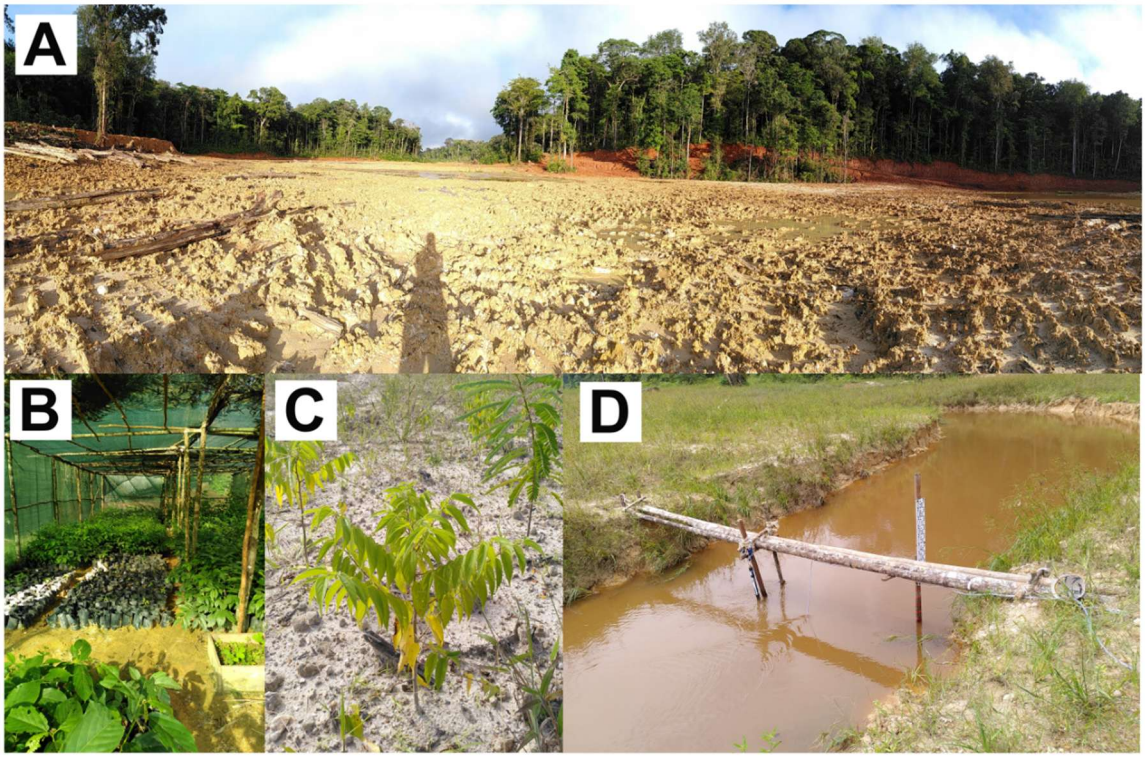

Figure 8.2. *Images prises sur le site minier Awa. A) le flat minier terrassé, B) les plantations d'arbres en pépinière, C) pousse de revégétalisation plantée sur le site, C) cours de rivière reconstruit.*

8.2.1.2. Sophie, site minier primaire

Le site minier Sophie est situé sur le bassin versant de la Mana (Figure 8.3). Il s'agit d'un site de gisements d'or primaire bien que la présence d'or alluvionnaire (dérivant des gisements primaires) ait été démontrée par des travaux de prospection. L'absence d'activités d'extraction d'or alluvial sur ce site peut s'expliquer par i) la proximité de sites riches en or qui auraient pu détourner les mineurs de sites un peu moins rentables comme celui-ci, et ii) l'importante couverture de limon (>7 m) sur le gravier aurifère, qui le rend inaccessible aux mineurs informels sans machines lourdes, et pas économiquement viable pour les petites sociétés minières.

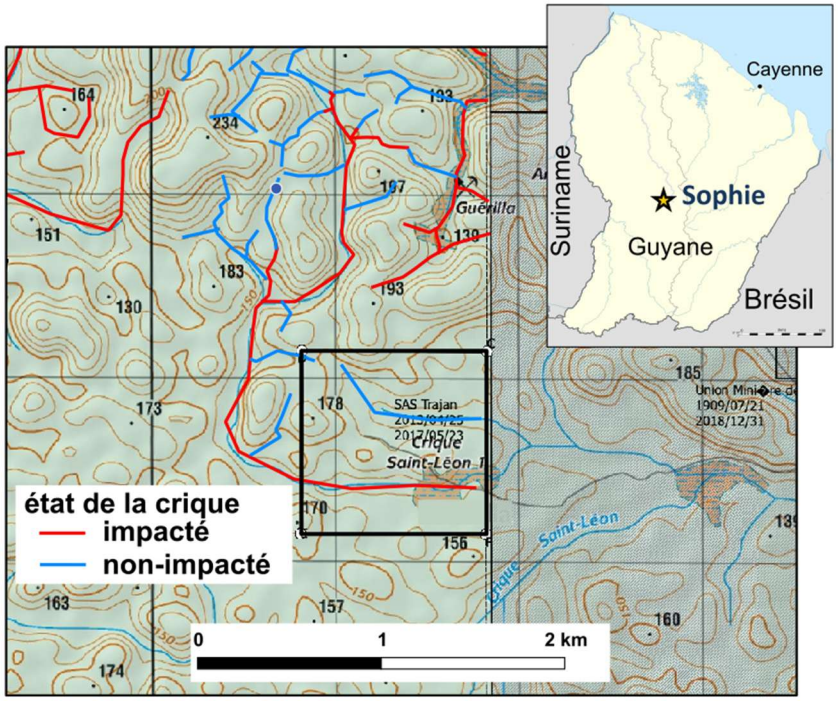

Figure 8.3. *Site minier de Sophie (limites du PER dans le carré noir). Les criques autour du site minier sont indiquées en bleu avec les criques impactées par de l'activité illégale en rouge (évaluation qualitative basée sur des observations visuelles).*

La société minière SAS GAIA a obtenu un permis d'exploration (PER) afin de déterminer la teneur en or des sols et d'évaluer si l'exploitation de la zone serait rentable. Des carottages de 10 m de profondeur ont été effectués sur une grille du site de prospection, et des échantillonnages supplémentaires de 100 m de profondeur ont ensuite été effectués sur des points ciblés. Aucune activité d'exploitation légale n'a eu lieu pendant la durée de ce travail de doctorat. De plus, aucune activité historique d'extraction d'or n'a été enregistrée sur le site minier Sophie. Cependant, la présence d'activités illégales d'extraction d'or au cours des 20 dernières années est documentée par la présence de puits d'extraction (Figure 8.4A) et d'anciens campements disséminés autour du site minier Sophie. Le minerai y était extrait par des tunnels rudimentaires, concassé et broyé en surface, puis mélangé à de l'eau et lavé sur des plaques de cuivre recouvertes de Hg pour retenir l'or (Le Tourneau 2020).

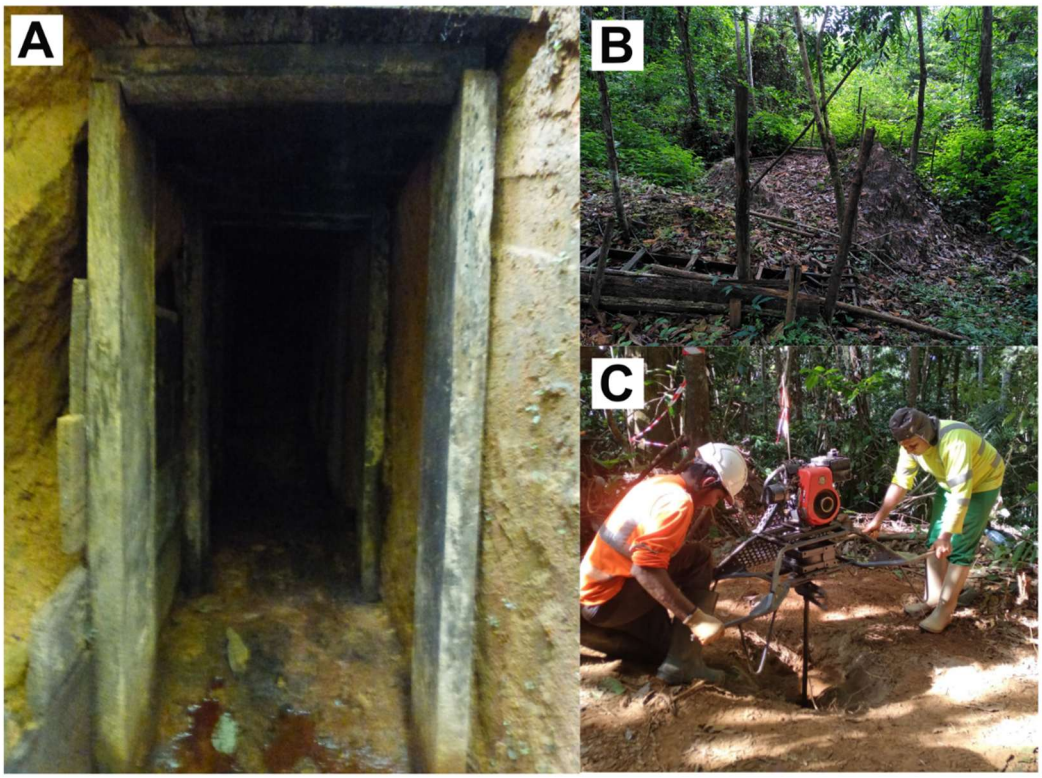

Figure 8.4. *Images du site de Sophie. A) tunnels construits par les orpailleurs clandestins pour accéder aux filons aurifères, B) site de lavage, C) échantillonnage de 10m de profondeur pour analyse des teneurs en or lors de l'étape de prospection.*

8.3. Résultats

8.3.1. Evolution de l'export de particules et des fonctions biologiques du sol sur un site minier réhabilité

Introduction

La forêt amazonienne subit une déforestation importante liée à l'agriculture et à l'orpaillage, entraînant pertes de biodiversité et dégradation des sols. L'orpaillage, notamment en Guyane, cause une érosion accrue, ce qui induit une pollution des rivières par les particules fines et le mercure géogénique, affectant les écosystèmes aquatiques et la santé des populations locales. En Guyane, la réhabilitation des sites miniers vise à stabiliser les sols et à favoriser la régénération forestière. Peu d'études ont évalué la récupération des fonctions du sol après réhabilitation, notamment la diversité microbienne. Pour évaluer le succès de la réhabilitation du site minier de l'entreprise SAS GAIA, l'évolution temporelle de l'export de particules et de métaux (mercure, plomb, arsenic) a été mesurée, ainsi que plusieurs paramètres liés aux fonctions du sol (carbone et azote du sol, diversité microbienne, activités enzymatiques).

Méthodes

Quatre campagnes d'échantillonnage ont été réalisées sur trois ans (de 2022 à 2024) pour suivre l'évolution de la réhabilitation du flat minier : G1 (04/22), G2 (12/22), G3 (05/23), G4 (04/24), sur deux emplacements différents du site minier. L'un a été terrassé et replanté en avril 2022, juste avant la première campagne d'échantillonnage, et l'autre a été réhabilité trois ans auparavant. Ci-après, les deux sites sont appelés respectivement « terrassé» et «revégétalisé». Les échantillons prélevés ont été labellisés en fonction du temps écoulé depuis la réhabilitation, les échantillons du site terrassé étant labellisés T=0 mois (G1), T=8 mois (G2), T=13 mois (G3) et T=24 mois (G4) et les échantillons du site revégétalisé étant étiquetés T=36 mois (G1), T=44 mois (G2), T=49 mois (G3) et T=60 mois (G4).

Des placettes d'érosion ont été installées en trois exemplaires sur chaque site d'échantillonnage afin de récupérer le sol érodé dans une zone définie lors d'un événement pluvieux. Chaque placette était constituée de panneaux de bois (2 m × 2 m, 4 m²) insérés à 10 cm dans le sol et s'étendant à 15 cm au-dessus du sol. Chaque placette était reliée à un seau de 80 litres installé au point le plus bas de la pente et enterré dans le sol. L'eau de ruissellement et les particules ont été collectées après chaque événement pluvieux. Le volume total d'eau a été mesuré, un aliquot de 250 ml de la suspension a été prélevé dans une bouteille FEP, afin de mesurer à la fois les SPM, la spéciation du Hg et les éléments majeurs et traces dans les fractions filtrées et particulaires. Le reste a été jeté et les matières grossières sédimentées au fond ont été récupérées, lyophilisées et pesées.

Des cubes de sol 10×10×10 cm ont été prélevés sur différents emplacements. Le sol a été pesé, séché puis pesé à nouveau pour quantifier sa densité apparente (DA). Les racines ainsi que la partie aérienne ont été séparées, nettoyées, puis séchées et pesées pour déterminer la densité racinaire, et la biomasse aérienne (AGB) respectivement.

La granulométrie des échantillons solides (sols et sédiments) a été obtenue avec un granulomètre laser (Malvern, Mastersizer 2000) en suivant des protocoles établis (Grangeon et al. 2012).

Les concentrations en matière en suspension (MES) ont été déterminées après filtration des échantillons d'eau sur des filtres PVDF 0.45 µm pré-lavés et pré-pesés. Après filtration, les filtres ont été séchés sous hotte à flux laminaire puis pesés pour obtenir la concentration en MES.

Les concentrations de Hg et de MeHg dans la fraction particulaire et filtrée ont été mesurées par chromatographie gazeuse liée à un spectromètre de masse à plasma à couplage inductif (GC-ICP-MS) comme décrit précédemment (Monperrus et al. 2008, Sharif et al. 2014). Les éléments traces ont été mesurés par ICP-MS (Agilent). Les teneurs en carbone organique et azote ont été obtenues en utilisant un analyseur élémentaire Flash Smart (TermoFisher Scientific) comme décrit précédemment (Piton et al. 2020).

Les activités enzymatiques extracellulaires du sol de l'arylsulfatase (ARS), de la β-glucosidase (β-GLU), de la N-acétyl-glucosaminidase (NAG) et de la phosphatase (PHOS) ont été mesurées conformément à la norme ISO 20130:2018. L'ADN du sol a été extrait à l'aide du kit FastDNA® SPIN pour le sol (MP Biomedicals, Illkirch, France). La réaction en chaîne de la polymérase quantitative en temps réel (qPCR) a été réalisée pour évaluer l'abondance de gènes (ARNr 16S, *narG*, *amoA*, *nosZ*, *nifH*, *nirS*). La diversité des bactéries et des archées a été déterminée par le metabarcoding du gène de l'ARNr 16S.

Résultats

Les résultats montrent une diminution rapide de l'export de particules d'un facteur 3 dans les 8 premiers mois. Cette diminution atteint un facteur 2000 4 ans après réhabilitation si la totalité de l'export particulaire est pris en compte, et tout de même un facteur 200 si seulement la fraction fine (particules en suspension) est intégrée (Figure 8.5A). La réduction de l'export de particules est concomitante à une augmentation de la colonisation spontanée par les plantes herbacées observée par l'augmentation de la densité racinaire (Figure 8.5E). Cette diminution de l'export de particules a induit une diminution efficace (facteur 100 – 200) de l'export de métaux (Hg, Pb, As), principalement associés à la fraction particulaire.

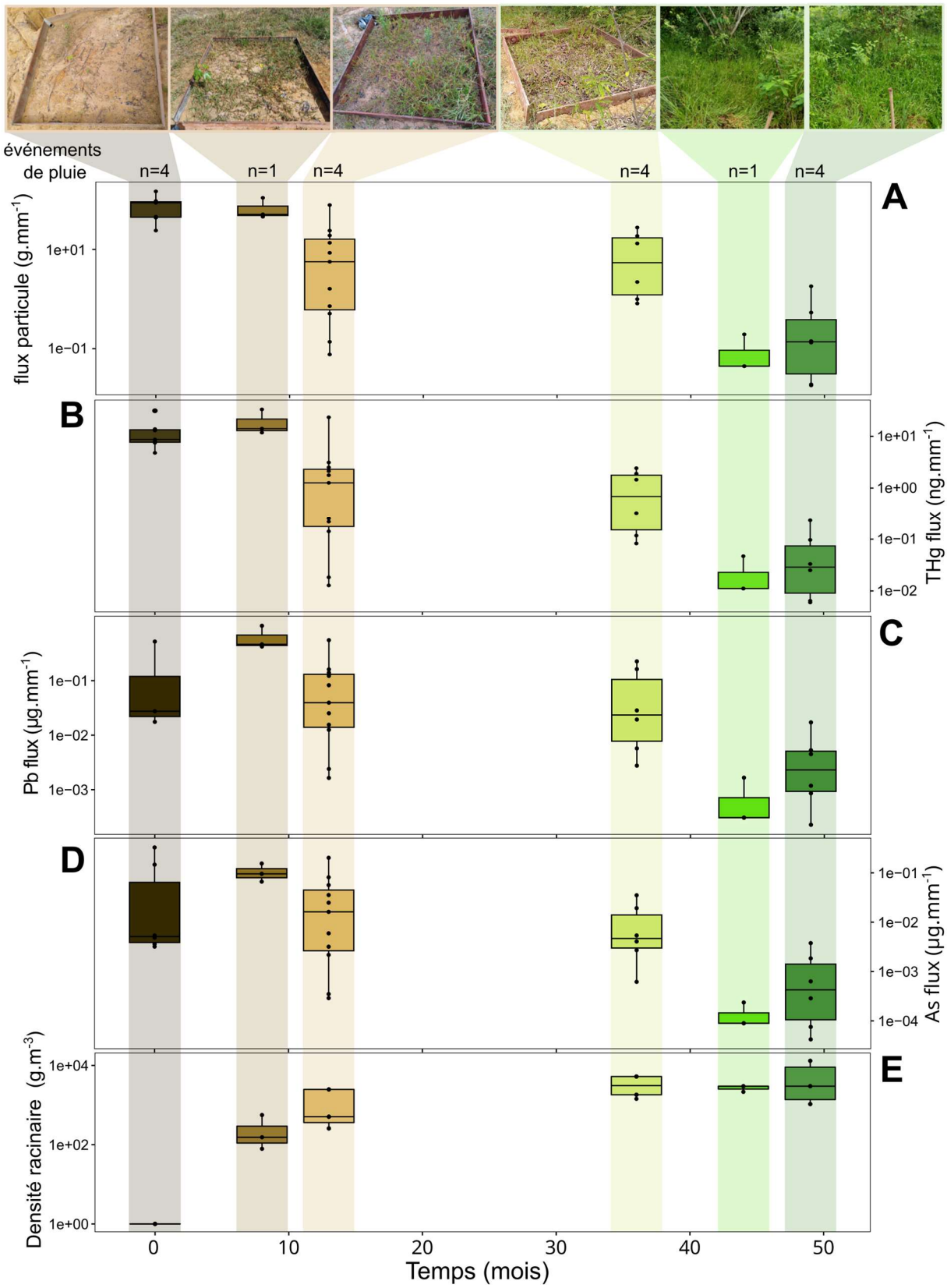

Figure 8.5. *Évolution des exports de A) particules, B) Hg, C) Pb, D) As normalisées par les précipitations (mm) et E) densité des racines au fil du temps après la réhabilitation.*

D'un autre côté, des analyses d'activité enzymatique, abondance et diversité microbienne, ont été effectuées sur les sols des sites terrassés et revégétalisés sur les mêmes campagnes d'échantillonnage.

Les paramètres associés aux fonctions écologiques n'ont pas montré d'augmentation significative dans les 5 ans suivant la réhabilitation. Les concentrations de carbone et d'azote dans le sol semblent même diminuer dans l'année après la réhabilitation, puis rester basses pendant les 5 ans qui suivent. Ceci est potentiellement dû à l'épuisement des stocks d'azote par la croissance des herbacées qui induit une compétition pour les ressources avec les communautés microbiennes du sol (Figure 8.6). Les communautés microbiennes du site minier ont connu des évolutions significatives au cours des cinq années suivant la réhabilitation, sans convergence visible avec les communautés du sol forestier, mais en soulignant la capacité d'adaptation aux conditions climatiques et à un environnement changeant.

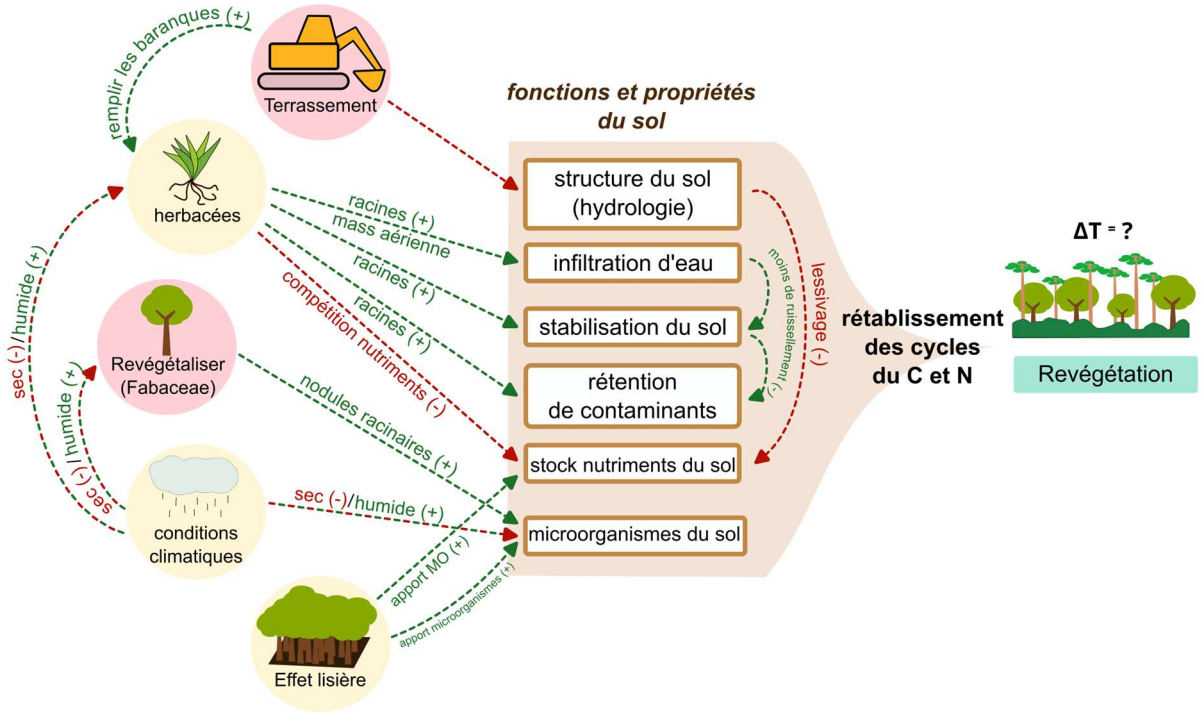

Figure 8.6. *Synthèse des paramètres influençant la réhabilitation d'un sol orpaillé. Les paramètres naturels sont représentés par des cercles jaunes et l'intervention humaine par des cercles rouges. Les flèches rouges représentent l'impact négatif et les flèches vertes l'impact positif.*

Conclusion

Ces résultats montrent que les pratiques actuelles de réhabilitation sont efficaces pour limiter l'exportation de particules et de contaminants majeurs, mais qu'il faut accorder plus d'attention au rétablissement des fonctions du sol et des activités biologiques.

8.3.2. Influence du flat minier sur les exports de particules et contaminants à l'échelle du bassin versant

Introduction

Le chapitre précédent analysait l'évolution d'un site minier réhabilité et les pertes de matériaux et méta(loïdes) lors des épisodes pluvieux. L'érosion nuit à la revégétalisation du site par la perte de matière organique et de graines. Cette matière érodée peut ensuite être transportée vers les rivières où l'augmentation de la turbidité impacte les écosystèmes fluviaux. Ce nouveau chapitre élargit l'échelle d'étude pour évaluer l'export de particules et de métaux et métalloïdes à l'échelle du bassin versant. Afin d'étudier l'étendue de l'export de particules et métaux provenant d'un site minier aurifère réhabilité, des mesures de concentrations de matières en suspension (MES) et du débit ont été effectuées dans la rivière en amont et en aval du site minier réhabilité. De plus, les concentrations en Hg, Pb et As ont été mesurées dans les fractions filtrées et particulaires de l'eau de rivière

Méthodes

Une station hydrologique a été installée sur chaque site (amont et aval), comprenant : i) une sonde de turbidité, ii) une sonde de pression pour mesurer la hauteur d'eau, et iii) un échantillonneur automatique (ISCO 3700, Teledyne). Les sondes de turbidité et de hauteur d'eau étaient installées même en dehors des missions d'échantillonnage et mesuraient à un pas de temps de 1h. Deux événements de crue (evt-1 et evt-2) ont été suivis à l'aide de traceurs géochimiques dans les fractions particulaires et filtrées (concentrations multi-élémentaires et données de spectroscopie infrarouge à transformée de Fourier, FTIR).

Résultats – A) Export de particules et de carbone

Les résultats montrent que dans l'année qui suit le terrassement, le flat minier reste une source importante de particules et de carbone pour la rivière. Lors de l'evt-1 (8 mois après terrassement), une augmentation d'un facteur 2 des exports de MES est observé en aval par rapport à l'amont (**Table 8.1**). Ceci induit un excès de 100-300 $kg.km^{-2}$ de particules exportées dans la rivière en aval du site minier par rapport à l'amont. De plus, les exports spécifiques de carbone s'élèvent à 9.8 $tC\ an^{-1}\ km^{-2}$, ce qui est comparable aux exports observés dans des bassins versants plus importants dans la région de l'Amazone et en Guyane (Moreira-Turcq et al. 2003, Gallay et al. 2017).

Table 8.1. *Bilan hydro-sédimentaire en amont et en aval du flat minier pour deux événements enregistrés au cours de saisons différentes (événement-1 en petite saison des pluies, miR, et événement-2 en grande saison des pluies, MaR).*

	Evt-1 (miR)		**Evt-2 (MaR)**	
	Amont	Aval	Amont	Aval
Vol_cumul (mm)	4.5	7.3	5.4	4.6
MES/aire ($kg.km^{-2}$)	252	594	381	476
MES/vol ($mg.L^{-1}$)	56	81	71	103

Les traceurs géochimiques dans la fraction filtrée ont permis de tracer l'origine de l'eau dans la rivière (écoulement de surface ou eaux de sub-surface). Un coefficient d'écoulement de 9 % est observé pour l'evt-1 et de 6 % pour l'evt-2. Cette différence est potentiellement due à une différence saisonnière, avec des sols très secs et donc moins perméables couplé à une connectivité hydrologique faible lors de l'evt-1. En effet, l'evt-1 a eu lieu au début de la petite saison des pluies, après une longue saison sèche, alors que l'evt-2 a eu lieu lors de la grande saison des pluies. Cependant, aucune différence de coefficient d'écoulement n'est observée entre le site amont et aval du site minier, ce qui signifie que le fonctionnement hydrologique global du bassin versant n'est pas affecté significativement par la présence du flat minier.

Dans la fraction particulaire, l'analyse multi-élémentaire et FT-IR indiquent que la principale source de particules en suspension est l'érosion des berges et la remobilisation des sédiments du lit de la rivière plutôt que la remobilisation du flat minier (Figure 8.7).

Les résultats de cette partie soulignent l'importance de la reformation du lit de la rivière et de la stabilisation de ses berges dans le processus de restauration d'une mine d'or.

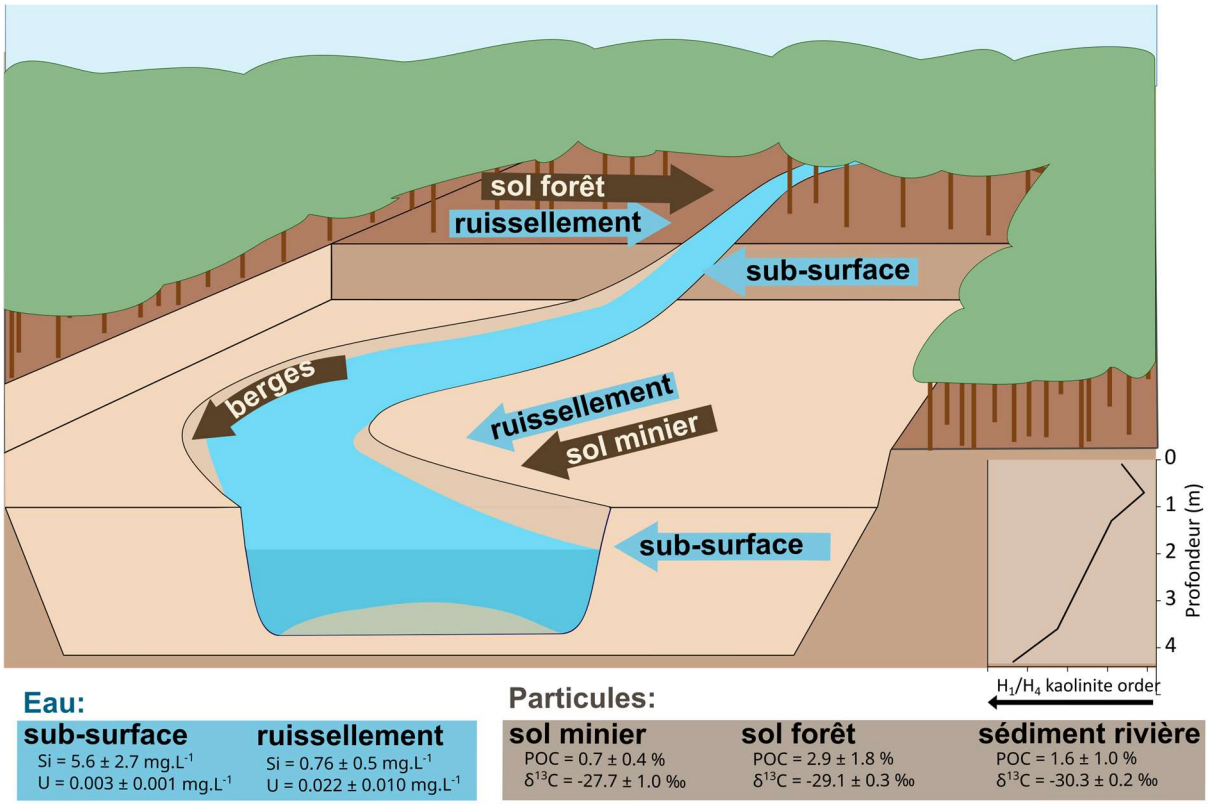

Figure 8.7. *Traceurs sélectionné dans les différentes sources de la fraction filtrée (Si et U, bleu) et de la fraction particulaire (POC et δ13C, brun) sur une rivière orpaillée réhabilitée.*

Résultats – B) Export de métaux et métalloïdes (Hg, Pb, As)

Cette partie utilise les résultats de la partie précédente et va plus loin. L'objectif est de comprendre la distribution des contaminants (mercure, plomb, arsenic), la spéciation du mercure (mercure total, méthylmercure et mercure gazeux dissous), et l'impact d'un flat minier réhabilité sur leurs exports. Pour ce faire, un échantillonnage discret à haute résolution des mêmes événements de crue au cours de différentes saisons a été couplé à des données horaires de concentration de sédiments en suspension et de débit en amont et en aval d'une rivière exploitée pour l'or.

Il a été démontré que le mercure total particulaire provient de l'érosion du flat minier. D'un autre côté, les concentrations de méthylmercure (MeHg) particulaire ont diminué pendant la crue, en raison de la dilution avec des particules pauvres en MeHg provenant de la remobilisation des sédiments du lit de la rivière. La zone d'orpaillage restaurée a multiplié par deux l'export de contaminants huit mois après la réhabilitation, mais n'a pas induit d'augmentation significative douze mois après la réhabilitation.

Des relations significatives ont été observées entre les flux des contaminants et le débit de la rivière, ainsi qu'entre les concentrations de contaminants et les concentrations de MES dans la rivière. Ceci permet une estimation des exports annuels de contaminants grâce aux sondes de hauteur d'eau et de

turbidité présentes sur le site minier (Figure 8.8). L'estimation de cet export annuel montre que la saison des pluies est responsable de la majorité de l'export pour tous les contaminants (66 ± 6 %).

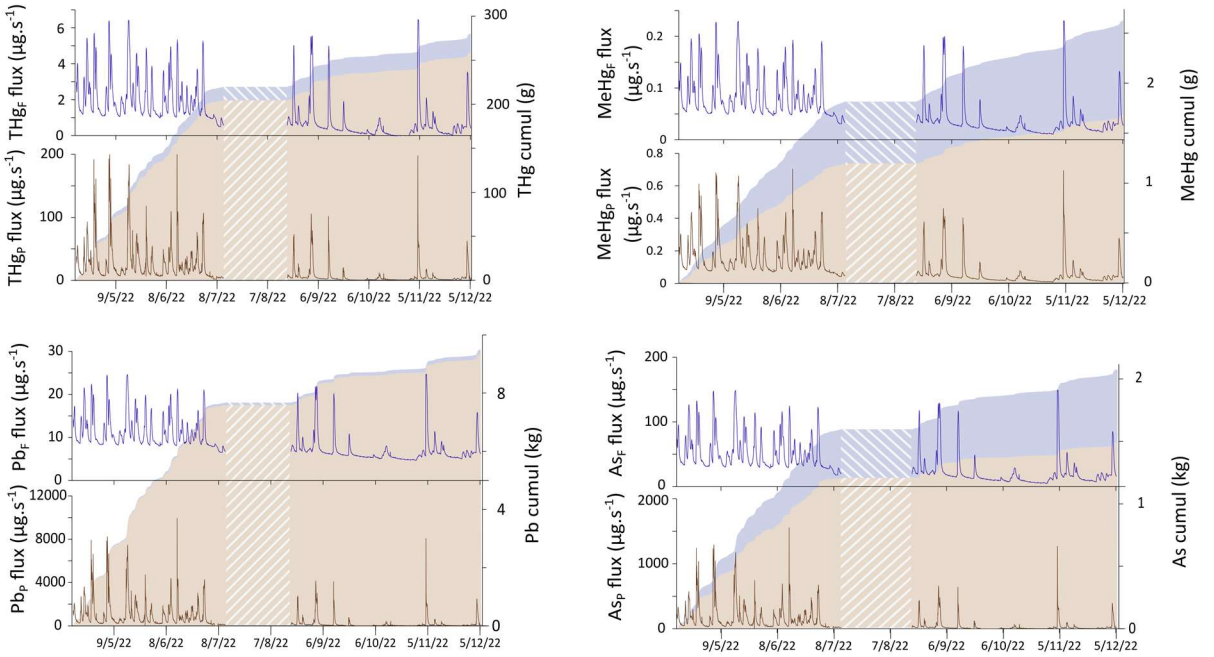

Figure 8.8. *Estimation des exports saisonniers de métaux et métalloïdes filtrés (lignes et zones bleues) et particulaires (lignes et zones brunes) en aval du flat minier. Les zones en pointillés représentent une période pendant laquelle les données de débit étaient manquantes.*

L'étalonnage du système fluvial par des mesures discrètes des concentrations de contaminants ainsi que du débit et des MES pendant plusieurs crues et au cours de différentes saisons a permis d'estimer les exportations de ces contaminants tout au long de l'année. Ceci est particulièrement utile pour les sites tropicaux éloignés, tels que les sites miniers, qui ne sont accessibles que par des vols d'hélicoptère coûteux ou des trajets en bateau qui prennent beaucoup de temps. Les sondes de turbidité et de débit sont robustes, peuvent être déployées à long terme et ne nécessitent qu'un entretien minimal. Bien qu'elles ne puissent pas remplacer totalement la surveillance discrète, l'utilisation de ces sondes peut constituer une alternative rentable à la surveillance des cours d'eau dans les endroits isolés. Elles pourraient être utilisées par les compagnies minières elles-mêmes, ou par les agences d'État qui supervisent leurs travaux, pour surveiller l'impact du site minier sur les flux de contaminants.

Conclusion

Ces résultats montrent qu'il est possible de suivre les exports de particules et de métaux et métalloïdes provenant des pratiques d'orpaillage par des mesures continues de débit et turbidité, une fois que le système est calibré. De plus, la saisonnalité joue un rôle important dans les exports de métaux.

8.3.3. Evaluation de la répartition du Hg, et ses transferts dans différents compartiments sur un site

Introduction

Les deux chapitres précédents ont évalué l'impact de l'extraction de l'or sur les exports de particules et de métaux à différentes échelles. La distribution du Hg, du Pb et de l'As a été évaluée dans les matériaux érodés, les ruissellements de surface et l'eau des rivières. Le chapitre suivant se concentre sur le Hg et sur sa distribution dans différents compartiments sur et autour du site minier. En effet, le Hg a cette particularité par rapport au Pb et à l'As, d'être utilisé par les mineurs illégaux pour extraire l'or. Ceci entraîne une contamination par le Hg anthropogénique, en plus des exports de Hg "naturel". Cette partie vise à étudier le stockage et le transfert de Hg entre les compartiments d'un site minier réhabilité, ainsi que la pertinence des indicateurs pour évaluer les sources et les transferts. Pour ce faire, les concentrations et la spéciation de Hg ont été mesurées dans divers compartiments : eau de la rivière et des bassins de décantation (baranque), sol, sédiments, atmosphère, végétation. En outre, la composition en isotopes stables du Hg a été mesurée dans les sols, les sédiments et la végétation.

Méthodes

Les concentrations en matière en suspension (MES) ont été déterminées après filtration des échantillons d'eau sur des filtres PVDF 0.45 µm pré-lavés et pré-pesés. Après filtration, les filtres ont été séchés sous hotte à flux laminaire puis pesés pour obtenir la concentration en MES.

Les concentrations de Hg et de MeHg dans la fraction particulaire et filtrée ont été mesurées par chromatographie gazeuse liée à un spectromètre de masse à plasma à couplage inductif (GC-ICP-MS) comme décrit précédemment (Monperrus et al. 2008, Sharif et al. 2014). Les éléments traces ont été mesurés par ICP-MS (Agilent). Les teneurs en carbone organique et azote ont été obtenues en utilisant un analyseur élémentaire Flash Smart (ThermoFisher Scientific) comme décrit précédemment (Piton et al. 2020).

Les isotopes du Hg ont été mesurés après digestion acide (HNO_3) par ICP-MS multicollecteur (MC-ICP-MS) comme décrit dans Guédron et al. (2018).

Le mercure gazeux atmosphérique (TGM) a été mesuré en prélevant un volume défini d'air dans un piège d'or. Le mercure gazeux dissous dans l'eau (DGM) a été mesuré en purgeant les échantillons d'eau suivi d'une rétention sur piège d'or. Ces pièges ont ensuite été analysés directement sur site, ou bien dans un laboratoire à Cayenne par double amalgamation et analyse par spectrométrie de fluorescence atomique (AFS Tekran-2500)

Résultats

Les compositions des isotopes stables du Hg ont mis en évidence une dissémination importante du Hg anthropique dans les sédiments des bassins miniers et dans le sol des zones d'exploitation minière illégale (3 - 82 %), ainsi que son incorporation dans la végétation environnante (racines et feuilles). La contamination par le Hg anthropique était limitée aux zones d'exploitation minière illégale, sans impact visible sur les sols exploités légalement. Cependant, la composition isotopique du Hg a montré une augmentation de la contribution anthropique du Hg dans les sédiments de rivière en aval du site minier. Ainsi, les isotopes du Hg sont un outil efficace pour suivre l'orpaillage illégal passé.

Les concentrations atmosphériques de Hg directement mesurées au cours des campagnes d'échantillonnage par échantillonnage actif étaient de 7.5 ± 6.3 ng.m^{-3} (Figure 8.9), ce qui est légèrement supérieur aux niveaux observés dans les régions éloignées (Amouroux et al. 1999). Les mesures de Hg atmosphérique intégrées sur trois mois et effectuées à l'aide d'échantillonneurs passifs donnent des concentrations plus basses (1.4 ± 0.7 ng.m^{-3}). Une tendance saisonnière a été observée, avec une augmentation des concentrations pendant la saison sèche.

Les fortes concentrations de mercure gazeux dissous (DGM) relevées dans certains bassins miniers (30 – 7000 ng.m^{-3}, médiane 1300 ng.m^{-3}) confirment que les eaux stagnantes sont une source de Hg élémentaire dans l'atmosphère par volatilisation. Cependant, les réémissions de Hg à partir des sols et des environnements miniers remaniés n'ont pas encore été caractérisées.

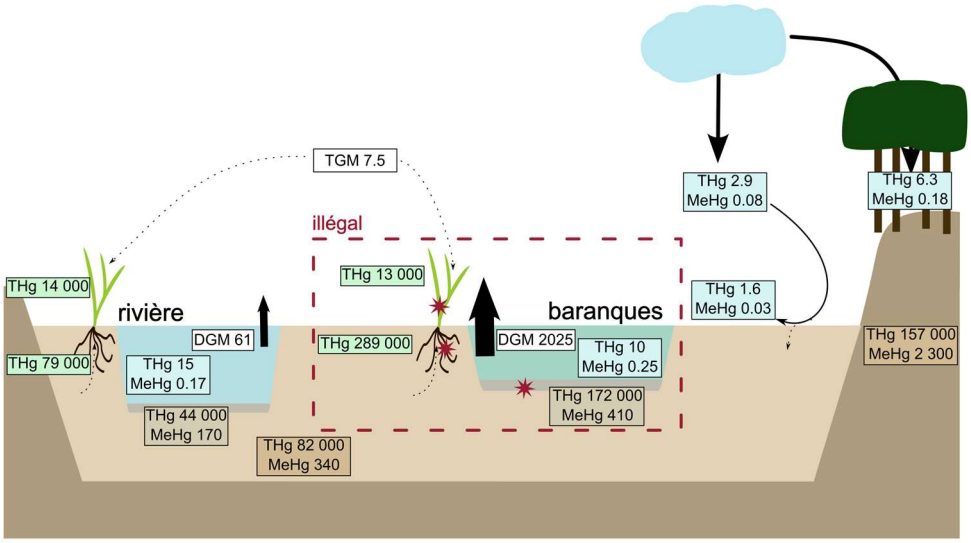

Figure 8.9. *Synthèse des pools de mercure et spéciation sur un site minier alluvial en Guyane française. Les compartiments représentés sont la végétation (vert), l'eau (bleu), les sédiments et sols (brun), et le Hg gazeux (blanc). Le THg et le MeHg sont des valeurs de concentrations moyennes exprimées en ng.kg^{-1}, le Hg^0 dans TGM et DGM est en ng.m^{-3}, dans le compartiment eau, les valeurs correspondent à la somme des fractions particulaires et filtrées sauf pour les dépôts humides, l'eau de ruissellement de la végétation, et le ruissellement de surface où seule la fraction filtrée est affichée. Le carré rouge en pointillé représente une section illégalement exploitée du site minier, et les étoiles rouges représentent les compartiments dans lesquels la présence de Hg anthropique a été mise en évidence à l'aide d'isotopes stables du Hg.*

Conclusion

Les concentrations élevées de DGM dans les bassins miniers résultant d'une contamination anthropique par le Hg^0 et/ou d'un potentiel de réduction accru font de ces bassins une source importante de Hg élémentaire dans l'atmosphère.

Les isotopes stables du Hg ont démontré une contamination anthropique localisée principalement dans et autour des bassins miniers illégaux, les sols légaux affichant une composition isotopique du Hg "naturel". Cependant, les résultats préliminaires indiquent une contamination des sédiments en aval par le Hg anthropique, soulignant le potentiel des isotopes du Hg dans les sédiments en tant qu'outil permettant de suivre les activités illégales passées. Le chapitre suivant utilisera la composition isotopique du Hg dans les sédiments fluviaux des principaux bassins versants de la Guyane française pour évaluer son potentiel en tant qu'outil de suivi de l'orpaillage illégal.

8.3.4. Evaluation de la contamination au Hg par l'orpaillage en Guyane à l'échelle du bassin versant en utilisant la composition isotopique du Hg dans les sédiments de rivières

Introduction

Le chapitre précédent a montré que les sédiments en aval d'un site légal d'orpaillage présentaient une signature isotopique du mercure (Hg) plus anthropique que ceux en amont ou d'une rivière non exploitée. Toutefois, ces données ne suffisent pas à confirmer l'impact des activités illégales sur cette contamination. Ce dernier chapitre étudie donc, à l'échelle de la Guyane, la contribution du Hg d'origine anthropique liée à l'orpaillage illégal, grâce à l'analyse de la composition isotopique du Hg dans des sédiments d'archives.

Pour évaluer les contributions relatives du Hg anthropique (utilisé lors du procédé d'amalgamation de l'or), et du Hg naturellement présent dans les sols, la composition en isotopes stables du Hg ainsi que des variables géochimiques ont été déterminées dans des échantillons de sédiments prélevés au début des années 2000 dans les principaux bassins hydrographiques de la Guyane française.

Les méthodes d'analyse de concentration du Hg et de sa composition isotopique sont les mêmes que celles décrites dans le chapitre précédent (8.3.3)

Résultats

Les analyses géochimiques montrent que le mercure dans les sédiments est principalement associé à la matière organique et aux oxydes de Fe/Al.

Les concentrations totales de Hg sont corrélées ($p < 0,001$) au fractionnement dépendant de la masse (MDF, $\delta^{202}Hg$) et au fractionnement indépendant de la masse impair (MIF, $\Delta^{199}Hg$) dans les sédiments du plus grand fleuve de Guyane, le Maroni. Ceci indique que la composition isotopique du Hg dans les sédiments de rivière reflète l'étendue de la contamination.

Deux "sources" isotopiques ont été définies :

i) les sédiments contenant du Hg "naturel" ou "géogénique" présentent une composition isotopique très négative ($\delta^{202}Hg$ = -2.53 ± 0.23 ‰, $\Delta^{199}Hg$ = -0.62 ± 0.10‰), alors que

ii) dans les sédiments contaminés par l'orpaillage illégal, le Hg possède une composition isotopique proche de zéro ($\delta^{202}Hg$ = -0.42 ± 0.20 ‰, $\Delta^{199}Hg$ = -0.01 ± 0.07 ‰).

Un modèle de mélange binaire a été effectué avec ces deux sources et a montré que la contribution du Hg anthropique dans les sédiments fluviaux varie considérablement (de 0 à 100 %). Le pourcentage de Hg anthropique est corrélé à l'étendue géographique des activités d'orpaillage en Guyane sur cette période (Blancodini 2019) comme présenté en Figure 8.10.

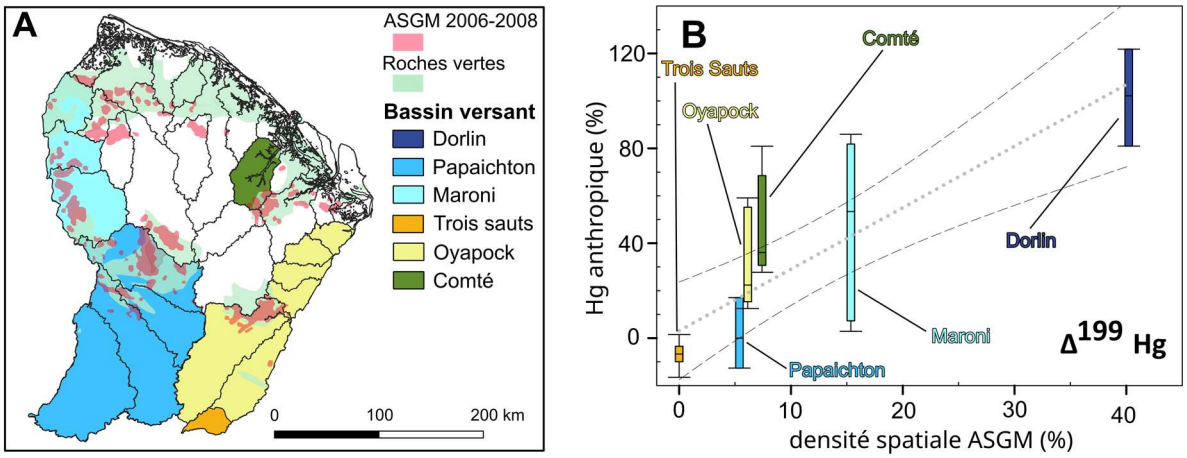

Figure 8.10. *(A) Carte de la Guyane colorée par bassin versant et surface de l'ASGM en rouge clair et (B) contribution théorique du mercure anthropique dans les échantillons de sédiments (Hg anthropique) en fonction de la densité spatiale de l'orpaillage (B). La régression* Hg_{anth} *= 3.49 + 2.60 × densité orpaillage,* R^2 *= 0.91, p = 0.0031, avec l'intervalle de confiance à 95 % en pointillés.*

Conclusion

Ces résultats soulignent que les mesures isotopiques du Hg dans les sédiments archivés permettent une évaluation rétrospective de la pollution par le Hg dans les régions impactées par l'ASGM et une évaluation de son évolution temporelle. Il serait intéressant d'effectuer le même type de mesures sur une cartographie de sédiments plus récents pour voir si l'évolution de l'orpaillage illégal au cours des dernières décennies peut être tracée par la composition du Hg dans les sédiments.

8.4. Conclusions et propositions et conseils pour la réhabilitation minière

La section suivante propose une compilation de « bonnes pratiques » en matière de réhabilitation d'une mine d'or résultant de ce travail. Plusieurs points ont déjà été soulevés ou sont déjà mis en œuvre dans la réglementation en place mais ne sont pas toujours respectés sur le terrain.

- La **réhabilitation rapide** après l'exploitation minière est essentielle et facile à mettre en œuvre. Dans les zones tropicales, la couche organique stockée pendant l'exploitation est vite dégradée par l'érosion et les pluies fréquentes, ce qui entraîne une perte de nutriments, de micro-organismes et de graines. Une remise en place rapide favorise la revégétalisation spontanée, qui limite l'érosion des sols et l'export de contaminants vers les rivières. Elle permet probablement aussi une meilleure stabilisation du sol et un rétablissement plus rapide des fonctions biologiques, en particulier des cycles du carbone et de l'azote, ouvrant la voie à la régénération d'une forêt secondaire.
- La **plantation d'arbres** joue un rôle secondaire dans la stabilisation du sol, mais elle reste essentielle pour restaurer l'écosystème. Elle permet d'apporter de la litière, relançant les cycles du carbone et de l'azote, et favorisant le retour des fonctions du sol. Les espèces de la famille des fabacées, si associées à des bactéries fixatrices d'azote, enrichissent le sol en azote. De plus, leur ombre, tolérante à l'ensoleillement, facilite l'installation d'autres espèces végétales, augmentant ainsi la diversité des arbres et encourageant la régénération d'une forêt secondaire.
- Les résultats présentés au chapitre II-a montrent que 8 mois après la réhabilitation, la principale source de particules dans les rivières provient de l'érosion des berges. Par conséquent, il convient de mettre l'accent sur la **stabilisation des berges**. Les compagnies minières tentent déjà de recréer le tracé original de la rivière pendant la phase de réhabilitation, en incluant des méandres pour ralentir le débit de l'eau et limiter l'érosion des berges.
- Enfin, les mines légales travaillent souvent dans des zones marquées par une exploitation illégale, mais ne sont pas obligées de réhabiliter ces anciens **bassins de décantation**. Or, ces bassins contiennent de fortes concentrations de mercure sous différentes formes (DGM, THg, MeHg), et leur réhabilitation risquerait de libérer d'importantes quantités de mercure dans les rivières. D'un autre côté, si elles sont laissées en l'état, elles constituent une source de Hg gazeux dans l'atmosphère par volatilisation du DGM. Cependant, la quantité de Hg exporté par volatilisation reste moindre au Hg qui serait probablement libéré vers les rivières dans le cas de leur réhabilitation (vidange du bassin et remaniement du sol pour le terrassement). Ceci joue en faveur de laisser ces bassins dans leur état d'origine.

References

Achá, D., H. Hintelmann and J. Yee (2011). "Importance of sulfate reducing bacteria in mercury methylation and demethylation in periphyton from Bolivian Amazon region." Chemosphere **82**(6): 911-916. doi: 10.1016/j.chemosphere.2010.10.050.

ACTO/OTCA (2018). "Strategic Action Program: Regional Strategy for Integrated Water Resources Management in the Amazon Basin.": 204p. doi: 978-85-61873-17-2.

Adler Miserendino, R., J. R. D. Guimarães, G. Schudel, S. Ghosh, J. M. Godoy, E. K. Silbergeld, P. S. J. Lees and B. A. Bergquist (2018). "Mercury Pollution in Amapá, Brazil: Mercury Amalgamation in Artisanal and Small-Scale Gold Mining or Land-Cover and Land-Use Changes?" ACS Earth and Space Chemistry **2**(5): 441-450. doi: 10.1021/acsearthspacechem.7b00089.

Almeida, M. D., R. V. Marins, H. H. Paraquetti, W. R. Bastos and L. D. Lacerda (2009). "Mercury degassing from forested and open field soils in Rondonia, Western Amazon, Brazil." Chemosphere **77**(1): 60-66. doi: 10.1016/j.chemosphere.2009.05.018.

AMAP/UNEP (2019). Technical background report for the global mercury assessment 2018, Arctic Monitoring and Assessment Programme, Oslo, Norway / UN Environment Programe, Geneva, Switzerland.

Amouroux, D., J. C. Wasserman, E. Tessier and O. F. X. Donard (1999). "Elemental Mercury in the Atmosphere of a Tropical Amazonian Forest (French Guiana)." Environmental Science & Technology **33**(17): 3044-3048. doi: 10.1021/es990119b.

Andersson, M. E., K. Gardfeldt, I. Wangberg and D. Stromberg (2008). "Determination of Henry's law constant for elemental mercury." Chemosphere **73**(4): 587-592. doi: 10.1016/j.chemosphere.2008.05.067.

Andrieu, A., P. Brousse, A. Zeghnoun, A. Verrier, A. Saoudi, E. Martin, J. Clouzeau, A. Jolivet, M. Pecheux and C. Rousseau (2020). "Blood lead level in children 1 – 6 years old, in French Guiana, 2015–2016 - Impregnation par le plomb des enfants de 1 a 6 ans en Guyane, 2015–2016." Bulletin Epidemiologique Hebdomadaire (BEH), Santé Publique France.

Angulo-Martínez, M., S. Beguería, A. Navas and J. Machín (2012). "Splash erosion under natural rainfall on three soil types in NE Spain." Geomorphology **175-176**: 38-44. doi: 10.1016/j.geomorph.2012.06.016.

Antoninka, A., A. Faist, E. Rodriguez-Caballero, K. E. Young, V. B. Chaudhary, L. A. Condon and D. A. Pyke (2020). "Biological soil crusts in ecological restoration: emerging research and perspectives." Restoration Ecology **28**(S2). doi: 10.1111/rec.13201.

Armijos, E., A. Crave, J. C. Espinoza, N. Filizola, R. Espinoza-Villar, Ayes, P. Fonseca, P. Fraizy, O. Gutierrez, P. Vauchel, B. Camenen, J. M. Martiınez, A. Dos Santos, W. Santini, G. Cochonneau and J. L. Guyot (2020). "Rainfall control on Amazon sediment flux: synthesis from 20 years of monitoring." Environmental Research Communications **2**(5): 051008. doi: 10.1088/2515-7620/ab9003.

Artaxo, P. (2023). "Amazon deforestation implications in local/regional climate change." Proc Natl Acad Sci U S A **120**(50): e2317456120. doi: 10.1073/pnas.2317456120.

Azevedo-Silva, C. E., R. Almeida, D. P. Carvalho, J. Ometto, P. B. de Camargo, P. R. Dorneles, A. Azeredo, W. R. Bastos, O. Malm and J. P. M. Torres (2016). "Mercury biomagnification and the trophic structure of the ichthyofauna from a remote lake in the Brazilian Amazon." Environ Res **151**: 286-296. doi: 10.1016/j.envres.2016.07.035.

Balan, E., E. Fritsch, T. Allard and G. Calas (2007). "Inheritance vs. neoformation of kaolinite during lateritic soil formation: A case study in the middle Amazon basin." Clays and Clay Minerals **55**(3): 253-259. doi: 10.1346/ccmn.2007.0550303.

Balslev-Clausen, D., T. W. Dahl, N. Saad and M. T. Rosing (2013). "Precise and accurate δ13C analysis of rock samples using Flash Combustion–Cavity Ring Down Laser Spectroscopy." Journal of Analytical Atomic Spectrometry **28**(4): 516. doi: 10.1039/c2ja30240c.

Barre, J. P. G., G. Deletraz, C. Sola-Larranaga, J. M. Santamaria, S. Berail, O. F. X. Donard and D. Amouroux (2018). "Multi-element isotopic signature (C, N, Pb, Hg) in epiphytic lichens to discriminate atmospheric contamination as a function of land-use characteristics (Pyrenees-Atlantiques, SW France)." Environ Pollut **243**(Pt B): 961-971. doi: 10.1016/j.envpol.2018.09.003.

Barron, A. R., N. Wurzburger, J. P. Bellenger, S. J. Wright, A. M. L. Kraepiel and L. O. Hedin (2008). "Molybdenum limitation of asymbiotic nitrogen fixation in tropical forest soils." Nature Geoscience **2**(1): 42-45. doi: 10.1038/ngeo366.

Barron, E. J., C. Harrison, G.A., J. L. Sloan II and W. W. Hay (1981). "Paleogeography, 180 million years ago to the present." Eclogae geologicae Helvetiae **71/2**: 443-470.

Bass, A. M., M. I. Bird, M. J. Liddell and P. N. Nelson (2011). "Fluvial dynamics of dissolved and particulate organic carbon during periodic discharge events in a steep tropical rainforest catchment." Limnology and Oceanography **56**(6): 2282-2292. doi: 10.4319/lo.2011.56.6.2282.

Basta, P. C., A. C. S. de Vasconcellos, G. Hallwass, D. Yokota, D. Pinto, D. S. de Aguiar, C. C. de Souza and M. Oliveira-da-Costa (2023). "Risk Assessment of Mercury-Contaminated Fish Consumption in the Brazilian Amazon: An Ecological Study." Toxics **11**(9). doi: 10.3390/toxics11090800.

Baumes Malfant, C. (2020). "Lutter ensemble contre la Montagne d'or. Les mobilisations anti-extractives à l'épreuve des fractures ethno-raciales." Cahiers des Amériques latines **1**(93): 133-152. doi: 10.4000/cal.10854.

Baya, P. A., M. Gosselin, I. Lehnherr, V. L. St Louis and H. Hintelmann (2015). "Determination of monomethylmercury and dimethylmercury in the Arctic marine boundary layer." Environ Sci Technol **49**(1): 223-232. doi: 10.1021/es502601z.

Beliveau, A., M. Lucotte, R. Davidson, S. Paquet, F. Mertens, C. J. Passos and C. A. Romana (2017). "Reduction of soil erosion and mercury losses in agroforestry systems compared to forests and cultivated fields in the Brazilian Amazon." J Environ Manage **203**(Pt 1): 522-532. doi: 10.1016/j.jenvman.2017.07.037.

Bérail, S., J. Cavalheiro, E. Tessier, J. P. G. Barre, Z. Pedrero, O. F. X. Donard and D. Amouroux (2017). "Determination of total Hg isotopic composition at ultra-trace levels by on line cold vapor generation and dual gold-amalgamation coupled to MC-ICP-MS." Journal of Analytical Atomic Spectrometry **32**(2): 373-384. doi: 10.1039/c6ja00375c.

Bergquist, B. A. and J. D. Blum (2007). "Mass-Dependent and -Independent Fractionation of Hg Isotopes by Photoreduction in Aquatic Systems." Science **318**(5849): 417-420.

Bergquist, B. A. and J. D. Blum (2009). "The Odds and Evens of Mercury Isotopes: Applications of Mass-Dependent and Mass-Independent Isotope Fractionation." Elements **5**(6): 353-357. doi: 10.2113/gselements.5.6.353.

Bernstein, P. (2012). The power of gold: the history of an obsession, John Wiley & Sons.

Bidone, E., R. Cesar, M. C. Santos, R. Sierpe, E. V. Silva-Filho, V. Kutter, L. I. Dias da Silva and Z. Castilhos (2018). "Mass balance of arsenic fluxes in rivers impacted by gold mining activities in Paracatu (Minas Gerais State, Brazil)." Environ Sci Pollut Res Int **25**(9): 9085-9100. doi: 10.1007/s11356-018-1215-z.

Bird, M. I., W. S. Fyfe, D. Pinheiro-Dick and A. R. Chivas (2012). "Carbon isotope indicators of catchment vegetation in the Brazilian Amazon." Global Biogeochemical Cycles **6**(3): 293-306. doi: 10.1029/92gb01652.

Blancodini, P. (2019). "La frontière Suriname – Guyane française : géopolitique d'un tracé qui reste à fixer." Géoconfluences.

Blum, J. D. and B. A. Bergquist (2007). "Reporting of variations in the natural isotopic composition of mercury." Analytical and Bioanalytical Chemistry **388**(2): 353-359. doi: 10.1007/s00216-007-1236-9.

Blum, J. D., L. S. Sherman and M. W. Johnson (2014). "Mercury Isotopes in Earth and Environmental Sciences." Annual Review of Earth and Planetary Sciences **42**(1): 249-269. doi: 10.1146/annurev-earth-050212-124107.

Bouchez, J., J. Gaillardet, C. France-Lanord, L. Maurice and P. Dutra-Maia (2011). "Grain size control of river suspended sediment geochemistry: Clues from Amazon River depth profiles." Geochemistry, Geophysics, Geosystems **12**(3). doi: 10.1029/2010gc003380.

Boudou, A., R. Maury-Brachet, M. Coquery, G. Durrieu and D. Cossa (2005). "Synergic Effect of Gold Mining and Damming on Mercury Contamination in Fish." Environmental Science \& Technology **39**(8): 2448-2454. doi: 10.1021/es049149r.

Boulet, R., Y. Lucas, E. Fritsch and H. Paquet (1993). "Géochimie des paysages: le rôle des couvertures pédologiques." Coll Acad Sci. "Sédimentologie et Géochimie de la Surface" à la mémoire de Georges MILLOT: 55-77.

Brandão, D. O., L. E. S. Barata and C. A. Nobre (2022). "The Effects of Environmental Changes on Plant Species and Forest Dependent Communities in the Amazon Region." Forests **13**(3): 466. doi: 10.3390/f13030466.

Bravo, A. G., D. N. Kothawala, K. Attermeyer, E. Tessier, P. Bodmer and D. Amouroux (2018). "Cleaning and sampling protocol for analysis of mercury and dissolved organic matter in freshwater systems." MethodsX **5**: 1017-1026. doi: 10.1016/j.mex.2018.08.002.

Bueno Guerra, M. B., C. de Oliveira, M. Rocha de Carvalho, A. O. Silva, I. F. Santana Alvarenga, M. V. Barbosa, M. M. Feitosa, E. S. Penido, J. Valentim dos Santos, M. A. Carbone Carneiro, J. Bundschuh and L. R. Guimarães Guilherme (2023). "Increased mobilization of geogenic arsenic by anthropogenic activities: The Brazilian experience in mining and agricultural areas." Current Opinion in Environmental Science & Health **33**: 100472. doi: 10.1016/j.coesh.2023.100472.

Burch, G. J., I. D. Moore and J. Burns (1989). "Soil hydrophobic effects on infiltration and catchment runoff." Hydrological Processes **3**(3): 211-222. doi: 10.1002/hyp.3360030302.

Butt, E. W., J. C. A. Baker, F. G. S. Bezerra, C. von Randow, A. P. D. Aguiar and D. V. Spracklen (2023). "Amazon deforestation causes strong regional warming." Proc Natl Acad Sci U S A **120**(45): e2309123120. doi: 10.1073/pnas.2309123120.

Buttle, J. M. and D. S. Turcotte (1999). "Runoff Processes on a Forested Slope on the Canadian Shield." Hydrology Research **30**(1): 1-20. doi: 10.2166/nh.1999.0001.

Cai, H. and J. Chen (2016). "Mass-independent fractionation of even mercury isotopes." Science Bulletin **61**(2): 116-124. doi: 10.1007/s11434-015-0968-8.

Camino. ([last accessed 10 April 2025]). "https://camino.beta.gouv.fr." Retrieved 06.02.2025, from https://camino.beta.gouv.fr/statistiques/guyane.

Cardona, G. I., M. C. Escobar, A. Acosta-Gonzalez, N. Diaz-Ruiz, J. P. Nino-Garcia, Y. Vasquez, J. Marrugo-Negrete and S. Marques (2024). "Microbial diversity and abundance of Hg related genes from water, sediment and soil the Colombian amazon ecosystems impacted by artisanal and small-scale gold mining." Chemosphere **352**: 141348. doi: 10.1016/j.chemosphere.2024.141348.

Carignan, J., N. Estrade, J. E. Sonke and O. F. Donard (2009). "Odd isotope deficits in atmospheric Hg measured in lichens." Environ Sci Technol **43**(15): 5660-5664. doi: 10.1021/es900578v.

Carmouze, J.-P. and M. B. Lucotte, A. , Eds. (2001). Le mercure en Amazonie : rôle de l'homme et de l'environnement, risques sanitaires. Expertise Collégiale. Paris, IRD.

Casagrande, G. C. R., J. Dambros, E. A. de Andrade, F. Martello, T. Sobral-Souza, M. I. C. Moreno, L. D. Battirola and R. L. T. de Andrade (2023). "Atmospheric mercury in forests: accumulation analysis in a gold mining area in the southern Amazon, Brazil." Environ Monit Assess **195**(4): 477. doi: 10.1007/s10661-023-11063-6.

Castellanos, A., P. Chaparro-Narvaez, C. D. Morales-Plaza, A. Alzate, J. Padilla, M. Arevalo and S. Herrera (2016). "Malaria in gold-mining areas in Colombia." Mem Inst Oswaldo Cruz **111**(1): 59-66. doi: 10.1590/0074-02760150382.

Cavalheiro, J., C. Sola, J. Baldanza, E. Tessier, F. Lestremau, F. Botta, H. Preud'homme, M. Monperrus and D. Amouroux (2016). "Assessment of background concentrations of organometallic compounds (methylmercury, ethyllead and butyl- and phenyltin) in French aquatic environments." Water Res **94**: 32-41. doi: 10.1016/j.watres.2016.02.010.

Chadwick, S. P., C. L. Babiarz, J. P. Hurley and D. E. Armstrong (2006). "Influences of iron, manganese, and dissolved organic carbon on the hypolimnetic cycling of amended mercury." Sci Total Environ **368**(1): 177-188. doi: 10.1016/j.scitotenv.2005.09.039.

Chambi-Legoas, R., D. R. Ortega Rodriguez, F. d. M. d. Figueiredo, J. Peña Valdeiglesias, P. A. Zevallos Pollito, J. L. Marcelo-Peña and D. C. Rother (2021). "Natural Regeneration After Gold Mining in the Peruvian Amazon: Implications for Restoration of Tropical Forests." Frontiers in Forests and Global Change **4**. doi: 10.3389/ffgc.2021.594627.

Chaves, J., C. Neill, S. Germer, S. G. Neto, A. Krusche and H. Elsenbeer (2008). "Land management impacts on runoff sources in small Amazon watersheds." Hydrological Processes **22**(12): 1766-1775. doi: 10.1002/hyp.6803.

Clarke, R. G., S. J. Klapstein, R. Keenan and N. J. O'Driscoll (2023). "Salinity and total suspended solids control mercury speciation in a tidal river: Comparisons with a photochemical mercury model." Chemosphere **344**: 140313. doi: 10.1016/j.chemosphere.2023.140313.

Clavier, S., G. Periat, W. Montaigne, D. Schlunke, E. Brunstein, J. Brunstein, H. Décourcière, J. Paris, C. Pernaut and J. Neto (2024). REStauration des CRIques Orpaillées – Projet RESCRIOR. Rapport ONIKHA**:** 71.

Cole, J. J. and N. F. Caraco (1998). "Atmospheric exchange of carbon dioxide in a low-wind oligotrophic lake measured by the addition of SF6." Limnology and Oceanography **43**(4): 647-656. doi: 10.4319/lo.1998.43.4.0647.

Conrado da Cruz, D., J. M. Rey Benayas, G. Costa Ferreira and S. Santos Ribeiro (2020). "Tree Communities in Three-Year-Old Post-Mining Sites Under Different Forest Restoration Techniques in the Brazilian Amazon." Forests **11**(5): 527. doi: 10.3390/f11050527.

Cordier, S., M. Garel, L. Mandereau, H. Morcel, P. Doineau, S. Gosme-Seguret, D. Josse, R. White and C. Amiel-Tison (2002). "Neurodevelopmental Investigations among Methylmercury-Exposed Children in French Guiana." Environmental Research **89**(1): 1-11. doi: 10.1006/enrs.2002.4349.

Couic, E., V. Alphonse, A. Livet, S. Giusti-Miller and N. Bousserrhine (2021). "Influence of Ecological Restoration on Mercury Mobility and Microbial Activities on Former Guyanese Mining Sites." Applied Sciences **11**(5): 2231. doi: 10.3390/app11052231.

Couic, E., M. Grimaldi, V. Alphonse, C. Balland-Bolou-Bi, A. Livet, S. Giusti-Miller, M. Sarrazin and N. Bousserrhine (2018). "Mercury behaviour and C, N, and P biogeochemical cycles during ecological restoration processes of old mining sites in French Guiana." Environ Sci Process Impacts **20**(4): 657-672. doi: 10.1039/c8em00016f.

Couic, E., A. Tribondeau, V. Alphonse, A. Livet and N. Bousserrhine (2022). "Positive Effect of Ecological Restoration with Fabaceous Species on Microbial Activities of Former Guyanese Mining Sites." Molecules **27**(6). doi: 10.3390/molecules27061768.

Crespo-Lopez, M. E., M. Augusto-Oliveira, A. Lopes-Araujo, L. Santos-Sacramento, P. Yuki Takeda, B. M. Macchi, J. L. M. do Nascimento, C. S. F. Maia, R. R. Lima and G. P. Arrifano (2021). "Mercury: What can we learn from the Amazon?" Environ Int **146**: 106223. doi: 10.1016/j.envint.2020.106223.

Crouzeilles, R., M. S. Ferreira, R. L. Chazdon, D. B. Lindenmayer, J. B. B. Sansevero, L. Monteiro, A. Iribarrem, A. E. Latawiec and B. B. N. Strassburg (2017). "Ecological restoration success is higher for natural regeneration than for active restoration in tropical forests." Sci Adv **3**(11): e1701345. doi: 10.1126/sciadv.1701345.

Csillik, O. and G. P. Asner (2020). "Aboveground carbon emissions from gold mining in the Peruvian Amazon." Environmental Research Letters **15**(1): 014006. doi: 10.1088/1748-9326/ab639c.

Cunha, H. F. V., K. M. Andersen, L. F. Lugli, F. D. Santana, I. F. Aleixo, A. M. Moraes, S. Garcia, R. Di Ponzio, E. O. Mendoza, B. Brum, J. S. Rosa, A. L. Cordeiro, B. T. T. Portela, G. Ribeiro, S. D.

Coelho, S. T. de Souza, L. S. Silva, F. Antonieto, M. Pires, A. C. Salomao, A. C. Miron, R. L. de Assis, T. F. Domingues, L. Aragao, P. Meir, J. L. Camargo, A. O. Manzi, L. Nagy, L. M. Mercado, I. P. Hartley and C. A. Quesada (2022). "Direct evidence for phosphorus limitation on Amazon forest productivity." Nature **608**(7923): 558-562. doi: 10.1038/s41586-022-05085-2.

Cusack, D. F., D. Ashdown, L. H. Dietterich, A. Neupane, M. Ciochina and B. L. Turner (2019). "Seasonal changes in soil respiration linked to soil moisture and phosphorus availability along a tropical rainfall gradient." Biogeochemistry **145**(3): 235-254. doi: 10.1007/s10533-019-00602-4.

da Cruz, D. C., J. M. R. Benayas, G. C. Ferreira, S. R. Santos and G. Schwartz (2020). "An overview of forest loss and restoration in the Brazilian Amazon." New Forests **52**(1): 1-16. doi: 10.1007/s11056-020-09777-3.

da Silva Junior, E. C., G. C. Martins, L. H. de Oliveira Wadt, K. E. da Silva, R. M. B. de Lima, K. D. Batista, M. C. Guedes, R. C. de Oliveira Junior, A. R. Reis, G. Lopes, M. D. de Menezes, M. R. Broadley, S. D. Young and L. R. G. Guilherme (2019). "Natural variation of arsenic fractions in soils of the Brazilian Amazon." Sci Total Environ **687**: 1219-1231. doi: 10.1016/j.scitotenv.2019.05.446.

da Silva, W. B., E. Périco, M. S. Dalzochio, M. Santos and R. L. Cajaiba (2018). "Are litterfall and litter decomposition processes indicators of forest regeneration in the neotropics? Insights from a case study in the Brazilian Amazon." Forest Ecology and Management **429**: 189-197. doi: 10.1016/j.foreco.2018.07.020.

Danielson, R. E. and J. L. Mazza Rodrigues (2022). "Impacts of land-use change on soil microbial communities and their function in the Amazon Rainforest." **175**: 179-258. doi: 10.1016/bs.agron.2022.04.001.

David, M. B., M. J. Mitchell and J. P. Nakas (1982). "Organic and Inorganic Sulfur Constituents of a Forest Soil and Their Relationship to Microbial Activity." Soil Science Society of America Journal **46**(4): 847-852. doi: 10.2136/sssaj1982.03615995004600040036x.

de Araújo, A. C., J. P. H. B. Ometto, A. J. Dolman, B. Kruijt, M. J. Waterloo and J. R. Ehleringer (2008). "Implications of CO2 pooling on δ13C of ecosystem respiration and leaves in Amazonian forest." Biogeosciences **5**(3): 779-795. doi: 10.5194/bg-5-779-2008.

de Freitas, F., K. Solera, V. J. S. Lopes, M. O. Cordova, L. Cavalheiro, M. I. C. Moreno, L. D. Battirola and R. L. T. de Andrade (2024). "Native accumulator plants with a differential mercury phytoremediation potential in a region in Southern Amazon." Environ Sci Pollut Res Int **31**(54): 63120-63135. doi: 10.1007/s11356-024-35407-y.

de Lucia Lobo, F., E. Márcia Leão de Moraes Novo, C. Clemente Faria Barbosa and V. Hugo Fernandes de Vasconcelos (2019). "Monitoring Water Siltation Caused by Small-Scale Gold Mining in Amazonian Rivers Using Multi-Satellite Images." doi: 10.5772/intechopen.79725.

de Meyer, C. M. C., J. M. Rodriguez, E. A. Carpio, P. A. Garcia, C. Stengel and M. Berg (2017). "Arsenic, manganese and aluminum contamination in groundwater resources of Western Amazonia (Peru)." Sci Total Environ **607-608**: 1437-1450. doi: 10.1016/j.scitotenv.2017.07.059.

de Meyer, C. M. C., I. Wahnfried, J. M. Rodriguez Rodriguez, R. Kipfer, P. A. Garcia Avelino, E. A. Carpio Deza and M. Berg (2023). "Hotspots of geogenic arsenic and manganese contamination in groundwater of the floodplains in lowland Amazonia (South America)." Sci Total Environ **860**: 160407. doi: 10.1016/j.scitotenv.2022.160407.

de Oliveira, S. M. B., A. J. Melfi, A. H. Fostier, M. C. Forti, D. I. T. Fávaro and R. Boulet (2001). "Soils as an Important Sink for Mercury in the Amazon." Water, Air, and Soil Pollution **126**(3/4): 321-337. doi: 10.1023/a:1005239627632.

Delnatte, C. and J.-Y. Meyer (2011). "Plant introduction, naturalization, and invasion in French Guiana (South America)." Biological Invasions **14**(5): 915-927. doi: 10.1007/s10530-011-0129-1.

Demsar, J., T. Curk, A. Erjavec, C. Gorup, T. Hocevar, M. Milutinovic, M. Mozina, M. Polajnar, M. Toplak , A. Staric, M. Stajdohar, L. Umek, L. Zagar, J. Zbontar, M. Zitnik and B. Zupan (2013). "Orange: Data Mining Toolbox in Python." Journal of Machine Learning Research 14 2349-2353.

Dethier, E. N., S. L. Sartain and D. A. Lutz (2019). "Heightened levels and seasonal inversion of riverine suspended sediment in a tropical biodiversity hot spot due to artisanal gold mining." Proc Natl Acad Sci U S A **116**(48): 23936-23941. doi: 10.1073/pnas.1907842116.

Diringer, S. E., A. J. Berky, M. Marani, E. J. Ortiz, O. Karatum, D. L. Plata, W. K. Pan and H. Hsu-Kim (2020). "Deforestation Due to Artisanal and Small-Scale Gold Mining Exacerbates Soil and Mercury Mobilization in Madre de Dios, Peru." Environ Sci Technol **54**(1): 286-296. doi: 10.1021/acs.est.9b06620.

Diringer, S. E., B. J. Feingold, E. J. Ortiz, J. A. Gallis, J. M. Arajo-Flores, A. Berky, W. K. Y. Pan and H. Hsu-Kim (2015). "River transport of mercury from artisanal and small-scale gold mining and risks for dietary mercury exposure in Madre de Dios, Peru." Environmental Science: Processes {\&} Impacts **17**(2): 478-487. doi: 10.1039/c4em00567h.

Dolbec, J., D. Mergler, C. J. Sousa Passos, S. Sousa de Morais and J. Lebel (2000). "Methylmercury exposure affects motor performance of a riverine population of the Tapajos river, Brazilian Amazon." Int Arch Occup Environ Health **73**(3): 195-203. doi: 10.1007/s004200050027.

Dos Santos, J. V., W. de Melo Rangel, A. Azarias Guimaraes, P. M. Duque Jaramillo, M. Rufini, L. M. Marra, M. Varon Lopez, M. A. Pereira da Silva, C. R. Fonseca Sousa Soares and F. M. de Souza Moreira (2013). "Soil biological attributes in arsenic-contaminated gold mining sites after revegetation." Ecotoxicology **22**(10): 1526-1537. doi: 10.1007/s10646-013-1139-9.

dos Santos Pinheiro, G. M., F. Poitrasson, F. Sondag, G. Cochonneau and L. C. Vieira (2014). "Contrasting iron isotopic compositions in river suspended particulate matter: the Negro and the Amazon annual river cycles." Earth and Planetary Science Letters **394**: 168-178. doi: 10.1016/j.epsl.2014.03.006.

Douine, M., V. Korsec, A. Sanna, L. Plessis, T. Bardon, A. Adenis, M. Nacher, M. Suarez-Mutis, S. Vreden, O. Mathieu and Y. Lambert (2025). "Prevalence of lead poisoning among artisanal gold miners in French Guiana in 2022." doi: 10.1101/2025.01.31.25321474.

Douine, M., Y. Lambert, L. Musset, H. Hiwat, L. R. Blume, P. Marchesini, G. G. Moresco, H. Cox, J. F. Sanchez, L. Villegas, V. P. de Santi, A. Sanna, S. Vreden and M. Suarez-Mutis (2020). "Malaria in Gold Miners in the Guianas and the Amazon: Current Knowledge and Challenges." Current Tropical Medicine Reports **7**(2): 37-47. doi: 10.1007/s40475-020-00202-5.

Douine, M., Y. Lambert, L. Plessis, I. Jimeno, M. Galindo, T. Bardon, F. M. Le Tourneau, P. Molinie, A. Vie, A. Adenis, M. Nacher, A. Figueira da Silva, S. Vreden, M. C. Suarez-Mutis and A. Sanna (2023). "Social determinants of health among people working on informal gold mines in French Guiana: a multicentre cross-sectional survey." BMJ Glob Health **8**(12). doi: 10.1136/bmjgh-2023-012991.

Drits, V. A., B. B. Zviagina, B. A. Sakharov, O. V. Dorzhieva and A. T. Savichev (2021). "New Insight into the Relationships Between Structural and Ftir Spectroscopic Features of Kaolinites." Clays and Clay Minerals **69**(3): 366-388. doi: 10.1007/s42860-021-00133-w.

Durrieu, G., R. Maury-Brachet and A. Boudou (2005). "Goldmining and mercury contamination of the piscivorous fish Hoplias aimara in French Guiana (Amazon basin)." Ecotoxicology and Environmental Safety **60**(3): 315-323. doi: 10.1016/j.ecoenv.2004.05.004.

Duval, B., E. Tessier, L. Kortazar, L. A. Fernandez, A. de Diego and D. Amouroux (2023). "Dynamics, distribution, and transformations of mercury species from pyrenean high-altitude lakes." Environ Res **216**(Pt 2): 114611. doi: 10.1016/j.envres.2022.114611.

Egmann, G., P. Tattevin, R. Palancade and M. Nacher (2018). "Prehospital Emergencies in Illegal Gold Mining Sites in French Guiana." Wilderness Environ Med **29**(1): 72-77. doi: 10.1016/j.wem.2017.09.008.

Eklof, K., K. Bishop, S. Bertilsson, E. Bjorn, M. Buck, U. Skyllberg, O. A. Osman, R. M. Kronberg and A. G. Bravo (2018). "Formation of mercury methylation hotspots as a consequence of forestry operations." Sci Total Environ **613-614**: 1069-1078. doi: 10.1016/j.scitotenv.2017.09.151.

Enrico, M., G. Le Roux, L. E. Heimburger, P. Van Beek, M. Souhaut, J. Chmeleff and J. E. Sonke (2017). "Holocene Atmospheric Mercury Levels Reconstructed from Peat Bog Mercury Stable Isotopes." Environ Sci Technol **51**(11): 5899-5906. doi: 10.1021/acs.est.6b05804.

Escat, S. (2015). "Lutte contre l'orpaillage clandestin en Guyane : ce n'est pas gagné !" Revue Défense Nationale **N° 779**(4): 44-46. doi: 10.3917/rdna.779.0044.

Escudie, F., L. Auer, M. Bernard, M. Mariadassou, L. Cauquil, K. Vidal, S. Maman, G. Hernandez-Raquet, S. Combes and G. Pascal (2018). "FROGS: Find, Rapidly, OTUs with Galaxy Solution." Bioinformatics **34**(8): 1287-1294. doi: 10.1093/bioinformatics/btx791.

Esdaile, L. J. and J. M. Chalker (2018). "The Mercury Problem in Artisanal and Small-Scale Gold Mining." Chemistry **24**(27): 6905-6916. doi: 10.1002/chem.201704840.

Eva, H. D. and O. Huber (2005). "A Proposal for Defining the Geographic Boundaries of Amazonia: Synthesis of the Results from An Expert Consultation Workshop Organized by the European Commission in Collaboration with the Amazon Cooperation Treaty Organization—JRC Ispra, 7–8 June 2005." Luxembourg: Office for Official Publications of the European Communities.

Fearnside, P. M. (2005). "Deforestation in Brazilian Amazonia: History, Rates, and Consequences." Conservation Biology **19**(3): 680-688. doi: 10.1111/j.1523-1739.2005.00697.x.

Feinberg, A., T. Dlamini, M. Jiskra, V. Shah and N. E. Selin (2022). "Evaluating atmospheric mercury (Hg) uptake by vegetation in a chemistry-transport model." Environ Sci Process Impacts **24**(9): 1303-1318. doi: 10.1039/d2em00032f.

Figueiredo, B. R., A. B. De Campos, R. Da Silva and N. C. Hoffman (2018). "Mercury sink in Amazon rainforest: soil geochemical data from the Tapajos National Forest, Brazil." Environmental Earth Sciences **77**(8). doi: 10.1007/s12665-018-7471-x.

Figueiredo, V., A. Enrich-Prast and T. Rutting (2019). "Evolution of nitrogen cycling in regrowing Amazonian rainforest." Sci Rep **9**(1): 8538. doi: 10.1038/s41598-019-43963-4.

Fikri, M., C. Joulian, M. Motelica-Heino, M. P. Norini and J. Hellal (2021). "Resistance and Resilience of Soil Nitrogen Cycling to Drought and Heat Stress in Rehabilitated Urban Soils." Front Microbiol **12**: 727468. doi: 10.3389/fmicb.2021.727468.

Fisher, J. A., L. Schneider, A. H. Fostier, S. Guerrero, J. R. D. Guimaraes, C. Labuschagne, J. J. Leaner, L. G. Martin, R. P. Mason, V. Somerset and C. Walters (2023). "A synthesis of mercury research in the Southern Hemisphere, part 2: Anthropogenic perturbations." Ambio **52**(5): 918-937. doi: 10.1007/s13280-023-01840-5.

Fostier, A. H., D. Amouroux, E. Tessier, J. L. M. Viana and L. Richter (2023). "Methylmercury content in soil and litter from the Amazonian rainforest and its potential fate during forest fires." Frontiers in Environmental Chemistry **4**. doi: 10.3389/fenvc.2023.1242915.

Fostier, A. H., M. C. Forti, J. R. Guimaraes, A. J. Melfi, R. Boulet, C. M. Espirito Santo and F. J. Krug (2000). "Mercury fluxes in a natural forested Amazonian catchment (Serra do Navio, Amapa State, Brazil)." Sci Total Environ **260**(1-3): 201-211. doi: 10.1016/s0048-9697(00)00564-7.

Fostier, A. H., J. J. Melendez-Perez and L. Richter (2015). "Litter mercury deposition in the Amazonian rainforest." Environmental Pollution **206**: 605-610. doi: 10.1016/j.envpol.2015.08.010.

Franco-Solís, A. and C. V. Montanía (2021). "Dynamics of deforestation worldwide: A structural decomposition analysis of agricultural land use in South America." Land Use Policy **109**: 105619. doi: 10.1016/j.landusepol.2021.105619.

Franco, A. L. C., B. W. Sobral, A. L. C. Silva and D. H. Wall (2019). "Amazonian deforestation and soil biodiversity." Conserv Biol **33**(3): 590-600. doi: 10.1111/cobi.13234.

Fritsch, E., E. Balan, N. Régina Do Nascimento, T. Allard, M. Bardy, G. Bueno, S. Derenne, A. J. Melfi and G. Calas (2011). "Deciphering the weathering processes using environmental mineralogy and geochemistry: Towards an integrated model of laterite and podzol genesis in the Upper Amazon Basin." Comptes Rendus. Géoscience **343**(2-3): 188-198. doi: 10.1016/j.crte.2010.11.002.

Fu, P., F. Wu, C. Liu, F. Wang, W. Li, L. Yue and Q. Guo (2007). "Fluorescence characterization of dissolved organic matter in an urban river and its complexation with Hg(II)." Applied Geochemistry **22**(8): 1668-1679. doi: 10.1016/j.apgeochem.2007.03.041.

Gaby, J. C. and D. H. Buckley (2012). "A comprehensive evaluation of PCR primers to amplify the nifH gene of nitrogenase." PLoS One **7**(7): e42149. doi: 10.1371/journal.pone.0042149.

Galaxy, C. (2022). "The Galaxy platform for accessible, reproducible and collaborative biomedical analyses: 2022 update." Nucleic Acids Res **50**(W1): W345-W351. doi: 10.1093/nar/gkac247.

Gallay, M., J. M. Martinez, S. Allo, A. Mora, G. Cochonneau, A. Gardel, J. C. Doudou, M. Sarrazin, F. Chow-Toun and A. Laraque (2018). "Impact of land degradation from mining activities on the sediment fluxes in two large rivers of French Guiana." Land Degradation & Development **29**(12): 4323-4336. doi: 10.1002/ldr.3150.

Gallay, M., A. Mora, J. M. Martinez, A. Gardel, A. Laraque, M. Sarrazin, E. Beaucher, J. C. Doudou and C. Lagane (2017). "Dynamics and fluxes of organic carbon and nitrogen in two Guiana Shield river basins impacted by deforestation and mining activities." Hydrological Processes **32**(1): 17-29. doi: 10.1002/hyp.11394.

Gao, X., W. Yuan, J. Chen, F. Huang, Z. Wang, Y. Gong, Y. Zhang, Y. Liu, T. Zhang and W. Zheng (2023). "Tracing the source and transport of Hg during pedogenesis in strongly weathered tropical soil using Hg isotopes." Geochimica et Cosmochimica Acta **361**: 101-112. doi: 10.1016/j.gca.2023.10.009.

Garate-Quispe, J., M. Velásquez Ramírez, E. Becerra-Lira, S. Baez-Quispe, M. Abril-Surichaqui, L. Rodriguez-Achata, A. Muñoz-Ushñahua, P. Nascimento Herbay, Y. Fernandez-Mamani, G. Alarcon-Aguirre, M. Herrera-Machaca, L. Hilares Vargas, R. Corvera Gomringer and D. del Castillo Torres (2023). "Influence of Distance from Forest Edges on Spontaneous Vegetation Succession Following Small-Scale Gold Mining in the Southeast Peruvian Amazon." Diversity **15**(6): 793. doi: 10.3390/d15060793.

Gastauer, M., W. R. Nascimento, C. F. Caldeira, S. J. Ramos, P. W. M. Souza-Filho and J.-B. Féret (2022). "Spectral diversity allows remote detection of the rehabilitation status in an Amazonian iron mining complex." International Journal of Applied Earth Observation and Geoinformation **106**: 102653. doi: 10.1016/j.jag.2021.102653.

Gerson, J. R., N. Szponar, A. A. Zambrano, B. Bergquist, E. Broadbent, C. T. Driscoll, G. Erkenswick, D. C. Evers, L. E. Fernandez, H. Hsu-Kim, G. Inga, K. N. Lansdale, M. J. Marchese, A. Martinez, C. Moore, W. K. Pan, R. P. Purizaca, V. Sanchez, M. Silman, E. A. Ury, C. Vega, M. Watsa and E. S. Bernhardt (2022). "Amazon forests capture high levels of atmospheric mercury pollution from artisanal gold mining." Nat Commun **13**(1): 559. doi: 10.1038/s41467-022-27997-3.

Gerson, J. R., S. N. Topp, C. M. Vega, J. R. Gardner, X. Yang, L. E. Fernandez, E. S. Bernhardt and T. M. Pavelsky (2020). "Artificial lake expansion amplifies mercury pollution from gold mining." Sci Adv **6**(48). doi: 10.1126/sciadv.abd4953.

Gibb, H. and K. G. O'Leary (2014). "Mercury exposure and health impacts among individuals in the artisanal and small-scale gold mining community: a comprehensive review." Environ Health Perspect **122**(7): 667-672. doi: 10.1289/ehp.1307864.

Gilmour, C. C., M. Podar, A. L. Bullock, A. M. Graham, S. D. Brown, A. C. Somenahally, A. Johs, R. A. Hurt, Jr., K. L. Bailey and D. A. Elias (2013). "Mercury methylation by novel microorganisms from new environments." Environ Sci Technol **47**(20): 11810-11820. doi: 10.1021/es403075t.

Goix, S., L. Maurice, L. Laffont, R. Rinaldo, C. Lagane, J. Chmeleff, J. Menges, L.-E. Heimbürger, R. Maury-Brachet and J. E. Sonke (2019). "Quantifying the impacts of artisanal gold mining on a tropical river system using mercury isotopes." Chemosphere **219**: 684-694. doi: 10.1016/j.chemosphere.2018.12.036.

Gomes, A. C. S. and F. J. Luizão (2011). "Leaf and Soil Nutrients in a Chronosequence of Second-Growth Forest in Central Amazonia: Implications for Restoration of Abandoned Lands." Restoration Ecology **20**(3): 339-345. doi: 10.1111/j.1526-100X.2011.00773.x.

Gomi, T., R. C. Sidle, M. Ueno, S. Miyata and K. i. Kosugi (2008). "Characteristics of overland flow generation on steep forested hillslopes of central Japan." Journal of Hydrology **361**(3-4): 275-290. doi: 10.1016/j.jhydrol.2008.07.045.

Grangeon, T., C. Legout, M. Esteves, N. Gratiot and O. Navratil (2012). "Variability of the particle size of suspended sediment during highly concentrated flood events in a small mountainous catchment." Journal of Soils and Sediments **12**(10): 1549-1558. doi: 10.1007/s11368-012-0562-5.

Gray, J. E., M. J. Pribil and P. L. Higueras (2013). "Mercury isotope fractionation during ore retorting in the Almadén mining district, Spain." Chemical Geology **357**: 150-157. doi: 10.1016/j.chemgeo.2013.08.036.

Gray, J. E., M. J. Pribil, P. C. Van Metre, D. M. Borrok and A. Thapalia (2013). "Identification of contamination in a lake sediment core using Hg and Pb isotopic compositions, Lake Ballinger, Washington, USA." Applied Geochemistry **29**: 1-12. doi: 10.1016/j.apgeochem.2012.12.001.

Graydon, J. A., V. L. St Louis, H. Hintelmann, S. E. Lindberg, K. A. Sandilands, J. W. Rudd, C. A. Kelly, M. T. Tate, D. P. Krabbenhoft and I. Lehnherr (2009). "Investigation of uptake and retention of atmospheric Hg(II) by boreal forest plants using stable Hg isotopes." Environ Sci Technol **43**(13): 4960-4966. doi: 10.1021/es900357s.

Greene, A. C. (2014). "The Family Desulfuromonadaceae." The Prokaryotes: 143-155. doi: 10.1007/978-3-642-39044-9_380.

Grimaldi, C., M. Grimaldi and S. Guedron (2008). "Mercury distribution in tropical soil profiles related to origin of mercury and soil processes." Science of The Total Environment **401**(1-3): 121-129. doi: 10.1016/j.scitotenv.2008.04.001.

Grimaldi, C., M. Grimaldi, A. Millet, T. Bariac and J. Boulègue (2003). "Behaviour of chemical solutes during a storm in a rainforested headwater catchment." Hydrological Processes **18**(1): 93-106. doi: 10.1002/hyp.1314.

Grimaldi, M., A. D., C. Grimaldi, L. Spadini, E. Tessier, G. Dutin and M. Sarrazin (2002). "Programme mercure en Guyane. Rapport final, deuxième partie : région du Haut-Maroni et bassins versants ECEREX." CNRS-PEVS.

Grimaldi, M., J. Gaudet, C. Grimaldi, M.-A. Melieres and L. Spadini (2001). "Programme de recheche Le Mercure en Guyane Française Rapport final, partie I : la région de St Elie et le réservoir de Petit Saut." CNRS-PEVS.

Grimaldi, M., S. Guédron and C. Grimaldi (2015). Impact of gold mining on mercury contamination and soil degradation in Amazonian ecosystems of French Guiana. Land-use change impacts on soil processes: tropical and savannah ecosystems. F. Q. Brearley, Thomas, A. D. Wallingford, UK, CABI**:** 95-107.

Guédron, S., D. Amouroux, E. Tessier, C. Grimaldi, J. Barre, S. Berail, V. Perrot and M. Grimaldi (2018). "Mercury Isotopic Fractionation during Pedogenesis in a Tropical Forest Soil Catena (French Guiana): Deciphering the Impact of Historical Gold Mining." Environmental science & technology **52**(20): 11573–11582. doi: 10.1021/acs.est.8b02186.

Guédron, S., D. Cossa, M. Grimaldi and L. Charlet (2011). "Methylmercury in tailings ponds of Amazonian gold mines (French Guiana): Field observations and an experimental flocculation method for *in situ* remediation." Appl. Geochem. **26**(2): 222-229. doi: 10.1016/j.apgeochem.2010.11.022.

Guédron, S., S. Grangeon, B. Lanson and M. Grimaldi (2009). "Mercury speciation in a tropical soil association; Consequence of gold mining on Hg distribution in French Guiana." Geoderma **153**: 331-346. doi: 10.1016/j.geoderma.2009.08.017.

Guédron, S., C. Grimaldi, C. Chauvel, C. Spadini and M. Grimaldi (2006). "Weathering versus atmospheric contributions to mercury concentrations in French Guiana soils." Appl. Geochem. **21**: 2010-2022. doi: 10.1016/j.apgeochem.2006.08.011.

Guédron, S., M. Grimaldi, C. Grimaldi, D. Cossa, D. Tisserand and L. Charlet (2011). "Amazonian former gold mined soils as a source of methylmercury: Evidence from a small scale watershed in French Guiana." Wat. Res. **45**(8): 2659-2669. doi: 10.1016/j.watres.2011.02.022.

Guédron, S., J. Tolu, E. Brisset, P. Sabatier, V. Perrot, S. Bouchet, A. L. Develle, R. Bindler, D. Cossa and S. C. Fritz (2019). "Late Holocene volcanic and anthropogenic mercury deposition in the western Central Andes (Lake Chungará, Chile)." Science of the total environment **662**: 903-914. doi: 10.1016/j.scitotenv.2019.01.294.

Guimarães, J. R. D., M. Meili, O. Malm and E. Maria de Souza Brito (1998). "Hg methylation in sediments and floating meadows of a tropical lake in the Pantanal floodplain, Brazil." Science of The Total Environment **213**(1-3): 165-175. doi: 10.1016/s0048-9697(98)00089-8.

Gurjão, R. d. S., V. P. Lemos, M. L. d. Costa, H. A. D. Filho, K. d. G. F. Dantas, W. T. d. S. Lima and D. C. Kern (2010). "Comportamento do mercúrio em perfis de solos do sítio Ilha de Terra-Caxiuanã, Pará." Química Nova **33**(4): 821-826. doi: 10.1590/s0100-40422010000400011.

Guzmán-Uria, F., I. Morales-Belpaire, D. Achá and M. Pouilly (2020). "Particulate Mercury and Particulate Organic Matter in the Itenez Basin (Bolivia)." Applied Sciences **10**(23): 8407. doi: 10.3390/app10238407.

Hachiya, N., Y. Takizawa, S. Hisamatsu, T. Abe, Y. Abe and Y. Motohashi (1998). "Atmospheric mercury concentrations in the basin of the amazon, Brazil." Environ Health Prev Med **2**(4): 183-187. doi: 10.1007/BF02931699.

Hacon, S., P. Artaxo, F. Gerab, M. A. Yamasoe, R. C. Campos, L. F. Conti and L. D. De Lacerda (1995). "Atmospheric mercury and trace elements in the region of Alta Floresta in the Amazon Basin." Water, Air, and Soil Pollution **80**(1-4): 273-283. doi: 10.1007/bf01189677.

Hacon, S. S., M. Oliveira-da-Costa, C. S. Gama, R. Ferreira, P. C. Basta, A. Schramm and D. Yokota (2020). "Mercury Exposure through Fish Consumption in Traditional Communities in the Brazilian Northern Amazon." Int J Environ Res Public Health **17**(15). doi: 10.3390/ijerph17155269.

Haddad, H. (2022). Dynamique des dépôts de sédiments cohésifs dans les rivières à graviers : approche combinant suivi in situ et modélisation numérique. Ph.D.

Hammond, D. S., V. Gond, B. d. Thoisy, P.-M. Forget and B. P. E. DeDijn (2007). "Causes and Consequences of a Tropical Forest Gold Rush in the Guiana Shield, South America." AMBIO: A Journal of the Human Environment **36**(8): 661-670. doi: 10.1579/0044-7447(2007)36[661:cacoat]2.0.co;2.

Hänggli, A., S. A. Levy, D. Armenteras, C. I. Bovolo, J. Brandão, X. Rueda and R. D. Garrett (2023). "A systematic comparison of deforestation drivers and policy effectiveness across the Amazon biome." Environmental Research Letters **18**(7): 073001. doi: 10.1088/1748-9326/acd408.

Harada, M. (1995). "Minamata disease: methylmercury poisoning in Japan caused by environmental pollution." Crit Rev Toxicol **25**(1): 1-24. doi: 10.3109/10408449509089885.

Harlow, D. E., K. Hurley, A. Fox, A. Vargas-Guerra and J. Gibson (2019). Small-Scale & Artisanal Mining - Impacts on Biodiversity in Latin America, USAID.

Harris-Hellal, J., M. Grimaldi, E. Garnier-Zarli and N. Bousserrhine (2011). "Mercury mobilization by chemical and microbial iron oxide reduction in soils of French Guyana." Biogeochemistry **103**(1-3): 223-234. doi: 10.1007/s10533-010-9457-y.

Hartanto, H., R. Prabhu, A. S. E. Widayat and C. Asdak (2003). "Factors affecting runoff and soil erosion: plot-level soil loss monitoring for assessing sustainability of forest management." Forest Ecology and Management **180**(1-3): 361-374. doi: 10.1016/s0378-1127(02)00656-4.

Hauptmann, A. and S. Klein (2009). "Bronze Age gold in Southern Georgia." ArchéoSciences **33**: 75-82. doi: 10.4000/archeosciences.2037.

Hellal, J., J. Schäfer, R. Vigouroux, L. Lanceleur and V. Laperche (2020). "Impact of Old and Recent Gold Mining Sites on Mercury Fluxes in Suspended Particulate Matter, Water and Sediment in French Guiana." Applied Sciences **10**(21): 7829. doi: 10.3390/app10217829.

Höppner, N., F. Lucassen, C. M. Chiessi, A. O. Sawakuchi and S. A. Kasemann (2018). "Holocene provenance shift of suspended particulate matter in the Amazon River basin." Quaternary Science Reviews **190**: 66-80. doi: 10.1016/j.quascirev.2018.04.021.

Huang, T.-H., Y.-H. Fu, P.-Y. Pan and C.-T. A. Chen (2012). "Fluvial carbon fluxes in tropical rivers." Current Opinion in Environmental Sustainability **4**(2): 162-169. doi: 10.1016/j.cosust.2012.02.004.

Huguet, L., S. Castelle, J. Schäfer, G. Blanc, R. Maury-Brachet, C. Reynouard and F. Jorand (2010). "Mercury methylation rates of biofilm and plankton microorganisms from a hydroelectric

reservoir in French Guiana." Science of The Total Environment **408**(6): 1338-1348. doi: 10.1016/j.scitotenv.2009.10.058.

INSEE. (last accessed 10 April 2025). "https://www.insee.fr."

Iza, E. R. H. F., A. M. C. Horbe, C. C. Castro and I. L. I. E. Herrera (2018). "Integration of Geochemical and Geophysical Data to Characterize and Map Lateritic Regolith: An Example in the Brazilian Amazon." Geochemistry, Geophysics, Geosystems **19**(9): 3254-3271. doi: 10.1029/2017gc007352.

Jähne, B., G. Heinz and W. Dietrich (1987). "Measurement of the diffusion coefficients of sparingly soluble gases in water." Journal of Geophysical Research: Oceans **92**(C10): 10767-10776. doi: 10.1029/JC092iC10p10767.

Janssen, S. E., M. W. Johnson, J. D. Blum, T. Barkay and J. R. Reinfelder (2015). "Separation of monomethylmercury from estuarine sediments for mercury isotope analysis." Chemical Geology **411**: 19-25. doi: 10.1016/j.chemgeo.2015.06.017.

Jardim, W. F., M. C. Bisinoti, P. S. Fadini and G. S. da Silva (2009). "Mercury Redox Chemistry in the Negro River Basin, Amazon: The Role of Organic Matter and Solar Light." Aquatic Geochemistry **16**(2): 267-278. doi: 10.1007/s10498-009-9086-z.

Jébrak, M., A. Heuret and P. Rostan (2021). "The gold, peoples and multiple frontiers of French Guiana." The Extractive Industries and Society **8**(1): 8-22. doi: 10.1016/j.exis.2020.11.005.

Jiménez-Moreno, M., J. P. G. Barre, V. Perrot, S. Bérail, R. C. Rodríguez Martín-Doimeadios and D. Amouroux (2016). "Sources and fate of mercury pollution in Almadén mining district (Spain): Evidences from mercury isotopic compositions in sediments and lichens." Chemosphere **147**: 430-438. doi: 10.1016/j.chemosphere.2015.12.094.

Jiskra, M., J. G. Wiederhold, B. Bourdon and R. Kretzschmar (2012). "Solution speciation controls mercury isotope fractionation of Hg(II) sorption to goethite." Environ Sci Technol **46**(12): 6654-6662. doi: 10.1021/es3008112.

Jiskra, M., J. G. Wiederhold, U. Skyllberg, R. M. Kronberg, I. Hajdas and R. Kretzschmar (2015). "Mercury deposition and re-emission pathways in boreal forest soils investigated with Hg isotope signatures." Environ Sci Technol **49**(12): 7188-7196. doi: 10.1021/acs.est.5b00742.

Joensuu, M., C. A. Pilditch, R. Harris, S. Hietanen, H. Pettersson and A. Norkko (2017). "Sediment properties, biota, and local habitat structure explain variation in the erodibility of coastal sediments." Limnology and Oceanography **63**(1): 173-186. doi: 10.1002/lno.10622.

Jonsson, S., N. M. Mazrui and R. P. Mason (2016). "Dimethylmercury Formation Mediated by Inorganic and Organic Reduced Sulfur Surfaces." Sci Rep **6**: 27958. doi: 10.1038/srep27958.

JORF (2022). Ordonnance n° 2022-537 du 13 avril 2022 relative à l'adaptation outre-mer du code minier, Ministère de la Transition Ecologique.

Kalamandeen, M., E. Gloor, I. Johnson, S. Agard, M. Katow, A. Vanbrooke, D. Ashley, S. A. Batterman, G. Ziv, K. Holder-Collins, O. L. Phillips, E. S. Brondizio, I. Vieira, D. Galbraith and A. Magrach (2020). "Limited biomass recovery from gold mining in Amazonian forests." Journal of Applied Ecology **57**(9): 1730-1740. doi: 10.1111/1365-2664.13669.

Kapaj, S., H. Peterson, K. Liber and P. Bhattacharya (2006). "Human health effects from chronic arsenic poisoning--a review." J Environ Sci Health A Tox Hazard Subst Environ Eng **41**(10): 2399-2428. doi: 10.1080/10934520600873571.

Katuwal, S., J. Vermang, W. M. Cornelis, D. Gabriels, P. Moldrup and L. W. de Jonge (2013). "Effect of Root Density on Erosion and Erodibility of a Loamy Soil Under Simulated Rain." Soil Science **178**(1): 29-36. doi: 10.1097/SS.0b013e318285b052.

Keane, S., L. Bernaudat, K. J. Davis, M. Stylo, N. Mutemeri, P. Singo, P. Twala, I. Mutemeri, A. Nakafeero and I. D. Etui (2023). "Mercury and artisanal and small-scale gold mining: Review of global use estimates and considerations for promoting mercury-free alternatives." Ambio **52**(5): 833-852. doi: 10.1007/s13280-023-01843-2.

Kleindienst, A., I. Zivkovic, E. Tessier, A. Koenig, L. E. Heimburger-Boavida, M. Horvat and D. Amouroux (2023). "Assessing comparability and uncertainty of analytical methods for

methylated mercury species in seawater." Anal Chim Acta **1278**: 341735. doi: 10.1016/j.aca.2023.341735.

Körtzinger, A., P. D. Quay and R. E. Sonnerup (2003). "Relationship between anthropogenic CO2and the13C Suess effect in the North Atlantic Ocean." Global Biogeochemical Cycles **17**(1). doi: 10.1029/2001gb001427.

Krishna, M. P. and M. Mohan (2017). "Litter decomposition in forest ecosystems: a review." Energy, Ecology and Environment **2**(4): 236-249. doi: 10.1007/s40974-017-0064-9.

Kritee, K., J. D. Blum, M. W. Johnson, B. A. Bergquist and T. Barkay (2007). "Mercury stable isotope fractionation during reduction of Hg(II) to Hg(0) by mercury resistant microorganisms." Environ Sci Technol **41**(6): 1889-1895. doi: 10.1021/es062019t.

Kronberg, R. M., M. Jiskra, J. G. Wiederhold, E. Bjorn and U. Skyllberg (2016). "Methyl Mercury Formation in Hillslope Soils of Boreal Forests: The Role of Forest Harvest and Anaerobic Microbes." Environ Sci Technol **50**(17): 9177-9186. doi: 10.1021/acs.est.6b00762.

Kroonenberg, S., P. R. D. Masson, L. Kriegman, E. W. F. de Roever and T. E. Wong (2019). "Geology and mineral deposits of the Guiana Shield." Mededeling Geologisch Mijnbouwkundige Dienst Suriname 29: 111 - 115.

Kroonenberg, S., T. Wong, G. Bijnaar, R. Finkie, K. Goenopawiro, S. Asneel, M. Lin-Tsung, R. Nanan, K. Ramdas and P. Sitaram (2022). "Mercury background values in soils and saprolites in the gold-rich greenstone belt of Suriname, Guiana Shield: The role of parent rock and residual enrichment." Sci Total Environ **848**: 157631. doi: 10.1016/j.scitotenv.2022.157631.

Kroonenberg, S. B., E. W. F. de Roever, L. M. Fraga, N. J. Reis, T. Faraco, J. M. Lafon, U. Cordani and T. E. Wong (2016). "Paleoproterozoic evolution of the Guiana Shield in Suriname: A revised model." Netherlands Journal of Geosciences - Geologie en Mijnbouw **95**(4): 491-522. doi: 10.1017/njg.2016.10.

Kylander, M. E., A. Martínez-Cortizas, J. K. Sjöström, J. Gåling, R. Gyllencreutz, R. Bindler, H. Alexanderson, F. Schenk, B. T. I. Reinardy, B. M. P. Chandler and K. Gallagher (2023). "Storm chasing: Tracking Holocene storminess in southern Sweden using mineral proxies from inland and coastal peat bogs." Quaternary Science Reviews **299**: 107854. doi: 10.1016/j.quascirev.2022.107854.

Labrière, N., B. Locatelli, Y. Laumonier, V. Freycon and M. Bernoux (2015). "Soil erosion in the humid tropics: A systematic quantitative review." Agriculture, Ecosystems & Environment **203**: 127-139. doi: 10.1016/j.agee.2015.01.027.

Lacerda, L. D., W. R. Bastos and M. D. Almeida (2012). "The impacts of land use changes in the mercury flux in the Madeira River, Western Amazon." An Acad Bras Cienc **84**(1): 69-78. doi: 10.1590/s0001-37652012000100007.

Laffont, L., J. Menges, S. Goix, S. Gents, R. Maury-Brachet, J. E. Sonke, A. Legeay, P. Gonzalez, R. Rinaldo and L. Maurice (2021). "Hg concentrations and stable isotope variations in tropical fish species of a gold-mining-impacted watershed in French Guiana." Environmental Science and Pollution Research. doi: 10.1007/s11356-021-14858-7.

Laffont, L., J. E. Sonke, L. Maurice, S. L. Monrroy, J. Chincheros, D. Amouroux and P. Behra (2011). "Hg Speciation and Stable Isotope Signatures in Human Hair As a Tracer for Dietary and Occupational Exposure to Mercury." Environmental Science \& Technology **45**(23): 9910-9916. doi: 10.1021/es202353m.

Lal, R. (1990). "Soil Erosion in the tropics: principles and management." McGraw-Hill, New York. doi: 978-0-07-036087-7.

Lamborg, C. H., C. R. Hammerschmidt and K. L. Bowman (2016). "An examination of the role of particles in oceanic mercury cycling." Philos Trans A Math Phys Eng Sci **374**(2081). doi: 10.1098/rsta.2015.0297.

Lange, D. F., S. A. Schröter, F. M. da Luz, E. Pires, Y. R. Santos, J. S. da Silva, S. Hildmann, T. Hoffmann, S. J. F. Ferreira, T. Schäfer, C. A. Quesada, C. Simon and G. Gleixner (2024). "Cycling of dissolved organic nutrients and indications for nutrient limitations in contrasting Amazon

rainforest ecosystems." Biogeochemistry **167**(12): 1567-1588. doi: 10.1007/s10533-024-01187-3.

Lanphear, B. P., R. Hornung, J. Khoury, K. Yolton, P. Baghurst, D. C. Bellinger, R. L. Canfield, K. N. Dietrich, R. Bornschein, T. Greene, S. J. Rothenberg, H. L. Needleman, L. Schnaas, G. Wasserman, J. Graziano and R. Roberts (2005). "Low-level environmental lead exposure and children's intellectual function: an international pooled analysis." Environ Health Perspect **113**(7): 894-899. doi: 10.1289/ehp.7688.

Lanuru, M., R. Riethmüller, C. van Bernem and K. Heymann (2007). "The effect of bedforms (crest and trough systems) on sediment erodibility on a back-barrier tidal flat of the East Frisian Wadden Sea, Germany." Estuarine, Coastal and Shelf Science **72**(4): 603-614. doi: 10.1016/j.ecss.2006.11.009.

Laperche, V., J. Hellal, R. Maury-Brachet, B. Joseph, P. Laporte, D. Breeze and F. Blanchard (2014). "Regional distribution of mercury in sediments of the main rivers of French Guiana (Amazonian basin)." SpringerPlus **3**(1): 322. doi: 10.1186/2193-1801-3-322.

Laraque, A., C. Bernal, L. Bourrel, J. Darrozes, F. Christophoul, E. Armijos, P. Fraizy, R. Pombosa and J. L. Guyot (2009). "Sediment budget of the Napo River, Amazon basin, Ecuador and Peru." Hydrological Processes **23**(25): 3509-3524. doi: 10.1002/hyp.7463.

Le Tourneau, F.-M. (2020). "Chercheurs d'or - L'orpaillage clandestin en Guyane française." CNRS Editions.

Le Tourneau, F.-M. (2021). "Brazilian illegal gold miners resilience in French Guiana: The garimpo as an economic and social system." European Review of Latin American and Caribbean Studies(112): 1-27. doi: 10.32992/erlacs.10767.

Legout, C., S. Leguédois, Y. Le Bissonnais and O. Malam Issa (2005). "Splash distance and size distributions for various soils." Geoderma **124**(3-4): 279-292. doi: 10.1016/j.geoderma.2004.05.006.

Lemaire, J., R. Mangione, S. Caut and P. Bustamante (2024). "Mercury biomagnification in the food web of Agami Pond, Kaw-Roura Nature Reserve, French Guiana." Heliyon **10**(7): e28859. doi: 10.1016/j.heliyon.2024.e28859.

Lezak, S., C. Wilson, A. Ansar and M. Bazilian (2022). "The case against gold mining." Environmental Research Letters **18**(1): 011001. doi: 10.1088/1748-9326/ac9f26.

Lima, L. S., M. T. Coe, B. S. Soares Filho, S. V. Cuadra, L. C. P. Dias, M. H. Costa, L. S. Lima and H. O. Rodrigues (2013). "Feedbacks between deforestation, climate, and hydrology in the Southwestern Amazon: implications for the provision of ecosystem services." Landscape Ecology **29**(2): 261-274. doi: 10.1007/s10980-013-9962-1.

Linarès, S., M. André, J. Commins, P. Joubert and V. Gond (2024). The observatory of mining activities in French Guiana : 20 years of remote sensing applied to mining deforestation. XXI SIMPÓSIO INTERNACIONAL SELPER. Belem, Brazil.

Lino, A. S., D. Kasper, Y. S. Guida, J. R. Thomaz and O. Malm (2019). "Total and methyl mercury distribution in water, sediment, plankton and fish along the Tapajos River basin in the Brazilian Amazon." Chemosphere **235**: 690-700. doi: 10.1016/j.chemosphere.2019.06.212.

Lobo, F., M. Costa, E. Novo and K. Telmer (2016). "Distribution of Artisanal and Small-Scale Gold Mining in the Tapajós River Basin (Brazilian Amazon) over the Past 40 Years and Relationship with Water Siltation." Remote Sensing **8**(7): 579. doi: 10.3390/rs8070579.

Lobo, F., M. Costa, E. Novo and K. Telmer (2017). "Effects of Small-Scale Gold Mining Tailings on the Underwater Light Field in the Tapajós River Basin, Brazilian Amazon." Remote Sensing **9**(8): 861. doi: 10.3390/rs9080861.

Madegwa, Y. M. and Y. Uchida (2021). "Land use and season drive changes in soil microbial communities and related functions in agricultural soils." Environmental DNA **3**(6): 1214-1228. doi: 10.1002/edn3.244.

Magarelli, G. and A. Fostier (2005). "Influence of deforestation on the mercury air/soil exchange in the Negro River Basin, Amazon." Atmospheric Environment **39**(39): 7518-7528. doi: 10.1016/j.atmosenv.2005.07.067.

Maia, P. D., L. Maurice, E. Tessier, D. Amouroux, D. Cossa, M. Perez, P. Moreira-Turcq and I. Rheault (2009). "Mercury distribution and exchanges between the Amazon River and connected floodplain lakes." Sci Total Environ **407**(23): 6073-6084. doi: 10.1016/j.scitotenv.2009.08.015.

Marchant, B. P., N. P. A. Saby and D. Arrouays (2017). "A survey of topsoil arsenic and mercury concentrations across France." Chemosphere **181**: 635-644. doi: 10.1016/j.chemosphere.2017.04.106.

Marquis, F. (2015). "Activite miniere et aurifere en Guyane et reglementation." DEAL Guyane, Unité Mines et Carrières.

Martínez-Ruiz, C., A. I. Milder, D. López-Marcos, P. Zaldívar and B. Fernández-Santos (2021). "Effect of the Forest-Mine Boundary Form on Woody Colonization and Forest Expansion in Degraded Ecosystems." Forests **12**(6): 773. doi: 10.3390/f12060773.

Martínez Cortizas, A., L. López-Merino, N. Silva-Sánchez, J. K. Sjöström and M. E. Kylander (2021). "Investigating the Mineral Composition of Peat by Combining FTIR-ATR and Multivariate Analysis." Minerals **11**(10): 1084. doi: 10.3390/min11101084.

Martínez Cortizas, A., M. Traoré, O. López-Costas, J. K. Sjöström and M. E. Kylander (2024). "Beyond the Obvious: Exploring Peat Vibrational Spectroscopy (FTIR-ATR) Data Using Principal Components Analysis on Transposed Data Matrix (tPCA), Store Mosse Bog (Sweden)." 217-247. doi: 10.1007/978-3-031-50503-4_11.

Martinez, G., S. McCord, C. Driscoll, S. Todorova, S. Wu, J. Arajo, C. Vega and L. Fernandez (2018). "Mercury Contamination in Riverine Sediments and Fish Associated with Artisanal and Small-Scale Gold Mining in Madre de Dios, Peru." International Journal of Environmental Research and Public Health **15**(8): 1584. doi: 10.3390/ijerph15081584.

Martins, N. P., L. Fuchslueger, K. Fleischer, K. M. Andersen, R. L. Assis, F. B. Baccaro, P. B. Camargo, A. L. Cordeiro, A. Grandis, I. P. Hartley, F. Hofhansl, L. F. Lugli, D. M. Lapola, J. G. Menezes, R. J. Norby, A. Rammig, J. S. Rosa, K. J. Schaap, B. Takeshi, O. J. Valverde-Barrantes and C. A. Quesada (2021). "Fine roots stimulate nutrient release during early stages of leaf litter decomposition in a Central Amazon rainforest." Plant and Soil **469**(1-2): 287-303. doi: 10.1007/s11104-021-05148-9.

Matschullat, J., K. Birmann, R. P. Borba, V. Ciminelli, E. M. Deschamps, B. R. Figueiredo, T. Gabrio, S. Haßler, A. Hilscher, I. Junghänel, N. de Oliveira, K. Raßbach, H. Schmidt, M. Schwenk, M. J. de Oliveira Vilhena and U. Weidner (2007). "Long-term environmental impact of arsenic-dispersion in Minas Gerais, Brazil." **9**: 365-382. doi: 10.1016/s1875-1121(06)09014-6.

Maurice, L., F. Barraza, I. Blondet, A. C. M. Ho, J. Tablon, P. Brousse, M. Demar and E. Schreck (2021). "Childhood lead exposure of Amerindian communities in French Guiana: an isotopic approach to tracing sources." Environ Geochem Health **43**(11): 4741-4757. doi: 10.1007/s10653-021-00944-9.

Maury-Brachet, R., A. Boudou, L. Charlet, D. Cossa and M. Grimaldi (2008). "Programme mercure en Guyane. (Phase II)."

Maury-Brachet, R., G. Durrieu, D. Yannick and A. Boudou (2006). "Mercury distribution in fish organs and food regimes: Significant relationships from twelve species collected in French Guiana (Amazonian basin)." Sci Total Environ **368**(1): 262-270. doi: 10.1016/j.scitotenv.2005.09.077.

Maury-Brachet, R., S. Gentes, E. P. Dassié, A. Feurtet-Mazel, R. Vigouroux, V. Laperche, P. Gonzalez, V. Hanquiez, N. Mesmer-Dudons, G. Durrieu and A. Legeay (2019). "Mercury contamination levels in the bioindicator piscivorous fish Hoplias aïmara in French Guiana rivers: mapping for risk assessment." Environmental Science and Pollution Research **27**(4): 3624-3636. doi: 10.1007/s11356-018-3983-x

McLagan, D. S., M. E. E. Mazur, C. P. J. Mitchell and F. Wania (2016). "Passive air sampling of gaseous elemental mercury: a critical review." Atmospheric Chemistry and Physics **16**(5): 3061-3076. doi: 10.5194/acp-16-3061-2016.

McLagan, D. S., C. P. J. Mitchell, H. Huang, B. Abdul Hussain, Y. D. Lei and F. Wania (2017). "The effects of meteorological parameters and diffusive barrier reuse on the sampling rate of

a passive air sampler for gaseous mercury." Atmospheric Measurement Techniques **10**(10): 3651-3660. doi: 10.5194/amt-10-3651-2017.

McLagan, D. S., C. P. J. Mitchell, H. Huang, Y. D. Lei, A. S. Cole, A. Steffen, H. Hung and F. Wania (2016). "A High-Precision Passive Air Sampler for Gaseous Mercury." Environmental Science & Technology Letters **3**(1): 24-29. doi: 10.1021/acs.estlett.5b00319.

Meli, P., K. D. Holl, J. M. Rey Benayas, H. P. Jones, P. C. Jones, D. Montoya and D. Moreno Mateos (2017). "A global review of past land use, climate, and active vs. passive restoration effects on forest recovery." PLoS One **12**(2): e0171368. doi: 10.1371/journal.pone.0171368.

Melun, G., M. Le Bihan and V. de Billy (2021). Guide de préconisations techniques pour l'exploitation alluvionnaire et la réhabilitation hydromorphologique des criques guyanaise. Guides et protocoles. OFB.

meteo.data.gouv.fr ([last accessed on 3rd February 2025]). "https://meteo.data.gouv.fr/form."

Michel, C., N. Baran, L. Andre, M. Charron and C. Joulian (2021). "Side Effects of Pesticides and Metabolites in Groundwater: Impact on Denitrification." Front Microbiol **12**: 662727. doi: 10.3389/fmicb.2021.662727.

Michelazzo, P. A. M., A. H. Fostier, G. Magarelli, J. C. Santos and J. A. de Carvalho (2010). "Mercury emissions from forest burning in southern Amazon." Geophysical Research Letters **37**(9). doi: 10.1029/2009gl042220.

Minamata_Convention_on_Mercury (2023). "Minamata Convention in 2022: Progress report on activities." UNEP.

Moe, B., H. Peng, X. Lu, B. Chen, L. W. L. Chen, S. Gabos, X. F. Li and X. C. Le (2016). "Comparative cytotoxicity of fourteen trivalent and pentavalent arsenic species determined using real-time cell sensing." J Environ Sci (China) **49**: 113-124. doi: 10.1016/j.jes.2016.10.004.

Mol, J. H. and P. E. Ouboter (2004). "Downstream Effects of Erosion from Small-Scale Gold Mining on the Instream Habitat and Fish Community of a Small Neotropical Rainforest Stream." Conservation Biology **18**(1): 201-214. doi: 10.1111/j.1523-1739.2004.00080.x.

Monfort, M. and L. Ruf (2005). "Régime hydrologique des fleuves guyanais : étude fréquentielle des débits." Direction régionale de l'environnement de Guyane, Cayenne.

Monperrus, M., P. Rodriguez Gonzalez, D. Amouroux, J. I. Garcia Alonso and O. F. Donard (2008). "Evaluating the potential and limitations of double-spiking species-specific isotope dilution analysis for the accurate quantification of mercury species in different environmental matrices." Anal Bioanal Chem **390**(2): 655-666. doi: 10.1007/s00216-007-1598-z.

Monperrus, M., E. Tessier, S. Veschambre, D. Amouroux and O. Donard (2005). "Simultaneous speciation of mercury and butyltin compounds in natural waters and snow by propylation and species-specific isotope dilution mass spectrometry analysis." Anal Bioanal Chem **381**(4): 854-862. doi: 10.1007/s00216-004-2973-7.

Montanher, O. C., E. M. L. d. M. Novo and E. E. d. Souza Filho (2018). "Temporal trend of the suspended sediment transport of the Amazon River (1984–2016)." Hydrological Sciences Journal **63**(13-14): 1901-1912. doi: 10.1080/02626667.2018.1546387.

Moreira-Turcq, P., P. Seyler, J. L. Guyot and H. Etcheber (2003). "Exportation of organic carbon from the Amazon River and its main tributaries." Hydrological Processes **17**(7): 1329-1344. doi: 10.1002/hyp.1287.

Moreno-Brush, M., D. S. McLagan and H. Biester (2020). "Fate of mercury from artisanal and small-scale gold mining in tropical rivers: Hydrological and biogeochemical controls. A critical review." Critical Reviews in Environmental Science and Technology **50**(5): 437-475. doi: 10.1080/10643389.2019.1629793.

Moreno-Brush, M., J. Rydberg, N. Gamboa, I. Storch and H. Biester (2016). "Is mercury from small-scale gold mining prevalent in the southeastern Peruvian Amazon?" Environmental Pollution **218**: 150-159. doi: 10.1016/j.envpol.2016.08.038.

Mortillaro, J. M., G. Abril, P. Moreira-Turcq, R. L. Sobrinho, M. Perez and T. Meziane (2011). "Fatty acid and stable isotope (δ13C, δ15N) signatures of particulate organic matter in the lower Amazon River: Seasonal contrasts and connectivity between floodplain lakes and the

mainstem." Organic Geochemistry **42**(10): 1159-1168. doi: 10.1016/j.orggeochem.2011.08.011.

Mosnier, E., F. Niemetzky, J. Stroot, V. Pommier de Santi, P. Brousse, B. Guarmit, D. Blanchet, M. Ville, P. Abboud, F. Djossou and M. Nacher (2017). "A Large Outbreak of Thiamine Deficiency Among Illegal Gold Miners in French Guiana." Am J Trop Med Hyg **96**(5): 1248-1252. doi: 10.4269/ajtmh.15-0906.

Moulatlet, G. M., N. Yacelga, A. Rico, A. Mora, R. A. Hauser-Davis, M. Cabrera and M. V. Capparelli (2023). "A systematic review on metal contamination due to mining activities in the Amazon basin and associated environmental hazards." Chemosphere **339**: 139700. doi: 10.1016/j.chemosphere.2023.139700.

Mügler, C., O. Ribolzi, J.-L. Janeau, E. Rochelle-Newall, K. Latsachack, C. Thammahacksa, M. Viguier, E. Jardé, T. Henri-Des-Tureaux, O. Sengtaheuanghoung and C. Valentin (2019). "Experimental and modelling evidence of short-term effect of raindrop impact on hydraulic conductivity and overland flow intensity." Journal of Hydrology **570**: 401-410. doi: 10.1016/j.jhydrol.2018.12.046.

Muresan, B., D. Cossa, M. Coquery and S. Richard (2008). "Mercury sources and transformations in a man-perturbed tidal estuary: The Sinnamary Estuary, French Guiana." Geochimica et Cosmochimica Acta **72**(22): 5416-5430. doi: 10.1016/j.gca.2008.08.021.

Muresan, B., D. Cossa, S. Richard and B. Burban (2007). "Mercury speciation and exchanges at the air-water interface of a tropical artificial reservoir, French Guiana." Sci Total Environ **385**(1-3): 132-145. doi: 10.1016/j.scitotenv.2007.06.013.

Naccarato, A., A. Tassone, M. Martino, S. Moretti, A. Macagnano, E. Zampetti, P. Papa, J. Avossa, N. Pirrone, M. Nerentorp, J. Munthe, I. Wängberg, G. W. Stupple, C. P. J. Mitchell, A. R. Martin, A. Steffen, D. Babi, E. M. Prestbo, F. Sprovieri and F. Wania (2021). "A field intercomparison of three passive air samplers for gaseous mercury in ambient air." Atmospheric Measurement Techniques **14**(5): 3657-3672. doi: 10.5194/amt-14-3657-2021.

Nardoto, G. B., J. P. H. B. Ometto, J. R. Ehleringer, N. Higuchi, M. M. d. C. Bustamante and L. A. Martinelli (2008). "Understanding the Influences of Spatial Patterns on N Availability Within the Brazilian Amazon Forest." Ecosystems **11**(8): 1234-1246. doi: 10.1007/s10021-008-9189-1.

Neelin, J. D., M. Munnich, H. Su, J. E. Meyerson and C. E. Holloway (2006). "Tropical drying trends in global warming models and observations." Proc Natl Acad Sci U S A **103**(16): 6110-6115. doi: 10.1073/pnas.0601798103.

Neill, C., J. E. Chaves, T. Biggs, L. A. Deegan, H. Elsenbeer, R. O. Figueiredo, S. Germer, M. S. Johnson, J. Lehmann, D. Markewitz and M. C. Piccolo (2011). "Runoff sources and land cover change in the Amazon: an end-member mixing analysis from small watersheds." Biogeochemistry **105**(1-3): 7-18. doi: 10.1007/s10533-011-9597-8.

Nitschke, N., S. Guédron, E. Tessier, D. Tisserand, S. Campillo and D. Amouroux (2024). "Evaluation of the Hg Contamination from Gold Mining in French Guiana at the Watershed Scale Using Hg Isotopic Composition in River Sediments." ACS ES&T Water **4**(8): 3443-3452. doi: 10.1021/acsestwater.4c00270.

Nogueira, E. M., A. M. Yanai, F. O. Fonseca and P. M. Fearnside (2015). "Carbon stock loss from deforestation through 2013 in Brazilian Amazonia." Glob Chang Biol **21**(3): 1271-1292. doi: 10.1111/gcb.12798.

Obrist, D., J. L. Kirk, L. Zhang, E. M. Sunderland, M. Jiskra and N. E. Selin (2018). "A review of global environmental mercury processes in response to human and natural perturbations: Changes of emissions, climate, and land use." Ambio **47**(2): 116-140. doi: 10.1007/s13280-017-1004-9.

Oeurng, C., S. Sauvage, A. Coynel, E. Maneux, H. Etcheber and J. M. Sánchez-Pérez (2011). "Fluvial transport of suspended sediment and organic carbon during flood events in a large agricultural catchment in southwest France." Hydrological Processes **25**(15): 2365-2378. doi: 10.1002/hyp.7999.

Oliveira, M. F. and A. S. Maciel-Silva (2022). "Biological soil crusts and how they might colonize other worlds: insights from these Brazilian ecosystem engineers." J Exp Bot **73**(13): 4362-4379. doi: 10.1093/jxb/erac162.

Ono, F. B., L. R. Guilherme, E. S. Penido, G. S. Carvalho, B. Hale, R. Toujaguez and J. Bundschuh (2012). "Arsenic bioaccessibility in a gold mining area: a health risk assessment for children." Environ Geochem Health **34**(4): 457-465. doi: 10.1007/s10653-011-9444-9.

Ouboter, P. E., G. A. Landburg, J. H. Quik, J. H. Mol and F. van der Lugt (2012). "Mercury levels in pristine and gold mining impacted aquatic ecosystems of Suriname, South America." Ambio **41**(8): 873-882. doi: 10.1007/s13280-012-0299-9.

Pandey, S. K., K.-H. Kim and R. J. C. Brown (2011). "Measurement techniques for mercury species in ambient air." TrAC Trends in Analytical Chemistry **30**(6): 899-917. doi: 10.1016/j.trac.2011.01.017.

Parrotta, J. A. and O. H. Knowles (2001). "Restoring tropical forests on lands mined for bauxite: Examples from the Brazilian Amazon." Ecological Engineering **17**(2-3): 219-239. doi: 10.1016/s0925-8574(00)00141-5.

Pfeiffer, W. C., L. D. de Lacerda, O. Malm, C. M. Souza, E. G. da Silveira and W. R. Bastos (1989). "Mercury concentrations in inland waters of gold-mining areas in Rondonia, Brazil." Sci Total Environ **87-88**: 233-240. doi: 10.1016/0048-9697(89)90238-6.

Pignoux, R., P.-Y. Gourves, M. Sow and R. Maury-Brachet (2019). "Imprégnation mercurielle des femmes enceintes de Guyane (Haut Maroni) : étude et prévention." Toxicologie Analytique et Clinique **31**(1): 37-48. doi: 10.1016/j.toxac.2018.12.002.

Piton, G., N. Legay, C. Arnoldi, S. Lavorel, J.-C. Clément, A. Foulquier and E. Lamb (2020). "Using proxies of microbial community-weighted means traits to explain the cascading effect of management intensity, soil and plant traits on ecosystem resilience in mountain grasslands." Journal of Ecology **108**(3): 876-893. doi: 10.1111/1365-2745.13327.

planetGOLD (2023). "planetGOLD 2022-2023 Annual Progress Report."

Pochon, A., A.-M. Desaulty, L. Bailly and P. Lach (2021). "Challenging the traceability of natural gold by combining geochemical methods: French Guiana example." Applied Geochemistry **129**: 104952. doi: 10.1016/j.apgeochem.2021.104952.

Qian, Y., D. A. Ralescu and B. Zhang (2019). "The analysis of factors affecting global gold price." Resources Policy **64**: 101478. doi: 10.1016/j.resourpol.2019.101478.

Quast, C., E. Pruesse, P. Yilmaz, J. Gerken, T. Schweer, P. Yarza, J. Peplies and F. O. Glockner (2013). "The SILVA ribosomal RNA gene database project: improved data processing and web-based tools." Nucleic Acids Res **41**(Database issue): D590-596. doi: 10.1093/nar/gks1219.

Quesada, C. A., J. Lloyd, M. Schwarz, S. Patiño, T. R. Baker, C. Czimczik, N. M. Fyllas, L. Martinelli, G. B. Nardoto, J. Schmerler, A. J. B. Santos, M. G. Hodnett, R. Herrera, F. J. Luizão, A. Arneth, G. Lloyd, N. Dezzeo, I. Hilke, I. Kuhlmann, M. Raessler, W. A. Brand, H. Geilmann, J. O. Moraes Filho, F. P. Carvalho, R. N. Araujo Filho, J. E. Chaves, O. F. Cruz Junior, T. P. Pimentel and R. Paiva (2010). "Variations in chemical and physical properties of Amazon forest soils in relation to their genesis." Biogeosciences **7**(5): 1515-1541. doi: 10.5194/bg-7-1515-2010.

Rahm, M., T. Smartt, J. Totaram, B. Sukhu, D. Thornhill-Gillis, N. Amin, R. Thomas, C. Sookdeo, C. Paloeng, C. Kasanpawiro, V. Moe Soe Let, I. Hoepel, C. Pichot, C. Bedeau, P. Farias, R. Carvalho, J. Weber and C. Lardeux (2020). "Mapping land use land cover change in the Guiana shield from 2000 to 2015." ECOSEO project: 69.

Ramraj, R. (2002). "Guyana's Border Disputes with Venezuela and Suriname." The Geographical Bulletin **44**(1).

Ravichandran, M. (2004). "Interactions between mercury and dissolved organic matter--a review." Chemosphere **55**(3): 319-331. doi: 10.1016/j.chemosphere.2003.11.011.

Reid, J. L., M. E. Fagan and R. A. Zahawi (2018). "Positive site selection bias in meta-analyses comparing natural regeneration to active forest restoration." Sci Adv **4**(5): eaas9143. doi: 10.1126/sciadv.aas9143.

Reinfelder, J. R. and S. E. Janssen (2019). "Tracking legacy mercury in the Hackensack River estuary using mercury stable isotopes." J Hazard Mater **375**: 121-129. doi: 10.1016/j.jhazmat.2019.04.074.

Ren, C., J. Chen, X. Lu, R. Doughty, F. Zhao, Z. Zhong, X. Han, G. Yang, Y. Feng and G. Ren (2018). "Responses of soil total microbial biomass and community compositions to rainfall reductions." Soil Biology and Biochemistry **116**: 4-10. doi: 10.1016/j.soilbio.2017.09.028.

Richardson, A. E. and R. J. Simpson (2011). "Soil microorganisms mediating phosphorus availability update on microbial phosphorus." Plant Physiol **156**(3): 989-996. doi: 10.1104/pp.111.175448.

Richey, J. E., J. I. Hedges, A. H. Devol, P. D. Quay, R. Victoria, L. Martinelli and B. R. Forsberg (1990). "Biogeochemistry of carbon in the Amazon River." Limnology and Oceanography **35**(2): 352-371. doi: 10.4319/lo.1990.35.2.0352.

Richey, J. E., J. M. Melack, A. K. Aufdenkampe, V. M. Ballester and L. L. Hess (2002). "Outgassing from Amazonian rivers and wetlands as a large tropical source of atmospheric CO2." Nature **416**(6881): 617-620. doi: 10.1038/416617a.

Richter, L., D. Amouroux, E. Tessier and A. H. Fostier (2023). "Impact of forest fire on the mercury stable isotope composition in litter and soil in the Amazon." Chemosphere **339**: 139779. doi: 10.1016/j.chemosphere.2023.139779.

Rimbaud, D., M. Restrepo, A. Louison, R. Boukhari, V. Ardillon, G. Carles, V. Lambert and A. Jolivet (2017). "Blood lead levels and risk factors for lead exposure among pregnant women in western French Guiana: the role of manioc consumption." J Toxicol Environ Health A **80**(6): 382-393. doi: 10.1080/15287394.2017.1331490.

Rocha, A. and K. A. Trujillo (2019). "Neurotoxicity of low-level lead exposure: History, mechanisms of action, and behavioral effects in humans and preclinical models." Neurotoxicology **73**: 58-80. doi: 10.1016/j.neuro.2019.02.021.

Rocha, N. and C. Mahler (2023). "Analysis of sorption/desorption of cadmium and lead in the legal amazon soils." Soils and Rocks **47**(1): e2024014022. doi: 10.28927/sr.2024.014022.

Rodriguez Martin-Doimeadios, R. C., E. Krupp, D. Amouroux and O. F. Donard (2002). "Application of isotopically labeled methylmercury for isotope dilution analysis of biological samples using gas chromatography/ICPMS." Anal Chem **74**(11): 2505-2512. doi: 10.1021/ac011157s.

Roos-Barraclough, F., N. Givelet, A. Martinez-Cortizas, M. E. Goodsite, H. Biester and W. Shotyk (2002). "An analytical protocol for the determination of total mercury concentrations in solid peat samples." Sci Total Environ **292**(1-2): 129-139. doi: 10.1016/s0048-9697(02)00035-9.

Rorive, S., R. Boukhari and D. Harrois (2015). "Saturnisme: Un premier cas en Guyane découvert sur le frottis sanguin." Revue Francophone des Laboratoires **2015**(473): 79-80. doi: 10.1016/s1773-035x(15)30164-7.

Roulet, M. and C. Grimaldi (2001). Le mercure dans les sols d'Amazonie. Le mercure en Amazonie, Rôle de l'homme et de l'environnement, risques sanitaires. I. é.-E. Collégiale. Paris, France.

Roulet, M., J. R. D. Guimarães and M. Lucotte (2001). "Methylmercury Production and Accumulation in Sediments and Soils of an Amazonian Floodplain – Effect of Seasonal Inundation." Water, Air, and Soil Pollution **128**(1/2): 41-60. doi: 10.1023/a:1010379103335.

Roulet, M. and M. Lucotte (1995). "Geochemistry of mercury in pristine and flooded ferralitic soils of a tropical rain forest in French Guiana, South America." Water, Air, & Soil Pollution **80**(1-4): 1079-1088. doi: 10.1007/bf01189768.

Roulet, M., M. Lucotte, A. Saint-Aubin, S. Tran, I. Rheault, N. Farella, E. De Jesus Da silva, J. Dezencourt, C. J. Sousa Passos, G. Santos Soares, J. R. Guimaraes, D. Mergler and M. Amorim (1998). "The geochemistry of mercury in central Amazonian soils developed on the Alter-do-Chao formation of the lower Tapajos River Valley, Para state, Brazil." Sci Total Environ **223**(1): 1-24. doi: 10.1016/s0048-9697(98)00265-4.

Rousseau, T. C. C., M. Roddaz, J.-S. Moquet, H. Handt Delgado, G. Calves and G. Bayon (2019). "Controls on the geochemistry of suspended sediments from large tropical South American

rivers (Amazon, Orinoco and Maroni)." Chemical Geology **522**: 38-54. doi: 10.1016/j.chemgeo.2019.05.027.

Salman, T. and M. de Theije (2017). "Analysing conflicts around small-scale gold mining in the Amazon: The contribution of a multi-temporal model." The Extractive Industries and Society **4**(3): 586-594. doi: 10.1016/j.exis.2017.03.007.

Salomão, G., R. Dall'Agnol, P. Sahoo, J. Ferreira-Júnior, M. Silva, P. Souza-Filho, J. F. Berrêdo, W. Nascimento-Junior and M. Costa (2018). "Geochemical distribution and threshold values determination of heavy metals in stream water in the sub-basins of Vermelho and Sororó rivers, Itacaiúnas River watershed, Eastern Amazon, Brazil." Geochimica Brasiliensis **32**(2): 180-198. doi: 10.21715/gb2358-2812.2018322180.

Salomon, L., E. Brunstein and M. Laloua (2016). Etude des conditions de reprise de la végétation sur les sites miniers alluvionnaires. DEAL_Guyane.

Saplairoles, M., P. Lecomte and B. Joseph (2010). "Contrôle de surveillance de la qualité physico-chimique des eaux continentales de surface de Guyane - Campagne 2010. Rapport final." BRGM/RP-59830-FR.

Scarpelli, W. (2005). "Arsenic in the rivers of the Amazon Basin." TERRÆ.

Scherrer, S., F. Naef, A. O. Faeh and I. Cordery (2007). "Formation of runoff at the hillslope scale during intense precipitation." Hydrology and Earth System Sciences **11**(2): 907-922. doi: 10.5194/hess-11-907-2007.

Schimann, H., C. Petit-Jean, S. Guitet, T. Reis, A. M. Domenach and J.-C. Roggy (2012). "Microbial bioindicators of soil functioning after disturbance: The case of gold mining in tropical rainforests of French Guiana." Ecological Indicators **20**: 34-41. doi: 10.1016/j.ecolind.2012.01.021.

Schudel, G., R. Adler Miserendino, M. M. Veiga, P. C. Velasquez-López, P. S. J. Lees, S. Winland-Gaetz, J. R. D. Guimarães and B. A. Bergquist (2018). "An investigation of mercury sources in the Puyango-Tumbes River: Using stable Hg isotopes to characterize transboundary Hg pollution." Chemosphere **202**: 777-787. doi: 10.1016/j.chemosphere.2018.03.081.

Schudel, G., R. Kaplan, R. Adler Miserendino, M. M. Veiga, P. C. Velasquez-López, J. R. D. Guimarães and B. A. Bergquist (2019). "Mercury isotopic signatures of tailings from artisanal and small-scale gold mining (ASGM) in southwestern Ecuador." Science of The Total Environment **686**: 301-310. doi: 10.1016/j.scitotenv.2019.06.004.

Schünemann, M. and H. Kühl (1991). A device for erosion measurements an naturally formed, muddy sediments: the EROMES system, GKSS-Forschungszentrum.

Seitz, S., M. Nebel, P. Goebes, K. Käppeler, K. Schmidt, X. Shi, Z. Song, C. L. Webber, B. Weber and T. Scholten (2017). "Bryophyte-dominated biological soil crusts mitigate soil erosion in an early successional Chinese subtropical forest." Biogeosciences **14**(24): 5775-5788. doi: 10.5194/bg-14-5775-2017.

Selin, N. E. (2009). "Global Biogeochemical Cycling of Mercury: A Review." Annual Review of Environment and Resources **34**(1): 43-63. doi: 10.1146/annurev.environ.051308.084314.

Sharif, A., M. Monperrus, E. Tessier, S. Bouchet, H. Pinaly, P. Rodriguez-Gonzalez, P. Maron and D. Amouroux (2014). "Fate of mercury species in the coastal plume of the Adour River estuary (Bay of Biscay, SW France)." Sci Total Environ **496**: 701-713. doi: 10.1016/j.scitotenv.2014.06.116.

Sherman, L. S. and J. D. Blum (2013). "Mercury stable isotopes in sediments and largemouth bass from Florida lakes, USA." Sci Total Environ **448**: 163-175. doi: 10.1016/j.scitotenv.2012.09.038.

Sherman, L. S., J. D. Blum, K. P. Johnson, G. J. Keeler, J. A. Barres and T. A. Douglas (2010). "Mass-independent fractionation of mercury isotopes in Arctic snow driven by sunlight." Nature Geoscience **3**(3): 173-177. doi: 10.1038/ngeo758.

Silva-Olaya, A. M., D. A. Mora-Motta, M. R. Cherubin, D. Grados, A. Somenahally and F. A. Ortiz-Morea (2021). "Soil enzyme responses to land use change in the tropical rainforest of the Colombian Amazon region." PLoS One **16**(8): e0255669. doi: 10.1371/journal.pone.0255669.

So, H. B., I. R. da Silva, L. C. Gomes and T. S. de Oliveira (2022). "Subsoil and Surface Soil Constraints of Mined Land and Tailings." 161-177. doi: 10.1007/978-3-031-00317-2_7.

Sondag, F., J. L. Guyot, J. S. Moquet, A. Laraque, G. Adele, G. Cochonneau, J. C. Doudou, C. Lagane and P. Vauchel (2010). "Suspended sediment and dissolved load budgets of two Amazonian rivers from the Guiana Shield: Maroni River at Langa Tabiki and Oyapock River at Saut Maripa (French Guiana)." Hydrological Processes **24**(11): 1433-1445. doi: 10.1002/hyp.7603.

Sonter, L. J., D. Herrera, D. J. Barrett, G. L. Galford, C. J. Moran and B. S. Soares-Filho (2017). "Mining drives extensive deforestation in the Brazilian Amazon." Nat Commun **8**(1): 1013. doi: 10.1038/s41467-017-00557-w.

Sprovieri, F., N. Pirrone, M. Bencardino, F. D'Amore, F. Carbone, S. Cinnirella, V. Mannarino, M. Landis, R. Ebinghaus, A. Weigelt, E. G. Brunke, C. Labuschagne, L. Martin, J. Munthe, I. Wangberg, P. Artaxo, F. Morais, H. de Melo Jorge Barbosa, J. Brito, W. Cairns, C. Barbante, M. Del Carmen Dieguez, P. E. Garcia, A. Dommergue, H. Angot, O. Magand, H. Skov, M. Horvat, J. Kotnik, K. A. Read, L. M. Neves, B. M. Gawlik, F. Sena, N. Mashyanov, V. Obolkin, D. Wip, X. B. Feng, H. Zhang, X. Fu, R. Ramachandran, D. Cossa, J. Knoery, N. Marusczak, M. Nerentorp and C. Norstrom (2016). "Atmospheric mercury concentrations observed at ground-based monitoring sites globally distributed in the framework of the GMOS network." Atmos Chem Phys **16**(18): 11915-11935. doi: 10.5194/acp-16-11915-2016.

Stach, N., A. Salvado, M. Petit, J. F. Faure, L. Durieux, C. Corbane, P. Joubert, D. Lasselin and M. Deshayes (2009). "Land use monitoring by remote sensing in tropical forest areas in support of the Kyoto Protocol: the case of French Guiana." International Journal of Remote Sensing **30**(19): 5133-5149. doi: 10.1080/01431160903022969.

Stoichev, T., D. Amouroux, R. C. R. Martin-Doimeadios, M. Monperrus, O. F. X. Donard and D. L. Tsalev (2006). "Speciation Analysis of Mercury in Aquatic Environment." Applied Spectroscopy Reviews **41**(6): 591-619. doi: 10.1080/05704920600929415.

Stoichev, T., E. Tessier, D. Amouroux, C. M. Almeida, M. C. P. Basto and V. M. Vasconcelos (2016). "Multiple regression analysis to assess the role of plankton on the distribution and speciation of mercury in water of a contaminated lagoon." J Hazard Mater **318**: 711-722. doi: 10.1016/j.jhazmat.2016.07.061.

Striegl, R. G., M. M. Dornblaser, C. P. McDonald, J. A. Rover and E. G. Stets (2012). "Carbon dioxide and methane emissions from the Yukon River system." Global Biogeochemical Cycles **26**(4). doi: 10.1029/2012gb004306.

Strobel, M.-B. (1998). "Les gens de l'or: Mémoire des orpailleurs créoles du Maroni." Ibis rouge éditions: p. 400.

Stupple, G. W., D. S. McLagan and A. Steffan (2018). In situ reactive gaseous mercury uptake on Radiello diffusive barrier, cation exchange membrane and Teflon filter membranes during atmospheric mercury depletion events. 14th International Conference on Mercury as a Global Pollutant, Krakow, Poland.

Suess, H. (1953). "Proceedings of the conference on nuclear processes in geological settings."

Sun, R., D. G. Streets, H. M. Horowitz, H. M. Amos, G. Liu, V. Perrot, J.-P. Toutain, H. Hintelmann, E. M. Sunderland, J. E. Sonke, J. D. Blum and R. Mason (2016). "Historical (1850–2010) mercury stable isotope inventory from anthropogenic sources to the atmosphere." Elementa: Science of the Anthropocene **4**. doi: 10.12952/journal.elementa.000091.

Szponar, N., C. M. Vega, J. Gerson, D. S. McLagan, M. Pillaca, S. Delgado, D. Lee, N. Rahman, L. E. Fernandez, E. S. Bernhardt, A. M. Kiefer, C. P. J. Mitchell, F. Wania and B. A. Bergquist (2025). "Tracing Atmospheric Mercury from Artisanal and Small-Scale Gold Mining." Environ Sci Technol. doi: 10.1021/acs.est.4c10521.

Tarras-Wahlberg, N. H., A. Flachier, S. N. Lane and O. Sangfors (2001). "Environmental impacts and metal exposure of aquatic ecosystems in rivers contaminated by small scale gold mining: the Puyango River basin, southern Ecuador." Sci Total Environ **278**(1-3): 239-261. doi: 10.1016/s0048-9697(01)00655-6.

Telmer, K., M. Costa, R. Simoes Angelica, E. S. Araujo and Y. Maurice (2006). "The source and fate of sediment and mercury in the Tapajos River, Para, Brazilian Amazon: Ground- and space-based evidence." J Environ Manage **81**(2): 101-113. doi: 10.1016/j.jenvman.2005.09.027.

Tessier, E., D. Amouroux, M. Grimaldi, T. Stoichev, C. Grimaldi, G. Dutin and O. F. X. Donard (2003). "Mercury mobilization in soil from a rainfall event in a Tropical forest (French Guyana)." Journal de Physique IV (Proceedings) **107**: 1301-1304. doi: 10.1051/jp4:20030539.

Thomassin, J.-F., P. Urien, L. Verneyre, C. N., G. R., D. Guillon, M. Boudrie, C. A., M. P., O. C. and T. D. (2017). "Exploration et exploitation minière en Guyane." Collection « La mine en France ».

Throback, I. N., K. Enwall, A. Jarvis and S. Hallin (2004). "Reassessing PCR primers targeting nirS, nirK and nosZ genes for community surveys of denitrifying bacteria with DGGE." FEMS Microbiol Ecol **49**(3): 401-417. doi: 10.1016/j.femsec.2004.04.011.

Tiessen, H., J. W. B. Stewart and C. V. Cole (1984). "Pathways of Phosphorus Transformations in Soils of Differing Pedogenesis." Soil Science Society of America Journal **48**(4): 853-858. doi: 10.2136/sssaj1984.03615995004800040031x.

Tisserand, D., D. Daval, L. Truche, A. Fernandez-Martinez, G. Sarret, L. Spadini and J. Nemery (2024). "Recommendations and good practices for dissolved organic carbon (DOC) analyses at low concentrations." MethodsX **12**: 102663. doi: 10.1016/j.mex.2024.102663.

Trükmann, K., R. Horn and E. Reintam (2009). "Impact Of Roots On Soil Stabilisation In Grassland." ISTRO 18 th Triennial Conference Proceedings.

Tsui, M. T.-K., J. D. Blum and S. Y. Kwon (2020). "Review of stable mercury isotopes in ecology and biogeochemistry." Science of The Total Environment **716**: 135386. doi: 10.1016/j.scitotenv.2019.135386.

Tsui, M. T. K., J. D. Blum, S. Y. Kwon, J. C. Finlay, S. J. Balogh and Y. H. Nollet (2012). "Sources and Transfers of Methylmercury in Adjacent River and Forest Food Webs." Environmental Science {\&} Technology **46**(20): 10957-10964.

Tudesque, L., G. Grenouillet, M. Gevrey, K. Khazraie and S. Brosse (2012). "Influence of small-scale gold mining on French Guiana streams: Are diatom assemblages valid disturbance sensors?" Ecological Indicators **14**(1): 100-106. doi: 10.1016/j.ecolind.2011.07.018.

Tufekcioglu, A., J. W. Raich, T. M. Isenhart and R. C. Schultz (1998). "Fine root dynamics, coarse root biomass, root distribution, and soil respiration in a multispecies riparian buffer in Central Iowa, USA." Agroforestry Systems **44**(2/3): 163-174. doi: 10.1023/a:1006221921806.

Vainio, E. J. and J. Hantula (2000). "Direct analysis of wood-inhabiting fungi using denaturing gradient gel electrophoresis of amplified ribosomal DNA." Mycological Research **104**(8): 927-936. doi: 10.1017/s0953756200002471.

Vanolli, B. S., N. de Andrade, L. P. Canisares, A. L. C. Franco, A. P. A. Pereira and M. R. Cherubin (2024). "Edaphic mesofauna responses to land use change for sugarcane cultivation: insights from contrasting soil textures." Frontiers in Ecology and Evolution **11**. doi: 10.3389/fevo.2023.1305115.

Veit, P. and P. Quijano Vallejos (2020). "COVID-19, Rising Gold Prices and Illegal Mining Threaten Indigenous Lands in the Amazon." World Resources Institute: Washington, DC, USA.

Velasquez Ramirez, M. G., C. M. Vega Ruiz, R. C. Gomringer, M. Pillaca, E. Thomas, P. M. Stewart, L. A. Gamarra Miranda, F. R. Danobeytia, J. A. Guerrero Barrantes, M. C. Gushiken, J. V. Bardales, M. Silman, L. Fernandez, C. Ascorra and D. D. C. Torres (2021). "Mercury in soils impacted by alluvial gold mining in the Peruvian Amazon." J Environ Manage **288**: 112364. doi: 10.1016/j.jenvman.2021.112364.

Veldkamp, E., M. Schmidt, J. S. Powers and M. D. Corre (2020). "Deforestation and reforestation impacts on soils in the tropics." Nature Reviews Earth & Environment **1**(11): 590-605. doi: 10.1038/s43017-020-0091-5.

Viers, J., G. Barroux, M. Pinelli, P. Seyler, P. Oliva, B. Dupre and G. R. Boaventura (2005). "The influence of the Amazonian floodplain ecosystems on the trace element dynamics of the Amazon River mainstem (Brazil)." Sci Total Environ **339**(1-3): 219-232. doi: 10.1016/j.scitotenv.2004.07.034.

Wagg, C., S. F. Bender, F. Widmer and M. G. van der Heijden (2014). "Soil biodiversity and soil community composition determine ecosystem multifunctionality." Proc Natl Acad Sci U S A **111**(14): 5266-5270. doi: 10.1073/pnas.1320054111.

Wallschläger, D., H. Hintelmann, R. D. Evans and R. D. Wilken (1995). "Volatilization of demethylmercury and elemental mercury from river Elbe floodplain soils." Water, Air, & Soil Pollution **80**(1-4): 1325-1329. doi: 10.1007/bf01189798.

Wang, X., Z. Bao, C. J. Lin, W. Yuan and X. Feng (2016). "Assessment of Global Mercury Deposition through Litterfall." Environ Sci Technol **50**(16): 8548-8557. doi: 10.1021/acs.est.5b06351.

Wang, Z., T. Sun, C. T. Driscoll, H. Zhang and X. Zhang (2019). "Dimethylmercury in Floodwaters of Mercury Contaminated Rice Paddies." Environ Sci Technol **53**(16): 9453-9461. doi: 10.1021/acs.est.8b07180.

Wang, Z., J. Tollervey, M. Briese, D. Turner and J. Ule (2009). "CLIP: construction of cDNA libraries for high-throughput sequencing from RNAs cross-linked to proteins in vivo." Methods **48**(3): 287-293. doi: 10.1016/j.ymeth.2009.02.021.

Wantzen, K. and J. Mol (2013). "Soil Erosion from Agriculture and Mining: A Threat to Tropical Stream Ecosystems." Agriculture **3**(4): 660-683. doi: 10.3390/agriculture3040660.

WHO (2021). "WHO guideline for the clinical management of exposure to lead." Geneva: World Health Organization.

Wiederhold, J. G. (2015). "Metal stable isotope signatures as tracers in environmental geochemistry." Environ Sci Technol **49**(5): 2606-2624. doi: 10.1021/es504683e.

Wiederhold, J. G., C. J. Cramer, K. Daniel, I. Infante, B. Bourdon and R. Kretzschmar (2010). "Equilibrium mercury isotope fractionation between dissolved Hg(II) species and thiol-bound Hg." Environ Sci Technol **44**(11): 4191-4197. doi: 10.1021/es100205t.

Wright, J. L., B. Bomfim, C. I. Wong, B. H. Marimon-Junior, B. S. Marimon and L. C. R. Silva (2021). "Sixteen hundred years of increasing tree cover prior to modern deforestation in Southern Amazon and Central Brazilian savannas." Glob Chang Biol **27**(1): 136-150. doi: 10.1111/gcb.15382.

Wright, L. P., L. Zhang and F. J. Marsik (2016). "Overview of mercury dry deposition, litterfall, and throughfall studies." Atmospheric Chemistry and Physics **16**(21): 13399-13416. doi: 10.5194/acp-16-13399-2016.

Wynn, J. G., M. I. Bird and V. N. L. Wong (2005). "Rayleigh distillation and the depth profile of 13C/12C ratios of soil organic carbon from soils of disparate texture in Iron Range National Park, Far North Queensland, Australia." Geochimica et Cosmochimica Acta **69**(8): 1961-1973. doi: 10.1016/j.gca.2004.09.003.

Xia, S., W. Yuan, L. Lin, X. Yang, X. Feng, X. Li, X. Liu, P. Chen, S. Zeng, D. Wang, Q. Su and X. Wang (2022). "Latitudinal gradient for mercury accumulation and isotopic evidence for post-depositional processes among three tropical forests in Southwest China." J Hazard Mater **429**: 128295. doi: 10.1016/j.jhazmat.2022.128295.

Xiao, X., C. M. Biradar, C. Czarnecki, T. Alabi and M. Keller (2009). "A Simple Algorithm for Large-Scale Mapping of Evergreen Forests in Tropical America, Africa and Asia." Remote Sensing **1**(3): 355-374. doi: 10.3390/rs1030355.

Xiong, J., L. Dong, J. Lu, W. Hu, H. Gong, S. Xie, D. Zhao, Y. Zhang, X. Wang, Y. Deng, J. Ran, K. J. Niklas, A. Degen and J. Deng (2021). "Variation in plant carbon, nitrogen and phosphorus contents across the drylands of China." Functional Ecology **36**(1): 174-186. doi: 10.1111/1365-2435.13937.

Yamada, T. and Y. Sekiguchi (2018). "Anaerolineae." Bergey's Manual of Systematics of Archaea and Bacteria: 1-2. doi: 10.1002/9781118960608.cbm00064.

Yamakawa, A., D. Amouroux, E. Tessier, S. Berail, I. Fettig, J. P. G. Barre, J. Koschorreck, H. Rudel and O. F. X. Donard (2021). "Hg isotopic composition of one-year-old spruce shoots: Application to long-term Hg atmospheric monitoring in Germany." Chemosphere **279**: 130631. doi: 10.1016/j.chemosphere.2021.130631.

Yao, J.-j., J.-h. Cheng, Z.-d. Zhou, L. Sun and H.-j. Zhang (2018). "Effects of herbaceous vegetation coverage and rainfall intensity on splash characteristics in northern China." Catena **167**: 411-421. doi: 10.1016/j.catena.2018.05.019.

Yin, R., X. Feng and B. Meng (2013). "Stable mercury isotope variation in rice plants (Oryza sativa L.) from the Wanshan mercury mining district, SW China." Environ Sci Technol **47**(5): 2238-2245. doi: 10.1021/es304302a.

Yin, R., X. Feng and W. Shi (2010). "Application of the stable-isotope system to the study of sources and fate of Hg in the environment: A review." Applied Geochemistry **25**(10): 1467-1477. doi: 10.1016/j.apgeochem.2010.07.007.

Yuan, W., X. Wang, C. J. Lin, J. O. Sommar, B. Wang, Z. Lu and X. Feng (2021). "Quantification of Atmospheric Mercury Deposition to and Legacy Re-emission from a Subtropical Forest Floor by Mercury Isotopes." Environ Sci Technol **55**(18): 12352-12361. doi: 10.1021/acs.est.1c02744.

Zhang, H., X. Fu, X. Wang and X. Feng (2019). "Measurements and Distribution of Atmospheric Particulate-Bound Mercury: A Review." Bull Environ Contam Toxicol **103**(1): 48-54. doi: 10.1007/s00128-019-02663-5.

Zhang, J.-Y., P. F. Gu, L. Y. Li, L. Y. Zong and W.-J. Zhao (2016). "Changes of soil particle size fraction along a chronosequence in sandy desertified land: a fundamental process for ecosystem succession and ecological restoration." Journal of Soils and Sediments **16**(12): 2651-2656. doi: 10.1007/s11368-016-1454-x.

Zheng, W. and H. Hintelmann (2010). "Nuclear field shift effect in isotope fractionation of mercury during abiotic reduction in the absence of light." J Phys Chem A **114**(12): 4238-4245. doi: 10.1021/jp910353y.

Zinger, L., P. Taberlet, H. Schimann, A. Bonin, F. Boyer, M. De Barba, P. Gaucher, L. Gielly, C. Giguet-Covex, A. Iribar, M. Rejou-Mechain, G. Raye, D. Rioux, V. Schilling, B. Tymen, J. Viers, C. Zouiten, W. Thuiller, E. Coissac and J. Chave (2019). "Body size determines soil community assembly in a tropical forest." Mol Ecol **28**(3): 528-543. doi: 10.1111/mec.14919.